The Influence of the Drainage Regime on the Installation and the Response to Vertical Cyclic Loading of Suction Caissons

Vom Promotionsausschuss der
Technischen Universität Hamburg

zur Erlangung des akademischen Grades

Doktor-Ingenieur (Dr.-Ing.)

genehmigte Dissertation

von
Marc Stapelfeldt

aus
Reinbek

2020

1. Gutachter:	Univ.-Prof. Dr.-Ing. Jürgen Grabe
2. Gutachter:	Univ.-Prof. Dr.-Ing. Frank Rackwitz
3. Gutachter:	Univ.-Prof. Dr.-Ing. habil. Alexander Düster

Tag der mündlichen Prüfung: 17.11.2020

Contents

1 Introduction 1

2 Previous research 5

2.1 Suction caissons for offshore wind turbines 5
2.2 Suction caisson installation 6
2.3 Installation and load bearing behaviour in sand 6
2.4 Installation and load bearing behaviour in layered soil 8

3 Objectives 11

4 Methods 13

4.1 Centrifuge tests 13
    4.1.1 Centrifuge testing for offshore geotechnical engineering 13
    4.1.2 Scaling laws for centrifuge tests in saturated soil 15
    4.1.3 Digital image correlation in a centrifuge environment 16
4.2 Material point method 16
    4.2.1 General concept 16
    4.2.2 Axisymmetric material point method 18
    4.2.3 Boundary conditions on material points 20
    4.2.4 Implementation of the axisymmetric formulation 21
4.3 Finite element method 23
    4.3.1 Requirements for the numerical modelling of suction caissons 23
    4.3.2 Modelling approach for the detachment of the caisson lid 25
    4.3.3 Constitutive modelling 25
4.4 Analytical prediction method 26
    4.4.1 General concept and basic assumptions 27
    4.4.2 Calculation scheme for compression 27
    4.4.3 Calculation scheme for tension 28

5 Installation in sand 31

5.1 Centrifuge tests 31
    5.1.1 Experimental arrangement and testing procedure 31
    5.1.2 Results and discussion 37
    5.1.3 Remarks on the centrifuge tests 44
5.2 Numerical simulations 45
    5.2.1 Numerical modelling and testing procedure 46
    5.2.2 Results and discussion 48
    5.2.3 Remarks on the numerical simulations 59
5.3 Concluding remarks on the suction caisson installation in sand 59

6 Load bearing behaviour in sand **61**
6.1 Centrifuge tests . . . 61
6.1.1 Experimental arrangement and testing procedure . . . 61
6.1.2 Results and discussion . . . 64
6.1.3 Remarks on the centrifuge tests . . . 73
6.2 Numerical simulations . . . 73
6.2.1 Numerical modelling and testing procedure . . . 73
6.2.2 Results and discussion . . . 76
6.2.3 Remarks on the numerical simulations . . . 84
6.3 Simplified prediction method . . . 84
6.4 Concluding remarks on the response to vertical cyclic loading in sand . . . 86

7 Installation in layered soil **89**
7.1 Centrifuge tests . . . 89
7.1.1 Experimental arrangement and testing procedure . . . 89
7.1.2 Results and discussion . . . 97
7.1.3 Remarks on the centrifuge tests . . . 105
7.2 Numerical simulations . . . 105
7.2.1 Numerical modelling and testing procedure . . . 105
7.2.2 Results and discussion . . . 108
7.2.3 Remarks on the numerical simulations . . . 126
7.3 Concluding remarks on the suction caisson installation in layered soil . . . 127

8 Load bearing behaviour in layered soil **129**
8.1 Centrifuge tests . . . 129
8.1.1 Experimental arrangement and testing procedure . . . 129
8.1.2 Results and discussion: sand over clay . . . 131
8.1.3 Results and discussion: clay over sand . . . 141
8.1.4 Remarks on the centrifuge tests . . . 150
8.2 Numerical simulations . . . 151
8.2.1 Numerical modelling and testing procedure . . . 151
8.2.2 Results and discussion: sand over clay . . . 154
8.2.3 Results and discussion: clay over sand . . . 161
8.2.4 Remarks on the numerical simulations . . . 167
8.3 Concluding remarks on the response to vertical cyclic loading in layered soil 168

9 Conclusion **171**
9.1 Sand . . . 171
9.2 Layered soil . . . 172
9.2.1 Sand over clay . . . 172
9.2.2 Clay over sand . . . 173
9.3 Concluding remarks . . . 174

10 Summary **177**

Appendix A Notation **179**

Appendix B Experimental arrangement **187**
B.1 Centrifuge tests featuring CPTs inside the caisson in sand 187
B.2 Centrifuge tests featuring cyclic loading test in sand 192
B.3 Centrifuge tests featuring PIV post-analyses in layered soil 193
B.4 Centrifuge tests featuring cyclic loading test in layered soil 195

1 Introduction

The climate change has emerged to be an omnipresent challenge today. Following an era characterised by a relentless demand of energy – fossil fuels in particular – the climate change is not just the severe consequence of the industrialised world, but a major challenge for our society today and especially for engineers. Civil engineering's basic task is enabling modern human life. This implies a superior influence on the environment and therefore a key role opposing the climate crisis. The targeted abandonment from primarily fossil towards renewable energy sources is one of the major tasks for today's engineers. Electric power produced in wind farms is expected to provide a substantial share of the future energy mix. In order to achieve this milestone towards carbon neutral energy supply, numerous offshore wind farms have to be commissioned in the future.

The German sector of the North Sea, for example, has been subjected to reasonable development activity in the past two decades. However, further developments imply additional challenges, i. e. increasing water depth and soil characteristics changing from predominately dense sand towards layered soil profiles. This is a particular challenge for the design of foundation systems for offshore wind turbines because these structures differ considerably from platforms that were installed for oil and gas productions.

Figure 1.1a demonstrates the dimensions of the Troll A platform. The Troll A support structure is still the largest single object that has ever been moved and installed offshore. This massive concrete structure supports one of the largest platforms servicing as a gas producing facility at the Norwegian North Sea. Another remarkable mile stone in offshore engineering is the Draupner E platform, which is also located in the Norwegian North Sea. This platform withstood one of the largest waves that was ever detected by measuring equipment: The Draupner E platform survived the impact of a 25.7 m high wave without damage despite the occurrence of tensile loads that exceeded the original design parameters (Hansteen et al., 2003). Both platforms are not just important because they are an integral part of Europe's gas supply, but their history contains lessons for the future: The Troll A and the Draupner E are based on suction caisson foundations, which are a suitable technology for many future offshore wind farm developments (Tjelta, 2015). Furthermore, the monster wave example showed the capability of this technology. However, the comparison between the massive Toll A and the offshore wind turbine shown in Figure 1.1b demonstrates substantial differences: Offshore wind turbines are significantly smaller, lighter and the centre of gravity is located at a relatively high altitude due to the nacelle and rotor position compared to the gas platform with its massive underwater support structure and storage tanks.

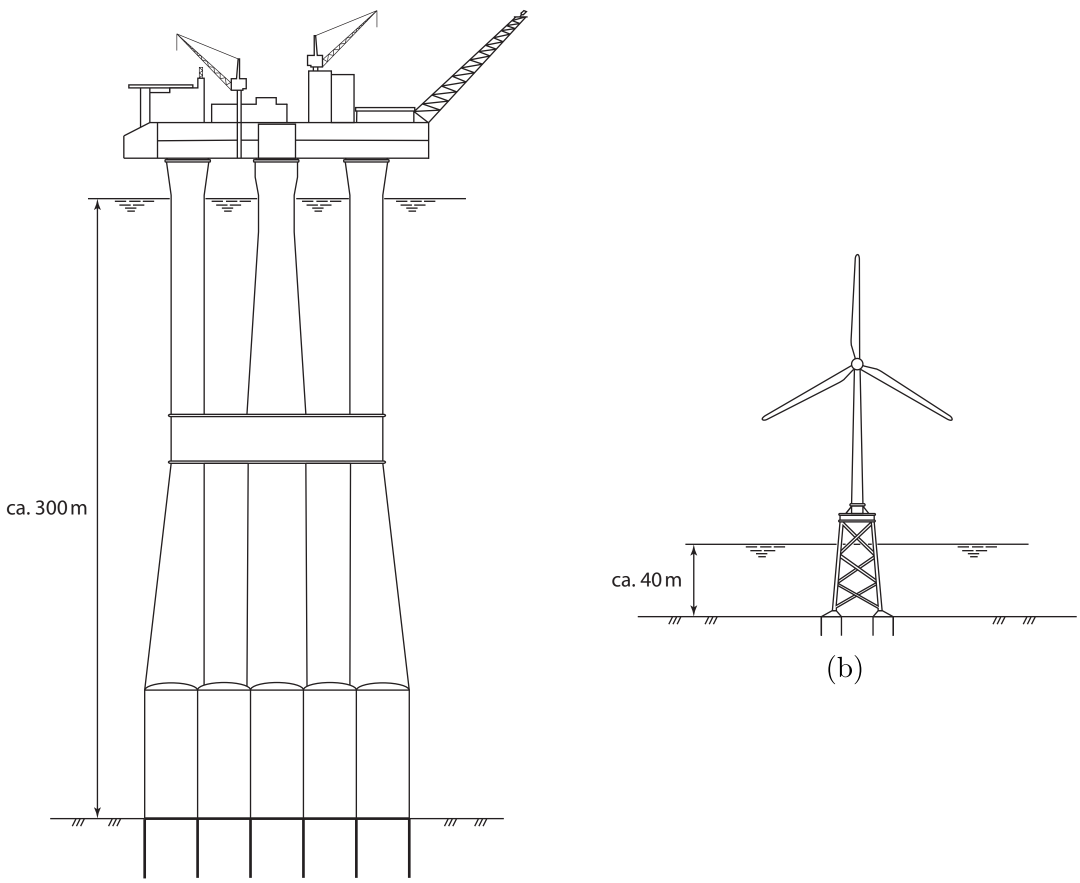

(a)

(b)

Figure 1.1: Suction caisson supported platform Troll A (a) and offshore wind turbine (b).

Hence, the technology transfer that started almost two decades ago (Byrne et al., 2002; Ibsen et al., 2005) must be continued in order to unlock the full potential of suction caisson foundations for offshore wind turbines. Current issues like a potential effect of the suction caisson installation on the in-service performance or the cyclic load bearing behaviour including excursions into tension need to be investigated. Furthermore, research on the utilisation of suction caissons supporting offshore wind turbines at locations that feature layered soil profiles is required: The understanding of the influence of low permeable layers on the suction installation and the load bearing behaviour is limited to date.

However, research on offshore technology implies a few challenges: Offshore platforms are usually located at remote locations, which are hardly accessible. There are foundations embedded below the sea floor in considerable water depth – a location that is basically impossible to reach. Offshore structures are extremely huge and therefore can not be manipulated without heavy equipment. Furthermore, the return period of the Draupner E monster wave was calculated to be 50 to 100 years (Hansteen et al., 2003). This loading scenario is hardly reproducible but nonetheless interesting in a research context. Consequently, emulating the sea floor environment in a laboratory and utilising a computer based numerical models are the most viable research methods.

Centrifuge experiments are particularly useful in order to study offshore foundation systems at a laboratory scale (Randolph and Gaudin, 2017). This thesis therefore contains multiple series of centrifuge tests investigating the installation and load bearing behaviour of suction caissons. The complied experimental data base adds comprehensive insights into current topics of research. However, centrifuge testing is complex, certainly time consuming and therefore only partially applicable on an industrial project scale. Therefore, virtual and almost universally accessible numerical models are developed and evaluated.

The drainage regime determines the course of the suction caisson installation and the load bearing behaviour. Changes of the pore water pressure inside the caisson crucially depend on the effective permeability. Soil profiles containing high permeable sand and low permeable clay layers add complexity to the mechanisms underlying the suction installation and the load bearing behaviour. The interplay of tip resistance, skirt friction, and internal pore water pressure depends on the drainage regime and determines the caisson performance during the suction installation and when subjected to vertical cyclic loading. The conducted experimental and numerical investigations considering the influence on the drainage regime on the installation and the vertical cyclic load bearing behaviour aim to reinforce certainty towards the design of suction caisson foundations for offshore wind turbines.

Hence, the presented work is dedicated to support the fight against mankind's arguably most threatening challenge: the climate change.

2 Previous research

2.1 Suction caissons for offshore wind turbines

Goodman (1961) published one of the first feasibility studies on the application of suction installed offshore foundation systems. Suction caissons, also called suction buckets, and suction anchors have been employed to support bottom fixed offshore platforms and anchor floating structures. Suction anchors typically feature large aspect ratios of $L/D \geq 2$, where L is the skirt length and D is the diameter. An eyelet connects a mooring line, which is subjected to tensile loads, to a suction anchor. These structures are utilised within mooring systems of floating oil and gas platforms, typically located in deep waters featuring seabeds that mainly consist of cohesive soil (Randolph et al., 1998; Colliat, 2002; Jostad and Andersen, 2015). Suction caissons, characterised by approximate aspect ratios of $L/D \leq 1$, are utilised to support gravity based concrete structures and bottom fixed jacket platforms. These structures are typically located in water depths of approximately $50 < h_w < 400\,\mathrm{m}$. Platforms were installed in various soil conditions, including both, sand and clay layers. Oil and gas platforms – supported by concrete and steel structures – are usually heavy because of the topside facilities. Hence, caisson foundations are subject to significant compressive loading (Hansen et al., 1992; Tjelta, 1994; Bye et al., 1995).

The utilisation of suction caisson foundations for bottom fixed offshore wind turbines (OWTs) adds to the range of the previously introduced applications. OWTs are significantly lighter than most oil and gas platforms. In addition, the centre of gravity is located at a high altitude, which is challenging – especially for an operational state in high velocity wind fields. Consequently, the vertical loads on the windward caissons of multipod jacket structures are small or even tensile, depending on the spacing between the caissons. Caisson foundations for OWTs typically feature aspect ratios between $0.5 \leq L/D \leq 1$. Caisson based jacked structures can be installed in shallow water depth as well as in waters deeper than $h_w = 50\,\mathrm{m}$ (Byrne et al., 2002; Bienen et al., 2018a).

Besides multipod jacket structures, OWTs can also be based on a single suction caisson. The loading regime of monopod structures is characterised by horizontal and momentum loading, rather than compressive and tensile loading. Monopods are large diameter structures with aspect ratios between $0.5 \leq L/D \leq 1$. This type of caisson foundation is suitable for a maximum water depth of $h_w \approx 50\,\mathrm{m}$ (Byrne et al., 2002; Ibsen et al., 2005; Nielsen et al., 2015).

2.2 Suction caisson installation

The suction caisson installation presented in Figure 2.1 starts with the caisson penetrating into the soil due to its self-weight and with a venting valve, before the actual suction installation commences. Therefore, suction pressure is generated inside the caisson while the valve is connected to a pumping system. The suction pressure provides an additional downward force that enables further penetration. Seepage flow additionally results in relatively high permeable soil due to the differential pressure between the caisson internal and ambient. The seepage flow reduces the tip resistance σ_{tip} and ensures further caisson penetration – even in dense and very dense sand (Tjelta, 1995; Houlsby et al., 2005).

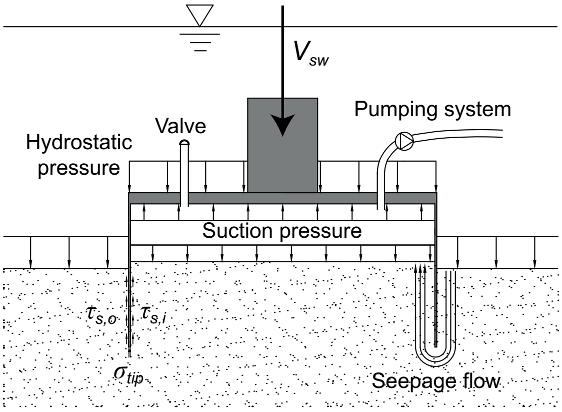

Figure 2.1: Suction installation in sand.

The suction installation in clay or sand can be predicted by different approaches published by Houlsby and Byrne (2005b), Houlsby and Byrne (2005a), Andersen et al. (2008) or Senders and Randolph (2009) for example.

2.3 Installation and load bearing behaviour in sand

Experience with suction caisson foundations for OWTs is limited to date. Monopod caisson were installed for academic studies at a test side in Frederikshavn (Ibsen, 2008), at offshore sites in the Horns Rev 2, and Dogger Bank wind farm (Tjelta, 2015). A suction caisson jacket was installed during the Borkum Riffgrund development in 2014 (Tjelta, 2015). Furthermore, Kelly et al. (2006a) and Houlsby et al. (2006) installed a single medium scale caisson near shore at Bothkennar and Luce Bay that was tested with a loading rig.

Small scale lab tests – mainly using a pressure chamber – were performed and published by Byrne and Houlsby (2002), Byrne and Houlsby (2004), Houlsby and Byrne (2005b), and Kelly et al. (2006b). Among others Foglia et al. (2012) and Nielsen et al. (2015) added to the existing database utilising similar small scale set-ups. Allersma et al. (2000) performed small scale experiments at $1g$ and $150g$ in a centrifuge. Based on the comparison to an extraction test, Allersma et al. (2000) demonstrated the importance of the stress level during the experiments. This comparison has been showing that dilatancy leads to different behaviour at low stress levels compared to prototype stress levels. Hence, a centrifuge environment that provides an increased g-level is required to reproduce prototype load bearing behaviour within a small scale test set-up.

Allersma (2003) and Allersma et al. (2000) also investigated the horizontal bearing capacity and the cyclic load bearing behaviour. Kita et al. (2018) performed similar centrifuge tests with different soil properties and investigated the surface deformation through camera observation. Fiumana et al. (2018) examined the extraction resistance of a suction caisson in sand. They utilised a system that was operated in-flight and actively generated suction pressure inside the caisson during the extraction. This apparatus was employed to demonstrate how active suction influences the extraction resistance of suction caissons embedded in sand. However, none of these studies included suction installation. Allersma et al. (1997) and Allersma et al. (2001) presented one of the first suction installations in a centrifuge environment and confirmed phenomena like the reduction of tip resistance and skirt friction due to seepage flow for instance. Allersma et al. (1997) also pointed out that further investigations have been required.

Among others M. N. Tran et al. (2004) and M. N. Tran (2005), M. N. Tran and Randolph (2008), and later Bienen et al. (2018a) performed centrifuge tests in sand which included controlled self-weight and in-flight suction installation. Ragni et al. (2018) and Ragni et al. (2019) present related studies where a half-model caisson was installed, while a perspex widow enabled particle image velocimetry (PIV) post analysis of the self-weight and suction installation (Stanier and White, 2013; Stanier et al., 2016a). The results of the image analysis indicate that suction installation can loosen the soil plug (Ragni et al., 2018; Ragni et al., 2019). However, this effect appears to be temporary, because investigations on the response to vertical cyclic loading appeared to be only marginally affected (Bienen et al., 2018b; Bienen et al., 2018a). Instead, the drainage conditions were found to govern the load-displacement behaviour of a suction caisson foundation (Bienen et al., 2018a).

Numerous studies – e. g. Achmus et al. (2013), Stapelfeldt et al. (2015), and Cerfontaine et al. (2016) – present results of investigations on the vertical load bearing behaviour of suction caissons for OWTs in sand utilising numerical simulations. Numerical studies have been limited in the past, because hardly any comprehensive experimental data was available for validation. This also often holds for simulations of monopod structures subjected to combined horizontal and momentum loading (Achmus et al., 2013; N. X. Tran et al., 2017; Skau et al., 2019). However, other investigations on the vertical or horizontal bearing capacity were validated through large scale model tests (Larsen, 2008; M. Liu et al., 2017) for example. Simulated extraction tests might be an exception here, as several validated studies employing similar numerical models exist (Achmus and Thieken, 2014; Shen et al., 2017; Whyte et al., 2020).

Despite a relatively large database for suction caisson installations compared to test results featuring cyclic loading, simulations of the suction caisson installation in sand are hardly available. Existing numerical models usually cover purely hydraulic calculations (M. N. Tran, 2005) or jacked installation (Zeinoddini et al., 2011). Furthermore, the structural behaviour of the caisson was investigated. Madsen et al. (2013) addressed buckling failure of a thin walled caisson for instance.

As prototype data often remains confidential and the existing experimental database was limited before recent additions, uncertainties regarding the suction installation and the in-service load bearing behaviour in sand still exist. A possible influence of the suction installation on the load bearing behaviour can not be ruled out yet. Further insights into the installation mechanism in sand are required. Furthermore, numerical simulations are naturally underdeveloped compared to physical models – especially because validation through comparison to experimental data is required. This applies in particular to the numerical modelling of the suction caisson installation in sand.

2.4 Installation and load bearing behaviour in layered soil

Offshore wind farms spread out in new areas with the growing demand of renewable energy. Consequently, the wind farm development locations shift from shallow water depths and predominantly sandy sea beds towards deeper water and sea beds often characterised by layered soil profiles. A suction anchor installation in the far south west of the Danish sector of the North Sea (Senpere and Auvergne, 1982) shows a possible environment for future offshore wind farms: This location features a water depth of $h_w \approx 40\,\text{m}$ and the sea bed consist of sand over clay (SoC). Suction caissons were also successfully installed and removed at shallow and deep water sites with a sea bed that contained clay over sand (CoS) and interbedded profiles during oil and gas field developments, e. g. located in the Norwegian and British sector of the North Sea or in the Gulf of Mexico (Tjelta et al., 1986; Watson et al., 2006; Broughton et al., 2013).

Tjelta (2015) concluded that suction caissons can be installed at any location at the North Sea. Bottom fixed jacket structures are expected to support OWTs located in water depths of $h_w \geq 40\,\text{m}$. Steel-made suction caissons with typical aspect ratios between $0.5 \leq L/D \leq 1$ are a suitable foundation system for such offshore platforms. With wall thickness t and diameter D ratios ranging from $t/D \approx 1/100$ to $t/D \approx 1/250$, these structures are relatively thin-walled in comparison to concrete caisson foundations typically featuring a skirt thickness of several decimetres (Tjelta et al., 1990; Masui et al., 2001; Tjelta, 2015).

Expertise regarding suction caisson foundations for OWTs in layered soil hardly exist and accessible data is restricted to experimental studies. The installation in layered soil was addressed in a limited number of small scale laboratory tests and centrifuge experiments (Raines et al., 2005; M. N. Tran, 2005; Watson et al., 2006; Senders and Randolph, 2007; Cotter, 2010). Investigations of different soil layer specifications demonstrated that a low permeable layer underlying sand yields an installation mode that is comparable to the installation in homogeneous clay. A low permeable layer overlying sand was found to prevent seepage flow within the sand, which eventually leads to premature refusal. Consequently, the installation in layered soils was initially evaluated to be problematical (Houlsby and

Byrne, 2005a). However, M. N. Tran (2005) and M. N. Tran et al. (2007) pointed out that an uplift of the soil plug might transfer the suction pressure into the underlying sand layer. Thus, seepage is expected to reduce the skirt tip resistance, which is known to facilitate the suction installation. Ragni et al. (2020) recently extended their studies towards layered soil profiles. This study underpins the feasibility of a suction caisson installation in SoC and CoS. Furthermore, the blockage of seepage flow due to a low permeable top-layer was reinforced. It was also found that clay plug uplift indeed transferred suction pressure into the underlying sand layer and does not necessarily lead to premature refusal. A high pumping flow rate was found to be beneficial regarding the achievable penetration depth.

Jeong et al. (2018) and Zografou et al. (2019) performed centrifuge tests on suction caisson foundations subjected to vertical cyclic loading in homogeneous sand or clay, respectively. Zhu et al. (2017), Zhu et al. (2018a), and Zhu et al. (2018b) published the only existing centrifuge test on suction caisson foundations embedded in sand over clay and subjected to cyclic loading. However, monopod caissons and therefore lateral and momentum loading were addressed. Without published prototype data, hardly any knowledge is available for suction caissons in layered soil that are subjected to vertical cyclic loading.

This also holds for studies based on numerical simulations. M. N. Tran (2005) and M. N. Tran et al. (2007) presented results obtained from numerical analyses that target the development of seepage flow around a fixed caisson skirt. These results underpin centrifuge experiments that showed that a low permeable silt layer effectively reduces the seepage flow into the caisson. Based on numerical analyses it was concluded that the suction pressure must be transferred to the underlying sand layer. The results published by Ibsen and Thilsted (2010) where obtained from a similar methodology employing large scale tests and numerical simulations for investigations on piping limits for the suction caisson installation in layered sand. Kim et al. (2013) utilised a centrifuge test and numerical simulations investigating the load bearing behaviour of a monopod suction caisson foundation in a stratified sand and silt profile. Kim et al. (2013) identified the vertical load, the elastic stiffness modulus and the shear strength as key parameters for the response to combined loading in layered soil under consideration of a specific prototype application. However, the prototype data was not published by Kim et al. (2013).

The existing database of numerical situations shows diverse soil profiles despite the limited number of publications. Each publication listed above includes comparison and validation with experimental data. However, a comprehensive study including investigations on the suction installation and the vertical load bearing behaviour in layered soils does not exist to the author's knowledge. This holds particularly for studies employing numerical simulations, because a database consisting of reproducible experimental data, which is required for validation of numerical models, is not available yet.

3 Objectives

The load displacement behaviour and a possible effect of the suction installation – especially when it comes to low magnitude compressive or tensile vertical loading – are crucial to the serviceability limit state of an OWT. Further investigations are necessary to increase confidence in the caisson foundation technology. As uniform dense sand and layered soils were found to be expected in regions of potential offshore wind farm developments, both are to be investigated. Uniform sand soil profiles are addressed first. SoC and CoS profiles are targeted secondly.

A first dual series of centrifuge tests was planned: The presented experiments aim to build on the latest test results published by Bienen et al. (2018a), Bienen et al. (2018b), Ragni et al. (2018), and Ragni et al. (2019). Numerical simulations are employed under consideration of the experimental results in order to provide additional insights. Both methods were utilised to target the following questions:

- Considerable seepage is present in the soil plug during suction installation, depending on the pumping flow rate. To what extend are the achievable penetration depth or the in-service foundation performance affected by the suction installation?
- The effective permeability and therefore the drainage regime is expected to affect the response to vertical cyclic loading. What level of tensile loads can safely be carried without considerable heave, i. e. without compromising serviceability criteria?

The second research package includes another dual series of centrifuge tests. The suction caisson installation into SoC and CoS as well as the response under subsequent subjected to vertical cyclic loading are targeted through centrifuge tests. Full model tests will be complemented by half-model tests with particle image velocimetry (PIV) post analysis of the images captured through a perspex window during the experiment in order to reveal the underlying mechanisms. Hence, the following questions are targeted:

- Phenomena like sudden rapid penetration into the clay layer underlying sand or clay plug uplift during penetration in CoS can occur during the suction installation in layered soil. Do consequences arise for the achievable penetration depth or in-service foundation performance from the suction installation?
- Layered soil profiles are alternating the drainage regime and therefore the underlying load transfer mechanisms. How can vertical cyclic loads including significant excursions into tension be sustained in SoC and CoS without compromising serviceability criteria?

4 Methods

The objectives are addressed through different methods. In general, each investigation that was carried out contains two methods: physical and numerical modelling. The mandatory comparison between both methods ensures validated results. Three different physical modelling set-ups were employed for the investigations on the suction caisson installation, while one of the set-ups also allowed cyclic loading tests. Furthermore, the small deformation based numerical model utilised for investigations on the load bearing behaviour of a caisson foundation does not capture the suction caisson installation. Hence, a second numerical model capturing large deformations was utilised. Consequently, a total of three physical modelling set-ups and two different numerical methods are required to provide insights into the suction caisson installation and the response to vertical cyclic loading in sand and layered soil profiles. In addition, this approach enabled the development of an analytical prediction method for the cyclic load bearing behaviour of suction caissons subjected to compressive and tensile vertical loading.

4.1 Centrifuge tests

4.1.1 Centrifuge testing for offshore geotechnical engineering

The first ideas of centrifuge testing in geotechnical engineering date back to the nineteenth century. However, the first centrifuge tests were not conducted before the early nineteen-thirties in Russia and the United States of America. Interrupted by the Second World War, researchers in England, Japan, Russia, and the United States of America dedicated their work to centrifuge testing and published more than 400 papers until the early nineteen-eighties. This reinforced centrifuge testing in geotechnical engineering (Taylor, 2011). The establishment of a centrifuge laboratory at the University of Western Australia (UWA) in Perth arguably spurred research on offshore foundations in the early nineteen-nineties. The Acutronic Model 661 beam centrifuge was utilised for countless testing series yielding in a remarkable number of publications. The C661 is still operated by the National Geotechnical Centrifuge Facility at the UWA (Randolph and Gaudin, 2017).

Research in offshore geotechnical engineering is challenged by two major difficulties: Everything of interest is underwater, which is hardly accessible for humans. Foundation systems are often embedded in the sea bed, a location that is arguably impossible to reach. Consequently, it appears to be obvious to shrink the sea bottom and relocate it into a laboratory. This move implies several requirements and advantages:

- The soil stress level at the laboratory has to be similar to the stress level offshore. This is particularity important when model foundations at reduced size are tested.

- The drainage conditions must be replicated correctly in the laboratory.
- The offshore installation techniques have to be recreated in the laboratory.
- Loading scenarios occurring offshore must be reproduced at the laboratory scale.
- An overall reduction of the soil sample and foundation size facilitates testing.
- A laboratory environment enables controlled preparation of the soil sample which reduces uncertainties and ensures repeatability of the experiments.
- Appropriate laboratory equipment enables investigations on extreme loading scenarios that hardly occur offshore, but could lead to catastrophic consequences.

Centrifuge testing matches all the listed requirements. The establishment of a realistic stress level and a suitable drainage regime are particularly important for centrifuge tests featuring suction caisson foundations. A suction caisson extraction from sand for instance demonstrates the importance: Allersma et al. (2000) compared a small scale model caisson test conducted at $1g$ and the same tests performed in a centrifuge at $150g$. This test demonstrated, that the stress level altered the load bearing behaviour, which is obvious since the internal friction and the dilatancy of soil are stress dependent (Lehane and Q. B. Liu, 2013). Furthermore, the drainage regime has a major influence on the load bearing behaviour of suction caissons – especially in relatively high permeable soil. Among others Tan and Scott (1987) and Taylor (2011) pointed out that the manipulation of the pore fluid viscosity is a proven technique to establish the required drainage regime.

Remote actuation inside a spinning centrifuge is a key technology, especially for more complex model set-ups like the suction caisson installation: The caisson installation requires a vertical actuator that is equipped with a load control system to imitate the self-weight. An in-flight manipulatable valve and a pumping system (House, 2002), i. e. two additional actuators, are required to enable the suction installation. Bearing in mind that this equipment travels at approximately $v = 200\,\mathrm{km/h}$ illustrates the complexity of a suction caisson installation in a centrifuge environment.

This thesis features a centrifuge test set-up that required further development within the scope of this thesis. The performance of an in-flight suction caisson installation with a subsequent cone penetration test (CPT) inside the caisson required the dual use of the vertical actuator. The vertical actuator carried a floating model caisson and the cone penetrometer and therefore enabled – to the author's knowledge – the first ever in-flight CPT inside a suction caisson without stopping the centrifuge. Further details and results are presented in chapter 5.

The investigation of the suction caisson installation in layered soil profiles required the utilisation of an even more sophisticated set-up: A half-model caisson was pressed against a perspex window with the horizontal axis of the actuator. In addition, two machine cameras recorded photographs from the outside of the perspex window. Hence, a total number of four actuator channels and two cameras – in addition to at least two other cameras providing views on crucial parts of the test set-up – were utilised simultaneously. The centrifuge test set-up enabling PIV post analyses of the suction caisson installation has been originally developed by Ragni et al. (2018). This thesis features the first successful reproduction of this testing set-up to the author's knowledge. Further details and results are presented in Chapter 7.

4.1.2 Scaling laws for centrifuge tests in saturated soil

Centrifuge modelling facilitates the achievement of similarity between a small scale model and the prototype. The N-times increased gravity yields a stress field which is similar to a prototype that is N-times larger than the model. The scaling factor for linear dimensions is $1 : N$. Consequently, strains and stresses are similar at prototype and model scale. This yields a scaling factor for forces of $1 : N^2$ (Taylor, 2011).

Centrifuge set-ups featuring saturated soil interacting with structures and therefore modelling consolidation and seepage flow require a modification of the pore fluid or the loading rate, because the time scaling factors for consolidation $1 : N^2$ and dynamic motion $1 : N$ differ. Utilising a pore fluid with an N-times increased dynamic viscosity η – e. g. silicone oil or methyl cellulose ether diluted in water – syncs the time scaling factors. Hence, similarity can be achieved (Taylor, 2011).

Taylor (2011) referred that a centrifuge is not a time machine, albeit it is mentioned, that consolidation processes can be modelled $1 : N^2$ faster than in prototype scale or earthquake events can be modelled N-times faster due to an increased model frequency $f_m = N f_p$, without violating similarity. However, time elapses at the same pace in the centrifuge as it does outside. Consequently, similarity is also reached taking a time scaling factor of $1 : 1$ into account and adapting the model velocity time scaling factors in accordance to the adapted linear dimensions. The scaling factors applying here are summarised in Table 4.1.

Table 4.1: Scaling factors (model : prototype) for centrifuge tests with and without increased pore fluid viscosity η.

Parameter	Dimension	Scaling factors	
		$(\eta_m = \eta_p)$	$(\eta_m = N\eta_p)$
Length, Displacement	L	$1 : N$	$1 : N$
Strain	LL^{-1}	$1 : 1$	$1 : 1$
Stress	FL^{-2}	$1 : 1$	$1 : 1$
Force	F	$1 : N^2$	$1 : N^2$
Time (consolidation)	T	$1 : N^2$	$1 : N$
Effective permeability	LT^{-1}	$1 : 1$	$N : 1$
Velocity (seepage flow)	LT^{-1}	$1 : N$	$1 : 1$
Time (motion)	T	$1 : N$	$1 : N$
Velocity (motion)	LT^{-1}	$1 : 1$	$1 : 1$

The artificially increased effective model permeability – $k_{f,m} = Nk_{f,p}$ practically implies that the pore fluid flows N-times slower in the model compared to the prototype. Since the model dimensions are N-times smaller compared to the prototype, similarity is satisfied only when the time is scaled $1 : 1$, i. e. the model test are conducted at real time. For instance, a caisson displacement amplitude of $a_m = 1\,\mathrm{mm}$ in model scale corresponds to a prototype displacement amplitude of $a_p = 10\,\mathrm{cm}$, while the frequency is $f_m = f_p$ and therefore the loading rate is $(\frac{V/A}{T})_m = N(\frac{V/A}{T})_p$. This is consistent with the hydraulic gradient $i_m = Ni_p$, i. e. the ratio of the pressure differential and length (Taylor, 2011).

4.1.3 Digital image correlation in a centrifuge environment

The measurement of soil deformations is one of the key tasks in geotechnical experiments. Measuring large scale deformation fields is challenging using sensing equipment only. Methods including the recording and analysing of images like x-ray and magnetic resonance imaging or digital image correlation (DIC) and PIV are able to provide insights beyond sensor based measurements (Stanier et al., 2016a). The DIC (Adrian, 1991) widely known as PIV (Sutton et al., 1983) evolved to be a proven method that is also applicable to investigate soil structure interaction in clay (Mana et al., 2012) and sand (Ragni et al., 2018) in centrifuge experiments.

Recording the images for PIV post analyses in a centrifuge requires machine cameras, sufficient illumination and data processing equipment in addition to the geotechnical test set-up that includes a transparent front revealing a soil sample cross section. The equipment and software environment utilised for testing in the Acutronic Model 661 centrifuge (Randolph et al., 1991; Randolph and Gaudin, 2017) at the University of Western Australia in this study is similar to the one described in Stanier et al. (2014).

The PIV post analyses are performed by the means of the software package GeoPIV RG (Stanier and White, 2013; Stanier et al., 2016a; Stanier et al., 2016b; Teng et al., 2017). GeoPIV RG is an enhanced version of the GeoPIV software. The development of GeoPIV is described in detail in White et al. (2001) and White et al. (2003). One of the most important enhancement of GeoPIV RG is the analysis stability in case of large deformations. This is particularly important, because of the targeted investigation of the suction caisson installation processes. Furthermore, GeoPIV RG was developed at the University of Western Australia. It is a proven tool for the post analysis of soil deformations from images of the suction caisson installation recorded during centrifuge tests (Ragni et al., 2019).

4.2 Material point method

4.2.1 General concept

The material point method (MPM) is a particle in cell (PIC) method that was introduced by Sulsky et al. (1994) and Sulsky et al. (1995). This numerical method is based on the finite element method (FEM), but particles, which are also called material points (MPs), represent the continuum. In contrast to conventional FEM, the MPs, i. e. the material continuum, can migrate arbitrarily through a fixed computational grid. Unlike Eulerian FEM, the MPs accommodate all properties like mass density, stresses, and strains, for example. Consequently, the mesh does not carry any information permanently as the following computational scheme is employed: The information stored in the MPs is mapped to the computational mesh during the *initialisation phase*. Subsequently, the equations of motion are solved at the nodes during the *Lagrangian phase*. The deformation of the mesh can be calculated during this phase, but this is not compulsory. The momentum and the position of the MPs is updated during the *convective phase*. This can be done with the node locations being updated or as they remain at their original position. Due to this concept, which is illustrated in Figure 4.1, the simulation of large deformation problems like impact, penetration or fluid-structure interaction becomes feasible (Sulsky et al., 1994; Sulsky et al., 1995).

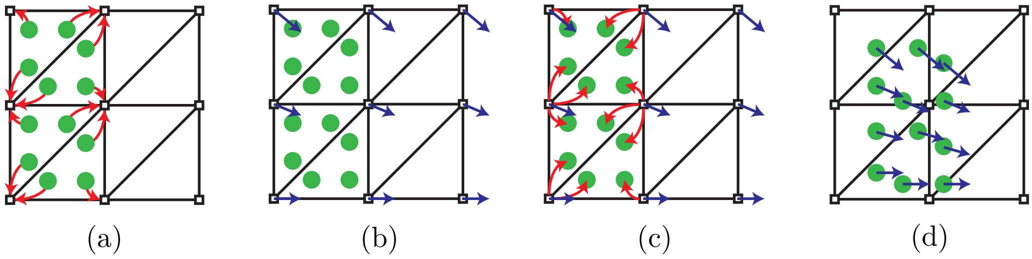

Figure 4.1: Scheme of the MPM approach: initialisation phase (a), Lagrangian phase (b), convective phase: mapping information to MPs (c), and convective phase: updating MP position (d).

The governing equations of the MPM imply the conservations laws of thermodynamics. Assuming that no MP enters or leaves the computational domain, the conservation of mass is satisfied by default. The conservation of momentum or Newton's second law of motion relates the motion of the continuum to the internal and external forces. It is noted that the accelerations terms have to be taken into account in a dynamic formulation. The conservation of energy within an MPM model also has to be satisfied (Sulsky et al., 1994; Sulsky et al., 1995).

Based on the governing equations a weak formulation is obtained through multiplication with the weight functions and integration. The momentum equations are solved on the computational mesh before the updated momentum is mapped back to the MPs. The constitutive equations are solved at the MPs. The constitutive behaviour relates the stresses and strains of a material to the momentum of each MP. Consequently, plastic and history-depended constitutive behaviour can be considered in large deformation analyses without mapping the required variables. This concept overcomes major shortcomings of purely Eulerian and arbitrary Lagrangian formulations (Sulsky et al., 1994; Sulsky et al., 1995).

The computational domain is discretised in space in two independent ways: First, the domain is decomposed into a finite number of subdomains, i. e. a finite number of elements.

Second, each element of the mesh accommodates a finite number of MPs in the beginning of an analysis. During the calculation, the number of MPs in an element can change arbitrarily. A MP represents a fixed fraction of the whole material continuum. In contrast to purely particle based methods, e. g. the discrete element method, where each grain is modelled by a single particle, the total volume or mass of a MP is not restricted. Thus, the total size of a MPM model is not limited through the computational demand by default (Sulsky et al., 1994; Sulsky et al., 1995).

Sulsky et al. (1994) and Sulsky et al. (1995) refer that their PIC method automatically includes sticky contact. Bardenhagen et al. (2000) introduce the MPM for granular materials as an extension of PIC presented by Sulsky et al. (1994) and Sulsky et al. (1995). They also emphasise the requirement of a contact algorithm that allows separation and sliding, including friction, but inhibits interpenetration. Bardenhagen et al. (2000) and Bardenhagen et al. (2001) introduce a contact algorithm that is applicable to any shape of body. This algorithm compares and corrects the velocity of the respective fields. In addition, a frictional coefficient μ is introduced for the correction of the tangential components. This enhancement enables the simulation of the interaction between multiple objects formed from MPs (Bardenhagen et al., 2000; Bardenhagen et al., 2001).

Among others Verruijt (2010), van Esch et al. (2011), and Jassim et al. (2013) present a framework for dynamic two-phase analyses in MPM. Jassim et al. (2013) summarise the implementation of a two-phase analysis procedure in the MPM framework based on the principles laid out by Zienkiewicz et al. (1980) and Zienkiewicz and Shiomi (1984). It is emphasised that a v-w-formulation, which takes all acceleration terms into account, is to be utilised instead of a simplified u-p-formulation. The requirement of a v-w-formulation for problems including rapid loading, e. g. to capture the second compressive wave in a consolidation analysis, is demonstrated by van Esch et al. (2011).

Zhang et al. (2017) and Fern et al. (2019) summarise the current state of development in the MPM. Considering the goal of the simulation of the suction installation process of a caisson foundation the following requirements arise: A numerical method that captures large deformations, a contact algorithm, a two-phase formulation, constitutive models for granular materials, and an axisymmetric formulation are required. In addition, solid stress, velocity, and hydraulic boundary conditions are mandatory. An evaluation of the currently available MPM programmes yields that an axisymmetric formulation exists, but is not implemented in an available programme environment. In addition, hydraulic boundary conditions are predominantly restricted to the mesh nodes. Besides these two key features the requirements for the simulation of the suction caisson installation are satisfied by the current state of development of the MPM (Fern et al., 2019).

4.2.2 Axisymmetric material point method

The axisymmetric form of the MPM was introduced to be an inexpensive extension from two-dimensional to three-dimensional problems having appropriate symmetry (Sulsky and Schreyer, 1996). Compared to three-dimensional MPM, the axisymmetric formulation enables simulations of circular problems, like cone penetration and pile or caisson installation, at significantly lower computational cost. The key features of axisymmetric MPM are presented in accordance to Fern et al. (2019).

Axisymmetric strains

The axisymmetric MPM utilises a cylindrical coordinate system, where u_y represents the vertical and u_r is the radial displacement. The strain tensor has got four non-zero components, which are the radial strain ε_r, the vertical strain ε_y, the shear strain γ, and the circumferential strain ε_θ:

$$\varepsilon_r = \frac{\partial u_r}{\partial r} \tag{4.1}$$

$$\varepsilon_y = \frac{\partial u_y}{\partial y} \tag{4.2}$$

$$\varepsilon_\theta = \frac{u_r}{r} \tag{4.3}$$

$$\gamma_{ry} = 2\gamma = \left(\frac{\partial u_r}{\partial y} + \frac{\partial u_y}{\partial r}\right) \tag{4.4}$$

The distance between the location of an MP and the axis of symmetry is denoted by the radius r. The strains are linked to displacements through Equations 4.5 and 4.6:

$$\boldsymbol{\varepsilon} = \sum_{i=1}^{N_n} \boldsymbol{B_i} \boldsymbol{u_i} \tag{4.5}$$

$$\boldsymbol{B_i} = \begin{Bmatrix} \dfrac{\partial N_i\left(x_{mp}\right)}{\partial r} & 0 \\ 0 & \dfrac{\partial N_i\left(x_{mp}\right)}{\partial y} \\ \dfrac{\partial N_i\left(x_{mp}\right)}{\partial y} & \dfrac{\partial N_i\left(x_{mp}\right)}{\partial r} \\ \dfrac{N_i\left(x_{mp}\right)}{r} & 0 \end{Bmatrix} \tag{4.6}$$

The vector $\boldsymbol{u_i}$ contains the nodal displacements of the node i. The matrix $\boldsymbol{B_i}$ is formed by the gradients of the shape functions N_i that contain the local coordinates for the MPs x_{mp}. In consequence, the strains in the axisymmetric formulation are given through summation across the element nodes N_n:

$$\left(\varepsilon_r\right)_{mp} = \sum_{i=1}^{N_n} u_{r,i} \frac{\partial N_i\left(x_{mp}\right)}{\partial r} \tag{4.7}$$

$$\left(\varepsilon_y\right)_{mp} = \sum_{i=1}^{N_n} u_{y,i} \frac{\partial N_i\left(x_{mp}\right)}{\partial y} \tag{4.8}$$

$$(\gamma_{rz})_{mp} = \sum_{i=1}^{N_n} \left(u_{y,i} \frac{\partial N_i(x_{mp})}{\partial r} + u_{r,i} \frac{\partial N_i(x_{mp})}{\partial y} \right) \tag{4.9}$$

$$(\varepsilon_\theta)_{mp} = \sum_{i=1}^{N_n} u_{r,i} \frac{N_i(x_{mp})}{r} \tag{4.10}$$

Internal forces

The internal forces $\boldsymbol{f_i^{int}}$ are calculated in a specific way in axisymmetric MPM, which is given here:

$$\boldsymbol{f_i^{int}} = \sum_{mp=1}^{N_{mp}} \boldsymbol{B_i^T}(x_{mp})\, \boldsymbol{\sigma_{mp}} \Omega_{mp} \tag{4.11}$$

N_{mp} represents the number of MPs located inside an element in the beginning of a time step. Ω_{mp} is the integration weight of a MP and $\boldsymbol{\sigma_{mp}}$ is the related stress tensor. The radial and vertical components are given in Equations 4.12 and 4.13:

$$f_{r,i}^{int} = \sum_{mp=1}^{N_{mp}} \left\{ \left((\sigma_r)_{mp} \frac{\partial N_i(x_{mp})}{\partial r} + (\sigma_{ry})_{mp} \frac{\partial N_i(x_{mp})}{\partial y} + (\sigma_{\theta\theta})_{mp} \frac{N_i(x_{mp})}{r} \right) \Omega_{mp} \right\} \tag{4.12}$$

$$f_{y,i}^{int} = \sum_{mp=1}^{N_{mp}} \left\{ \left((\sigma_y)_{mp} \frac{\partial N_i(x_{mp})}{\partial y} + (\sigma_{ry})_{mp} \frac{\partial N_i(x_{mp})}{\partial r} \right) \Omega_{mp} \right\} \tag{4.13}$$

Despite the presented differences, the calculation scheme of the axisymmetric formulation equals the procedure for a conventional plane-strain MPM, which is also presented in detail by Fern et al. (2019).

4.2.3 Boundary conditions on material points

Usually boundary conditions (BCs) are aligned with the nodes of the computational grid, which is similar to FEM analyses. However, the MPM provides the facility to apply BCs at MPs. This is especially handy, if a soil surface is intended to move independently from the mesh and a non-zero-traction boundary condition is to be imposed. This functionality is crucial, if the soil surface is subject to loading and the mesh is adopted due to a moving mesh algorithm, for instance. Since, a moving mesh is proposed to improve the detection of the contact surfaces in a penetration process, the application of BCs on MPs becomes necessary (Bardenhagen et al., 2000; Bardenhagen et al., 2001).

The pre-defined BCs – e. g. displacements, effective stresses or hydrostatic pressures – are mapped to the MPs in advance to the first load step. Within each load step, the corresponding traction stresses $\vec{f}^{trac}$ are mapped back to the mesh employing the shape functions of the respective element:

$$\vec{f}^{trac} = \sum_{el=1}^{n_{el}} \sum_{mp=1}^{n_{mp,el}} \mathbf{N}^T(\vec{\xi}_{mp}) \vec{f}^{trac}_{mp} \tag{4.14}$$

The BCs are mapped to mesh nodes in the beginning of the Lagrangian phase (Fern et al., 2019). Thus, the MPs that are associated with a BC are free to shift the element that contains them. This scheme allows the utilisation of a moving mesh in the simulation of the penetration of a caisson skirt with a simultaneous application of BCs on the soil surface. The BCs on MPs can be utilised to generate differential pressure between the inside of a suction caisson and ambient. This is a key-feature in order to enable an holistic simulation of the suction caisson installation.

4.2.4 Implementation of the axisymmetric formulation

Anura3D

Hamburg University of Technology (TUHH) currently holds a membership in the Anura3D Research Community. This membership allows access and personal development of the source code of Anura3D. This MPM programme is complementarily available, which automatically ensures reproducibility of results when personal developments are shared within the research community. Each commitment to the main source code has to pass certain quality standards, such as comprehensive benchmarking, to ensure general compatibility to each possible application of the programme. As soon as a novel development satisfies the quality standards, it is shared within the community. After further internal testing, the advanced code eventually becomes accessible to the general public. The quality management, maintenance and software releases are managed by the research community.

Anura3D (version 2019.1) already provided several key-features that are necessary for the simulation of the suction caisson installation: The MPM framework included a contact formulation so that simulation of penetration processes was feasible. A two-phase v-w-formulation, which is hardly available in other MPM programmes, was also available in Anura3D 2019.1. However, this version did not provide hydraulic BCs on MPs. Additionally, the version 2019.1 was restricted to three-dimensional analyses, which results in an excessive computational demand when it comes to the simulation of circular problems. Consequently, the axisymmetric formulation and a mapping function that allows the application of hydraulic BCs on MPs had to be implemented in order to facilitate the investigation of problems like the installation of a circularly shaped suction caisson.

Implementation

Due to the suitable environment of Anura3D, the accessibility to the source code, and the obvious entailment, the required features – the axisymmetric formulation and the hydraulic BCs on MPs – have been implemented in the Anura3D programme environment within the scope of this thesis. It is planned that these functionalities become available to the public in future versions of Anura3D.

This novel implementation of BCs on MPs allows the manipulation of the hydrostatic pressure at a free soil surface. This enables the simulation of problems containing a soil surface that is located partly or completely below the water level. This is particularly important when a local differential pressure is considered – e. g. for the simulation of the suction caisson installation.

The significant reduction of computational costs for the simulation of circular problems is the major upside of the axisymmetric formulation. The capability of the novel implementation is demonstrated through the re-calculation of a granular column collapse that was proposed by Fern et al. (2019). Regardless of the referred model parameters, the models are formed as described in Table 4.2. Dry granular material is utilised. The constitutive behaviour is modelled with an elastic-plastic Mohr-Coulomb-model (MCM). The required constitutive parameters are also presented in Table 4.2.

Table 4.2: Model for an axisymmetric column collapse.

Parameter	Symbol	Unit	Value
Model radius	r_m	(m)	3
Model height	h_m	(m)	1.1
Column radius	r_c	(m)	1
Column height	h_c	(m)	1
Initial porosity	n	(-)	0.4
Density solid	ρ_s	$(\mathrm{t/m^3})$	2.65
Lateral pressure coefficient	K_0	(-)	0.5
Young's modulus	E	(MPa)	1
Poisson's ratio	ν	(-)	0.3
Peak friction angle	φ'	(°)	30

The calculations are performed in $n_{LS} = 50$ load steps with a simulated time of $T = 0.01\,\mathrm{s}$ each. Stresses are initialised by means of a K_0-procedure prior to the first load step. A Courant number of $C = 0.98$ and no damping is utilised. The model is tested with different mesh configurations including structured and unstructured meshes for the three- and two-dimensional model, respectively. In addition, the mesh size is reduced twice starting from an element length of $l_e = \frac{1}{10} r_c$. Three MPs per element are used in the two-dimensional axisymmetric model and an element in the three-dimensional model contains four MPs. The three-dimensional analyses are performed with a 90°-wedge.

The results of this specific benchmark show that the two-dimensional axisymmetric model requires less than 5 % of the computational time that is necessary to compute the utilised three-dimensional model. The significantly lower number of MPs required for the axisymmetric model presumedly is the main reason for this remarkable speed-up. The calculation time for the simulation of a caisson skirt penetrating into saturated soil is expected to be reduced from approximately a week to several hours.

4.3 Finite element method

4.3.1 Requirements for the numerical modelling of suction caissons

The literature review presented in chapter 2 pointed out that the FEM is considered to be an established tool for the numerical simulation of geotechnical problems. This includes the numerical simulation of the load bearing behaviour of suction caisson foundations. However, the model design for a thin-walled suction caisson is complicated to date: The thin-walled skirt tip requires the utilisation of very small elements compared to the overall model dimensions. This area accommodates the largest deformations forming from loads introduced through the skirt. Furthermore, the skirt tip is located in an area of the numerical model that is also affected by the internal soil plug deformation. The utilisation of shell or structure elements would introduce a simplification to a crucial part of the problem – the tip resistance – and therefore is not applicable for numerical simulations targeting cyclic loading.

This example already demonstrates the complexity of the suction caisson model design. This aspect also implies that the application of the FEM is limited to small strain analysis. Besides issues, like data confidentiality and a fragmented experimental database for validation, the following requirements add further complexity for the development of a numerical model of a suction caisson foundation:

(1) A circular suction caisson allows the utilisation of an axisymmetric numerical model in order to minimise the computational costs compared to a three-dimensional model.

(2) A suction caisson is usually subjected to cyclic loading at loading rates that can introduce partially drained behaviour. Consequently, a coupled two-phase FEM formulation is required. The *u*-*p*- and *v*-*w*-formulation are possible coupling methods. The comparison discussed in van Esch et al. (2011) demonstrated the superiority of the *v*-*w*-formulation. However, the secondary compressive wave is not expected to be relevant at the loading rates expected for suction caisson foundation for offshore wind turbines. Hence, both techniques are considered to be applicable for this specific problem.

(3) A suction caisson model always includes two interacting material entities. Therefore, a contact formulation that allows slip between the steel skirt and the surrounding soil is required. Since structure soil interface modelling is often limited in universal FEM programme codes, additional functionality can be required to create a sufficient numerical model.

(4) Achmus and Thieken (2014) and Whyte et al. (2020) point out that the caisson lid can detach from the soil plug while the occurring gap is filled with water. These findings were underpinned through the recalculation of laboratory tests and suction caisson extraction tests with the exact same constitutive model and model parameters presented in Whyte et al. (2020). Since the soil and the pore water are combined in a single continuum material in FEM models, Achmus and Thieken (2014) introduced the water elements representing the extracted fluid volume in a simulated pull-out test. It is concluded that the simulation of a water filled gap is required as soon as the targeted caisson displacements result from a vertical loading regime that substantially exceeds the frictional capacity.

(5) The simulation of vertical cyclic loading that includes significant excursions into tension, can feature the opening and subsequent closing of the pore fluid gap at the lid invert. However, the water elements must contain a minimum stiffness (Achmus and Thieken, 2014). Consequently, the simulation of compressive loading utilising water elements is impossible. Cerfontaine et al. (2016) utilised an approach including a storage term maintaining the connection of the soil pore pressure to the lid invert while the soil entity is detached.

(6) The simulation of cyclic loading requires constitutive models that capture accumulative effects. For instance: The hypoplastic constitutive model including the intergranular strain anisotropy (ISA) is applicable for numerical simulations including cyclic loading in sand (Fuentes and Triantafyllidis, 2015b). A visco-hypoplastic constitutive model, also including the ISA formulation, can be utilised for numerical analysis including the response of clay soil subjected to cyclic loading (Fuentes et al., 2018).

(7) Depending on the volumetric strains – especially within the soil plug – the void ratio can be subject to considerable changes. Since the effective permeability is determined by the void ratio, significant changes of the *in situ* void ratio would require to capture this effect within the constitutive model. Achmus and Thieken (2014) proposed the Kozeny-Carman-equation to be a suitable approach, for example.

Based on these requirements, the current state of the art needs to be evaluated: Axisymmetric FEM formulations including quasi-static two-phase calculations are available in several programs like Plaxis or Abaqus. Most codes provide frictional interface models allowing slip between different materials entities. Advanced models, like the hypoplastic interface (Stutz et al., 2016; Stutz et al., 2017), can be implemented by means of a user interface, e. g. in Abaqus. Normal interaction between two materials involving coupled mechanical and hydraulic degrees of freedom and detachment and re-establishment of contact is hardly available in current software environments. Cerfontaine et al. (2016) present such a technique, but this code and the simulation data remains confidential to date. However, the introduction of the lid separation for the soil is found to be a crucial mechanism and is therefore prioritised to be implemented in the simulations targeting the vertical cyclic loading of suction caissons featuring excursions into tension.

4.3.2 Modelling approach for the detachment of the caisson lid

Achmus and Thieken (2014) and Cerfontaine et al. (2016) emphasised the importance of a temporary lid detachment from the soil plug. Since the method presented by Cerfontaine et al. (2016) remained confidential, improving the water element technique proposed by Achmus and Thieken (2014) is targeted within the scope of this thesis: The water elements featuring mechanical and pore water pressure degrees of freedom are maintained. However, the required minimum stiffness prevents the utilisation for compressive loading of a suction caisson. Therefore, a protective box, presented in Figure 4.2, was added in order to enable compressive loading. The displacements of the caisson and the box are coupled. Normal contact allowing temporary separation is postulated between the box and the soil plug surface. The top surface nodes of the water elements are coupled to the neighbouring nodes of the caisson. The soil and the water elements are connected by a tie constrain. This model configuration boxes the water elements at a minimum height in compression once lid contact is established. The water elements expand once the lid is detached from the soil plug surface in tension. This process works vice versa and can be repeated infinitely. Hence, the presented approach enables the utilisation of water elements – i. e. the consideration of lid detachment – in a simulation that features tensile and compressive loading for the first time to the author's knowledge.

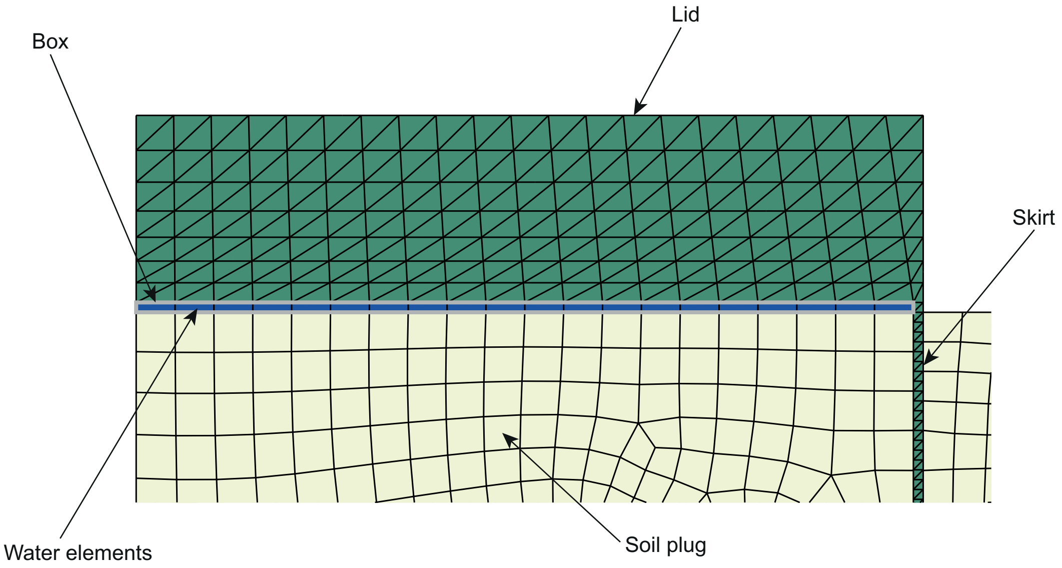

Figure 4.2: Boxed water element concept.

4.3.3 Constitutive modelling

Analyses targeting cyclic loading problems require advanced constitutive models in order to provide adequate results. The hypoplastic model for sand including the ISA, which has been utilised in Fuentes et al. (2017b) became publicly available in 2018. An analogue visco-hypoplastic model for clay (Fuentes et al., 2018) exists, but remains confidential to date. Updating the effective permeability based on the void ratio calculated from the hypoplastic constitutive model is a reasonable extension, which is currently not available to the public. However, this addition is only required in case of considerable changes of the void ratio calculated from a numerical model. Consequently, a low priority is given to a re-implementation of the Kozeny-Carman approach suggested and discussed in Achmus and Thieken (2014).

The hypoplastic constitutive model, originally published by von Wolffersdorff (1996), features void ratio (pyknotropy), stress (barotropy), and stress path depended response. Niemunis and Herle (1997) added the intergranular strain concept to the original model, which enables the simulation of static unloading and reloading utilising increased stiffness depending on the strain rate. Wegener and Herle (2013) added a reduction factor for the intergranular strain effect in order to reduce the overestimated accumulation of deformations resulting from repetitive loading and unloading. However, the purely elastic concept of the intergranular strains is maintained. The ISA concept introduced elastic plastic constitutive behaviour for small strain amplitudes (Fuentes and Triantafyllidis, 2015b). The implementation of hypo-elasticity, a critical state condition, and yield surfaces into the intergranular strain environment enable more accurate simulations of cyclic loading problems (Fuentes and Triantafyllidis, 2015a). Two additional extensions are also utilised: A reduction of the strain rate for a high number of repetitive loading cycles yields an improved response (Poblete et al., 2016; Fuentes et al., 2018). The introduction of the effect of cyclic mobility enables the simulation of liquefaction failure resulting from repetitive loading (Fuentes et al., 2019).

The development of the visco-plastic constitutive model formulation was presented in Niemunis (1996) and Niemunis and Krieg (1996). The intergranular strain concept has been introduced by Niemunis (2003). Extended visco-hypoplastic constitutive model capture strain rate dependency, viscous effects, and inherent anisotropy for monotonic loading and unloading (Niemunis et al., 2009; Mašín, 2019). Fuentes et al. (2017a), Fuentes et al. (2018), and Tafili and Triantafyllidis (2018) implemented the ISA-plasticity into the visco-hypoplastic constitutive model in order to improve the performance for the simulation of cyclic loading. This constitutive model is still under development including features like partial saturation, cementation, or anisotropy for overconsolidated clays. The ISA-plasticity extension is not publicly available to the author's knowledge.

4.4 Analytical prediction method

Among others Bienen et al. (2018a) and Bienen et al. (2018b) found that the drainage regime governs the vertical load bearing behaviour. Hence, it is considered to be reasonable to employ the approach introduced by Houlsby and Byrne (2005b) and Houlsby et al. (2005) for the development of a simplified prediction method of the response of suction caissons under vertical cyclic loading.

The presented approach was developed within the scope of this thesis. It includes the prediction of uplift and settlement in tension and compression, respectively. Classical consolidation theory is utilised to estimate vertical displacements in compression (Boussinesq, 1885; Terzaghi and Fröhlich, 1936). Positive values indicate compression and displacements in the downward direction, whereas negative values represent tension and displacements in the upward direction, although this may differ from the nomenclature in the original references.

4.4.1 General concept and basic assumptions

The presented method utilises different equations for different loading states. Therefore, the actual loading state is to be checked at the beginning of each calculation step. This is done as follows: First, the current load is evaluated as being compressive or tensile. Second, loading or unloading are differentiated. Consequently four different loading stages are possible: (1) compressive loading, (2) compressive unloading, (3) tensile loading, (4) tensile unloading.

Since the presented calculation method follows the principles as laid out by Houlsby and Byrne (2005b) and Houlsby et al. (2005), several assumptions and specifications are adopted. The load bearing behaviour is simplified as the calculation of the tip resistance is neglected. This assumption is considered to be reasonable since full lid contact is expected. This implies that the tip resistance carries only a marginal portion of the load compared to the lid under the assumption of full lid contact. Furthermore, it is expected that the soil at the skirt tip is disturbed during cyclic loading. The effective skirt friction is calculated in each time step under consideration of the actual excess pore pressure distribution. Changes in effective plug permeability during tensile loading and unloading are accounted for following the principles laid out by Houlsby and Byrne (2005b). Furthermore, the onset of liquefaction and cavitation due to rapid tensile loading is taken into account in accordance with Houlsby et al. (2005).

4.4.2 Calculation scheme for compression

The compressive differential stresses $\Delta\sigma_{v,j}$ can be calculated from Equation 4.15 (Boussinesq, 1885):

$$\Delta\sigma_{v,j} = \frac{V - F_{in} - F_{out}}{\frac{\pi D_{out}^2}{4}} \cdot \left(1 - \frac{1}{\left(\left(\frac{D_{out}}{2z_j}\right)^2 + 1\right)^{\frac{3}{2}}}\right) \tag{4.15}$$

where V is the vertical load. F_{in} and F_{out} are the internal and external skirt friction. The differential stresses are calculated for a finite number of fictive soil layers located in their respective depths z_j below the caisson lid, which are enumerated through the index j. According to Terzaghi and Fröhlich (1936), the coefficient of consolidation c_v and the dimensionless time factor τ yield the degree of consolidation μ_c:

$$\mu_c = 2 \cdot \sqrt[2]{\frac{\tau}{\pi}} = 2 \cdot \sqrt[2]{\frac{c_v t}{\pi L^2}} = 2 \cdot \sqrt[2]{\frac{E_s k_f t}{\gamma_w \pi L^2}} \tag{4.16}$$

The dimensionless vertical displacement $\Delta z/L$ resulting from compressive loading or unloading can be obtained from Equation 4.17:

$$\frac{\Delta z}{L} = \frac{\mu_c}{LE_s} \sum_{j=0}^{j=j_{max}} d_j \Delta\sigma_{v,j} \tag{4.17}$$

where d_j is the thickness of the respective soil layer and E_s represents the stiffness modulus, acknowledging that the actual soil stiffness depends on the loading history and direction.

4.4.3 Calculation scheme for tension

Tensile load is carried through the internal F_{in} and external F_{out} skirt friction and the differential pressure s at the lid invert (Houlsby et al., 2005):

$$V' = F_{in} + F_{out} + \frac{\pi D_{in}^2}{4} s \tag{4.18}$$

Differential pressure is mobilised if the applied load exceeds the frictional capacity. The internal and external skirt friction are obtained from Equations 4.19 and 4.20, which take the influence of the seepage flow into account. This approach was originally proposed by Houlsby and Byrne (2005b):

$$F_{in} = \frac{\pi L^2}{2} \left(\gamma' - \frac{(1-a)s}{L} \right) D_{in} (K \tan \delta)_{in} \tag{4.19}$$

$$F_{out} = \frac{\pi L^2}{2} \left(\gamma' + \frac{as}{L} \right) D_{out} (K \tan \delta)_{out} \tag{4.20}$$

The pressure factor a_p was determined from numerical calculations (Houlsby and Byrne, 2005b). The results can be recalculated by means of an analytical approximation:

$$a_p = \frac{a_1 k_F}{(1-a_1) + a k_F} \tag{4.21}$$

$$a_p = a_1 = c_0 - c_1 \left(1 - exp \left(-\frac{L}{c_2 D} \right) \right) \tag{4.22}$$

where $k_F = k_{in}/k_{out}$ represents the ratio between the effective internal k_{in} and external k_{out} effective permeability. The coefficients $c_0 = 0.45$, $c_1 = 0.36$, and $c_2 = 0.48$ are taken from Houlsby and Byrne (2005b). Equation 4.19 to 4.22 were originally developed for the prediction of the suction pressure required for the caisson installation in sand. The hydraulic mechanisms during tensile loading are comparable to those that are present during the suction installation. Hence, this approach was deemed applicable. However, a reversed seepage flow direction is present during unloading. Thus, the modified Equation 4.24 is required.

$$F_{in,ul} = \frac{\pi L^2}{2} \left(\gamma' + \frac{as}{L} \right) D_{in} (K \tan \delta)_{in} \tag{4.23}$$

$$F_{out,ul} = \frac{\pi L^2}{2} \left(\gamma' - \frac{(1-a)s}{L} \right) D_{out} (K \tan \delta)_{out} \tag{4.24}$$

4.4.3.1 Small displacement rates

The equations proposed by Houlsby and Byrne (2005b) and Houlsby et al. (2005) are combined and rearranged so that the differential pressure can be obtained:

$$s = \frac{V' - A}{B + C} \tag{4.25}$$

$$A = \frac{\gamma' \pi L^2}{2} \left(D_{in}(K \tan \delta)_{in} + D_{out}(K \tan \delta)_{out} \right) \tag{4.26}$$

$$B = \frac{\pi D_{in}^2}{4} \tag{4.27}$$

$$C = \frac{\pi L}{2} \left(D_{in}(K \tan \delta)_{in}(1 - a) + D_{out}(K \tan \delta)_{out}(a) \right) \tag{4.28}$$

The presented equations are applicable for relatively small displacement rates during tensile loading, which supposes the absence of liquefaction and cavitation. The calculation of the differential pressures during tensile unloading requires Equation 4.29.

$$C_{ul} = \frac{\pi L}{2} \left(D_{in}(K \tan \delta)_{in}(a) + D_{out}(K \tan \delta)_{out}(1 - a) \right) \tag{4.29}$$

4.4.3.2 Large displacement rates

Small displacements are considered to be exceeded as soon as cavitation or liquefaction occur. Cavitation or liquefaction can arise either independent from each other or simultaneously. Thus, each possible state is to be considered (Houlsby et al., 2005).

The differential pressure obtained for small displacement rates is limited by the cavitation pressure $s_{cav} = p_a(1 - f) + \gamma_w h_w$, which is the sum of the atmospheric and the hydrostatic pressures. The onset of plug liquefaction is reached as soon as the differential pressure exceeds $\gamma' L/(1 - a)$ (Houlsby et al., 2005). Thus, the differential pressure can be calculated from Equation 4.30 before the cavitation limit is reached.

$$s = s_{ul} = \frac{V'}{\frac{\pi D^2}{4}\left(1 + \frac{2L}{D}(K \tan \delta)_{out}\right)} \tag{4.30}$$

4.4.3.3 Calculation of vertical displacements

Once a differential pressure inside the caisson is present, seepage flow will occur. The inflow of water and therefore, the volume change of the plug can be obtained from Darcy's law. Based on the findings by Houlsby and Byrne (2005b) and Houlsby et al. (2005), the vertical displacement rate can be calculated as:

$$\dot{z} = \frac{F k_{in} s}{\frac{\pi D_{in}}{4} \gamma_w L} \tag{4.31}$$

where F_{flow} is the dimensionless flow factor for caissons with an aspect ratio of $0.1 \leq L/D \leq 0.8$, which is given through Equation 4.32:

$$F_{flow} = \frac{(1-a)\pi k_F}{4\frac{L}{D}} \tag{4.32}$$

In contrast to Houlsby et al. (2005), k_{in} instead of k_{out} is employed in Equation 4.31. This is reasonable for small displacement rates, since $k_F = 1$ was found to be reasonable here. Analogue to Houlsby et al. (2005), Equation 4.31 is also utilised when large displacement rates occur. Since the limitation of laminar flow in Darcy's law might be exceeded, the dimensionless flow factor is modified. The onset of liquefaction includes a significant increase in effective permeability. Thus, the dimensional flow factor during liquefaction is estimated by means of Equation 4.32, but it is recommended to consider upper bound k_F values.

Once the displacement rate is calculated, the normalised vertical displacement can be estimated through the multiplication with the corresponding differential time Δt:

$$\frac{\Delta z}{L} = \frac{\dot{z}\Delta t}{L} \tag{4.33}$$

The presented simplified prediction method is mainly based on the consolidation theory. This implies that volume changes and therefore caisson displacements depend on the drainage mechanism. Consequently, undrained response is not captured. However, this method is applicable for partially drained conditions, which are expected to be present around suction caisson foundations embedded in sand layers.

5 Installation in sand

This chapter features investigations on the suction caisson installation in sand. The results of two parallel series of centrifuge tests and numerical analyses are discussed. A potential influence of the suction installation on the load bearing behaviour is discussed in Chapter 6.

5.1 Centrifuge tests

5.1.1 Experimental arrangement and testing procedure

Two parallel series of centrifuge tests were performed: One series featured the suction installation with a subsequent CPT inside the suction caisson. The other series includes cyclic loading tests following the suction installation. The experiments were performed at 100g in the Acutronic Model 661 centrifuge (Randolph et al., 1991; Randolph and Gaudin, 2017) at UWA. These model scale tests had the following requirements to ensure a realistic stress state:

- Caisson penetration at stress levels representative for prototype scale was required. Thus, the caisson had to be suspended just above the sand surface until the centrifuge had reached the target acceleration.
- The installation was to be done in a controlled manner to ensure reproducible conditions for each subsequent testing procedure – i. e. CPTs or cyclic loading tests.
- The CPTs and the cyclic loading were to be performed without stoppage of the centrifuge to retain the soil stress state resulting from the suction installation.
- CPTs at free field sites were to be performed before and after the caisson tests to characterise the soil samples itself, to confirm uniformity of each sample used in this study and to facilitate comparisons between CPT profiles obtained within the suction caisson, and at the free field sites, respectively.

5.1.1.1 Centrifuge test arrangements

While similar conditions for the suction installation were targeted, different test arrangements were employed for the two complementary series of centrifuge tests discussed. All tests were conducted in strong boxes, which were 325 mm high, 350 mm long and 390 mm wide. The strong box was filled with a filter layer beneath the sand sample (see Figure 5.1). Both test series featured a minimum sample height of 200 mm. The water table had to be at least 100 mm above the sand surface to ensure that the model caisson, including the three way valve, was submerged to minimise changes in buoyancy during the installation.

5.1.1.2 Test set-up for CPTs inside the caisson

The performance of a CPT inside the caisson – a testing method inspired by the work of M. N. Tran (2005) – required several improvements before the suction caisson installation and the CPT in one flight became feasible. Two caissons with similar diameters and aspect ratios of $D/L = 0.5$ and $D/L = 1$ were manufactured and equipped with the same set of sensors. In this set-up the CPT was clamped to the actuator and the caisson was connected to the actuator with a steel wire. The purpose of this set-up presented in Figure 5.1 was suspension of the foundation prior to testing. In addition, this arrangement allowed self-weight penetration to take place at a controlled rate. It also enabled the performance of the CPT without stopping the centrifuge, which is a major improvement compared to the set-up presented by M. N. Tran (2005). Additional details of this centrifuge test set-up are presented in Appendix B.1.

In this arrangement, the model caisson and the CPT were lowered without relative displacement. The vertical movement was controlled via a feedback loop, maintaining a constant distance measured by the linear displacement transducer (LDT) shown in Figure 5.1. A guide rod arrangement ensured verticality during the installation. The rod connected to the caisson also contributed to the targeted self-weight of 350 N in model scale, i. e. 3.5 MN in prototype scale.

The miniature cone shown in Figure 5.1 had a diameter of $D_{cpt} = 6.3\,\text{mm}$ and was manufactured specifically for these tests. The cone tip was placed inside the caisson lid during the suction caisson installation. The opening was sealed with two o-rings. As described in detail in Stapelfeldt et al. (2018), the utilisation of this small diameter cone ensured the insertion of a minimum volume object while maximising its rigidity as well as its clearance from the skirt. Thus, a minimum distance between the cone and the skirt of at least three times the cone diameter was maintained.

5.1.1.3 Caisson model and test instrumentation

The model caissons had a diameter of $D = 80\,\text{mm}$ and a skirt length of $L = 40\,\text{mm}$, which when tested at $100g$ represents a diameter $D = 8\,\text{m}$ and a skirt length of $L = 4\,\text{m}$ in prototype scale. The model caisson without CPT inlet, previously used by Bienen et al. (2018a) and Bienen et al. (2018b), was manufactured from a solid block of aluminium (see Figure 5.1). The modified caissons for the tests including the CPT through the lid were manufactured with similar dimensions form a solid block of aluminium. The wall thickness of the skirt was $t = 0.5\,\text{mm}$, which corresponds to a prototype wall thickness of $t = 50\,\text{mm}$. In addition to this caisson with an aspect ratio $L/D = 0.5$ a second set of caissons with the same diameter but an aspect ratio $L/D = 1$ was also used. The skirt of this $L = 80\,\text{mm}$ long caisson also had a model wall thickness of $t = 0.5\,\text{mm}$. This yields a ratio of $D/t = 160$ for each model caisson.

Each caisson was equipped with a pore pressure transducer (PPT) and two total pressure transducers (TTP) – one at the lid invert and another one at the top of the lid. The caisson model was connected to a load cell with a maximum capacity of 8 kN by means of a rigid

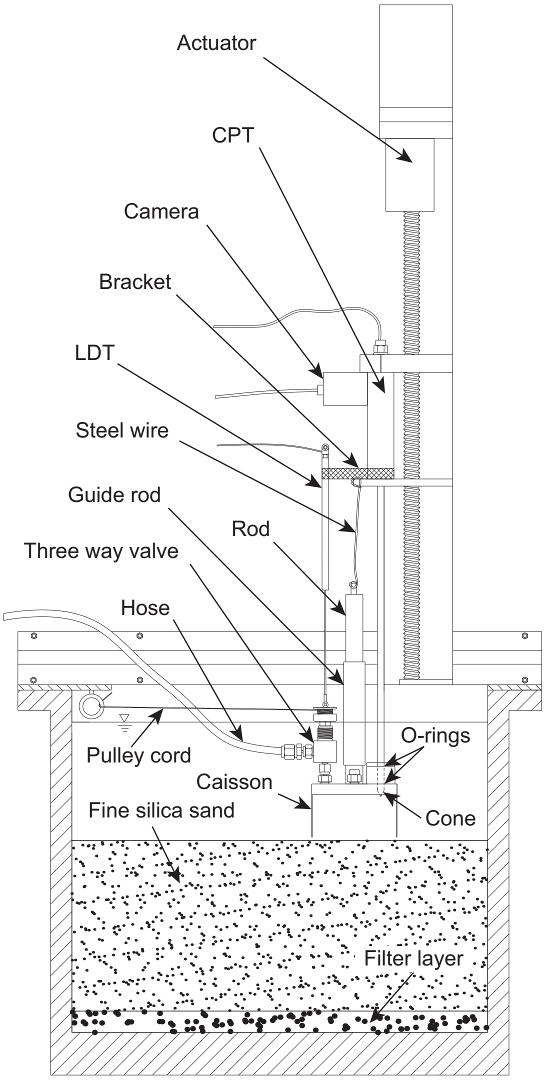

Figure 5.1: Centrifuge test set-up for the suction caisson installation followed by a CPT through the lid.

rod for the cyclic loading tests (see Chapter 6). The self-weight and the loading of the model caisson were applied with the actuator that was controlled through a feedback loop from the load cell. The displacement of the caisson was recorded by means of the LDT that had a maximum extension length of $L_{LDT,max} = 100\,\text{mm}$ in both test series.

A camera was mounted on top of the vertical actuator carriage with the purpose of showing the status of the three way valve. The three way valve on the caisson lid was able to vent to ambient, to connect the caisson to the syringe pump, and to be sealed (see Figure 5.1). The three way valve was operated by an electric winch positioned next to the actuator support beams by means of a pulley system. The syringe pump (House, 2002) was mounted on the back of the strong box as shown in Figure 6.1b.

The performance of the pulley system was controlled by an additional camera located on the edge of the strong box. This camera also provided a side view of the installation. The light panel next to the camera was required to ensure sufficient illumination of the experimental apparatus.

5.1.1.4 Soil sample and pore fluid preparation

The dry soil sample was prepared in two steps: First a filter layer consisting of coarse sand was constructed at the base of the strong box. This layer had a thickness of approximately 20 mm and was covered with a geotextile. The fine silica sand was pluviated from a height of approximately 1.2 m by means of an automatic pluviator. After reaching a total sample height of at least 200 mm, the surface was vacuum levelled. The unit weight was determined from weight and volume measurements. The relative densities D_r for the three samples used in this study were 0.84 ± 0.03. The peak friction angle of fine silica sand is $\varphi_p = 43\,°$ at $\sigma = 20\,\mathrm{kPa}$ (Lehane and Q. B. Liu, 2013). The particle size distribution of fine silica sand is presented in Figure 5.2. The minimum void ratio is $e_{min} = 0.46$ and the maximum void ratio is $e_{max} = 0.79$. The grain size distribution of Baskarp sand, which is similar to fine silica sand, is also presented. However, Baskarp sand has more angular grains and shows enhanced dilation compared to fine silica sand (Bienen et al., 2018b).

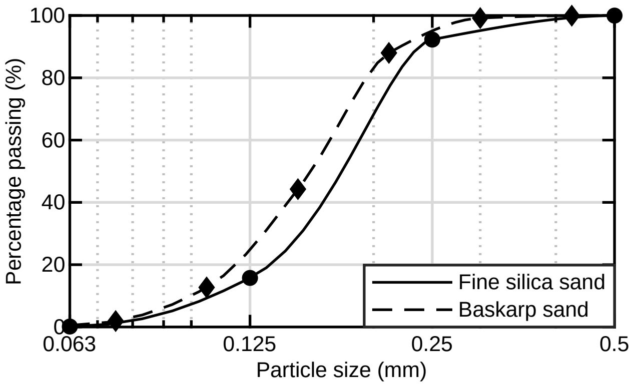

Figure 5.2: Particle size distributions.

Each sand sample was saturated from the base after the pluviation. Under consideration of scaling laws for cyclic loading at $100g$ conditions, the viscosity η of the pore fluid was increased from approximately $\eta_w = 1\,\mathrm{cSt}$ for water to $\eta = 100\,\mathrm{cSt}$ by means of the addition of methyl cellulose ether (DOW, 2002). Hereby, an effective permeability of the soil sample of $k_f = 1 \cdot 10^{-4}\,\mathrm{m/s}$ at $100g$ was targeted. The effective permeability of the saturated soil can be adjusted trough the amount of methyl cellulose ether powder diluted in water. Through the addition of more methyl cellulose ether powder, the viscosity of the pore fluid was increased to $\eta = 300\,\mathrm{cSt}$ in sample no. 2. Thus, a prototype effective permeability of $k_f = 3.3 \cdot 10^{-5}\,\mathrm{m/s}$ was achieved. This allowed investigation of the effect of uncertainty in the *in situ* effective permeability. The effective permeability coefficients are representative of typical North Sea sands (Tan and Scott, 1987; Taylor, 2011).

5.1.1.5 Sample characterisation: CPTs at free field sites

Before and after the suction caisson models were tested, CPTs were performed at $100g$. A centrifuge scale penetrometer with a model diameter of $D_{cpt} = 10\,\mathrm{mm}$ and a smaller one with a diameter of $D_{cpt} = 6.3\,\mathrm{mm}$ were penetrated into the soil at a constant rate of $v_{cpt} = 1\,\mathrm{mm/s}$, which is expected to result in drained conditions (Finnie and Randolph, 1994). The CPTs were performed to confirm the soil characteristics and the uniformity within and between each sample.

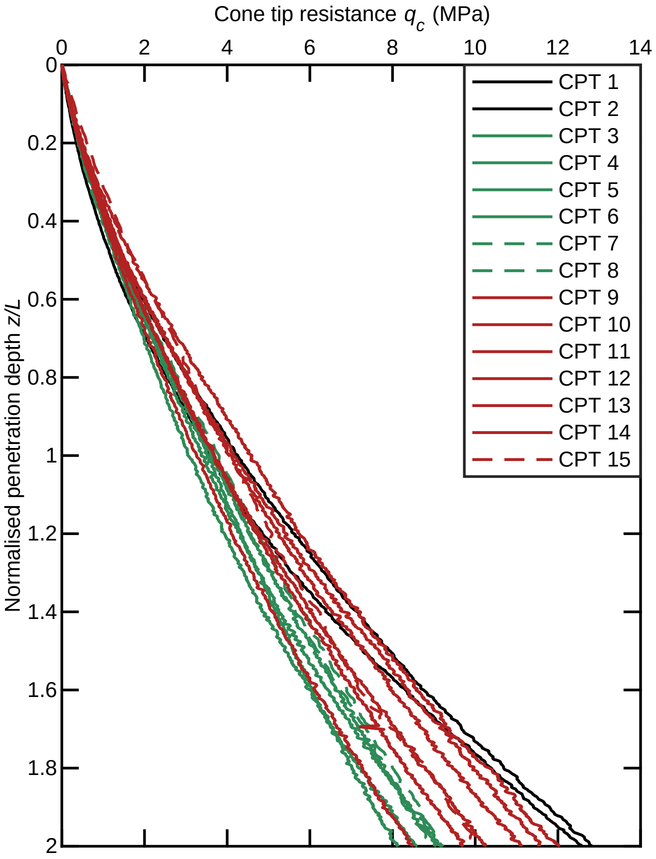

Figure 5.3: CPT profiles from soil sample no. 1 (CPT 1 & 2), sample no. 2 (CPT 3 to 8), and sample no. 3 (CPT 9 to 15).

Figure 5.3 shows all CPT profiles of cone tip resistance q_c with penetration depth z normalised by the caisson skirt length $L = 40\,\mathrm{mm}$. The presented profiles confirm the uniformity within and between each soil sample. CPTs with both penetrometers – $D_{cpt} = 10\,\mathrm{mm}$ (solid lines) and $D_{cpt} = 6.3\,\mathrm{mm}$ (dashed lines) – were conducted in sample no. 2 and no. 3. It is noted that CPT profiles from both penetrometers are similar. This ensures comparability between the cone tip resistance profiles obtained at the free field sites and those obtained from the $D_{cpt} = 6.3\,\mathrm{mm}$ CPTs through the caisson lid.

5.1.1.6 Testing nomenclature

Table 5.1 summarises all 15 suction caisson tests. The tests were named as follows:

- The letters INST characterise tests where a CPT was conducted through the lid following suction caisson installation. The letters CYC indicate that a cyclic loading test followed the suction installation.
- The numbers 1, 2, 3, 4, 5 form groups of tests that feature similar pumping flow rates during the suction caisson installation.
- The letter H represents tests in sand with a higher effective permeability, while L indicates a test in sand with a lower effective permeability.
- The last letter(s) indicate(s) different pumping flow rates: S = slow, MS = medium slow, M = moderate, F = fast, SF = super fast.

5.1.1.7 Testing procedure

Each test summarised in Table 5.1 was performed in a different location inside the strong boxes. A total of six cyclic loading tests that featured the same installation process as the corresponding tests with a CPT through the caisson lid were performed, which manifests the reproducibility of the utilised installation method. It is noted that all four installations conducted with suction caissons that had a model skirt length of $L = 80\,\text{mm}$ were not completed due to premature refusal. The CPTs were performed inside the incompletely installed caissons. However, test CYC-1-H-MS had to be terminated once the refusal occurred and no CPT was conducted.

Table 5.1: Centrifuge testing programme.

Test name		Permeability	PFLR[a]	Skirt length
CPT inside[b]	Cyclic load[b]	k_f (m/s)	q (mm^3/s)	L (mm)
INST-1-H-S	CYC-1-H-S	$1.0 \cdot 10^{-4}$	266.2 (512.4)[c]	40
INST-1-H-MS	CYC-1-H-MS	$1.0 \cdot 10^{-4}$	332.8	80
INST-2-H-M	CYC-2-H-M	$1.0 \cdot 10^{-4}$	665.6	40
INST-3-H-F	CYC-3-H-F	$1.0 \cdot 10^{-4}$	1664.0	40
INST-3-H-SF	-	$1.0 \cdot 10^{-4}$	2662.4	80
INST-4-L-M	CYC-4-L-M	$3.3 \cdot 10^{-5}$	665.6	40
INST-5-L-F	CYC-5-L-F	$3.3 \cdot 10^{-5}$	1664.0	40
INST-5-L-SF	-	$3.3 \cdot 10^{-5}$	2662.4	40
INST-5-L-SF2	-	$3.3 \cdot 10^{-5}$	2662.4	80

[a] PFLR = pumping flow rate

[b] Type of test after the installation

[c] Increased during the installation

5.1.1.8 Caisson installation

The suction caisson installation for both parallel series of tests was performed as follows:

(1) The self-weight penetration was performed under load control at a constant loading rate of 1 N/s in model scale. A total vertical load of $V = 350\,\mathrm{N}$ was applied on the model caisson, which equals $V = 3.5\,\mathrm{MN}$ or $V/A = 70\,\mathrm{kPa}$ in prototype scale. The initial load on the actuator during the installations for CPTs through the lid was equal to the submerged self-weight. This load was reduced to zero at a constant rate of 1 N/s during the self-weight penetration. At this point the steel wire went slack and the self-weight penetration terminated. The three way valve vented to ambient until the self-weight penetration completed.

(2) Once the self-weight penetration stopped, the valve was switched to achieve a hydraulic connection between the caisson internal and the syringe pump without stopping the centrifuge. A constant pumping flow rate was applied and maintained until the caisson penetration stopped.

(3) The in-flight suction caisson installation was completed by sealing the valve without stopping the centrifuge.

5.1.1.9 CPT through the caisson lid

The CPTs inside the caissons were performed subsequently to suction caisson installation as follows:

(1) A waiting period of at least 60 s at $100g$ was maintained before the CPT commenced to ensure that the suction pressure inside the caisson had dissipated.

(2) Subsequently and without stopping the centrifuge, the CPT was performed through the caisson lid at a constant penetration velocity of $v_{cpt} = 1\,\mathrm{mm/s}$, which is expected to result in drained conditions (Finnie and Randolph, 1994). The cone was penetrated into the soil sample until a a depth of at least $z/L = 1.2$ was reached. The maximum penetration depth was limited by the clearance between the guide rod and the bottom plate of the lower actuator clamp.

(3) Once the maximum penetration depth was reached, the cone penetrometer was extracted from the soil until the tip retracted inside the caisson lid again. The tests were terminated before the caisson was disturbed by subjecting the steel wire to tension.

5.1.2 Results and discussion

The experimental results are presented in non-dimensional form, unless stated otherwise. Positive values indicate compression and downward displacements, whereas negative values represent tension and upward displacements.

5.1.2.1 Suction caisson installation

Figure 5.4 shows the achieved self-weight and suction-assisted total penetration depths. The majority of installations were terminated at more than $z/L = 0.85$ skirt penetration. The soil displaced by the skirt volume increases the plug volume by approximately 2 % – assuming that 50 % of the displaced sand moves inwards during the self-weight penetration and 100 % moving into the caisson during the suction installation. Consequently, a skirt penetration of $z/L \approx 0.98$ indicates full installation without plug heave. Full installation is also indicated through the distinct change in gradient, which is visualised in Figures 5.5 and 5.6 – i. e. the establishment of lid contact is presumed to stop the caisson penetration. Table 5.2 shows that total skirt penetration depths of $z/L \leq 0.98$ were achieved in most tests. Thus, the occurrence of plug heave is likely.

Table 5.2: Normalised penetration depths including settlements after during static loading.

Test name	Penetration depth z/L			
	SWP[a]	SI[b]	SL[c]	SUL[d]
INST-1-H-S	0.478	0.930	-	-
INST-1-H-MS[e]	0.282	0.527	-	-
INST-2-H-M	0.363	0.803	-	-
INST-3-H-F	0.478	0.941	-	-
INST-3-H-SF[e]	0.189	0.460	-	-
INST-4-L-M	0.509	0.932	-	-
INST-5-L-F	0.568	0.954	-	-
INST-5-L-SF	0.459	0.937	-	-
INST-5-L-SF2[e]	0.213	0.440	-	-
CYC-1-H-S	0.562	0.967	0.971	0.968
CYC-2-H-M	0.515	0.867	0.873	0.870
CYC-3-H-F	0.471	0.913	0.926	0.924
CYC-4-L-M	0.483	0.905	0.908	0.906
CYC-5-L-F	0.575	0.992	0.996	0.995

[a]SWP = self-weight penetration; [b]SI = suction installation;
[c]SL = static loading; [d]SUL = static unloading; [e]$L = 80\,\text{mm}$

Table 5.2 shows a similar settlement response for each caisson when the static vertical load was increased to $V/A = 116\,\text{kPa}$. Since the sum of the calculated tip and measured skirt resistance $V/A \approx 88\,\text{kPa}$ is exceeded, the lid is expected to transfer stresses into the soil plug. This also indicates that partial or full lid contact is likely to be present in most tests regardless of the achieved skirt penetration depth.

Since different skirt penetration depths were achieved, a possible influence of the applied suction pressure is evaluated: The development of the normalised suction pressure during skirt penetration is presented in Figure 5.7 and follows an almost linear trend. Moreover, it appears to be independent of the pumping flow rate. This findings are reasonable since the measured values scatter around the predictions in accordance with Houlsby and Byrne (2005b), using $\varphi_p = 43\,°$, $m = 1.2$, $Ktan(\delta) = 0.15$, and $k_{in}/k_{out} = 1$.

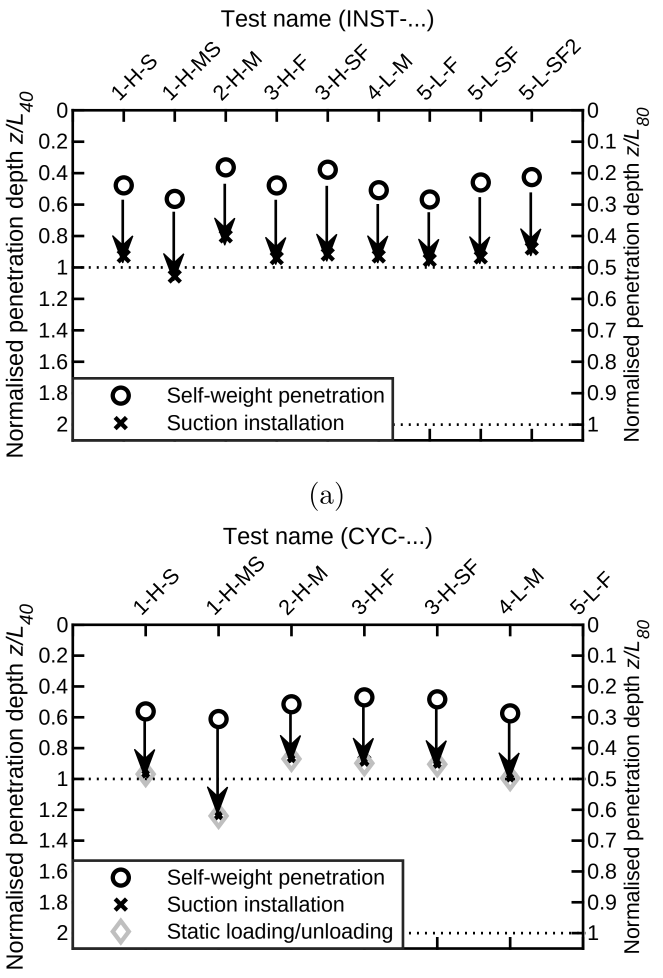

Figure 5.4: Normalised penetration depths of tests with CPT (a) and cyclic loading (b).

The curves shown in Figure 5.5a and 5.6a emphasise that a specific pumping flow rate leads to a related caisson penetration velocity. Furthermore, a comparison between suction caisson installations for tests with CPT through the lid and installations for cyclic loading test show a similar response to the same pumping flow rate. This demonstrates that the suction caisson installation is reproducible in the centrifuge environment at $100g$.

The test INST-1-H-S, INST-1-H-MS, CYC-1-H-S, and CYC-1-H-MS were installed at relatively slow pumping flow rates. This results in a prototype caisson penetration rate of $\Delta\dot{z} \approx 0.18\,\mathrm{m/h}$ in the beginning, which implies a prototype skirt penetration of two meters ($\Delta z/L = 0.5$) in $t \approx 11\,\mathrm{h}$ of suction installation. The penetration rate immediately slowed down and tended to zero at a relative penetration depth of $\Delta z/L \approx 0.2$. Hence, the pumping flow rate was doubled at this point to avoid premature refusal (see Table 5.1).

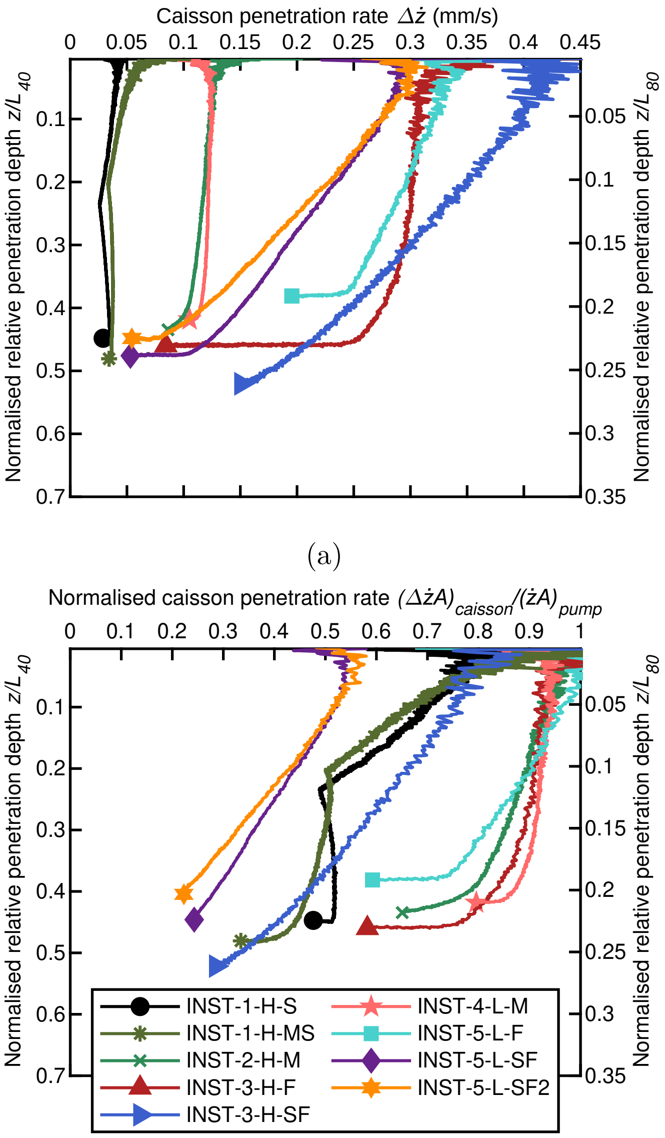

(a)

(b)

Figure 5.5: History of caisson penetration rates (a) and normalised caisson penetration rates (b) measured during the installations for CPTs through the lid.

Figures 5.5b and 5.6b show the history of the normalised caisson penetration rate that links the pumping flow rate to the suction pressure and the actual drainage conditions in accordance to Houlsby and Byrne (2005b). A value of $\Delta\dot{z}A_{caisson}/\Delta\dot{z}A_{pump} = 1$ implies no seepage losses, i. e. complete transferral of the pumping flow rate towards penetration of the suction caisson skirts; values less than 1 indicate seepage losses and hence less efficient suction installation. The normalised caisson penetration rate shown in Figure 5.5b and 5.6b and therefore the suction pressure transferral, rapidly decreased when a relatively slow pumping flow rate was applied. This behaviour indicates soil plug loosening due to the ongoing seepage flow and minimum caisson penetration rate. This implies that the skirt tip resistance is not reduced sufficiently, which eventually leads to premature refusal.

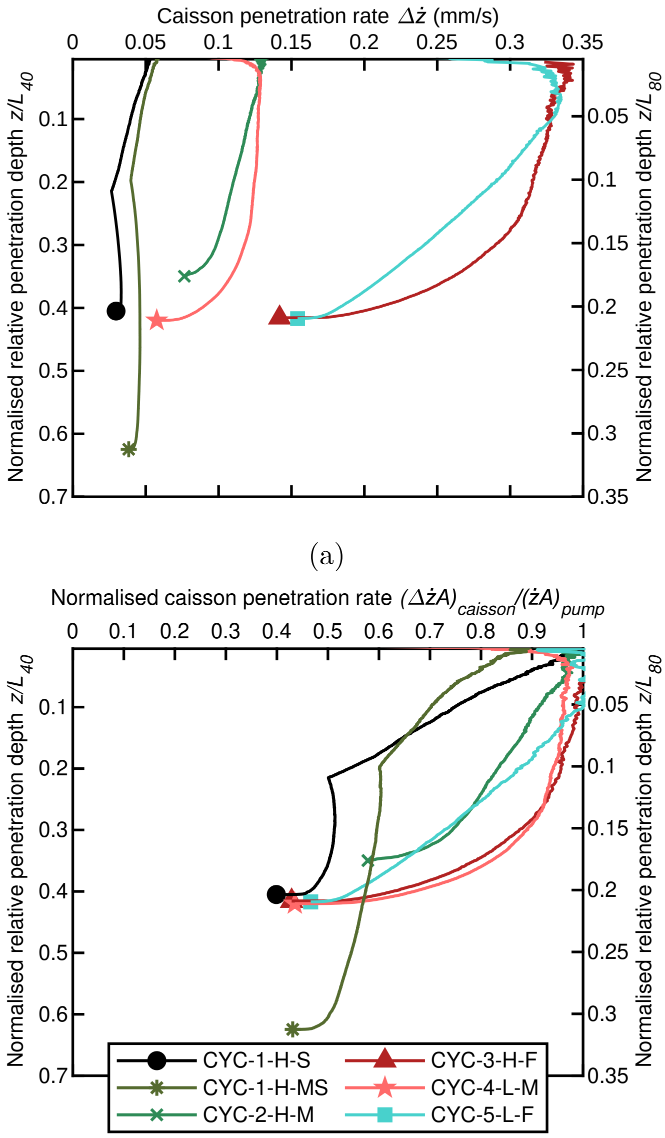

(a)

(b)

Figure 5.6: History of caisson penetration rates (a) and normalised caisson penetration rates (b) measured during the installations for cyclic loading tests.

Pivotal plug loosening is furthermore expected to be accompanied by a distinct drop in internal suction pressure. Since Figure 5.7 does not indicate this, an insufficient reduction of the tip resistance is found to be the primary reason of the decreasing caisson penetration rate. However, loosening is indicated by a decreasing normalised caisson penetration rate presented in Figures 5.5b and 5.6b. Consequently, plug loosening is present to a certain extent, but does not trigger premature refusal.

In order to prevent refusal from insufficiently reduced skirt tip resistance, the pumping flow rate was doubled, which marks the point of the distinct change in gradient of the (normalised) caisson penetration rate. Based on the overall behaviour represented by Figure 5.5

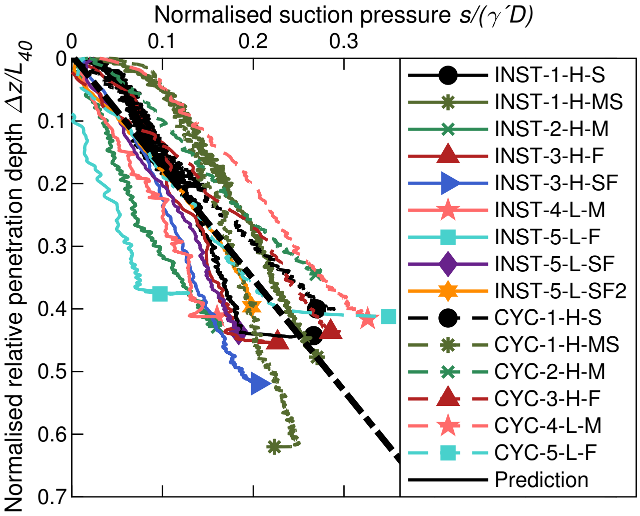

Figure 5.7: History of normalised suction pressure.

and 5.6 it is presumed, that the increased pumping flow rate ensured the maintenance of the suction pressure and therefore enabled a successful installation. The test results presented in Figure 5.5 and 5.6 confirm and extend the conclusion of Bienen et al. (2018b) as a more comprehensive range of caisson penetration rates was achieved.

The results from tests INST-2-H-M, INST-4-L-M, CYC-2-H-M, and CYC-4-L-M plotted in Figures 5.5 and 5.6 represent caissons installed at a moderate pumping flow rate. A moderate pumping flow rate is similar to a prototype caisson installation of two meters of skirt length in $t \approx 5.5\,\mathrm{h}$. A nominally constant model caisson penetration rate of $\Delta\dot{z} \approx 0.1\,\mathrm{mm/s}$ and a pumping flow rate transferral of $\Delta\dot{z}A_{caisson}/\Delta\dot{z}A_{pump} \approx 0.65$ to 0.85 was maintained for the majority of the suction installation process.

Those four moderate pumping flow rate tests provide insights into the following aspects: Compared to the installations at lower pumping flow rates, a more uniform caisson penetration rates are achieved. Moreover, this indicates that a moderate pumping flow rate in those particular tests provides a certain balance between seepage flow and caisson penetration velocity that favoured complete caisson installations. Furthermore, the comparison to tests conducted in higher (INST-1-H-MS and CYC-1-H-MS) and lower (INST-4-L-M and CYC-4-L-M) effective sample permeabilities confirms the expectation that a lower effective permeability benefits the uniformity of the caisson penetration rate as less seepage flow occurs (see Figures 5.5 and 5.6).

Maximum caisson penetration rates between $\Delta\dot{z} \approx 0.23$ and $0.33\,\mathrm{mm/s}$ were reached during the seven installations at relatively fast pumping flow rates. The seven caissons slowed down at a similar rate during the course of the installation. Increased seepage losses occurred in tests INST-5-L-F and CYC-5-L-F that were performed in less permeable soil than in tests INST-3-H-F and CYC-3-H-F, which were conducted in a more permeable soil sample. This is contradictory to the behaviour observed in tests at moderate pumping flow rates. However, the considered caissons were successfully installed at slightly larger penetration depths compared to the ones at moderate pumping flow rate. This also holds for test INST-5-L-SF, which is the caisson that was installed successfully at the fastest pumping flow rate applied during the presented series of experiments.

It is summarised that the results indicate that a slow pumping flow rates favours plug heave due to the presence of seepage flow and the absence of caisson penetration, which is consistent with M. N. Tran et al. (2004). The test results confirm that there is a certain minimum pumping flow rate above which suction installation is successful (Bienen et al., 2018b). The minimum pumping flow rate can be predicted in accordance with Houlsby and Byrne (2005b). Furthermore, the evaluation of test results featuring a wide range of pumping flow rates does not indicate any systematic correlation between pumping flow rate and the suction pressure, the plug heave, or the achieved penetration depths. Hence, it is presumed that the effect of the suction installation history is marginal.

5.1.2.2 CPTs characterisation of the soil plug

Four CPTs inside the installed suction caissons were conducted in addition to those presented in Stapelfeldt et al. (2018). All CPTs shown here are renamed to facilitate comparison. The tests discussed in Stapelfeldt et al. (2018) are marked with their previous names in addition. The CPTs inside the caisson are plotted together with the free field CPTs in Figure 5.8 for comparison. The free field CPTs were conducted in undisturbed soil at sites in the same soil samples.

Based on the CPTs discussed in Stapelfeldt et al. (2018) no clear influence of the suction installation on the cone tip resistance was found – although plug heave and loosening were considered as a probable result of fast installations. The additional tests provide a more comprehensive data base, which confirms the previous results. The CPT profiles obtained from test INST-3-H-F and INST-3-H-SF, which were installed at high pumping flow rates, show similar or higher cone tip resistance compared to test INST-3-H-M, which was referred to as Test 4 in Stapelfeldt et al. (2018).

The installation of the $L = 80\,\mathrm{mm}$ model caisson in test INST-3-H-SF terminated at $z/L_{80} = 0.46$, while test INST-3-H-F featuring the $L = 40\,\mathrm{mm}$ model caisson was installed completely. Stapelfeldt et al. (2018) supposed that an increased cone resistance results from regaining strength of the soil plug after the suction installation within the confinement of the caisson skirt – even without lid contact. These additional results confirm the conclusions of the previous study, because an increased cone resistance was measured inside completely (INST-3-H-SF) and partially (INST-3-H-F) installed caissons.

Furthermore, test INST-1-H-S shows a similar cone resistance compared to test INST-3-H-F before the gradient eventually changes close to a depth where the cone tip passes the skirt tip. Some plug heave was likely to occur in test INST-1-H-S as discussed above. The respective CPT inside the caisson does not indicate a permanent impact on the plug

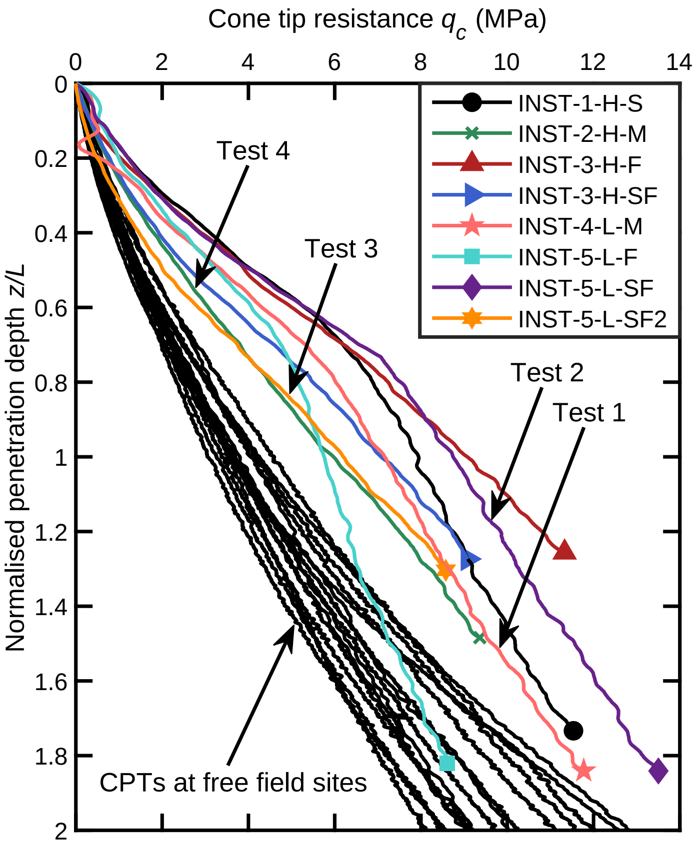

Figure 5.8: CPTs before and after caisson installation.

state – e. g. the presence of significantly lower cone resistance that would indicate plug loosening and therefore heave. Based on the achieved penetration depth of $z/L = 0.930$, it is likely that lid contact was present here. Consequently, the additional results confirm that lid contact rather than the suction installation dominate the stress state of the soil plug (Stapelfeldt et al., 2018) – i. e. the effect of the suction installation on the soil plug state is marginal.

5.1.3 Remarks on the centrifuge tests

The discussed results from two parallel series of centrifuge tests confirm that it is possible to install a suction caisson at a minimal pumping flow rate. A sufficient penetration depth close to full skirt penetration was also achieved at significantly higher pumping flow rates. The related cone tip resistance profiles inside the caisson do not indicate a major influence of the pumping flow rate on the formation of plug heave and loosening.

Several cone tip resistance profiles show a distinct change in gradient, but others do not. Stapelfeldt et al. (2018) found that the achieved penetration depths have an influence in this case. Test INST-3-H-F achieved a penetration depth of $z/L = 0.941$, which indicates that the lid is at least partially in contact with the soil plug. However, the corresponding cone tip resistance profile shows only a marginal change in gradient. Further investigations on a possible influence of plug loosening or partial lid contact were performed by Stapelfeldt et al. (2020). The presented results are based on finite element simulations and provide further insights: The discussed FEA results show that the confinement inside the skirt plays a certain role, but the compression applied to the soil plug through the lid invert determines the cone resistance inside the suction caisson. Partial lid contact has also been addressed by Stapelfeldt et al. (2020). The numerical analyses results suggest that this is the case in several centrifuge tests, which is plausible under consideration of the actually achieved penetration depth of $z/L \leq 1$. The presented numerical simulations therefore reinforce the findings obtained from the centrifuge experiments.

The additional FEM simulations clarify the matters considering the CPT inside the caisson. However, the mechanisms underlying the suction caisson installation remain invisible in the presented studies. Ragni et al. (2018) and Ragni et al. (2019) introduced a method that enables PIV post analysis of images obtained in a centrifuge environment to visualise the suction caisson installation. However, further investigations remain necessary:

(1) Centrifuge tests involving a half-model caisson for PIV analyses are limited to thick-walled model caissons yielding in $t/D = 25$ or less (Ragni et al., 2019). Are the mechanisms underlying the self-weight penetrations and the suction installation influenced by the t/D ratio?

(2) The existing database of half-model installation in sand is limited to a model caisson diameter of $D = 50\,\text{mm}$ (Ragni et al., 2018; Ragni et al., 2019). Could a larger diameter lead to different mechanisms as less confinement of the soil plug is present?

(3) Sand characterised by high friction angles is often utilised in laboratory tests. However, offshore sites may feature sand with lower friction angles. To what extend does the soil shear strength influence the mechanisms underlying the suction caisson installation?

(4) If the lid touches down on the soil plug, an inversion of the soil plug heave is expected up to a certain degree. But, this state was not evaluated in the experimental study presented by (Ragni et al., 2019). What are the mechanisms occurring when lid contact is established and how do they influence the soil plug state?

5.2 Numerical simulations

A MPM model capable of the simulation of the jacked penetration and suction installation of a caisson is utilised for further investigations. The numerical simulations target the visualisation of the mechanisms underlying the suction caisson installation. The study consists of two steps: First, a comparison to the centrifuge test results presented in Ragni et al. (2018) and Ragni et al. (2019) is employed for validation. In a second step, variations of the model dimensions and the material parameters are investigated in order to answer the questions above.

5.2.1 Numerical modelling and testing procedure

The numerical simulations are performed with a modified version of the MPM code Anura3D 2019.1. The modifications were discussed in Chapter 4. The numerical model has the following requirements:

- The simulation of a caisson skirt penetration into the soil has to be feasible. The caisson skirt penetration causes predominantly plastic deformations at the skirt tip. Thus, the numerical model has to capture large deformations and elastic-plastic constitutive behaviour.
- The skirt wall interacts with the surrounding soil through interface friction. Thus, a contact formulation accounting for friction and relative displacement between the skirt and the soil is required.
- The suction installation additionally requires the calculation of the pore pressure field resulting from a pressure differential between the internal suction pressure and the ambient hydrostatic pressure. The suction installation is dominated by the resulting pore pressure regime and ongoing large deformations at the skirt tip.

The numerical model for the MPM simulations shown in Figure 5.9 features the caisson that is pre-embedded in the soil. The dimensions shown in Figure 5.9a were derived from the centrifuge tests and are also found to minimise boundary effects in the numerical simulations. The two-dimensional axisymmetric model consists of triangular elements containing three MPs each in the beginning of the analysis. The mesh shown exemplary in Figure 5.9b illustrates small elements located close to the caisson. A more coarse mesh is utilised further away from the area where the largest deformations are expected. The model dimensions employed for each numerical simulation are summarised in Table 5.3.

Table 5.3: Numerical model caisson dimensions.

Model No.	D (m)	L (m)	t (cm)
10	5	5	20
11	5	5	5
20	8	4	20

The horizontal displacements are locked at the axis of symmetry and outside the vertical edge of the model geometry, while vertical displacements are permitted. The bottom features zero vertical displacement boundary conditions. These three edges are also hydraulically impermeable. The displacements at the soil surface are unlocked, while solid and liquid pressure boundary conditions applied on the MPs shown in Figure 5.9a are utilised to establish the differential pressure. The caisson is modelled as a quasi-rigid body as the horizontal displacement rate is $\dot{z}_h = 0$ and a prescribed vertical displacement rate $\dot{z}_v$ is utilised to control the caisson penetration.

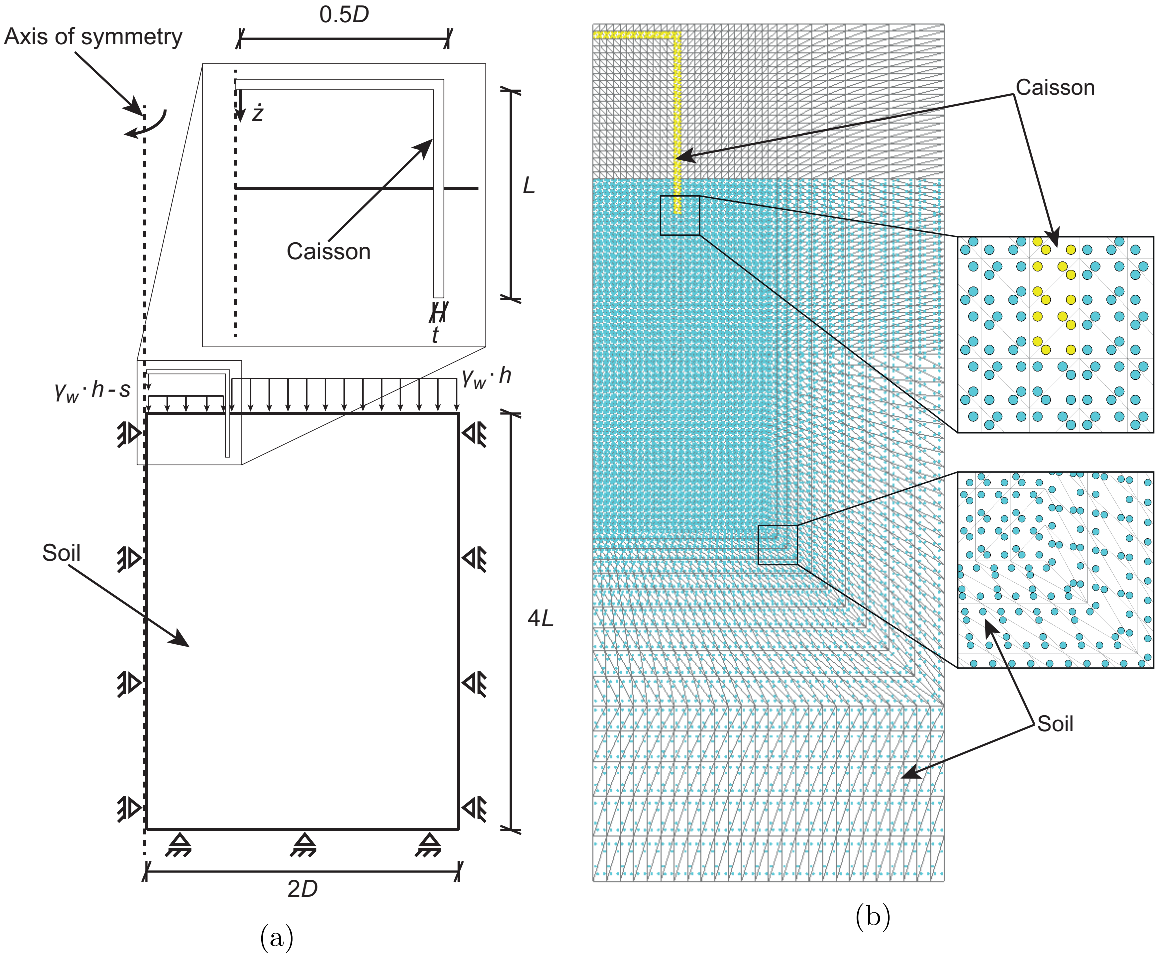

(a) (b)

Figure 5.9: Dimensions (a) and discretization (b) of the numerical model utilised for MPM analyses of the suction caisson installation in a uniform sand profile.

Drained conditions were present during the jacked self-weight penetration in the centrifuge test. This ensured minimal soil disturbance and was expected to be consistent with prototype installations. Hence, it was possible to model the soil as a one-phase continuum for this kind of simulations. A transient pore pressure regime determines the course of the suction installation. Thus, a v-w-formulation was employed for the numerical simulations of the suction installation. This results in a further requirement: The utilisation of the mixed integration scheme becomes necessary in order to minimise numerical errors due to grid crossing, which results in artificial stress and pore pressure peaks (Jassim et al., 2013; Fern et al., 2019). It is noted that advanced constitutive models – e. g. hypo-plasticity – are prone to inaccurate solutions utilising the mixed integration scheme. Comparably simple elastic-plastic models enable the visualisation of the underlying mechanisms. This satisfies the requirements in this study. The underlying mechanisms are furthermore determined by the pore pressure regime as well as large displacements and therefore mostly plastic deformation. Hence, the Mohr-Coulomb constitutive model is employed.

The model parameters summarised in Table 5.4 are determined under consideration of laboratory test results summarised in M. N. Tran (2005), Lehane and Q. B. Liu (2013), and Chow et al. (2018). The shear strength is slightly adjusted to ensure similarity between the experimentally determined mechanisms and the calculation results. A reduced liquid bulk modulus is utilised in order to minimise numerical errors. Furthermore, computational costs are reduced, which is particularly important when fine meshed models are calculated. The value given in Table 5.4 is a minimum value that avoids a major influence on the results (Fern et al., 2019). The initial porosity n and the interface friction coefficient μ are derived from the results of the centrifuge experiments referred in Section 5.1.

Table 5.4: Model parameters for MPM simulations featuring fine silica sand.

Parameter	Symbol	Unit	Fine silica sand
Friction angle	φ	(°)	$32 - 38$
Dilation angle	ψ	(°)	1
Effective cohesion	c'	(kPa)	0
Young's modulus	E	(MPa)	$40 - 60$
Poisson's ratio	ν	(-)	0.25
Intrinsic permeability	κ	(m^2)	$1 \cdot 10^{-11}$
Dynamic viscosity liquid	η_w	(kPa·s)	$1 \cdot 10^{-6}$
Bulk modulus liquid	K_w	(kPa)	20000
Density water	ρ_w	(t/m^3)	1
Initial porosity	n	(-)	$0.35 - 0.375$
Grain density solid	ρ_s	(t/m^3)	2.65
Interface friction coefficient	μ	(-)	0.15

The simulations are conducted according to the following procedure: First, the effective stresses and, if necessary the hydrostatic pressure, are applied during the K_0 procedure. The caisson is penetrated displacement controlled in a second step. The differential pressure is applied simultaneously, if required. The caisson penetration rate and suction pressure vary in each test. Therefore, the considered values are given in the following section.

5.2.2 Results and discussion

The MPM simulations were performed to address the remaining questions subjecting the suction caisson installation in sand. The calculated results are presented in non-dimensional form, unless stated otherwise. Positive values indicate compression and downward displacements, whereas negative values represent tension and upward displacements.

5.2.2.1 Suction caisson installation mechanisms

In advance to further investigations, the simulated suction caisson installation is compared to experimental results obtained from PIV analyses with the purpose to ensure that the model features the relevant installation mechanisms (Ragni et al., 2019). Figure 5.10 compares the experimental and the calculated results of a jacked caisson installation.

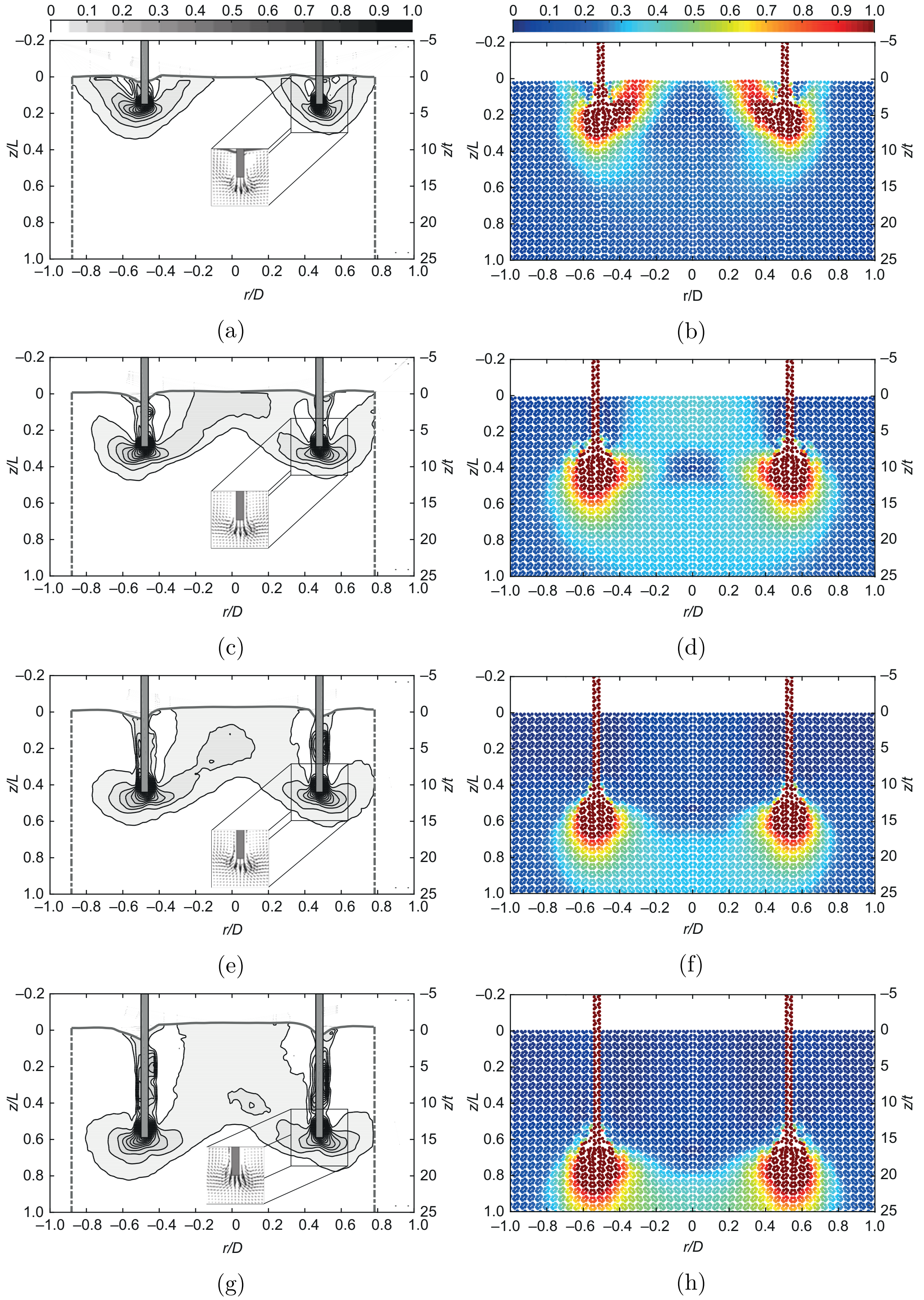

(a) (b) (c) (d) (e) (f) (g) (h)

Figure 5.10: Comparison between normalised resultant displacements during the self-weight penetration obtained from PIV analyses (Ragni et al., 2019) on the left hand side (LHS) and axisymmetric MPM analyses on the right hand side (RHS) at normalised penetration depths of $z/L = 0.15$ (a,b); $z/L = 0.30$ (c,d); $z/L = 0.45$ (e,f); $z/L = 0.60$ (g,h).

The numerical analysis results are obtained stepwise and are normalised in style of the approach discussed in Ragni et al. (2019). The calculated results show a separated mechanism at shallow penetration depths that is similar to the experiments also shown in Figure 5.10. A combined mechanism is present from a penetration depth of $z/L = 0.3$ in the experimental and the simulated results. The experimental results show some plug heave developing throughout the entire course of the penetration, while only minimal plug heave is visible in the calculated results at $z/L = 0.45$ and $z/L = 0.6$. It is additionally noted that the area of large displacements at the skirt tip is spreading out wider in the numerical simulations compared to the experiments.

The larger area affected by displacements below the skirt tip found in the simulation is plausible, since the skirt tip is the area where the highest stresses occur. The model Young's modulus does not increase with growing stresses, but the stiffness modulus of the soil utilised in the experiments does. Consequently, the resulting displacements are expected to differ. However, the key mechanism underlying the jacked installation is similar: The soil is displaced symmetrically at the skirt tip in the experiment and in the numerical simulation. This is plausible, because only a limited amount of plug heave is expected due to the soil volume that is displaced inwards into the confined environment of the caisson skirt. Hence, the numerical model is considered to be suitable for the simulation of the jacked caisson installation.

The simulation of the suction installation requires additional input: the caisson penetration rate $\dot{z}$ and the internal suction pressure s. The fast caisson penetration of Test 3 (Ragni et al., 2019) is utilised for comparison. The prototype and therefore the penetration rates in the numerical model vary between $\dot{z} = 0.2\,\mathrm{m/s}$ and $\dot{z} \approx 0.08\,\mathrm{m/s}$ with depth. The corresponding suction pressures shown in Figure 5.11 are calculated from the parameters given in Ragni et al. (2019). A lower and upper bound estimate was found through the variation

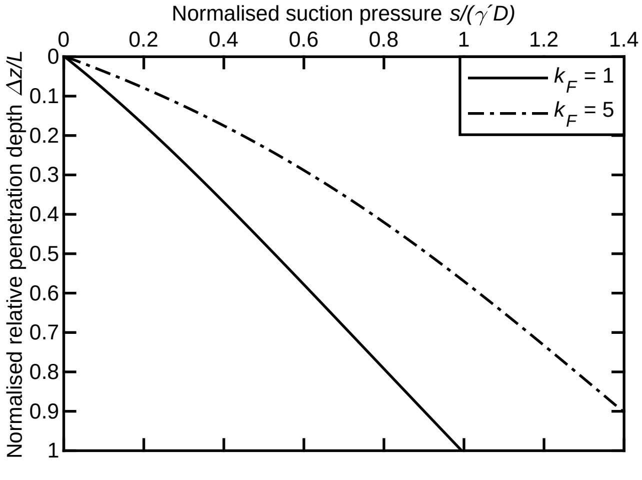

Figure 5.11: Calculated history of the required suction pressure for the installation of a thick-walled $L = D = 5\,\mathrm{m}$ caisson in sand (Ragni et al., 2019; Houlsby and Byrne, 2005b).

of $k_F = k_{in}/k_{out}$, while the calculations follow the procedure presented in Houlsby and Byrne (2005b). The suction pressure is normalised by the effective specific density of the sand $\gamma' = 10.5\,\mathrm{kN/m^3}$ and the caisson diameter $D = 5\,\mathrm{m}$.

The calculated results presented in Figure 5.12 feature the same inverted V-shaped mechanism that was observed by Ragni et al. (2019) at normalised penetration depth of $z/L = 0.28$ and $z/L = 0.51$. However, almost no additional plug heave is calculated at a

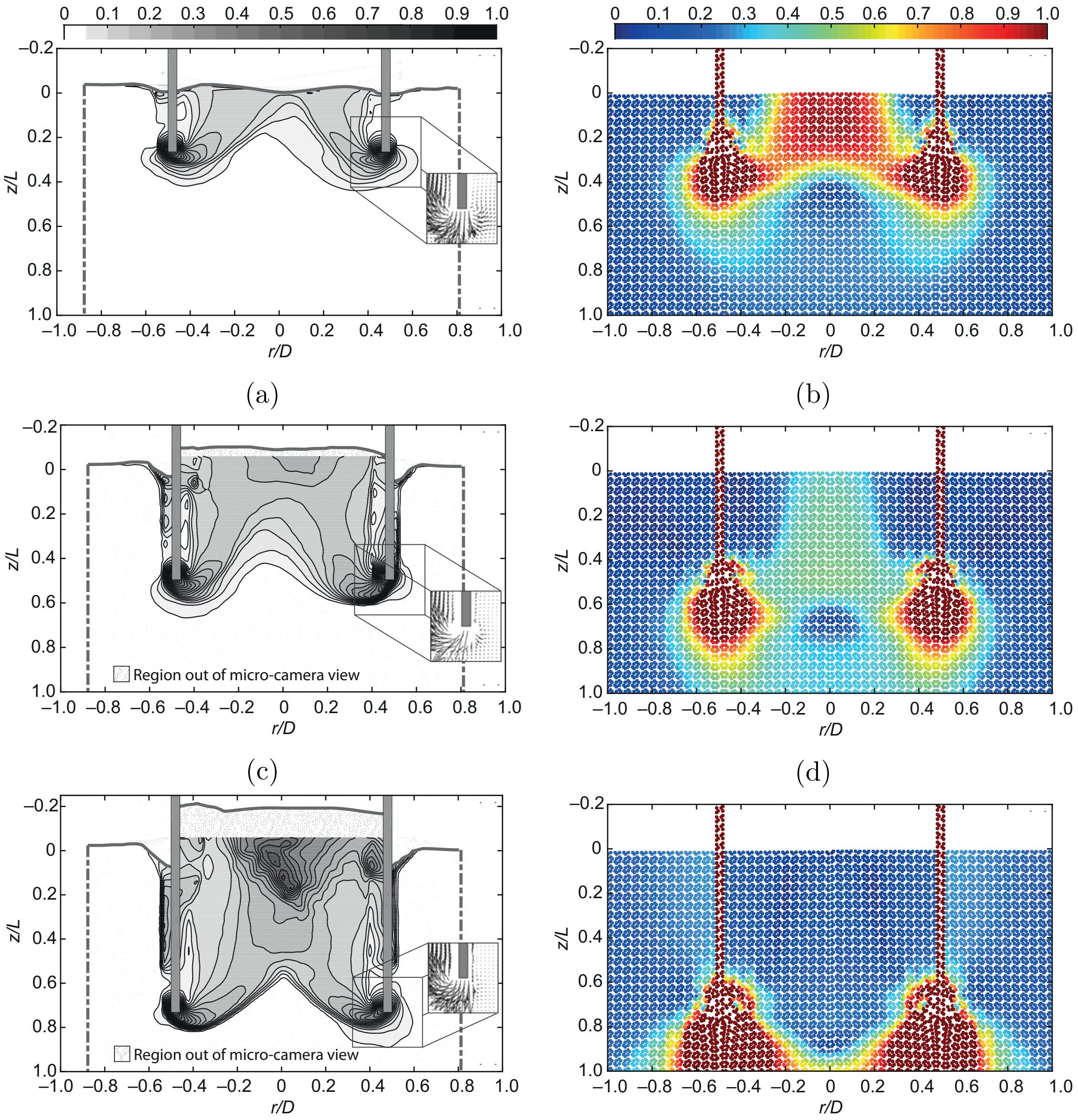

(a) (b)

(c) (d)

(e) (f)

Figure 5.12: Comparison between normalised resultant displacements during the suction installation in dense sand obtained from PIV (Ragni et al., 2019) (LHS) and axisymmetric MPM (LHS) analyses at increasing normalised penetration depths $z/L = 0.28$ (a,b); $z/L = 0.51$ (c,d); $z/L = 0.74$ (e,f).

normalised penetration depths of $z/L = 0.74$ despite the application of the upper bound suction pressure shown in Figure 5.11. The increase of the calculated suction pressure diminishes slightly with the course of the caisson skirt penetration. In contrast, suction pressures measured during experiments (see Figure 5.7) increase significantly as the target penetration depth is approached. Hence, the applied differential pressure is believed to be to small. Therefore, an additional calculation featuring a maximum differential of $s = 100\,\mathrm{kPa}$ was conducted.

The calculated displacement contours shown in Figure 5.13 show that plug heave indeed occurs due to the presence of increased internal suction pressure. The vertical displacements show downward movement of the soil outside the caisson skirt due to the frictional interaction. Upward displacement is observed inside the caisson. The largest heave occurs in the middle of the caisson. The internal frictional interaction reduces the heave close to the skirt. This behaviour is similar to the experimental results presented in Figure 5.12. Consequently, it is demonstrated that the presented numerical model is suitable for the simulation of the suction caisson installation in saturated sand.

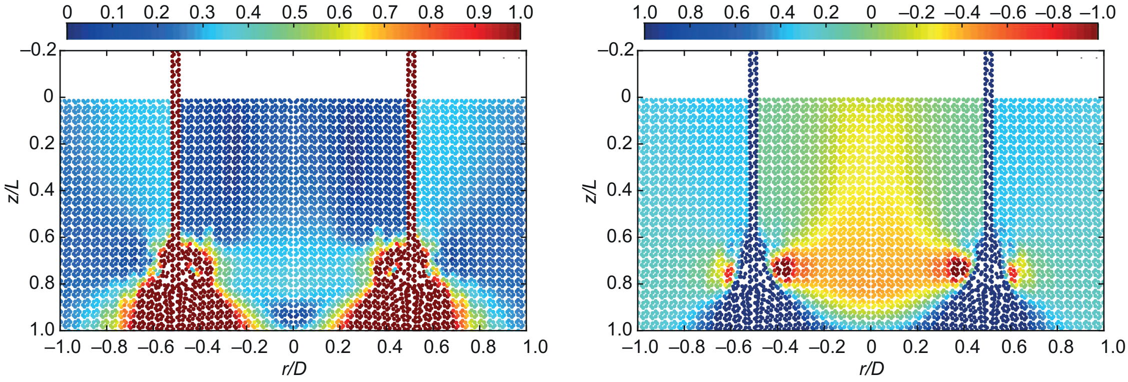

(a) (b)

Figure 5.13: Normalised resultant (a) and vertical (b) displacements during the suction installation in dense sand of a thick-walled caisson at a normalised penetration depths of $z/L = 0.75$.

5.2.2.2 Influence of the skirt wall thickness

A downside of the half-model centrifuge tests discussed in Ragni et al. (2019) and Ragni et al. (2019) is that they are limited to thick-walled model caissons due to the requirement of the attached seal. These circumstances yield a ratio of $t/D = 25$, which differs from prototype caissons usually featuring a considerably smaller skirt wall thickness featuring typical ratios of at least $t/D \geq 100$. Therefore, the MPM approach is utilised to examine the applicability of the half model caisson experiments towards prototype applications.

The numerical model no. 11, which features a wall thickness and diameter ratio of $t/D = 100$ instead of $t/D = 25$, is utilised for investigations on the skirt wall thickness. This required a refinement of the mesh, because at least one element had to be utilised to model the caisson skirt (see Figure 5.9). Hence, a sensitivity study was performed to ensure comparability between the previous results and the following ones. This study additionally provides insights into possible mesh dependency.

The geometry of model no. 10 was meshed with a four times finer mesh compared to the one utilised in the previous simulations. This modified model was utilised to recalculate suction assisted installation. A comparison between Figure 5.12b and Figure 5.14 reveals a slightly steeper and less united inverted V-shaped displacement contour. Thus, a certain mesh dependency is expectedly present as the investigated mechanism involves local shearing failure. However, both simulations overall yield displacements that are similar to the experimental results – i. e. plug heave is occurs in both calculations.

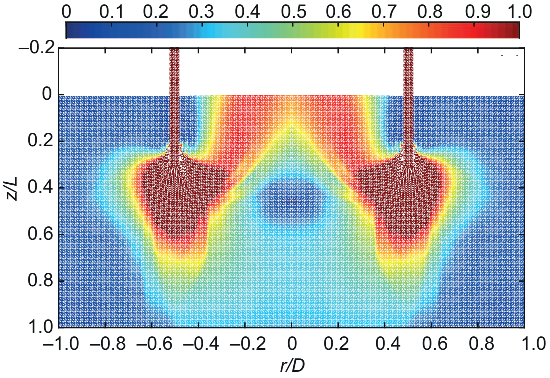

Figure 5.14: Normalised resultant displacements during the suction installation of a thick-walled $L = D = 5\,\mathrm{m}$ caisson in sand at a normalised penetration depth of $z/L = 0.3$ simulated with a fine mesh.

The installation of a thin-walled caisson requires less suction pressure in comparison to the previously investigated thick-walled caisson. Hence, the required suction pressure was re-calculated (Houlsby and Byrne, 2005b). The results are summarised in Figure 5.15 and are employed to apply the differential pressure to the MPM model. The caisson penetration rate from the previous analysis was maintained in order to ensure comparability.

The normalised resultant displacements around the skirt tip, which are visible in Figure 5.16, are similar to the ones observed in simulations with the thick-walled caisson. However, the displacements of the plug are significantly smaller compared to the ones illustrated in Figure 5.12b and 5.12d. This is plausible, because only approximately 1/8 of the soil volume is displaced during the course of the thin-walled caisson penetration. However, the mechanisms underlying the suction installation – i. e. predominately inwards directed soil displacement due to seepage flow, plug heave and the influence of the skirt friction – are occurring independently from the skirt wall thickness. The only distinction that is found here is the extend of the plug heave due to soil displacement. Hence, the results obtained from the numerical analyses reinforce the validity of the half-model centrifuge test results presented in Ragni et al. (2018) and Ragni et al. (2019).

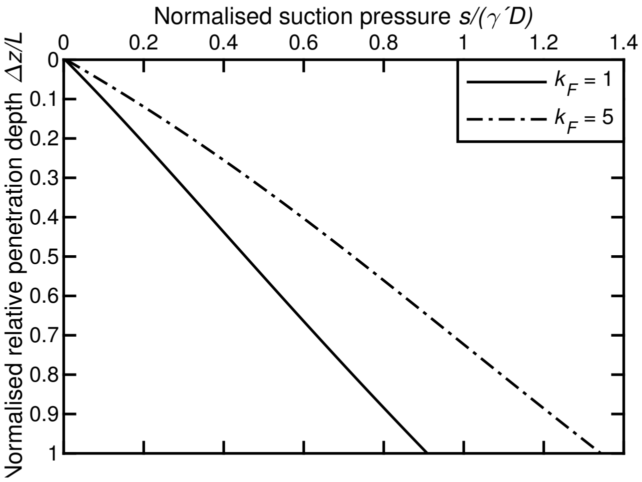

Figure 5.15: Calculated history of the required suction pressure during the installation of a thin-walled $L = D = 5\,\mathrm{m}$ caisson in sand (Houlsby and Byrne, 2005b).

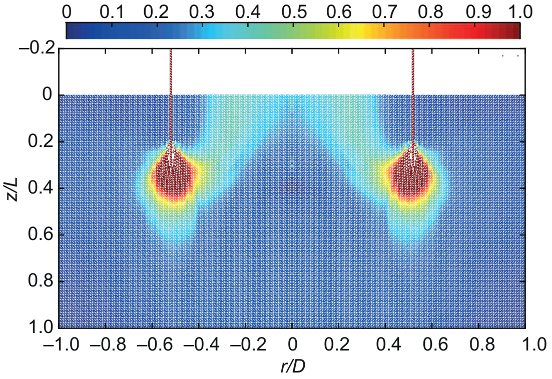

(a)

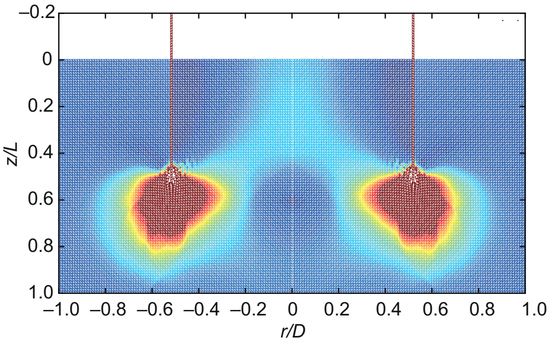

(b)

Figure 5.16: Normalised resultant displacements during the suction installation of a thin-walled caisson in dense sand at a normalised penetration depths of $z/L = 0.28$ (a) and $z/L = 0.51$ (b).

5.2.2.3 Influence of the caisson aspect ratio

The caisson aspect ratio and therefore the area of the soil plug could have an influence on mechanisms underlying the suction caisson installation: The confinement and the shape of the plug deformation contours can differ. The suction installation was therefore simulated employing model no. 20 that features a caisson with a diameter of $D = 8\,\mathrm{m}$, a skirt length of $L = 4\,\mathrm{m}$ yielding an aspect ratio of $L/D = 0.5$. The required suction pressure shown in Figure 5.17 was calculated utilising the approach presented by Houlsby and Byrne (2005b). The caisson penetration rate was taken from the previous tests.

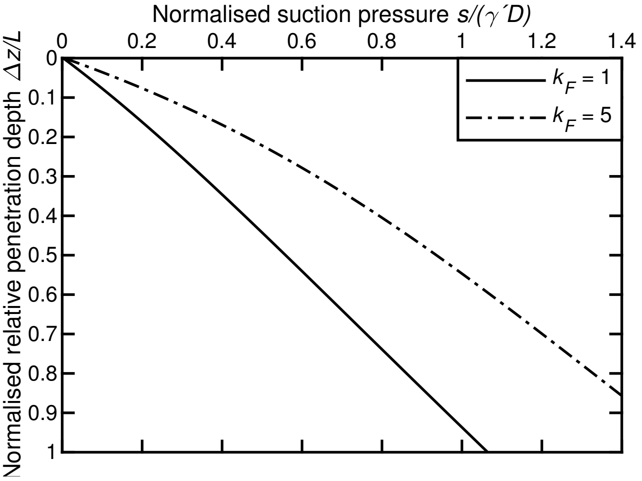

Figure 5.17: Calculated suction pressure required for the installation of a thick-walled $L = 4\,\mathrm{m}$ and $D = 8\,\mathrm{m}$ caisson in sand (Houlsby and Byrne, 2005b).

The results illustrated in Figure 5.18 reveal the presence of the same underlying mechanisms that occurred in the previous simulations. However, the extend of the plug heave is smaller compared to the $D = 5\,\mathrm{m}$ caisson. In addition, the mechanisms are almost separated and therefore hardly forming an inverted V due to the larger ratio of $t/D = 40$. Based on the results obtained from the numerical simulations it is concluded that inclined displacement zones occur independently from the caisson aspect ratio. However, a distinctly unified V-shaped plug heave mechanism requires a certain confinement, which is only present within caissons with an aspect ratio $L/D > 0.5$ in this study.

5.2.2.4 Effect of the relative density and shear strength

Dense sands characterised by a narrow grain size distribution and of more than $\varphi > 35\,°$ friction angle, like fine silica sand (Lehane and Q. B. Liu, 2013), are often utilised in experimental test series (Houlsby et al., 2005; Nielsen et al., 2015; Ragni et al., 2019). However, caisson foundations are also expected to be applicable at offshore sites that are characterised by medium dense sand featuring a lower shear strength. Therefore, the simulation of the suction installation presented in Figure 5.12 are re-calculated with modified soil parameters: The friction angle is set to be $\varphi = 32\,°$, the Young's modulus is reduced to $E = 40\,\mathrm{MPa}$, and the initial porosity is increased to be $n = 0.375$ in order to represent

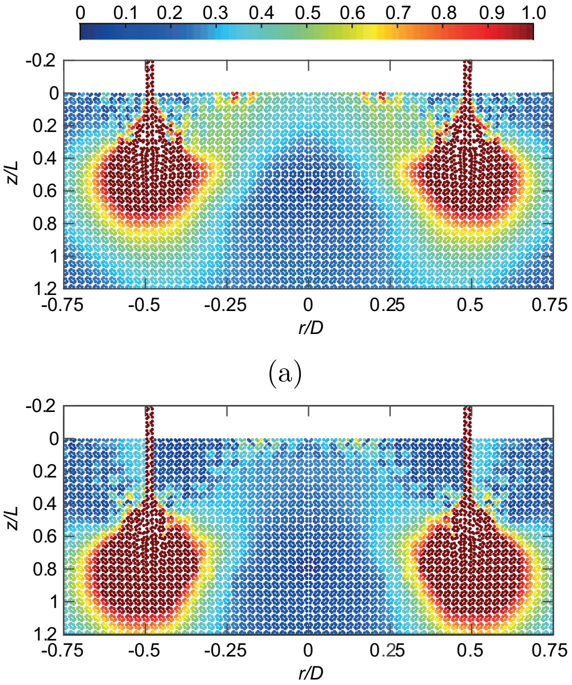

(a)

(b)

Figure 5.18: Normalised resultant displacements during the suction installation of a $L/D = 0.5$ caisson in dense sand at a normalised penetration depths of $z/L = 0.35$ (a) and $z/L = 0.56$ (b).

medium dense sand. The other soil parameters are taken from the previous analyses (see Table 5.4). The suction pressure is applied in accordance to Figure 5.19.

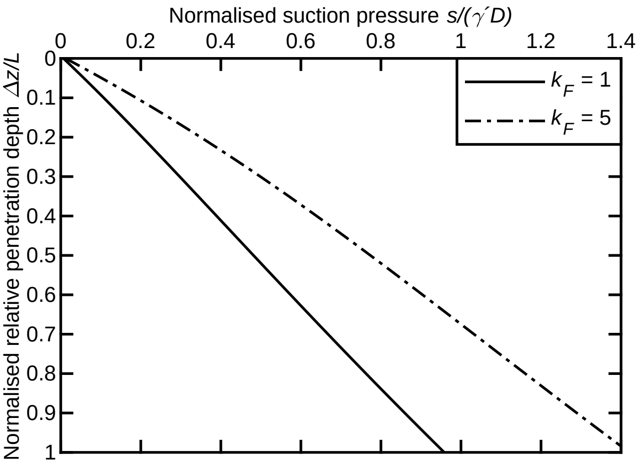

Figure 5.19: Calculated history of the required suction pressure during the installation of a thick-walled $L = D = 5\,\mathrm{m}$ caisson in medium dense sand (Houlsby and Byrne, 2005b).

The normalised resultant displacement contour illustrated in Figure 5.20 is similar to the ones presented in Figure 5.12. Hence, a decreased relative density does not effect the suction installation mechanisms occurring in the MPM simulation. This is consistent with the conclusions obtained from centrifuge Test 5 presented in Ragni et al. (2019). The calculated results additionally indicate that the friction angle has no distinct effect on the suction installation mechanism.

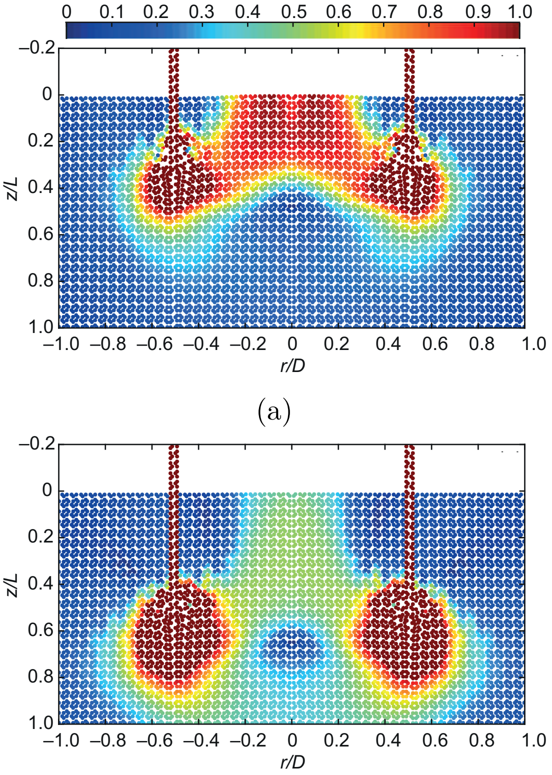

(a)

(b)

Figure 5.20: Normalised resultant displacements during suction installation of a $L/D = 0.5$ caisson in medium dense sand at a normalised penetration depths of $z/L = 0.35$ (a) and $z/L = 0.56$ (b).

5.2.2.5 Effect of the lid contact

The CPT profiles measured inside the model caisson discussed in Subsection 5.1.2.2 underpinned that lid contact has a crucial effect on the soil plug state. The MPM model therefore is employed to investigate this terminating stage of the suction caisson installation. A maximum suction pressure of $s = 100\,\mathrm{kPa}$ was applied as the internal pressure is expected to peak once the lid touches down. Furthermore, a relatively slow penetration rate of $\dot{z} = 0.01\,\mathrm{m/s}$ was applied to represent the slow down of the caisson. Normal contact between the soil and the approaching caisson lid entity establishes as soon as the distance between two MPs equals the height of an element of the background mesh. Consequently, a minor artificial gap is visible in Figure 5.21 despite the establishment of contact.

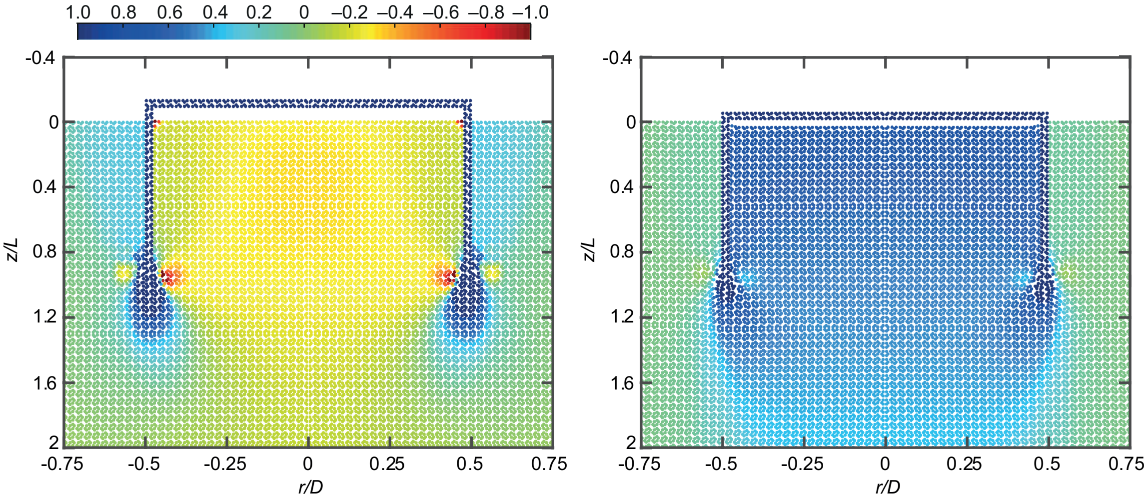

(a) (b)

Figure 5.21: Normalised vertical displacements during suction installation of a $L/D = 0.5$ caisson in medium dense sand at a normalised penetration depths of $z/L = 0.95$ (a) and $z/L \approx 1$ (b).

Plug heave is observed through the normalised vertical displacements presented in Figure 5.21a. Hence, the expected conditions close to the end of the suction caisson installation are established: A high suction pressure is present and the target penetration depth is almost reached. Figure 5.21b shows that the normalised displacements of the soil plug are inverted at the point of the lid touch down. It is noted that the suction pressure was maintained until the target penetration depth of $z/L = 1$ was reached (see Figure 5.22).

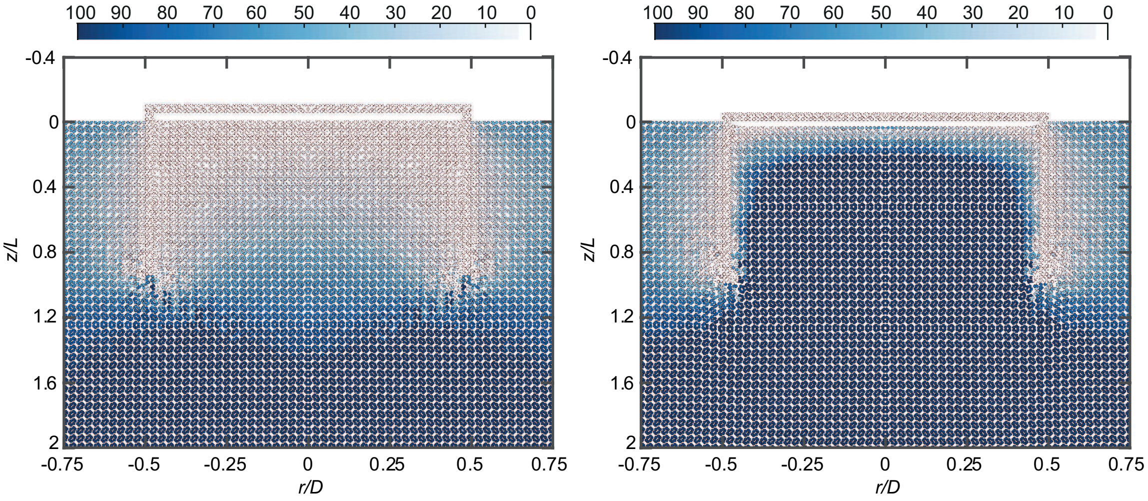

(a) (b)

Figure 5.22: Pore pressure contours (kPa) during suction installation of a $L/D = 0.5$ caisson in medium dense sand at a normalised penetration depths of $z/L = 0.95$ (a) and $z/L \approx 1$ (b).

The pore pressures are increasing due to the lid touch down shown in Figure 5.22b, but immediately dissipate towards the lid invert where suction pressure is still present. The ongoing evacuation of water though the pumping system is modelled by maintaining the suction pressure boundary conditions. This yields plug consolidation and therefore permanent settlements that counteract the previously present plug heave (compare Figure 5.21a and 5.21b).

5.2.3 Remarks on the numerical simulations

A MPM model capable of the simulation of the self-weight or jacked penetration and the suction installation of a caisson is established. The model is verified through the comparison to existing results obtained from centrifuge tests. The numerical analyses results visualise the underlying mechanisms and enabled further investigations on the influence of the t/D and L/D ratio and therefore the skirt wall thickness and the diameter. This enabled a re-evaluation of the centrifuge test and underpins the universal validity of the existing experiments. Furthermore, investigations on the soil shear strength and the effect of the lid contact add to the existing knowledge.

5.3 Concluding remarks on the suction caisson installation in sand

This chapter discusses the results of a series of centrifuge tests and numerical simulations of suction caisson installation in sand. The post installation condition of the soil plug was investigated by means of CPTs through the caisson lid in the centrifuge test. The numerical simulations featured the establishment of a MPM model for further investigations on the self-weight and suction installation mechanisms. The experimental and numerical investigations support the following findings:

(1) The pumping flow rate applied during suction caisson installation is not found to influence the soil plug, as shown by cone tip resistance profiles obtained inside the caisson following installation.

(2) The underlying mechanisms investigated by means of MPM simulations are found to be virtually independent from the caisson wall thickness and the diameter. Only the extend of deformations is influenced by the caisson dimensions.

(3) The soil plug state is dominated by the lid contact, not by the influence of the pumping flow rate applied during suction caisson installation. This confirms previous findings discussed in (Bienen et al., 2018b; Stapelfeldt et al., 2018) through the additional tests.

(4) The MPM simulations reveal the mechanisms occurring inside the soil as the suction installation terminates due to lid touch down. The results underpin the predominant influence of the lid contact on the soil plug state.

The results discussed in this chapter show that a permanent influence on the load bearing behaviour is unlikely. This aspect is expected to play a key role in further investigations on the vertical cyclic load bearing behaviour of suction caisson foundations.

6 Load bearing behaviour in sand

This chapter features investigations on the vertical cyclic load bearing behaviour in sand. The results of a series of centrifuge tests and numerical analyses are discussed. The investigations target a possible effect of the suction installation on the in-service performance of caissons subjected to vertical cyclic loading.

6.1 Centrifuge tests

6.1.1 Experimental arrangement and testing procedure

Two parallel series of centrifuge tests were performed to address the questions regarding the response of a suction caisson subjected to vertical cyclic loading in sand. These studies include an investigation of a possible effect of the suction installation in sand as referred in Chapter 3. The experiments were performed at $100g$ in the Acutronic Model 661 centrifuge (Randolph et al., 1991; Randolph and Gaudin, 2017) at UWA. The centrifuge tests had the following requirements to ensure a realistic stress state during the model scale experiments:

- A caisson penetration at stress levels representative for prototype scale was required. Thus, the caisson had to be suspended just above the sand surface until the centrifuge had reached the target acceleration.
- The installation was to be done in a controlled manner to ensure reproducible conditions for each subsequent cyclic loading test.
- The cyclic loading was to be performed without stoppage of the centrifuge in order to retain the soil stress state resulting from the suction installation.
- The CPTs at free field sites were to be performed before and after the caisson tests to characterise the soil samples themselves and to their confirm uniformity (see Section 5.1).

6.1.1.1 Test set-up for cyclic loading tests

The cyclic loading tests were performed subsequently to the suction caisson installation without stopping the centrifuge. This ensured similar conditions during suction installation and vertical cyclic loading. The centrifuge arrangement for the CPTs through the lid presented in Chapter 5 was modified for the cyclic loading tests. Additional details of this centrifuge test set-up are presented in Appendix B.2.

In this series of cyclic loading tests the model caisson was carried by an actuator, which was mounted on top of the strong box. A rod and a 8 kN load cell attached the model caisson to the actuator (see Figure 6.1). The LDT was placed on top of the model caisson on one end and the other end was clamped to the horizontal support beams of the actuator.

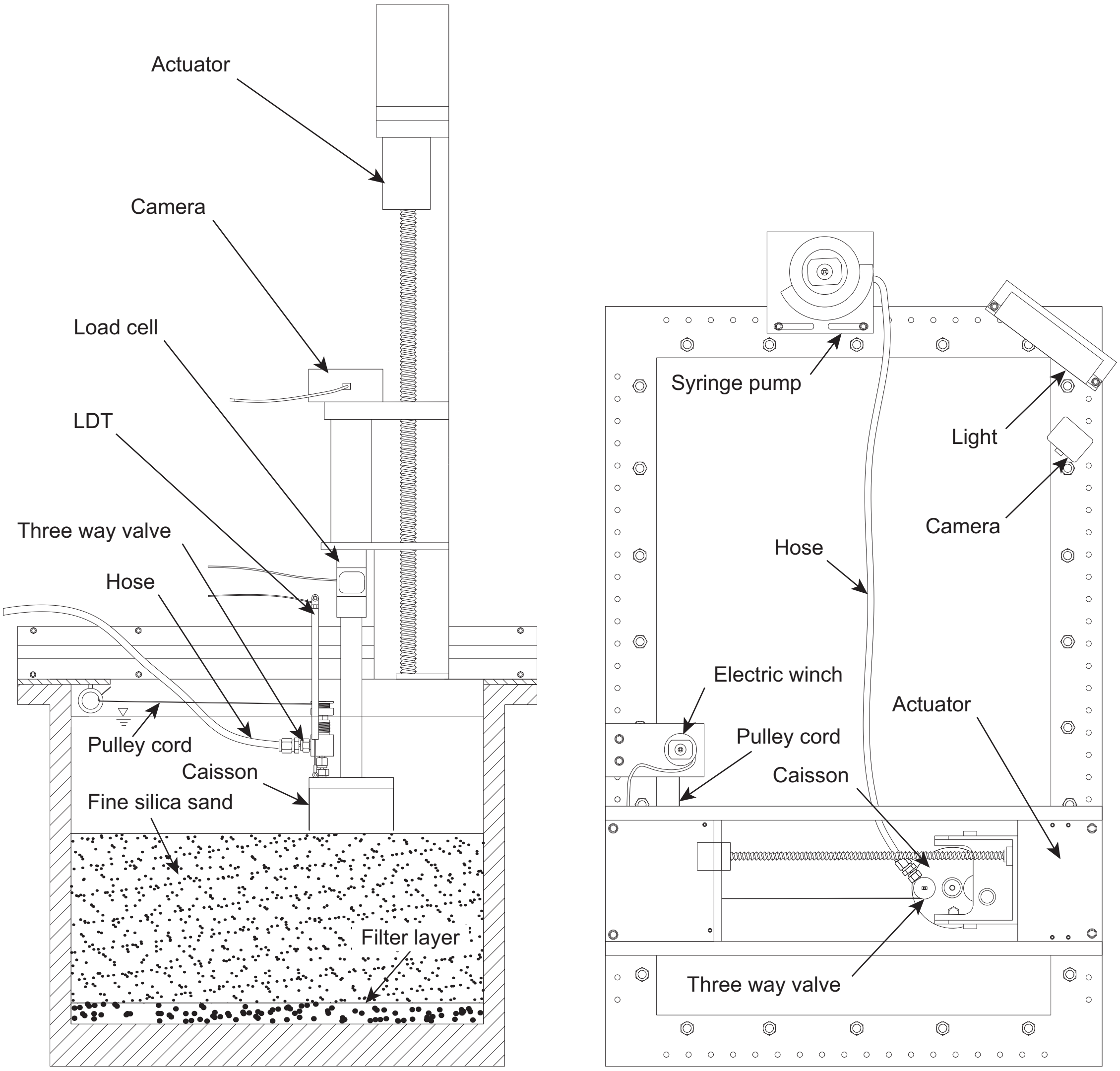

(a) (b)

Figure 6.1: Cross section (a) and top view (b) of the centrifuge test set-up for the suction caisson installation followed by a cyclic loading test.

The syringe pump and the pulley system consisting of a chord and an electric winch, which was controlled by an additional camera located on the edge of the strong box, are presented in Chapter 5. The cameras used during the installation also provided sight on the caisson during the loading tests.

6.1.1.2 Caisson model and test instrumentation

The caisson model was connected to a load cell with a maximum capacity of 8 kN by means of a rigid rod for the cyclic loading tests. The measurements from the load cell ensured accurate load application during the vertical cyclic loading tests. The displacements of the caisson were recorded by the means of the LDT that had a maximum extension length of $L_{LDT,max} = 100\,\text{mm}$. Additional details on the caisson instrumentation were provided in Subsection 5.1.1.3

6.1.1.3 Testing procedure

Each test summarised in Table 6.1 was performed in a different location inside the strong boxes. A total of six cyclic loading tests were performed. It is noted that test CYC-1-H-MS was terminated once premature refusal occurred during the suction installation.

Table 6.1: Centrifuge testing programme.

Test name	Permeability k_f (m/s)	Pumping flow rate q (mm^3/s)	Skirt length L (mm)
CYC-1-H-S	$1.0 \cdot 10^{-4}$	266.2 (512.4)[a]	40
CYC-1-H-MS	$1.0 \cdot 10^{-4}$	332.8	80
CYC-2-H-M	$1.0 \cdot 10^{-4}$	665.6	40
CYC-3-H-F	$1.0 \cdot 10^{-4}$	1664.0	40
CYC-4-L-M	$3.3 \cdot 10^{-5}$	665.6	40
CYC-5-L-F	$3.3 \cdot 10^{-5}$	1664.0	40

[a] Increased during the installation

6.1.1.4 Cyclic loading of the caisson

Following the suction caisson installation with different pumping flow rates in each test, the same cyclic loading history was applied to investigate the effect on the load-displacement behaviour. The cyclic loading history shown in Figure 6.2 subjects the caisson to tension and compression in each cycle. The same cyclic loading history, which was selected to represent the windward caisson of an 8 MW OWT with a jacket substructure in a water depth of $h_w = 40\,\text{m}$ under operational conditions, was also utilised in centrifuge tests performed on suction caissons in Baskarp sand at similar and lower effective permeabilities (Bienen et al., 2018a). Bienen et al. (2018a) evaluated this load history utilising an integrated in-house code featuring aero- and hydrodynamic, structural, and macro-element foundation models described in Bienen and Cassidy (2006) and Senders (2008). Neither the dimensions nor the loading conditions reflect any particular site. The cyclic loading test were performed as follows:

(1) A waiting period of at least 60 s at $100g$ was maintained before the loading test in order to ensure that the suction pressure inside the caisson dissipated.

(2) The self-weight was increased to $V = 585\,\mathrm{N}$ in model scale ($V/A = 116\,\mathrm{kPa}$). This represented the full self-weight of the jacket and the superstructure of the OWT – including tower, nacelle, and rotor – applied to the tested caisson. This vertical load was maintained until the excess pore pressure at the lid invert dissipated and no further settlements were observed.

(3) The vertical load was reduced to $V_{av} = 40\,\mathrm{N}$ in model scale ($(V/A)_{av} = 8\,\mathrm{kPa}$). This represents the average vertical load at the windward caisson of a suction caisson jacket. The average vertical stress of $(V/A)_{av} = 8\,\mathrm{kPa}$ was maintained throughout the entire cyclic loading test.

(4) The cyclic loading test was performed under load control. The cyclic loads were applied in packages of four sequences with four different increasing load amplitudes. The respective load amplitudes and the number of cycles per sequence are shown in Table 6.2. At least six load packages were applied in each test as presented in Figure 6.2. This yields a minimum of $n = 6666$ load cycles in each test.

Table 6.2: Cyclic loading sequences.

Sequence number	1	2	3	4
Number of cycles n	1000	100	10	1
Cyclic load amplitude V (N)	40 ± 80	40 ± 200	40 ± 400	40 ± 600
Cyclic stress amplitude V/A (kPa)	8 ± 16	8 ± 40	8 ± 80	8 ± 120

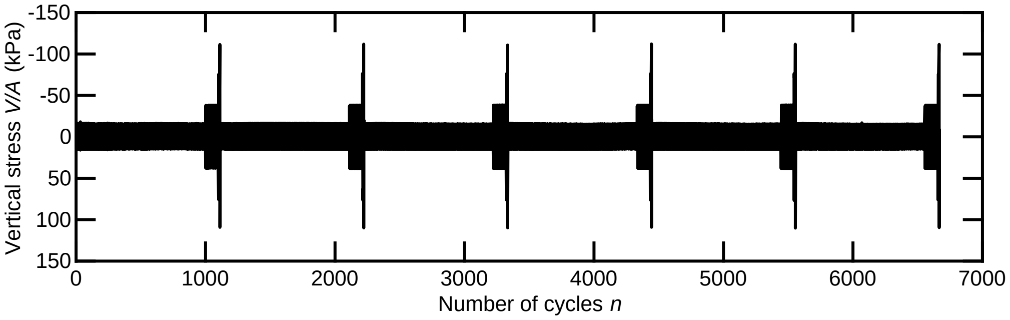

Figure 6.2: History of six vertical cyclic loading packages with four load sequences each.

The cyclic loads were applied at a loading frequency of $f = 0.5\,\mathrm{Hz}$ and with regular sinusoidal amplitude. Loading due to wind, waves, and current in a natural environment is expected to be highly irregular. However, the regular loading scheme was conceived to represent realistic drainage conditions in a reproducible manner. This approach also facilitates the evaluation of each load sequence (LSQ) and comparison between tests.

6.1.2 Results and discussion

The experimental results are presented in non-dimensional form, unless stated otherwise. Positive values indicate compression and downward displacements, whereas negative values represent tension and upward displacements.

6.1.2.1 Drained limiting capacities

The estimated drained compressive bearing capacity of the caisson foundations in dense silica sand exceeds $R_b = 6.5\,\mathrm{MPa}$. Since the maximum compressive stress in this study is $V/A = 128\,\mathrm{kPa}$, only a fraction of the bearing capacity is expected to be mobilised (Larsen, 2008). In contrast, the maximum drained tip resistance of $R_t = 76\,\mathrm{kPa}$ is exceeded during the static and cyclic loading sequences. The drained frictional capacity was estimated to be $R_s \approx 12\,\mathrm{kPa}$ in accordance to Houlsby and Byrne (2005b). The calculation result is confirmed through the two drained pull-out tests presented in Figure 6.3. The caisson was pulled out at a constant rate of $\dot{z} = 0.001\,\mathrm{mm/s}$. The maximum drained frictional capacity – i. e. the maximum skirt friction – is mobilised within $\Delta z/L \approx 2 \cdot 10^{-3}$ of upward displacement.

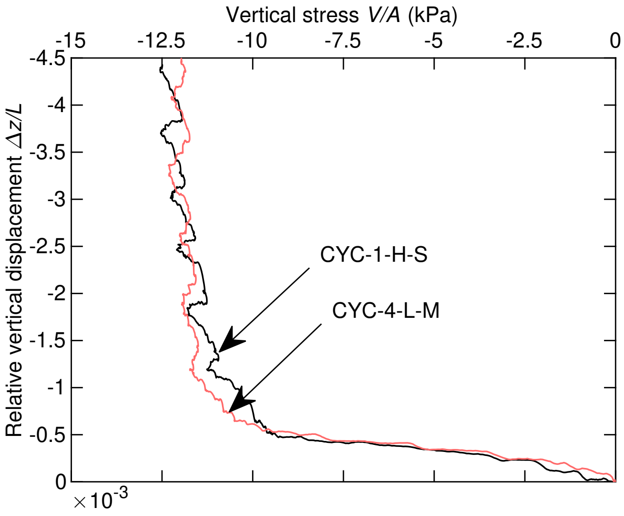

Figure 6.3: Drained pull-out resistance.

6.1.2.2 Response to cyclic loading

Since no significant influence of the pumping flow rate on the plug state was found, the effect on the cyclic load bearing behaviour is expected to be marginal. Bienen et al. (2018b) included three tests with different pumping flow rates: With the lowest pumping flow rate, the suction caisson could not be fully installed, as expected, even though the pumping flow rate was increased once the caisson penetration slowed down. The installation with the fastest pumping flow rate suggested loosening of the soil plug – but the behaviour under cyclic vertical loading did not differ significantly. However, the average applied vertical stress was substantially compressive in these tests. This is believed to determine the response, i. e. the behaviour is expected be different, if a lower average stress is to be applied, which is investigated in this study.

Based on the experiments discussed in Houlsby et al. (2005), the drainage regime is expected to play a major role for the suction caisson responding to rapid tensile loading.

These tests were performed with a small scale model caisson inside a pressure tank ensuring pore fluid response similarity only. Bienen et al. (2018a) investigated cyclic loading into tension in centrifuge experiments and also emphasised the major influence of the *in situ* effective permeability on the vertical cyclic load bearing behaviour.

Hence, the cyclic loading around a low compressive average load and the drainage regime were addressed with this series of cyclic loading tests. A total of five tests (see Table 6.1) were performed in accordance to the procedure outlined above. It is noted that relative displacements with regard to the achieved penetration depth after the installation are considered in the following sections.

Significance of the suction installation history

Based on the results discussed in Chapter 5, it is expected that the suction installation does not influence the in-service performance despite possible changes of the soil state during the suction installation – especially at extremely high or low pumping flow rates. The remaining uncertainties are addressed through three vertical cyclic loading tests featuring slow, moderate, and fast suction installation and cyclic loading around a low compressive average load.

Figure 6.4 shows the histories of five cyclic loading test, including the tests CYC-1-H-S, CYC-2-H-M, and CYC-3-H-F, which are considered here: The corresponding installation histories were presented in Figure 5.5a and 5.5b and discussed in Subsection 5.1.2.1. Based on the previous discussion, it is expected that caissons with a more extreme installation history will affect increased vertical displacements. A reduced relative density due to increased seepage flow can undermine the bearing capacity and the skirt friction. However, the vertical displacement response of tests CYC-1-H-S, CYC-2-H-M, and CYC-3-H-F pre-

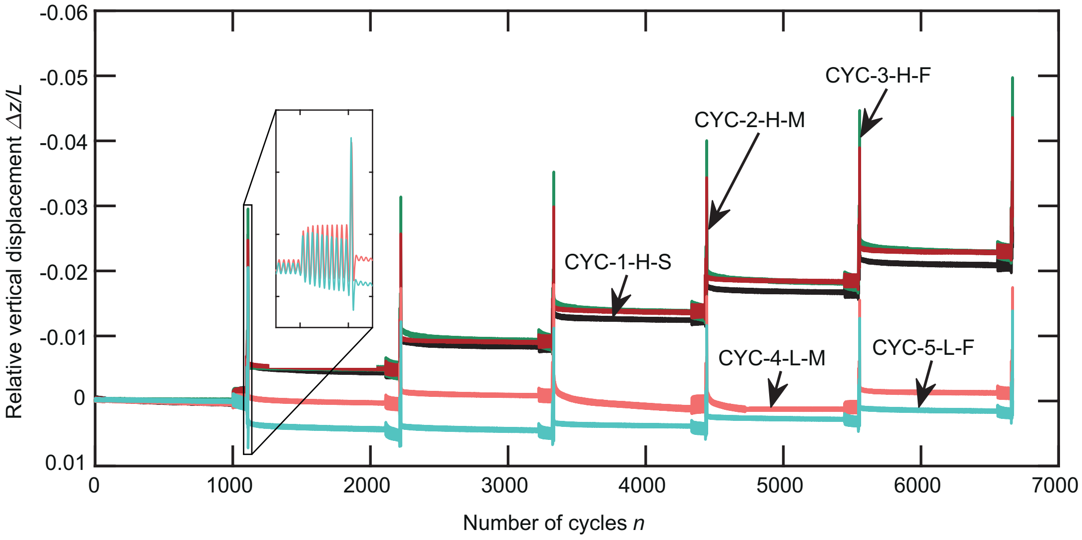

Figure 6.4: History of vertical displacements during cyclic loading.

sented in Figure 6.4 lie within a narrow range. Based on the presented data it is concluded that the influence of the suction installation on the vertical load bearing behaviour is indeed marginal.

A further comparison between the two tests CYC-4-L-M and CYC-5-L-F, which feature a lower effective permeability but the same loading history, underpins this conclusion. The respective vertical displacement response illustrated in Figure 6.4 does not reveal a major influence resulting from the differing suction installation either. Including the previous experiments discussed in Bienen et al. (2018b), tests were conducted with two different types of sand at different average vertical loads and loading amplitudes as well as a comprehensive range of the effective permeabilities. None of these tests provide evidence for a distinct influence of the suction installation on response to vertical cyclic loading.

Influence of the achieved penetration depth

A total skirt penetration depth of $z/L = 0.867$ was achieved in test CYC-2-H-M, which is the lowest value for a cyclic loading test in this study. Figure 6.4 shows that the largest displacements were reached in this test. This holds for both, the peak amplitude and the overall upward displacement in response to the applied vertical cyclic loading history. The comparison to test CYC-3-H-F, which had a skirt penetration of $z/L = 0.913$, shows similar displacement overall but differences in particular around peak loading. Figure 6.5 illustrates the following aspects:

(1) The caisson in test CYC-2-H-M settles in LSQ 2, while test CYC-3-H-F responds almost elastically at similar displacement amplitudes to the same cyclic load.

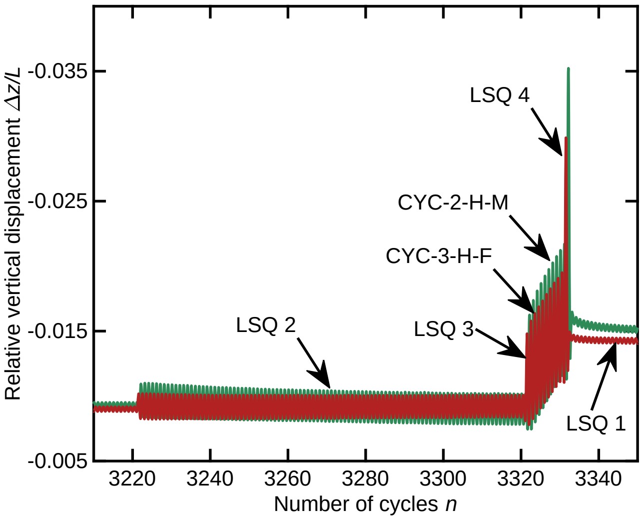

Figure 6.5: History of vertical displacements during cyclic loading as per LSQ 2, 3, and 4 of the third loading package.

(2) The peak upward displacement during LSQ 3 and 4 is significantly higher in test CYC-2-H-M, while the downward peaks show similar values. Eventually, this behaviour leads to a larger net uplift of CYC-2-H-M.

(3) LSQ 1 of the following loading package shows that test CYC-3-H-F responds almost elastic to small loading amplitudes. In contrast, the caisson displacements in test CYC-2-H-M show continuous net settlement over the following 15 to 20 load cycles of LSQ 1 of loading package three, such that the results approach those of CYC-3-H-F.

Test CYC-2-H-M of this study achieved a skirt penetration depth of $z/L < 0.867$, which is comparable to several tests performed in Baskarp sand. However, test CYC-2-H-M features a different cyclic loading history extending the previous tests results discussed in Bienen et al. (2018a). These results show that the caisson settles during cyclic loading under an average compressive load with a small cyclic amplitude that also extends into tension. It was found that an average tensile stress leads to significant uplift. Further evaluation of the results presented in Figures 6.4 and 6.5 shows that the highest peaks are often followed by successive settlement during the first few cycles of the following small loading amplitude sequence in presence of a compressive average stress. This holds for the tests conducted in high and low effective permeability soils in this study. Hence, this study confirms the occurrence of net settlement under low magnitude cyclic loading when the average stress is compressive.

It is likely that the lid loses contact – partially or completely – during high amplitude tensile loading in LSQ 3 and 4. This state is found to be indicated by the settlements occurring during the subsequent LSQ 1. The vertical loads are transferred by the skirt friction and the tip resistance alone, resulting in considerably soft response in compression. This yields settlements as the tip bearing is expected to be partially drained. The lid presumingly touches down after $n \approx 20$ cycles leading to a stiffer response and decaying downward movement resulting in predominately elastic response to the low amplitude cyclic loading in LSQ 1.

It is observed that lower achieved penetration depths lead to significantly softer response to tensile loading. However, the net vertical displacements after each loading package do not differ considerably, because lower skirt penetration depth also leads to increased settlements in compression. Since the response to rapid loading heavily depends on the drainage regime, it is assumed that the skirt penetration and therefore the length of the drainage path plays a governing role. For instance, the initial drainage path in test CYC-3-H-F is approximately 5 to 10 % longer than in it is in test CYC-2-H-M. Similarly, the drainage path in test CYC-5-L-F is approximately 8 to 16 % longer than it is in test CYC-4-L-M. Consistently, larger displacements can be observed in Figure 6.4 and 6.5 (see Table 5.2 in Subsection 5.1.2.1). Hence, the presumed influence of the achieved skirt penetration depth on the load bearing behaviour manifests itself through the influence on the drainage regime.

Effects of cyclic loading into tension

All cyclic loading tests in this study feature a compressive average stress of $V/A = 8\,\mathrm{kPa}$. Tension is reached in each of the four loading sequences of a loading package. The response to the first three loading packages of test CYC-3-H-F and CYC-5-L-F was found to be representative for the other tests, with no indication of a permanent influence of the differing installation histories on the tests. The results presented in Figure 6.6 allow the following observations:

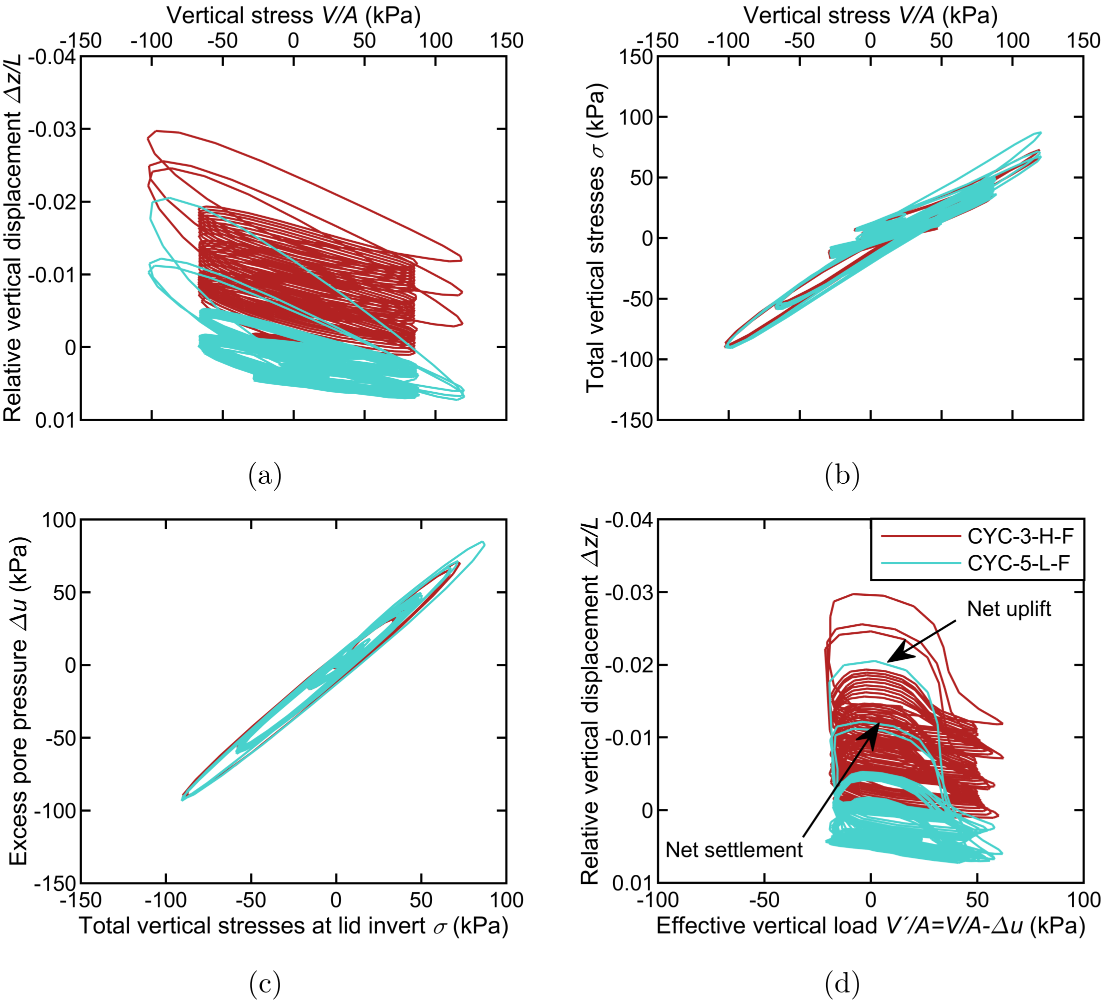

(a) (b)

(c) (d)

Figure 6.6: Effect of drainage on load transfer mechanism in tests with cyclic loading: applied stress (a), total stress at lid invert (b), drainage at lid invert (b), and effective load at lid invert (d).

(1) Predominantly elastic response – i. e. nearly zero net displacement – was measured during the first loading sequence (see also Figure 6.4). A peak tensile stress of $V/A = -8\,\mathrm{kPa}$ was applied during each of the 1000 cycles, which corresponds to approximately 75 % of the estimated drained frictional tensile capacity.

(2) Tension reaches more than 2.5 times the drained frictional capacity during LSQ 2 yielding primarily elastic response with occasional small magnitude settlements. Significant and permanent vertical displacements only occur if the tensile load exceeded the drained frictional capacity by six times or more during LSQ 3 and 4.

(3) Figure 6.6a and 6.6d show that the applied cyclic vertical loading history results in settlements and uplift in the higher and lower effective permeability sand, respectively. The cyclic loading of a caisson in more permeable soil results in net uplift after each loading package. Furthermore, Figure 6.4 and 6.6a indicates that the initial response to tensile loading is stiffer than it is during subsequent cyclic loading. However, there is no indication of considerable accumulative reduction of stiffness. In less permeable soil, the caisson settles during the first two or three loading packages before it starts to move upwards, similar to the suction caisson embedded in more permeable soil (see Figure 6.4 and 6.6d). The unloading stiffness is considerably lower than the initial stiffness in this case.

Observations (1) and (2) confirm previous findings and therefore underpin the conclusion that a suction caisson can withstand tensile loads exceeding the drained frictional capacity without permanent upward displacement. Observation (3) adds to the findings presented in Bienen et al. (2018b), where similar vertical cyclic loading resulted in net settlements in tests featuring a three times lower effective permeability than the lowest in this study. It is concluded that there must be a certain maximum effective permeability determining net uplift or net settlement response. This threshold depends on the drainage regime, which is determined by the loading rate and the granular characteristics of the soil.

Influence of the drainage regime on the load bearing mechanism

A comparison between vertical displacements, loading, excess pore pressures, and stresses is given in Figure 6.7 and 6.8. The total stresses and excess pore pressures were measured at the lid invert. Figure 6.8a and 6.8b show that the total stresses recorded at the lid invert are completely carried by the excess pore pressure. Thus, the response is considered to be undrained at the lid invert. Excess pore pressure accumulation is not observed as the excess pore pressure cycles with the total stresses. Figure 6.6c confirms this observation, because the gradient of the relation between excess pore pressure and total stresses is approximately one. Figure 6.6b shows similar relations of the applied vertical load with the total stress at the lid invert. Since test CYC-3-H-F and CYC-5-L-F show similar behaviour, it is assumed that the amount of load transferred to the lid is independent from the effective permeability within the investigated range.

Bienen et al. (2018a) emphasise the importance of the drainage regime for the vertical displacement response during vertical cyclic loading. The magnitude of vertical net displacement after three loading packages is approximately twice as large in test CYC-3-H-F as it was in a similar test conducted in Baskarp sand. Baskarp sand is slightly less permeable and tends to dilate at a higher rate than fine silica sand. Thus, excess pore pressures and therefore the resistance to tensile loading is mobilised earlier resulting in lower magnitude caisson displacements. It is noted that this coherence implies that the cavitation

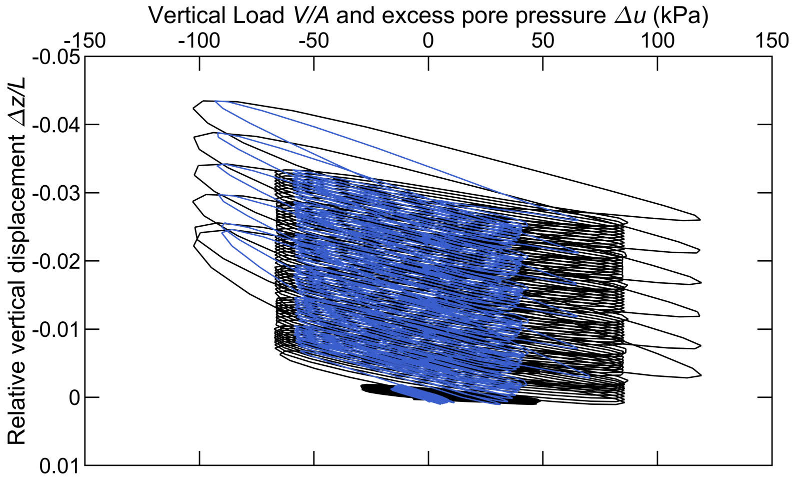

(a)

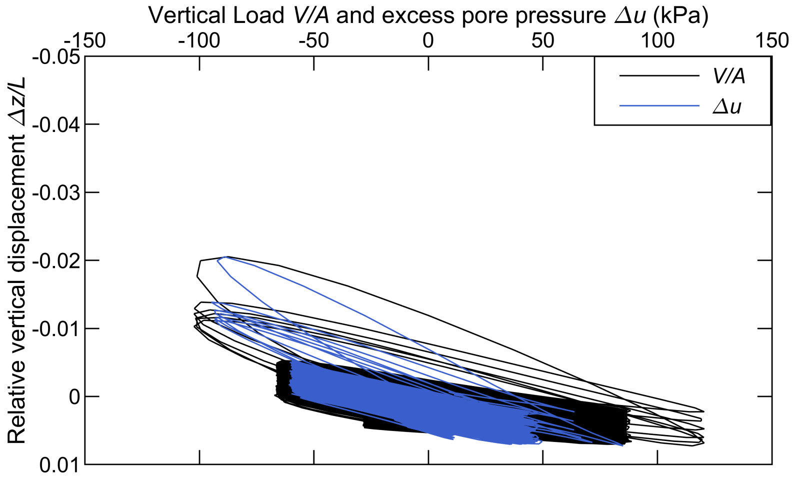

(b)

Figure 6.7: Applied stress and measured excess pore pressure at the lid invert during six loading packages in test CYC-3-H-F (a) and CYC-5-L-F (b).

limit of Baskarp sand is lower compared to fine silica sand. Consequently, the same loading regime can result in smaller or larger caisson displacements depending on the onset of cavitation.

Figure 6.7a and 6.7b show that the applied vertical stresses are partially carried by the skirt friction. Furthermore, the skirt tip carries a considerable portion of the vertical load in compression. The displacements in Figure 6.6d show a hard capped mobilisable effective resistance of $V'/A \approx 15\,\text{kPa}$ in tension and a flattening curve in compression once the drained frictional capacity is exceeded. This suggests that the skirt friction is fully mobilised at smaller relative displacements than the lid resistance. In addition, the maximum load transferred in compression is considerably higher than the sum of the skirt and tip

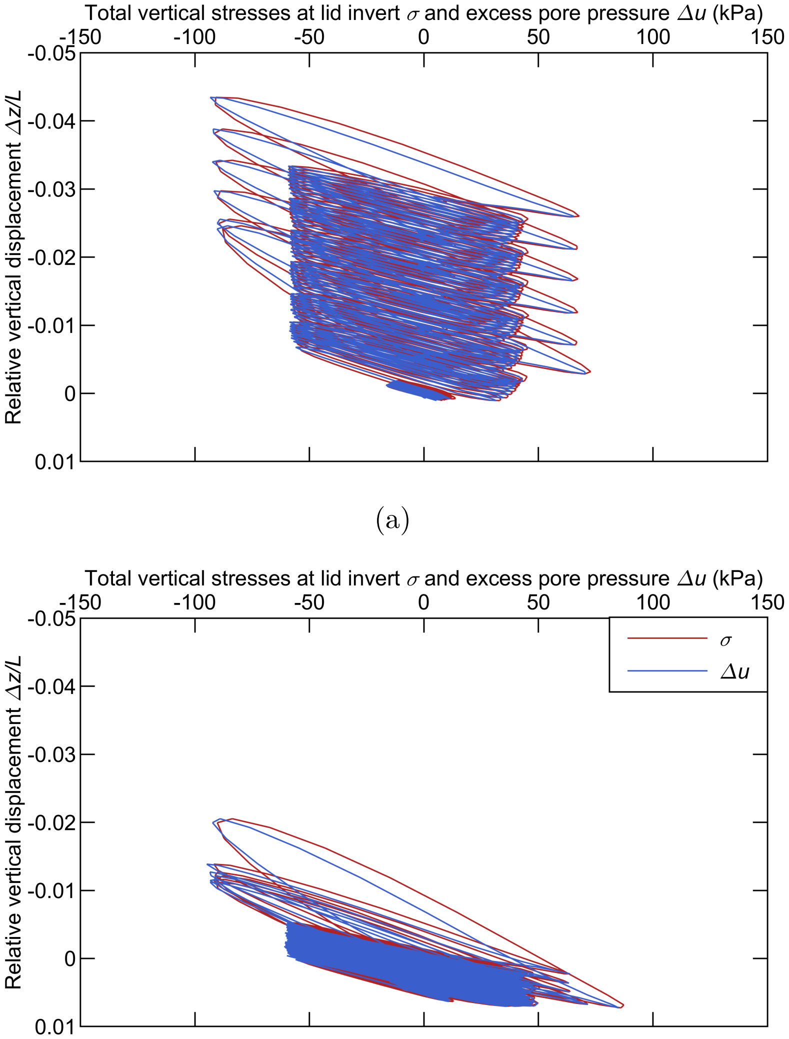

(a)

(b)

Figure 6.8: Measured total stress and excess pore pressure at the lid invert during six loading packages in test CYC-3-H-F (a) and CYC-5-L-F (b).

resistance. This reinforces the assumption of presence of lid contact in compression. The tests presented in Bienen et al. (2018a) show a similar load bearing behaviour in Baskarp sand.

The comparison between tests performed in higher (Figure 6.7a and 6.8a) and lower (Figure 6.7b and 6.8b) effective permeability soil samples shows a significantly different magnitude of vertical displacements. The drainage regime governs the response to cyclic loading in the presented tests, i. e. the uplift velocity and the effective permeability determine the excess pore pressures around the foundations and therefore critically influence the suction caisson behaviour.

6.1.3 Remarks on the centrifuge tests

The installation history does not influence the behaviour under vertical cyclic loading including excursions into tension. The achieved skirt penetration depth and therefore the length of the drainage path affects the response to cyclic loading in the tests performed in this study. The *in situ* effective soil permeability has a major influence on the displacement response under vertical cyclic loading. Low magnitude tensile loading leads to an almost elastic response, while high magnitude tensile loading causes permanent uplift in each loading cycle.

The major factors effecting the suction caisson response to vertical cyclic loading are identified through the experimental study. Further investigations remain necessary – e. g. on the influence of other caisson geometries. The centrifuge test results form a basis for the development and the validation of analytical and numerical calculation methods, which are certainly required for further investigations apart from experiments.

6.2 Numerical simulations

A FEM model capable of the simulation of the static and cyclic loading of a suction caisson foundation is utilised for further investigations. The numerical simulations target the visualisation underlying load bearing mechanisms and the prediction of the caisson load displacement behaviour. The study consists of two steps: First, the data calculated from the numerical model is compared to the centrifuge test results presented in Section 6.1. In a second step, variations of the model dimensions and the material parameters are investigated in order to clarify frontiers and capabilities of numerical simulations of suction caisson foundations subjected to vertical cyclic loading.

6.2.1 Numerical modelling and testing procedure

The numerical simulations are performed with Abaqus/Standard 2018 (Dassault Systèmes, 2018). The two-phase formulation is employed in order to capture the drainage behaviour of this soil-structure interaction problem. The numerical model utilised for the FEM simulations is shown in Figure 6.9. The dimensions of the soil entity of the numerical model shown in Figure 6.9a are increased compared to the centrifuge tests in order to minimise boundary effects. The two-dimensional axisymmetric model geometry is meshed with high order rectangular elements (CAX8P) featuring a pore pressure degree of freedom. The water elements are low order rectangular elements (CAX4P) also featuring a pore pressure degree of freedom. The caisson is a rigid body meshed with triangular elements (CAX6). A half circular shaped skirt tip reduces stress peaks. The box is modelled with an analytical rigid body (Dassault Systèmes, 2018). The entire mesh is shown exemplary in Figure 6.9b. It illustrates that small elements are located close to the caisson. A more coarse mesh is utilised further away from the area where the largest deformations are expected. The dimensions actually employed for each numerical model are listed in Table 6.3.

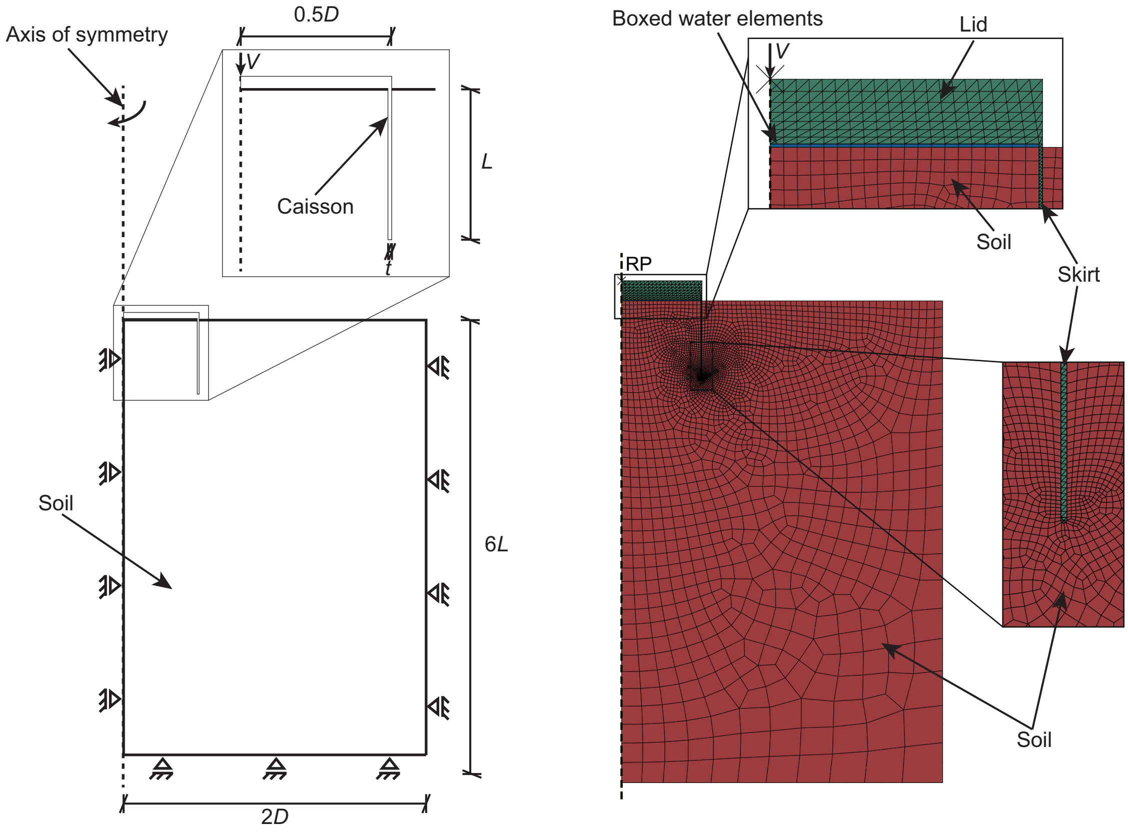

(a) (b)

Figure 6.9: Dimensions (a) and finite element mesh (b) of the numerical model utilised for FEM analyses of the suction caisson response to vertical cyclic loading in a uniform sand profile.

The horizontal displacements are locked at the axis of symmetry and the outside vertical edge, while vertical displacements are permitted. The bottom edge features a zero vertical displacement BC. These three edges are also hydraulically impermeable. The displacements at the soil surface are unlocked, while a pore pressure BC is applied on the top surface in order to allow drainage. The vertical load V is applied to the rigid caisson through a concentrated vertical force subjected at the reference point (RP) that is located at the axis of symmetry (see Figure 6.9b).

Table 6.3: Numerical model caisson dimensions.

Model No.	D (m)	L (m)	t (cm)
10	8	4	5
20	8	8	5

The parameters required for the utilised hypoplastic constitutive model (φ_c, h_s, n_B, e_{d0}, e_{c0}, e_{i0}, α, and β) summarised in Table 6.4 are determined under consideration of laboratory test results referred in M. N. Tran (2005), Pucker et al. (2012), and Chow et al. (2018). The additional parameters required as input for the ISA formulation (m_R, R, β_{h0}, χ_0, χ_{max}, c_a, c_z, and β_{hmax}) are found iteratively through numerical analyses and under consideration of the guidelines referred by Fuentes et al. (2019). The initial void ratio e_0 and the interface friction parameters (μ, τ_{max}, and γ_i) are derived from the results of the centrifuge experiments referred in Section 6.1.

Table 6.4: Model parameters for FEM simulations featuring fine silica sand.

Parameter	Symbol	Unit	Fine silica sand
Critical friction angle	φ_c	(°)	30
Granular hardness	h_s	(MPa)	1354
Barotropy exponent	n_B	(-)	0.34
Minimal void ratio	e_{d0}	(-)	0.49
Critical void ratio	e_{c0}	(-)	0.79
Maximum void ratio	e_{i0}	(-)	0.86
Dilatancy exponent	α	(-)	0.18
Pyknotropy exponent	β	(-)	1.27
Stiffness factor	m_R	(-)	4
IS yield surface	R	(-)	$1 \cdot 10^{-4}$
IS hardening exponent	β_{h0}	(-)	0.2
Minimum value of IS exponent	χ_0	(-)	4
Maximum value of IS exponent	χ_{max}	(-)	25
Accumulation rate factor	c_a	(-)	0.04
Cyclic mobility factor	c_z	(-)	150
Maximum IS hardening exponent	β_{hmax}	(-)	3
Effective permeability	k_f	(m/s)	$9.87 \cdot 10^{-5}$
Density water	ρ_w	(t/m^3)	1
Grain density solid	ρ_s	(t/m^3)	2.65
Interface friction coefficient	μ	(-)	0.15
Shear stress limit	τ_{max}	(kPa)	12
Allowable elastic slip	γ_i	(-)	0.005

The simulations are conducted according to the following procedure: First, the effective stresses and the hydrostatic pressure are applied during the K_0 procedure. A minimum load is applied at the caisson in order to minimise an effect on the K_0 conditions. Second, load controlled static and cyclic loading is subjected to the caisson.

The cyclic loading sequences applied in the numerical simulations aim to reproduce the BCs that are present during the centrifuge experiments. Hence, the loading amplitude and frequency from Table 6.2 are applied. The number of cycles is reduced to a minimum in order to reduce computational costs. The average load given in Table 6.5 is applied to the caisson first. A waiting period of $t = 60\,\mathrm{s}$ allowing consolidation commenced before the cyclic loading packages are applied in order to achieve initial conditions. This procedure ensured comparability to the centrifuge tests. The history of the vertical cyclic loading is shown in Figure 6.10.

Table 6.5: Load cases (LCs) and specifications of the four cyclic loading sequences applied in the numerical simulations in uniform sand.

LC	Sequence number	1	2	3	4
	Number of cycles n (-)	18	5	3	1
10N	Load amplitude V (N)	40 ± 80	40 ± 200	40 ± 400	40 ± 600
	Stress amplitude V/A (kPa)	8 ± 16	8 ± 40	8 ± 80	8 ± 120

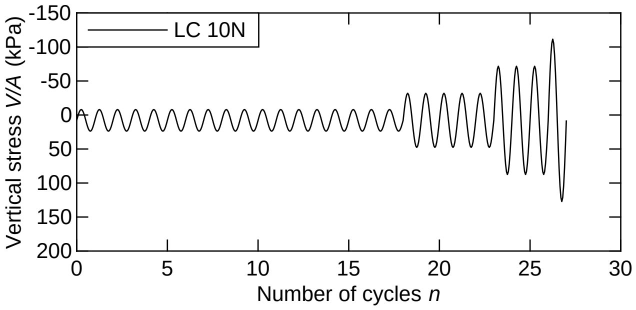

Figure 6.10: History of four vertical cyclic loading sequences in LC 10N.

6.2.2 Results and discussion

The calculated results are presented in non-dimensional form, unless stated otherwise. Positive values indicate compression and downward displacements, whereas negative values represent tension and upward displacements.

6.2.2.1 Monotonic load bearing mechanisms

The functionality of the newly developed boxed water element technique described in Section 4.3 must be evaluated. The results obtained from experiments and numerical simulations are compared. The first step includes compressive loading featuring consolidation. The slow – i. e. drained – and the rapid caisson extraction are investigated in a second step. Each calculations were performed with model no. 10 as referred in Table 6.3. Model no. 10 features a $L = 4\,\mathrm{m}$ and $D = 8\,\mathrm{m}$ caisson equipped with the boxed water elements.

The calculated settlement response to the application of a vertical load of $V = 5850\,\mathrm{kN}$ ($V/A = 116\,\mathrm{kPa}$) and subsequent unloading to $V = 400\,\mathrm{kN}$ ($V/A = 8\,\mathrm{kPa}$) is presented in Figure 6.11. The experimental measurements and the calculated vertical displacements have the same order of magnitude. However, an increased degree of consolidation is reached earlier in the experiments. The experimental results scatter considerably, which is assumed to result from the suction installation discussed in Chapter 5. The unloading stiffness appears to be slightly overestimated by the constitutive model yielding roughly 75 % of the

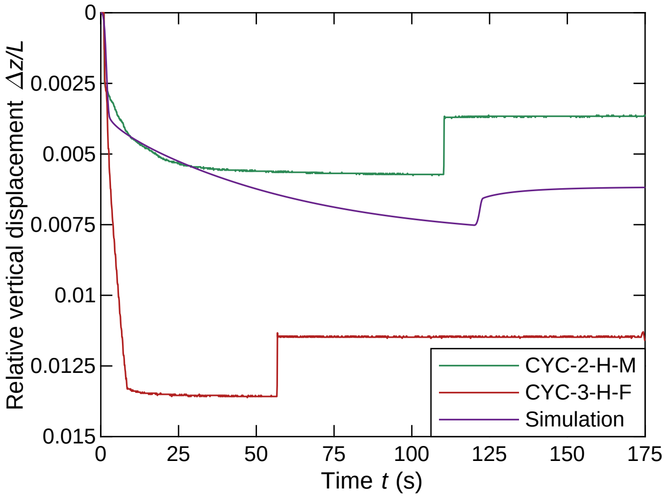

Figure 6.11: History of vertical displacements during static loading.

experimentally measured uplift during unloading. However, the calculated curve represents idealised conditions and is enveloped by the experimental results. Hence, the numerical model provides a sufficient estimate of the *in situ* caisson behaviour. The numerical model is considered to be suitable for the simulation of the monotonic vertical loading and unloading of a caisson foundation. Furthermore, the box protected the water elements from distortion. Hence, the applicability of the boxed water elements for the simulation of compressive loading is demonstrated.

Figure 6.12a shows the measured and calculated vertical stress required for the drained suction caisson extraction. A sufficiently low dimensionless loading rate $v' = (\Delta \dot{z} L)/c_v < 1$ (Finnie and Randolph, 1994) is applied to ensure drained conditions. The presented maximum drained frictional capacity and therefore the skirt friction is similar. The required distance is slightly underestimated in the numerical simulation. The contour plot presented in Figure 6.12b shows that no plug heave occurs. Instead a water filled gap, which is represented by the water elements, forms as the lid invert surface, represented by the box, separates from the soil surface. It is noted that Figure 6.12b contains an amplified deformation geometry. It is concluded that the numerical model is suitable for the simulation of the drained suction caisson extraction.

The results from the simulation of the rapid suction caisson extraction are presented in Figure 6.13. The calculated history of the vertical stresses and excess pore pressures shown in Figure 6.13a reveals that predominantly undrained response is present as a normalised displacement rate $v' > 30$ is applied. The calculated extraction resistance tends to approach a maximum, which is comparable to centrifuge tests conducted with Baskarp sand discussed in Bienen et al. (2018a). However, the calculation terminates at a relative vertical displacement of $\Delta z/L \approx 8 \cdot 10^{-3}$ due to plug liquefaction, which implies zero effective stress states that yield numerical instabilities within the hypoplastic constitutive model.

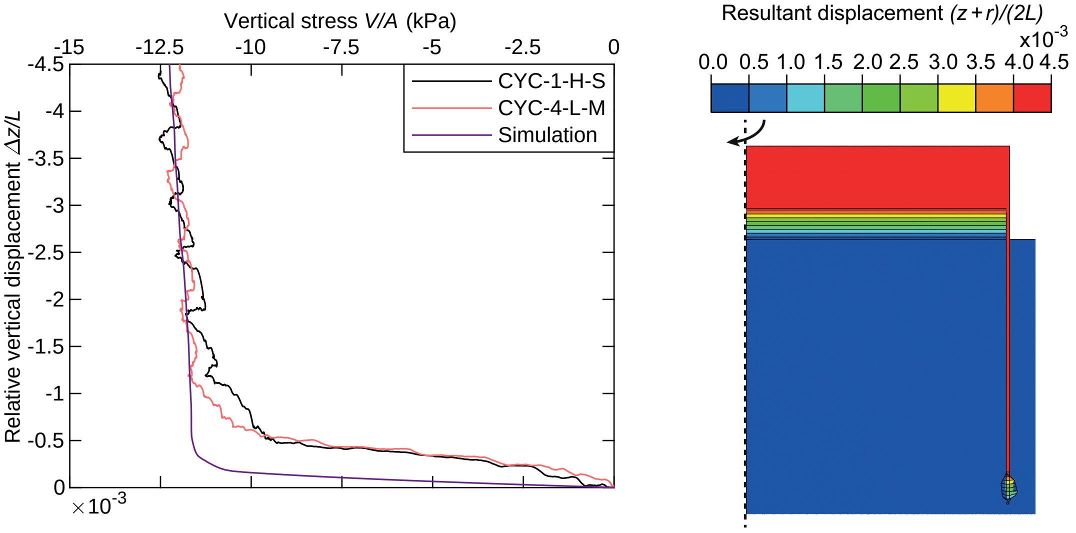

(a) (b)

Figure 6.12: Drained the extraction resistance (a) and resultant displacement contours at a relative caisson displacement of $\Delta z/L = 4.5 \cdot 10^{-3}$ (b).

Figure 6.14 shows that the liquefaction already starts at $\Delta z/L \approx 5.5 \cdot 10^{-3}$ as the effective stresses at the lid invert reach $\sigma' = 0$. It is noted that the calculated excess pore pressures exceed the cavitation limit, which is possible because a cavitation cut-off is not implemented in the presented numerical model.

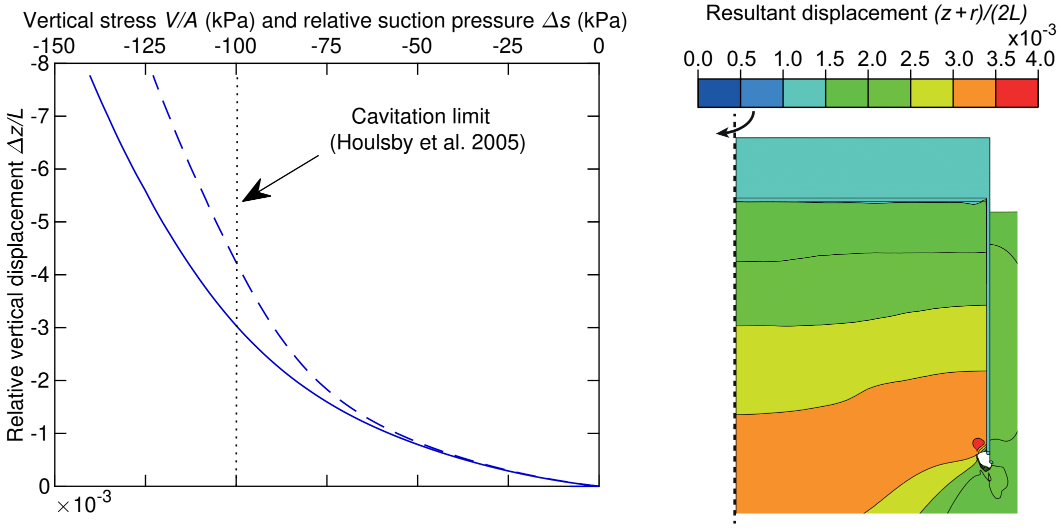

(a) (b)

Figure 6.13: Rapid extraction resistance (solid line) and relative suction pressure (dashed line) (a) and resultant displacement contours at a relative caisson displacement of $\Delta z/L \approx 8 \cdot 10^{-3}$ (b).

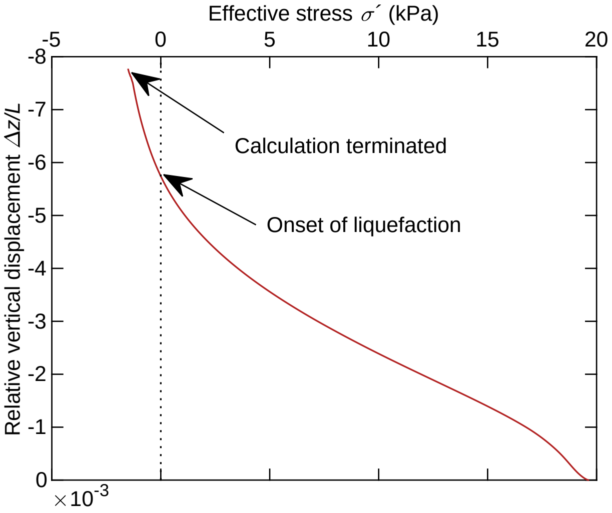

Figure 6.14: History of effective stresses during rapid suction caisson extraction.

The contour plot presented in Figure 6.13b reveals that the entire soil plug is lifted during rapid, i. e. undrained, extraction. The water elements do not expand, as expected. Consequently, plug uplift occurs and the lid invert (the bottom surface of the box) remains in contact with the soil surface. The largest resultant displacement occurs close to the soil tip, because a pre-loading of $V/A = 116\,\mathrm{kPa}$ and an unloading to $V/A = 8\,\mathrm{kPa}$ has been required in order to mobilise the maximum tensile capacity – otherwise the calculation terminates early due to the onset of liquefaction. This approach emulates the experimental procedure of the centrifuge tests. The numerical model is considered to be suitable for the simulation of rapid extraction of a suction caisson foundation, if cavitation is not reached. Furthermore, the applicability of the boxed water elements for the rapid caisson extraction is demonstrated.

6.2.2.2 Cyclic load bearing mechanisms

The first numerical investigation on cyclic loading targets further validation of the numerical model. The experimental results discussed in Section 6.1 and a numerical back analysis of the centrifuge tests are compared. It is noted that the number of simulated load cycles is limited to a minimum which is considered to maintain comparability between experimental and numerical investigations.

Comparing the caisson response to the second loading package presented in Figure 6.15 shows that the behaviour in LSQ 1 and 2 is similar: The vertical displacements accumulate within the fist 10 to 20 load cycles followed by almost elastic behaviour. The calculated displacement amplitudes are within a comparable magnitude of less than $\Delta z/L \leq 1 \cdot 10^{-3}$ in LSQ 1. However, the calculated displacement amplitudes of LSQ 2 shown in Figure 6.15b are smaller than the measured values presented in Figure 6.15a. The overall response to LSQ 3 is also similar as net uplift is calculated. The calculated displacement amplitude falls short again. The same holds for LSQ 4. Furthermore, net settlements result instead of net uplift – especially during LSQ 4. LSQ 1 of the third loading package following LSQ 4

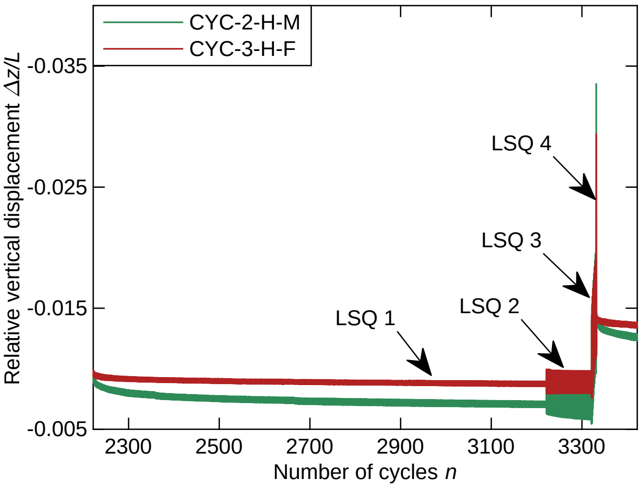

(a)

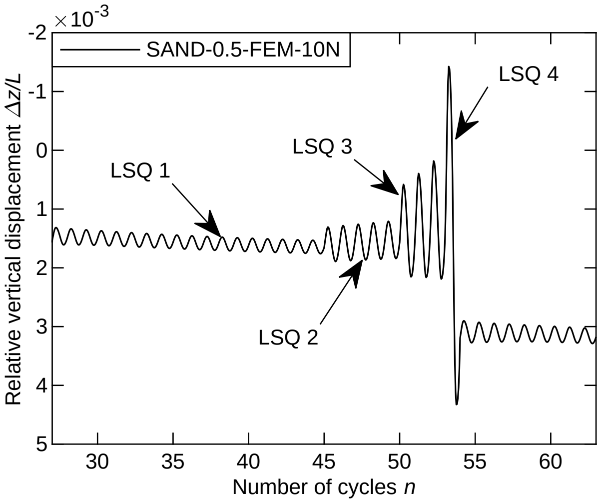

(b)

Figure 6.15: History of vertical displacements during cyclic loading obtained from experiments (a) and a numerical simulation (b).

(see Figure 6.15) shows minor net settlements followed by almost elastic response. This is similarly observed in the experimental and numerical investigation.

Figure 6.16 shows that the calculated pore pressure development at the lid invert is similar to the measured data presented in Figure 6.7a and discussed in Subsection 6.1.2.2. The pore pressures cycle with the vertical load. The skirt friction carries a portion of the vertical load in tension and compression, while the tip resistance is only mobilised in compression. Figure 6.16 shows that accumulated pore pressures resulting from LSQ 4 dissipate in the following LSQ 1. This behaviour occurs repeatedly in subsequent loading packages. Figure 6.15b shows that net settlements result from the excess pore pressure dissipation.

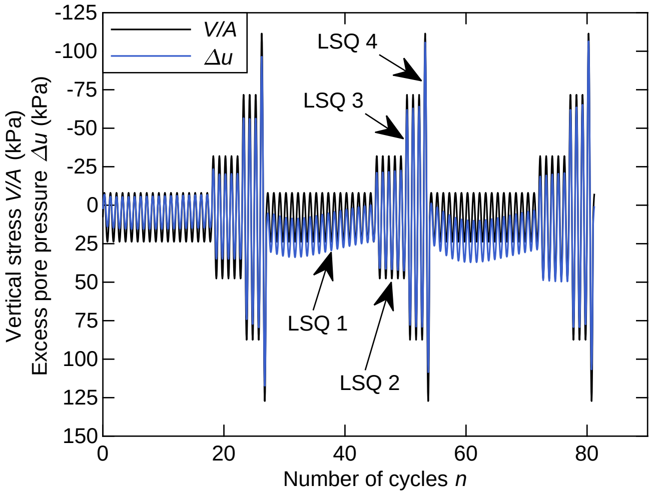

Figure 6.16: History of the applied stress and excess pore pressure at the lid invert during three loading packages in simulation SAND-0.5-FEM-10N.

Local or complete soil plug liquefaction plays a role in the development of the significant displacements measured in the centrifuge experiments during LSQ 3 and 4. The onset of liquefaction is captured by the constitutive model. However, a change of the void ratio does not affect the effective soil permeability within the numerical model. Consequently, the vertical displacements, which crucially depend on the effective permeability, are underestimated by the numerical model. Furthermore, the onset of plug liquefaction is characterised by a zero effective stresses state. This compromises the stability of the numerical analysis, if a constitutive model is utilised that cannot handle tensile stresses. This is the case with constitutive models commonly utilised for soil. Hence, this circumstances eventually lead to a premature termination of calculations featuring liquefaction failure.

The basic mechanisms underlying the cyclic load bearing behaviour – i. e. the interplay between tip and skirt resistance and internal pore pressures – are incorporated in the numerical model. The numerical model is considered to be suitable for the simulation of vertical cyclic loading of a suction caisson foundation embedded in uniform sand within certain boundaries: Moderate excursions into tension during LSQ 1 and 2 are captured sufficiently. Larger tensile loads including the onset of liquefaction yield insufficient results and numerical instability. Nevertheless, the maximum tensile stress applied in LSQ 2 is $V/A = 32\,\text{kPa}$, which is more than 2.5 times the frictional capacity (see Figure 6.12a). The crucial mechanisms underlying the response to LSQ 1 and 2 are sufficiently captured by the numerical model. Based on the discussion in Subsection 6.1.2.2, it is expected that the displacement amplitudes are affected by the penetration depths $z/L \leq 1$ achieved in the experimental results. This will be discussed in the following subsection.

6.2.2.3 Influence of the achieved penetration depth

The influence of the achieved penetration depth on the vertical load bearing behaviour has been discussed in Section 6.1. The achieved penetration depths of $z/L = 0.870$ in test CYC-2-H-M and $z/L = 0.924$ in test CYC-3-H-F differs from $z/L = 1$, which has not been taken into account in the numerical simulations, yet. Consequently, the measured and calculated displacement amplitudes compared in Figure 6.15 partially diverge.

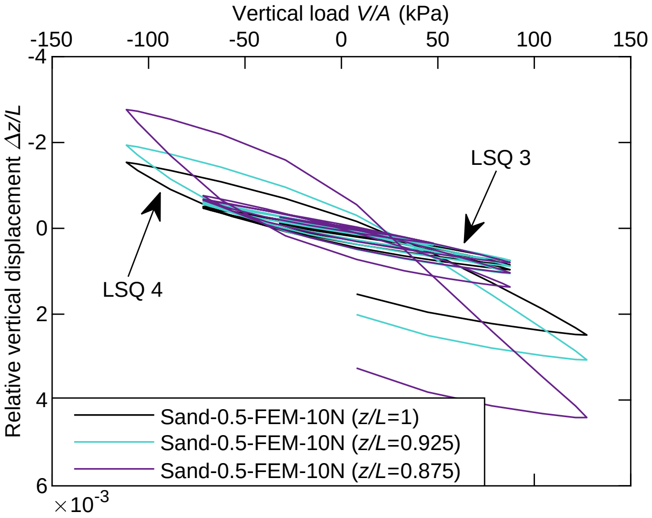

Figure 6.17: History of vertical displacements during cyclic loading featuring different skirt penetration depth z/L.

Figure 6.17 shows additional analyses considering a skirt penetration depth of $z/L = 0.925$ and $z/L = 0.875$. The presented comparison confirms that a reduced embedded skirt length yields increased vertical displacement amplitudes – especially in LSQ 3 and 4. These analyses results are plausible, because the length of the drainage path plays the distinct role in the utilised two-phase numerical model. The skirt friction and tip resistance transfer just a minor portion of the applied vertical load into the soil (see Figure 6.16).

6.2.2.4 Influence of the caisson aspect ratio

A cyclic loading test featuring a caisson with an aspect ratio of $L/D = 1$ was not performed in uniform sand profile within the series of centrifuge test discussed in Section 6.1. However, the embedded skirt length – i. e. the achieved penetration depth z/L and therefore the aspect ratio L/D – has a crucial influence on the load bearing behaviour as discussed in the previous subsection. A numerical simulation is utilised for an investigation on the influence of the aspect ratio of a suction caisson subjected to vertical cyclic loading.

The calculated results are presented in Figure 6.18a. They show a substantially stiffer response to loading as per LC 10N, if the aspect ratio is doubled – i. e. the caisson skirt length is $L = 8\,\text{m}$. This matches the expectations because of the longer skirt provides additional frictional resistance and an increased length of the drainage path. Comparing

Figure 6.16 and 6.18b shows that less excess pore pressure develops at the lid invert of the $L/D = 1$ caisson. Hence, the share of vertical load carried by the skirt is increased. However, an increased caisson aspect ratio does not lead to a more balanced uplift and settlement response, which leaves only the reduced displacement amplitudes to be beneficial for the in-service performance of a suction caisson foundation of an OWT.

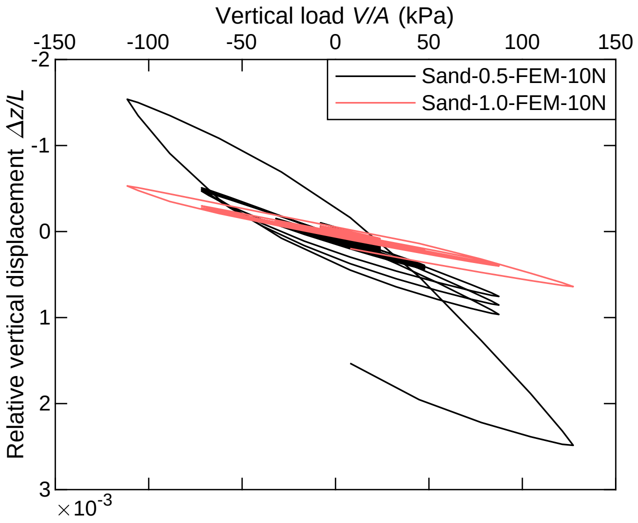

(a)

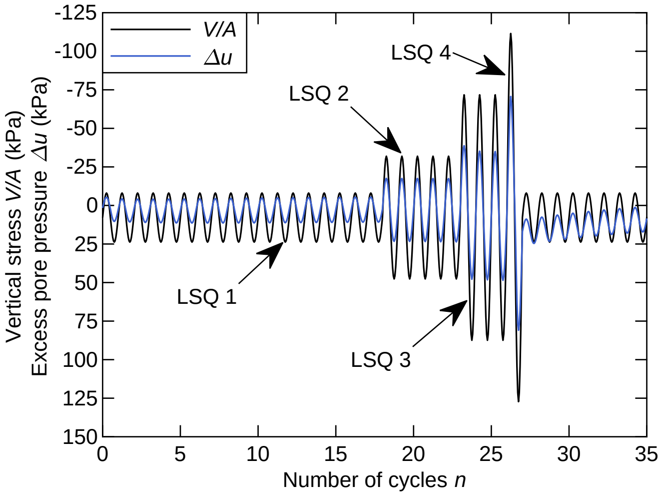

(b)

Figure 6.18: History of vertical displacements during cyclic loading of suction caissons with aspect ratios of $L/D = 0.5$ and $L/D = 1$ (a) and history of applied stress and excess pore pressure at the lid invert in simulation SAND-1.0-FEM-10N (b).

6.2.3 Remarks on the numerical simulations

The numerical analyses show that static loading is captured by the utilised FEM models. The experimental results of the consolidation time, settlements, and the drained extraction resistance are back calculated accurately. Hence, the numerical model is validated by the results. The rapid caisson extraction analyses results are not validated. Cavitation and liquefaction typically limit the rapid extraction resistance, which are not taken into account. If further insights into this specific topic become necessary, the implementation of a cavitation cut-off and constitutive model that captures liquefaction without numerical instability is required. The presented numerical simulations featuring cyclic loading are inaccurate, if substantial tensile loads are involved. The discussed numerical analyses provide sufficient results up to a tensile load that exceeds the drained resistance by up to three times. This threshold lays beyond today's typically recommended design limitations discussed in Sturm (2017).

The numerical simulation results underpin that internal suction pressure is generated and provides substantial tensile resistance. The achieved caisson penetration depths and the skirt length, i. e. the drainage path length, have a crucial influence on the displacement response. The numerical analyses results emphasise that the interplay between skirt friction, tip resistance, and excess pore pressure determines the suction caisson response under vertical cyclic loading.

6.3 Simplified prediction method

The simplified prediction method presented in Section 4.4 is employed for back calculations of the experimental results. This requires twelve input parameters, which are summarised in Table 6.6. These include the caisson dimensions and internal and external skirt friction factors. In this case the input parameters are determined from the drained pull-out tests presented in Subsection 6.1.2. Furthermore, soil material parameters – i. e. E_s, γ', and k_0 – and the cavitation limit s_{cav} are required. Because of the cyclic and the previous static loading an increased soil stiffness is expected. E_s was estimated from the re-loading stiffness obtained from oedometer test of fine silica sand. In addition, the k_F ratio for small loading rates and a value for $k_{F,L}$ is required for calculations including liquefaction. Based on the results of this study and the likelihood of a significant loss of effective permeability, upper bound values for $k_{F,L}$ from Houlsby and Byrne (2005b) were deemed to be suitable.

Figure 6.19 shows a section of the vertical displacement history. The third and fourth loading package are presented, because these were found to be representative for the general behaviour. The original test data presented in Figure 6.3 is plotted in black, while the estimated curves are coloured. It is demonstrated that the simplified calculations provide an appropriate prediction of the overall behaviour: The predominately elastic response to the LSQ 1 and 2 matches the magnitude of the experimental results. Once higher loading amplitudes are applied in LSQ 3 and 4 net heave is predicted, which is consistent with the experimental results.

Table 6.6: Input parameters for the simplified prediction method.

Parameter	Symbol	Unit	CYC-3-H-F	CYC-5-L-F
Skirt length	L	(m)	4	4
Caisson diameter	D	(m)	8	8
Skirt wall thickness	t	(cm)	5	5
External friction coefficient	$(K \tan \delta)_o$	(-)	0.15	0.15
Internal friction coefficient	$(K \tan \delta)_i$	(-)	0.15	0.15
Stiffness Modulus	E_s	(MPa)	138	138
Specific density sand	γ'	(kN/m^3)	10.5	10.5
Specific density water	γ_w	(kN/m^3)	10	10
External effective permeability	k_{out}	(m/s)	$1 \cdot 10^{-4}$	$3.3 \cdot 10^{-5}$
k_{in}/k_{out} ratio	k_F	(-)	1	1
k_{in}/k_{out} ratio at liquefaction	$k_{F,L}$	(-)	3.5 - 4	4.5 - 5
Cavitation limit	s_{cav}	(kPa)	100	100

The net heave resulting from each loading package is assumed to result from two major factors: the mobilised skirt tip resistance in compression and the changing seepage flow regime during tensile unloading, which affects the effective permeability. The degree of mobilisation of the tip resistance in disturbed soil is considered to be insignificant. Hence, it is assumed that a decreasing effective permeability is the pivotal factor. This is taken into account through the utilisation of the lower bound values for $k_{F,L}$ given in Table 6.6 for tensile unloading at the onset of liquefaction.

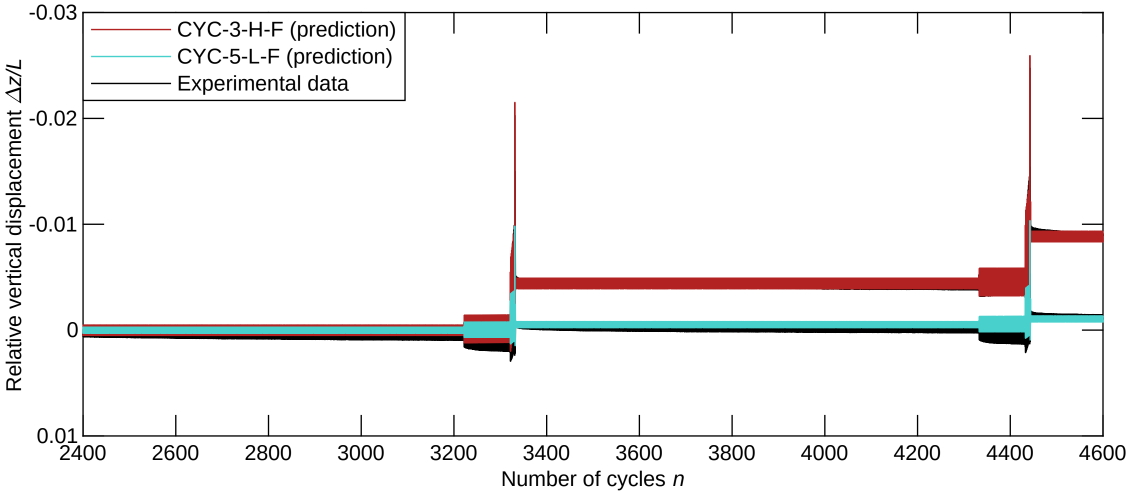

Figure 6.19: Predicted history of vertical displacements during cyclic loading.

This assumption is a reasonable albeit a major simplification. However, it enables the performance of an appropriate back calculation of the experimental results. Furthermore, it is shown that the presented method provides suitable results for the lower and upper bound permeabilities. This also emphasises the importance of accurate knowledge of the *in situ* effective permeability and the soil-structure interaction behaviour. Thus, the investigation of lower and upper bound permeabilities is recommended. Furthermore, it is suggested to slightly reduce the liquefaction limit $\gamma' L/(1-a)$ (Houlsby et al., 2005) in the prediction in order to gain further insight into the response to tensile loading.

6.4 Concluding remarks on the response to vertical cyclic loading in sand

This chapter discusses the results of a series of centrifuge tests investigating the suction caisson installation and their load behaviour in sand. This test series features cyclic loading tests with the purpose to investigate the possibility of a permanent effect of the suction installation on the in-service performance. The importance of the overall drainage regime on the vertical load bearing behaviour was also targeted through the centrifuge tests. The cyclic loading test results add to the existing database and lead to a simplified method, which enables the prediction of vertical displacements of caisson foundations under vertical cyclic loading. The experimental and numerical results support the following findings:

(1) The installation history was found not to significantly influence the behaviour under vertical cyclic loading into tension. However, the achieved skirt penetration depth and therefore the length of the drainage path affects the response to cyclic loading in the tests performed in this study.

(2) The excess pore pressures at the lid invert cycle with the applied stresses and there is no indication of accumulative effects. Undrained behaviour at the lid invert is concluded as the total stresses transferred to the lid are entirely carried by excess pore pressure. The magnitude of the respective vertical displacement was found to be highly depended on the *in situ* effective soil permeability.

(3) When subjected to tension during cyclic loading, the caisson foundation mobilises resistance beyond the drained frictional capacity without permanent displacement – i. e. predominately elastic response in LSQ 1 and 2. In contrast, the response to high magnitude tensile loads during LSQ 3 and 4 featured substantial and permanent net uplift, which is expected to be critical for the serviceability of an OWT.

(4) It is demonstrated that the boxed water element approach is applicable for static and cyclic loading. Hence, it is now feasible to utilise water elements in numerical analyses that include tensile and compressive loading. The presented numerical model covers vertical cyclic loading including excursions into tension within boundaries: Loading scenarios can be analysed with the presented numerical model until liquefaction or cavitation occur.

(5) Analyses targeting the role of the embedded skirt length confirm its crucial role on the caisson response to vertical cyclic loading.

(6) A simplified analytical method is presented for the prediction of the response of suction caissons under vertical cyclic loading. This method includes compressive and tensile loading and unloading and the occurrence of liquefaction and cavitation. The calculated predictions agree with centrifuge tests results considering the vertical cyclic load bearing behaviour in sand.

The discussed results show no permanent influence of the suction installation on static or cyclic loading of a caisson in sandy sea beds. However, the actual embedded depth of the caisson plays an important role. This is consistent with the main finding: The drainage regime and therefore the *in situ* effective permeability governs the response to vertical cyclic loading. This is considered in the development of the simplified prediction method. This aspect is deemed to play a key role in further research activities to unlock the full potential of caisson foundations for offshore wind turbines.

7 Installation in layered soil

This chapter features investigations of the suction caisson installation in layered soil profiles. The results of two parallel series of centrifuge tests (CoS and SoC) and numerical analyses are discussed. The investigations target the visualisation of the mechanisms underlying the suction caisson installation in layered soil profiles.

7.1 Centrifuge tests

7.1.1 Experimental arrangement and testing procedure

The experiments were performed at $100g$ in the Acutronic Model 661 centrifuge (Randolph et al., 1991; Randolph and Gaudin, 2017) at the UWA. These tests had the following requirements to ensure a realistic stress state during the model scale experiments:

- Caisson installation at stress levels representative for prototype scale was required. Thus, the caisson had to be suspended just above the sand surface until the centrifuge had reached the target acceleration.
- The installation was to be done in a controlled manner to ensure reproducible conditions for each cyclic loading test.
- The cyclic loading was to be performed without stoppage of the centrifuge to retain the soil stress state resulting from the suction installation.
- CPTs and T-bar tests were to be performed before and after the caisson tests to characterise the soil samples themselves and to confirm uniformity of each sample.

7.1.1.1 Caisson model, test arrangement and instrumentation

Full-model caisson tests were performed with the similar centrifuge arrangement (see Figure 7.1) as described in Section 5.1. Additional details of this centrifuge test set-up are presented in Appendix B.4. The anodised aluminium model caisson had a diameter of $D = 80\,\mathrm{mm}$ and a skirt length of $L = 40\,\mathrm{mm}$, which when tested at $100g$ represents a diameter $D = 8\,\mathrm{m}$ and a skirt length of $L = 4\,\mathrm{m}$ in prototype scale. In addition to this caisson with an aspect ratio $L/D = 0.5$, a second caisson with the same diameter but with an aspect ratio $L/D = 1$ was also tested in SoC. The skirt wall thickness was $t = 0.5\,\mathrm{mm}$, which corresponds to a prototype wall thickness of $t = 50\,\mathrm{mm}$. This yields a ratio of $D/t = 160$ for these two model caissons.

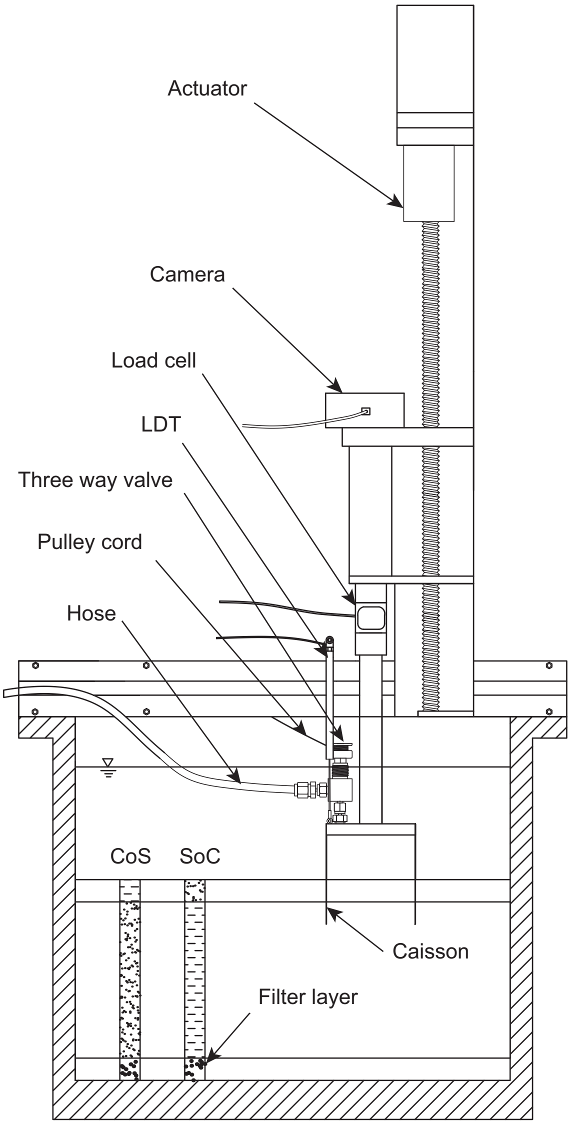

Figure 7.1: Centrifuge test set-up for full-model caisson tests in layered soil.

A half-model caisson, which had a diameter of $D = 80\,\mathrm{mm}$ and a skirt length of $L = 40\,\mathrm{mm}$, was manufactured for the PIV tests. The wall thickness of this suction caisson is $t = 2\,\mathrm{mm}$ for practical reasons (Ragni et al., 2018; Ragni et al., 2019). To facilitate comparison between half-model PIV tests and full-model caisson tests, an additional caisson with a diameter of $D = 80\,\mathrm{mm}$ and a skirt length of $L = 40\,\mathrm{mm}$, but a wall thickness of $t = 2\,\mathrm{mm}$, i. e. $D/t = 40$, was manufactured. Additional details of this centrifuge test set-up are presented in Appendix B.3.

Each caisson was equipped with two TTPs: one at the lid invert and another one at the top of the lid and a PPT at the lid invert. The caisson models were connected to a load cell with a maximum capacity of $3\,\mathrm{kN}$ by means of a rigid rod. This assembly was carried

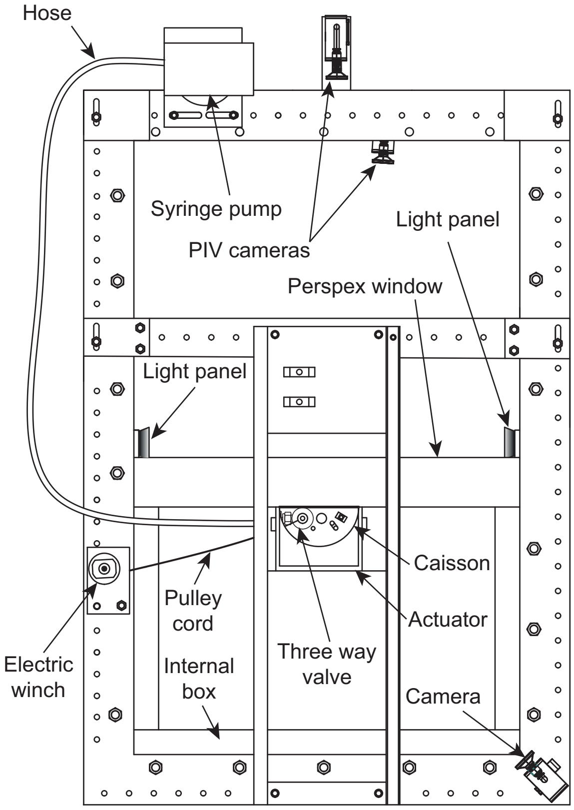

Figure 7.2: Centrifuge test set-up for half-model caisson tests in layered soil.

by an actuator, which was mounted on top of the strong box. The three way valve on the caisson lid was operated by an electric winch (see Figure 7.1). The valve was able to vent to ambient, to connect the caisson to the syringe pump (House, 2002), and to be sealed. The water table was at least 100 mm above the soil surface to ensure that the model caisson including the three way valve were submerged to minimise changes in buoyancy during the installation. The self-weight and the cyclic loading of the model caisson were applied with the actuator that was controlled through a feedback loop from the load cell. The displacement of the caisson was recorded by means of a LDT.

The half-model tests were conducted inside a smaller strong box equipped with a 50 mm perspex window, which had inner dimensions of 300 mm in height, 335 mm in length, and 225 mm in width. The small strong box sat inside a larger one that also carried the camera equipment, actuator, winch, and the syringe pump shown in Figure 7.2.

The half-model caisson tests required a set-up that allowed the self-weight and suction installation to be similar to the installations conducted with full-model-test. The PIV tests were performed with the testing arrangement developed by Ragni et al. (2018) and Ragni et al. (2019). The half-model was pressed against a window to enable photographs from the outside. The interface between the model caisson and the perspex window was sealed with a combination of a soft foam seal and a rubber seal at the skirt tips, which was lubricated with petroleum jelly. Two five megapixel machine vision cameras captured images through the perspex window. The master-camera – equipped with an 8 mm lens – provided an overview of the entire window, while the follower-camera had a 43 mm lens providing a micro view of the suction caisson and a close range of the surrounding soil. This set-up yields an approximately 20 times increased resolution in this area. Both cameras were operated in sync at a frequency of two images per second during the suction caisson installation resulting in at least 20 images per millimetre of caisson penetration. Two LED-light panels ensured uniform illumination of the perspex window (Teng et al., 2017; Ragni et al., 2019). The PIV post analysis also follows Ragni et al. (2018) and Ragni et al. (2019).

7.1.1.2 Soil sample and pore fluid preparation

Overconsolidated stiff clay and dense sand are used in this study, which creates the most onerous conditions for the suction caisson installation. Table 7.1 and 7.2 summarise the soil properties of the very fine silica sand and kaolin clay used in the centrifuge tests. Layered soil samples with a thickness of the top layer of 20 mm were prepared to create onerous conditions for suction caisson installation while facilitating comparison to previous studies (Zhu et al., 2018a; Ragni et al., 2020). The clay was prepared from slurry at a water content of $\approx 120\,\%$, mixed under vacuum, and consolidated in a hydraulic press under a vertical pressure of $\sigma_v = 350\,\text{kPa}$.

Table 7.1: Properties of fine silica sand (M. N. Tran, 2005; Lehane and Q. B. Liu, 2013; Chow et al., 2018).

Parameter	Symbol	Unit	Value
Grain density	ρ_s	(t/m^3)	2.67
Mean grain size	d_{50}	(mm)	0.18
Min. void ratio (-)	e_{min}	(-)	0.490
Max. void ratio	e_{max}	(-)	0.784
Peak friction angle	φ'	(°)	43.1
Effective permeability	k_f	(m/s)	$1 \cdot 10^{-4}$

Two SoC samples (one for the full model tests and one for the PIV test) were prepared by pluviation of dry sand into the strong box from a height of approximately 1.2 m by means of an automatic pluviator, which contained the previously consolidated clay layer. The clay layer height was approximately 140 mm after consolidation. The sand layer was vacuum levelled to a target thickness of 20 mm and subsequently saturated from the soil layer boundary.

The sand for both CoS samples (one for the full model tests and one for the PIV test) was dry pluviated and vacuum levelled at 140 mm above the base of the strong box including a coarser sand filter layer. Once the sand layer was saturated from the bottom, a clay layer with an approximate thickness of 20 mm was placed manually on top of the saturated sand. A similar total sample height of at least $4L$ for each sample was targeted

Table 7.2: Properties of kaolin clay (Al-Tabbaa and Wood, 1987; Colreavy et al., 2016).

Parameter	Symbol	Unit	Value
Grain density	ρ_s	(t/m^3)	2.6
Liquid limit	LL	(%)	61
Plastic limit	PL	(%)	27
Peak friction angle	φ'	(°)	23
Critical state friction coefficient	M	(-)	0.92
Void ratio at CSL[a]	e_{cs}	(-)	2.14
Slope NCL	λ	(-)	0.205
Slope URL	κ	(-)	0.044
Effective permeability	k_f	(m/s)	$1.7 \cdot 10^{-9}$
Coefficient of consolidation[b]	c_v	(m^2/a)	5.5

[a] $p' = 1\,\mathrm{kPa}$

[b] estimated for stress level at skirt tip and $OCR = 7.1$

to minimise boundary effects (M. N. Tran and Randolph, 2008). The sand unit weight was determined from weight and volume measurements. The relative densities D_r were $83 \pm 2\,\%$.

Under consideration of scaling laws governing suction caisson response, the viscosity η of the pore fluid was increased from approximately $\eta_w = 1\,\mathrm{cSt}$ for water to a target value of $\eta = 100\,\mathrm{cSt}$ (Taylor, 2011). Hereby an effective permeability of the soil sample – i. e. $k_f \approx 1 \cdot 10^{-4}\,\mathrm{m/s}$ – at $100g$ is targeted, which is representative of typical North Sea sands (Tan and Scott, 1985). The viscosity was increased through the addition of methyl cellulose ether (DOW, 2002). The targeted pore fluid viscosity was confirmed by measurements. The clay layer was water saturated.

7.1.1.3 Sample characterisation

CPTs were performed before and after the suction caisson test at $100g$. The utilised cone penetrometer had a diameter of $D_{cpt} = 7\,\mathrm{mm}$ and was penetrated at a velocity of $v_{cpt} = 1\,\mathrm{mm/s}$, which is expected to result in drained conditions in sand (Finnie and Randolph, 1994). The results shown in Figure 7.3 confirm similarity between and within each soil sample.

T-bar tests were conducted immediately after consolidation at $1g$ as well as before and after the suction caisson tests at $100g$. The miniature penetrometer had a width of $w_{Tbar} = 20\,\mathrm{mm}$, a plastic shear pin diameter of $D_{Tbar} = 5\,\mathrm{mm}$, and a shaft diameter of $D_{Tbar,s} = 6.3\,\mathrm{mm}$. The device was penetrated at $v_{Tbar} = 1\,\mathrm{mm/s}$, which is expected to result in undrained conditions in clay (Finnie and Randolph, 1994). A T-bar factor of $N_{c,Tbar} = 10.5$ (Low et al., 2010) was assumed to obtain the undrained shear strength profiles presented in Figure 7.4.

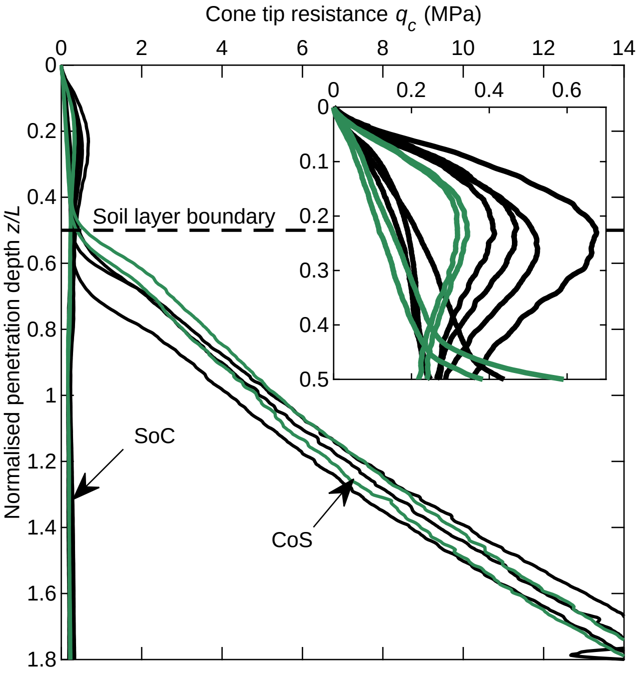

Figure 7.3: CPT profiles from soil samples for full-model tests (black) and half-model tests (green) in SoC and CoS.

The *in situ* undrained shear strength s_u of the clay layer depends on the vertical effective stress σ'_v and over-consolidation ratio OCR and can be calculated using Equation 7.1 (Ladd et al., 1977):

$$s_u = \sigma'_v \left(\frac{s_u}{\sigma'_v} \right)_{NC} OCR^{\Lambda} \tag{7.1}$$

where the plastic volumetric strain ratio is given in Equation 7.2, with the soil parameters listed in Table 7.2.

$$\Lambda = \frac{\lambda - \kappa}{\lambda} \tag{7.2}$$

The normally consolidated undrained shear strength ratio $(s_u/\sigma'_v)_{NC}$ ranges between 0.15 and 0.19 for kaolin clay (Lehane et al., 2009; Schofield and Wroth, 1968) – $(s_u/\sigma'_v)_{NC} = 0.19$ is assumed here. The undrained shear strength profiles, calculated with and without consideration of the overlying sand layer and assuming effective unit weights of $\gamma'_{sand} = 10.5\,\mathrm{kN/m^3}$, and $\gamma'_{clay} = 7.1\,\mathrm{kN/m^3}$, are included in Figure 7.4. Also included are the profiles from comparable tests calculated with the values given in Ragni et al. (2019) and Zhu et al. (2018b).

The results show similarity to the predictions, which do not account for shallow penetration depth effects. An increased moisture content of the clay close to the layer boundary, which was expected and represents *in situ* conditions, also reduces the measured T-bar penetration resistance and therefore the determined undrained shear strength s_u. Further-

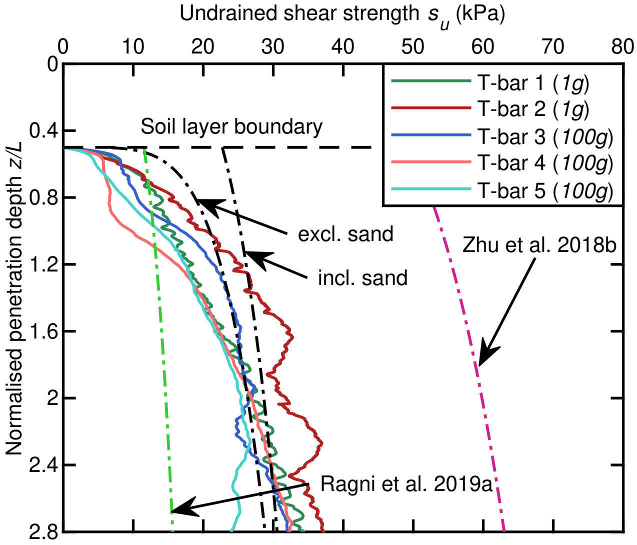

Figure 7.4: T-bar profiles from soil samples (solid lines) for full-model tests (T-bar 1, 3 & 4) and half-model tests (T-bar 2 & 5) including predictions of the presented and previous tests (dash-dotted lines).

more, the results from T-bar 2 show an increased undrained shear strength at 1g. However this was not confirmed in the related T-bar 5 conducted at 100g prior to the suction caisson tests. The T-bar profiles confirm that the undrained shear strength is higher than it was in Ragni et al. (2019) and lower than it was in Zhu et al. (2018b), as targeted.

7.1.1.4 Testing nomenclature

Table 7.3 summarises the caisson dimensions, applied vertical stress (self-weight) and pumping flow rate and applied cyclic load case of all 16 suction caisson tests. The 14th test failed due to an incorrect assembly of the pumping system. The tests were named as follows:

- The letters SoC and CoS indicate the stratification.
- The second number indicates the aspect ratio of the model suction caisson.
- A number letter combination indicates the installation method: J = jacked installation and SI = suction installation and s = slow and f = fast indicate variations of the pumping flow rate. The number represents the vertical load that was maintained during the installation of the model caisson. Tests with a displacement controlled self-weight installation are indicated by the letters DC instead of a number.
- The last number indicates the cyclic loading case. The half-model caisson tests are identified by the letters PIV instead of a load case.

7.1.1.5 Testing procedure

Each test listed in Table 7.3 was performed in a different location within the strong boxes.

Table 7.3: Centrifuge testing programme.

Test No.	Test name	Vertical stress V/A (kPa)	Pumping rate q (mm^3/s)	Model dimensions $D/L/t$ (mm)	Load Case
1	SoC-0.5-350J-10	70	jacked inst.	80/40/0.5	10
2	SoC-0.5-100SIs-30	20	196.4	80/40/0.5	30
3	SoC-0.5-125SI-20	25	392.7	80/40/0.5	20
4	SoC-0.5-150J-21	30	jacked inst.	80/40/0.5	21
5	SoC-1.0-125SI-20	25	392.7	80/80/0.5	20
6	SoC-1.0-150SI-21	30	392.7	80/80/0.5	21
7	SoC-0.5-DCSI-20	56	392.7	80/40/2.0	20
8	SoC-0.5-DCSI-PIV	24[a]	196.4[a]	80/40/2.0	PIV
9	CoS-0.5-350SI-10	70	392.7	80/40/0.5	10
10	CoS-0.5-350SI-20	70	392.7	80/40/0.5	20
11	CoS-0.5-350SI-21	70	392.7	80/40/0.5	21
12	CoS-0.5-350SIf-10	70	1963.5	80/40/0.5	10
13	CoS-0.5-350SI-11	70	392.7	80/40/0.5	11
14	CoS-0.5-DCSI-F	70	392.7[b]	80/40/0.5	-
15	CoS-0.5-DCSI-10	346	392.7	80/40/2.0	10
16	CoS-0.5-DCSI-PIV	127[a]	196.4[a]	80/40/2.0	PIV

[a] values apply to half-model [b] test failed during suction installation

7.1.1.6 Suction caisson installation

The suction caisson installation for both full- and half-model caisson tests was performed as follows:

(1) The caisson was suspended just above the soil surface until the centrifuge had reached the target acceleration to allow installation at stress levels representative of prototype conditions.

(2) The self-weight penetration was performed under load control at a constant loading rate of 1 N/s in model scale. The three way valve vented to ambient until the self-weight penetration completed. A low self-weight was applied in SoC to achieve self-weight penetration prior to peak resistance in the sand layer in order to investigate onerous conditions for suction caisson installation. In CoS, self-weight under realistic loads was assumed to penetrate the skirts to the underlying sand layer. The thick-walled full- and half-model caissons were penetrated in displacement control to comparable depths, which attracted higher loads. This self-weight was maintained through load control during the suction installation.

(3) Once the self-weight penetration stopped, the valve was switched to achieve a hydraulic connection between the caisson internal and the syringe pump without stopping the centrifuge. A constant pumping flow rate was applied and maintained until the caisson penetration stopped.

(4) The in-flight suction caisson installation was completed by sealing the valve without stopping the centrifuge.

Table 7.3 details the self-weight and pumping flow rate applied in each test.

7.1.2 Results and discussion

The experimental results are presented in non-dimensional form, unless stated otherwise. Positive values indicate compression and downward displacements, whereas negative values represent tension and upward displacements.

7.1.2.1 Sand over clay

Suction caisson installation in the SoC profile was unproblematic as expected, even with low self-weight of $V_{sw} = 100\,\mathrm{N}$ in model scale or $(V/A)_{sw} = 20\,\mathrm{kPa}$ and a minimum model pumping flow rate of $q = 196{,}4\,\mathrm{mm}^2/\mathrm{s}$ due to the low tip resistance, which was estimated at $R_T \approx 9\,\mathrm{kPa}$ (Houlsby et al., 2005; Ragni et al., 2020).

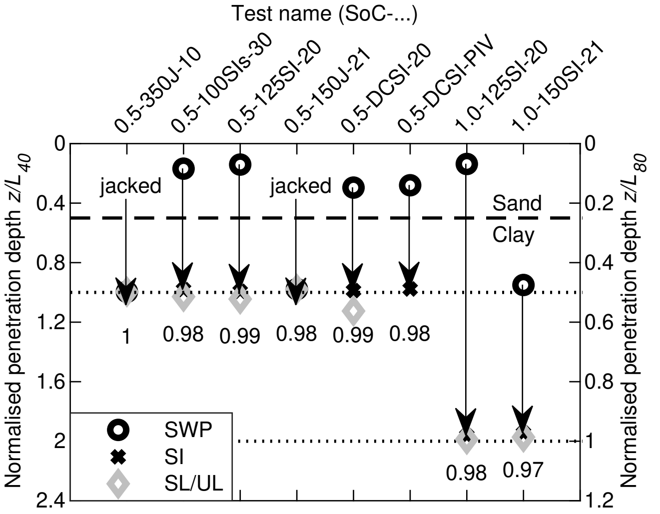

Figure 7.5: Normalised penetration depths achieved following the self-weight penetration (SWP), suction installation (SI), and after static loading and unloading (SL/UL) in SoC.

Figure 7.5 shows that the selected self-weight resulted in penetration depths within the sand layer, as intended. The thicker-walled caissons in tests SoC-0.5-DCSI-20 and SoC-0.5-DCSI-PIV, of course, attracted higher loads for self-weight penetration to approximately half of the sand layer. A vertical stress of $(V/A)_{sw} = 30\,\mathrm{kPa}$ in test SoC-1.0-150SI-21,

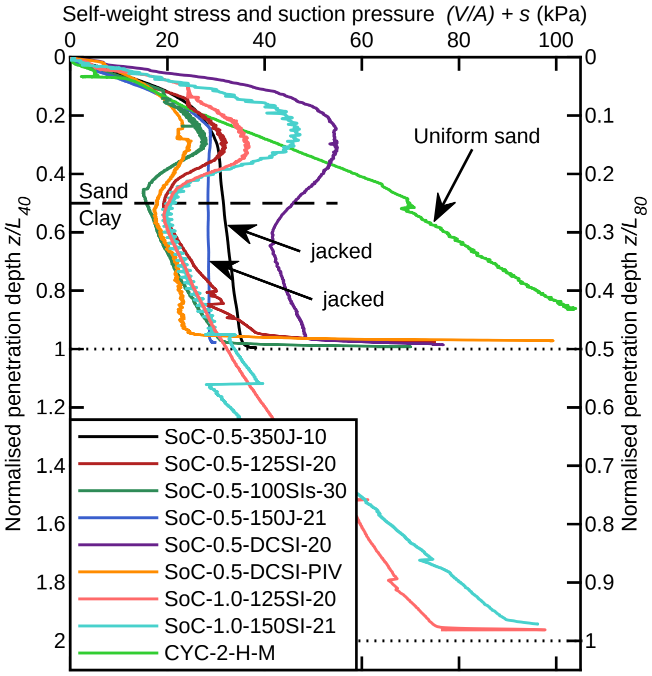

Figure 7.6: History of vertical stresses and suction pressure during installation in SoC and uniform sand profiles.

however, exceeded the capacity of the sand layer and resulted in rapid penetration into the underlying clay layer. The suction installation phase was unproblematic in all tests. Each suction caisson installed in the SoC soil reached full penetration ($z/L \approx 1$) in this study. This also holds for the results obtained from tests utilising the $L/D = 1$ model caisson, which are normalised by $L_{80} = 80\,\mathrm{mm}$ and $L_{40} = 40\,\mathrm{mm}$, respectively, to facilitate comparison between the tests.

Figure 7.6 shows the applied installation pressure $(V/A) + s$, which corresponds to the cone tip resistance profile shown in Figure 7.3. The nature of the cone tip resistance profile, with a nose in the sand layer followed by a reduction in resistance, carries the risk of rapid penetration. This occurred in test SoC-0.5-DCSI-20 and SoC-0.5-DCSI-PIV due to the increased self-weight (Table 7.3) upon the commencement of suction.

Figure 7.6 further compares the penetration resistance profiles in SoC during suction installation with jacked penetration and with suction installation in a uniform sand profile. The penetration resistance in SoC is significantly lower compared to the installation of the same model caisson in sand, requiring lower suction. The applied suction also reduces the penetration resistance compared to a jacked installation, as expected. This is consistent with predictions (Houlsby and Byrne, 2005b; Houlsby et al., 2005).

The distinctly decreasing normalised penetration rate observed in tests SoC-0.5-100SIs-30, SoC-0.5-125SIs-20, and SoC-1.0-125SI-20 indicates a significant amount of seepage flow and would lead to piping failure once the curves reach zero on the x-axis in Figure 7.7.

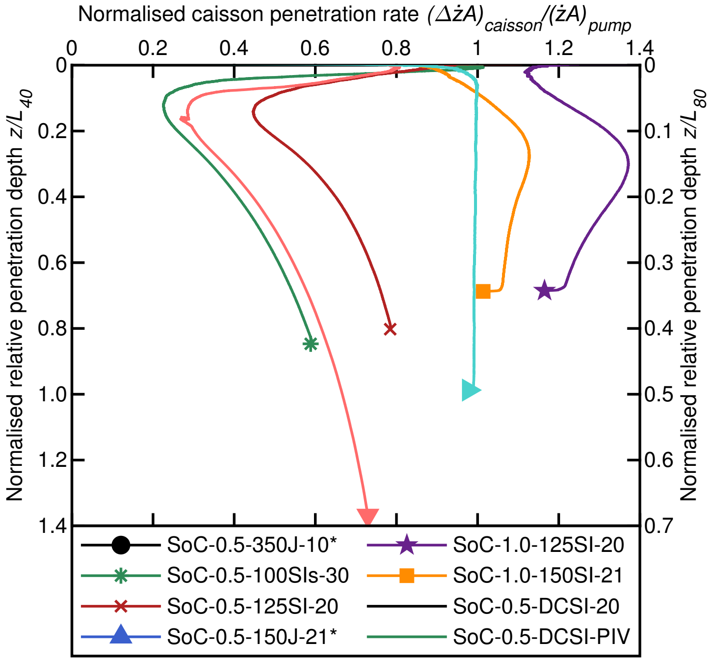

Figure 7.7: History of the normalised suction caisson penetration rate.

The constant normalised caisson penetration rate of $(\Delta\dot{z}A)_{caisson}/(\Delta\dot{z}A)_{pump} \approx 1$ observed in test SoC-1.0-150SI-20 means that no seepage occurred during the suction installation (Houlsby and Byrne, 2005b). This is plausible, since the skirt tip was already embedded in the clay layer during the self-weight penetration, whereby the water inside the caisson was sealed from ambient.

The results from PIV analyses presented in Figure 7.8a provide further insights, including soil plug heave developing in the early stages of suction installation, which remained approximately constant until the end of the suction installation (Figure 7.8a and 7.8b). However, the loosening was only temporary. The soil plug was compressed upon lid touch-down due to the vertical load and the ongoing evacuation of fluid from the caisson until the pumping system was stopped shortly after lid touch-down (Figure 7.8c). These results suggest that soil plug heave is reversible in SoC profiles.

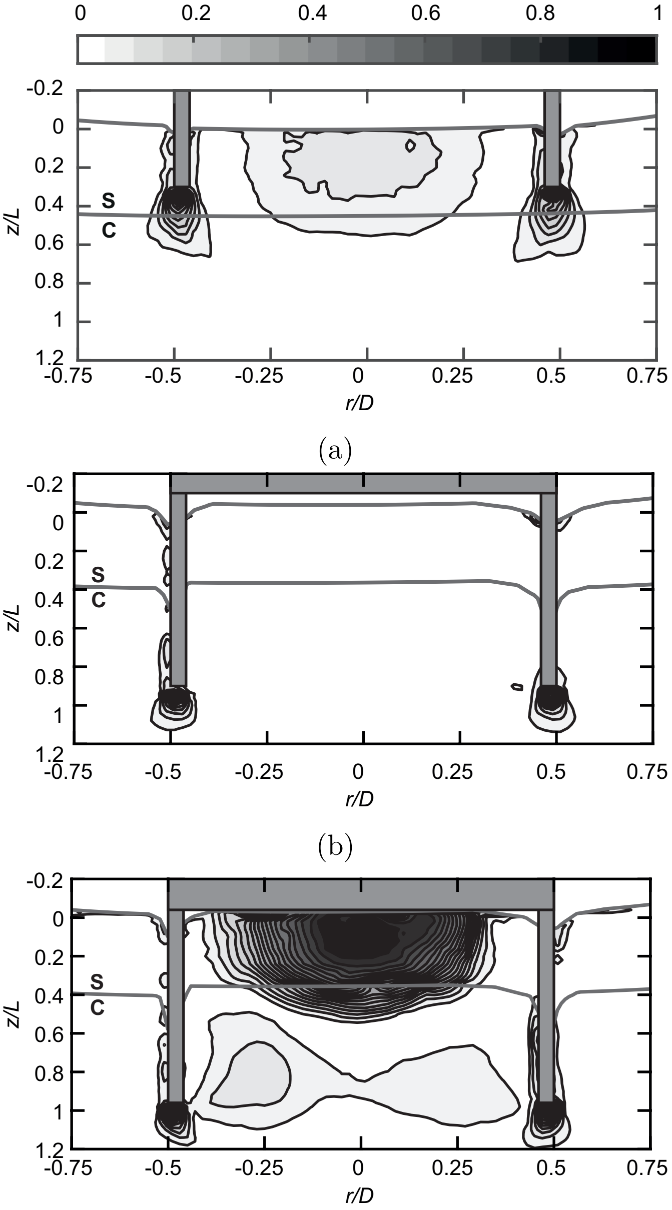

(a)

(b)

(c)

Figure 7.8: Normalised resultant displacement contours in the beginning (a), close to the end (b) of the suction, and after lid touch down (c) in a SoC profile.

7.1.2.2 Clay over sand

The self-weight installation, as detailed in Subsection 7.1.1.6, resulted in skirt penetration of at least $z/L = 0.5$ (Figure 7.9). Hence, the skirt tips were embedded in the underlying sand layer at the commencement of suction installation. Thus, the clay prevented a hydraulic connection between the sand and the syringe pump. Expectingly, hardly any seepage reached the pumping system during the suction installation in accordance to Figure 7.11. The distinct change in gradient of the normalised caisson penetration rate $(\Delta\dot{z}A)_{caisson}/(\Delta\dot{z}A)_{pump}$ leading to a plateau indicates lid touch down on the soil plug.

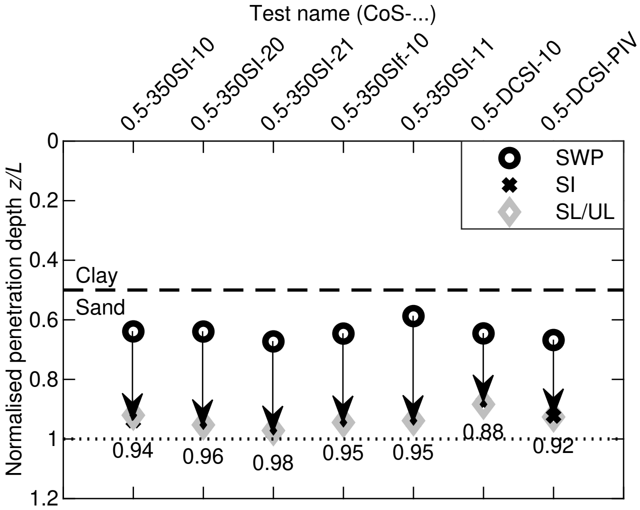

Figure 7.9: Normalised penetration depths achieved following the self-weight penetration (SWP), suction installation (SI), after static loading, and unloading (SL/UL) in CoS.

The results presented in Figure 7.9 show that the model caisson reached a total penetration depth of $z/L \geq 0.95$ in the majority of the tests. Assuming even distribution of soil flow around the penetrating skirt during self-weight installation (achieved penetration measured) and inward flow during suction installation (Ragni et al., 2018; Ragni et al., 2020), the soil plug heave due to the displaced volume can be calculated. Therefore, a penetration depth of $z/L > 0.98$ on average for $t = 0.5\,\text{mm}$ and $z/L > 0.92$ for $t = 2\,\text{mm}$ implies full skirt penetration. A distinct change in gradient at the end of the curves presented in Figure 7.10 and 7.11 indicates contact between the lid and the soil plug, with the difference between the calculated and the achieved (Figure 7.9) penetration implying soil plug heave.

Senders and Randolph (2007) and Ragni et al. (2020) pointed out that clay plug uplift is required to transfer suction pressure to initiate seepage flow and hence reduce skirt tip resistance in the underlying sand. The clay plug uplift resistance, which is composed of plug self-weight and internal skirt resistance, is estimated to be $(V/A)_{cp} \leq 15\,\text{kPa}$. This value is exceeded by the suction pressure applied in addition to the self-weight stress (Figure 7.10). Consequently, clay plug uplift is believed to have occurred in each test performed in this series of centrifuge tests. The results of the PIV analyses presented in Figure 7.12 confirm clay plug uplift as the occurrence of a distinct gap is visible in Figure 7.12c. Furthermore, the gradient of the curves representing the additionally applied suction pressure during the thin-walled suction caisson installations in CoS aligns with test results found in test conducted in homogeneous sand (see Section 5.1). This reinforces the observation of the seepage induced reduction of the skirt tip resistance in the underlying sand.

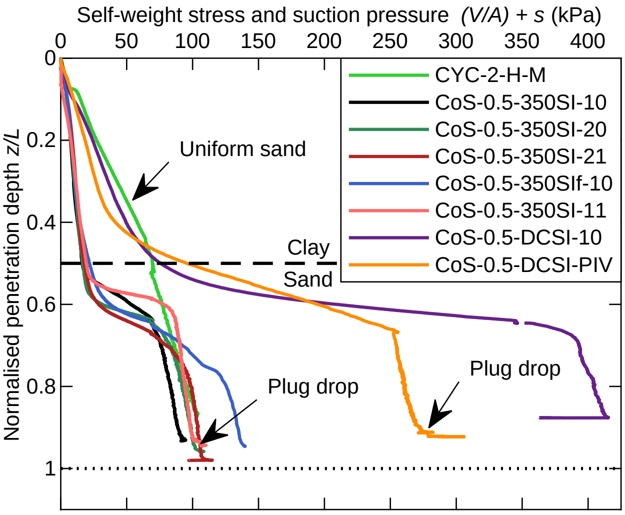

Figure 7.10: History of the vertical stresses and suction pressure during installation in CoS and uniform sand profiles (a).

The displacement controlled self-weight penetration of the thick-walled caissons yields vertical stresses of $V/A \approx 346\,\text{kPa}$ in test CoS-0.5-DCSI-10 and $V/A \approx 254\,\text{kPa}$ in test CoS-0.5-DCSI-PIV, which roughly matches the calculated jacked penetration resistance of $V/A = 259\,\text{kPa}$. This calculation performed in accordance to Houlsby and Byrne (2005b) furthermore provides an estimated required suction pressure of $s_{req} = 169\,\text{kPa}$, if the seepage induced reduction of the tip resistance is not taken into account. Thus, a thick-walled model caisson installation would result in premature refusal due to the occurrence of cavitation. However, Figures 7.9 and 7.10 show that considerably less suction is required in order to achieve a penetration depth of $\Delta z/L > 0.9$, which is feasible because of the presence of clay plug uplift induced seepage flow. These results underpin the findings derived from half-model caisson installation test and PIV analyses discussed above and in Ragni et al. (2020).

The maximum plug heave and resulting gap at the layer boundary is visualised in Figure 7.12c at a relative skirt penetration depth of $\Delta z/L = 0.9$. The course of the caisson penetration of test CoS-0.5-350SI-11 and CoS-0.5-DCSI-PIV features a jump close to the end of skirt penetration, which is visible in Figure 7.10. This jump indicates the sudden equalisation of the differential pressure between the top and bottom of the clay plug – i. e. a vertical fluid channel between clay layer and the skirt opens. The overall caisson internal suction pressure is maintained due to the drainage regime, which is present in the underlying sand. The results of the PIV analysis shown in Figure 7.12d reveal that the establishment of a flow channel is accompanied by a clay plug drop closing the gap shown in Figure 7.12c.

The results presented in Figures 7.9 to 7.12 confirm the feasibility of the suction caisson installation in CoS profiles at moderate and high pumping flow rates with similar governing mechanisms as revealed for the first time in Ragni et al. (2020), despite differences in clay layer strength and suction caisson aspect ratio. In each test discussed here, suction

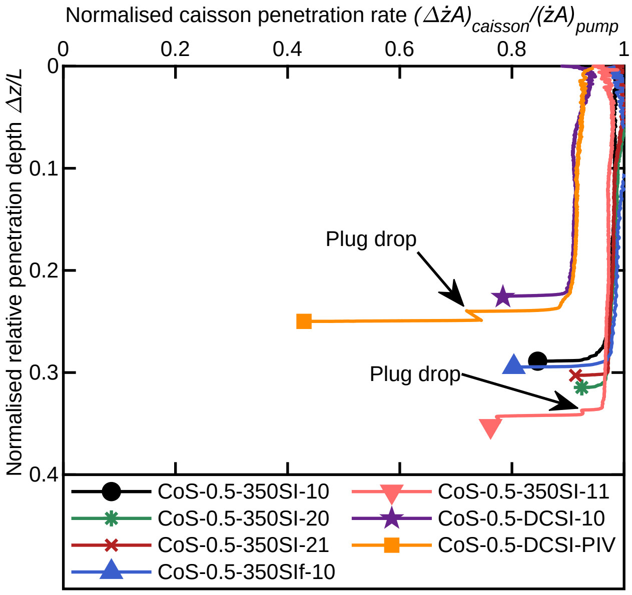

Figure 7.11: History of the normalised suction caisson penetration rate.

caisson installation in CoS resulted in less plug heave compared with installation in uniform sand (Bienen et al., 2018a; Ragni et al., 2019). This is consistent with the results presented in Ragni et al. (2020). This includes test CoS-0.5-350SIf-10, which was installed at the maximum possible pumping flow rate and the maximum suction pressure measured at the lid invert within this series of tests. The achieved penetration depth of this test is similar to all others conducted with the thin-walled model caisson.

However, the actual extent of the clay and sand plug heave remains invisible in the full model tests. The discussed previous and presented PIV analyses are based on experiments conducted with thick-walled model caissons. Consequently, the role of the skirt wall thickness is further discussed under consideration of possible consequences on the in-service performance in Chapter 8.

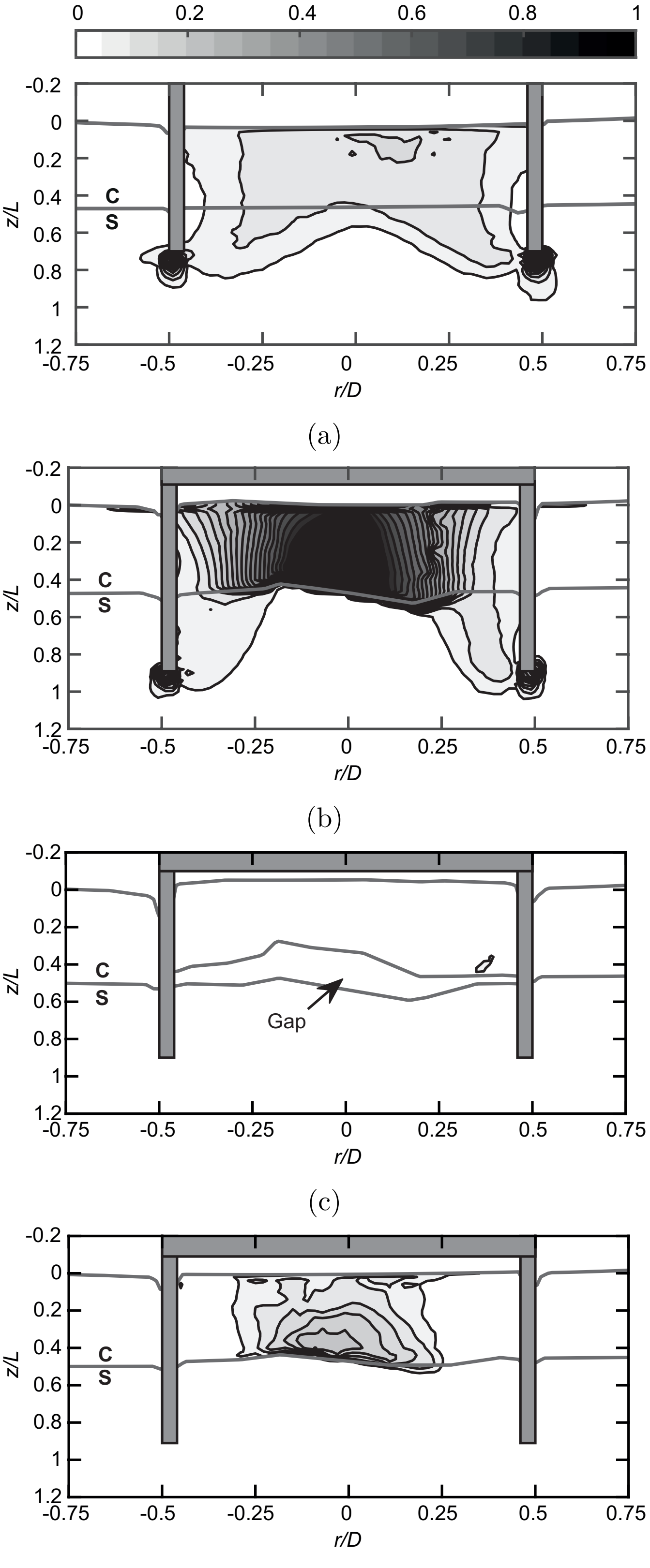

(a)

(b)

(c)

(d)

Figure 7.12: Normalised resultant displacement contours during clay plug heave without formation of a gap at $\Delta z/L = 0.7$ (a), during the formation of a gap at $\Delta z/L = 0.89$ (b), at the maximum opening of the gap at $\Delta z/L = 0.90$ (c), and after the plug drop down at $\Delta z/L = 0.91$ (d) in a CoS profile.

7.1.3 Remarks on the centrifuge tests

The experimental results obtained from PIV post analyses reveal the underlying mechanisms of the suction caisson in layered soil profiles. However, the experiments have several limitations: The shear strength of the kaolin clay has been limited due to the restrictions preventing damage to the laboratory equipment. Centrifuge tests involving suction caisson installation and PIV post analyses are complex and time consuming. Furthermore, a seal located at the perspex window interface requires a relatively thick-walled model caisson compared to prototype scale caissons. Hence, the scope of the centrifuge experiments might be compromised. Consequently, additional investigations are required. The following section therefore contains MPM simulations that aim clarification of the existing uncertainties.

7.2 Numerical simulations

The MPM model presented in Section 5.2 is adapted for analyses including layered soil profiles. The numerical simulations again target the visualisation of the mechanisms underlying the suction caisson installation. This study consists of two steps: First, a comparison between the centrifuge test results presented in the previous section and in Ragni et al. (2020) is employed for validation. Parametric studies are performed in the second step in order to provide insights into the questions formulated above.

7.2.1 Numerical modelling and testing procedure

The numerical simulations are performed with a modified version of the MPM code Anura3D 2019.1. The modifications are discussed in Chapter 4. The numerical model has the following requirement in addition to the ones listed in Section 5.2: Multiple soil layers have to be included in the numerical model in addition to the caisson structure. Interaction between the soil layers and the caisson have to be captured. Thus, a multi-material contact formulation is required.

The adapted model for the MPM simulations featuring layered soil profiles shown in Figure 7.13 includes a top layer in addition to the main soil layer. The layer thickness and the caisson pre-embedment may vary, but undrained response of the caisson internal top layer is expected in most cases that will be investigated. This simplifies the load application, which is shown in Figure 7.13a. The presented model dimensions are again derived from the centrifuge tests and are also found to minimise boundary effects in the simulations featuring layered soils. The actual model dimensions for each numerical simulation are summarised in Table 7.4.

The horizontal displacements are locked at the axis of symmetry and outside vertical edge of the model geometry, while vertical displacements are permitted. The bottom featured zero vertical displacements boundary conditions. These three edges are also hydraulically impermeable. The displacements at the soil surface are unlocked, while solid and liquid

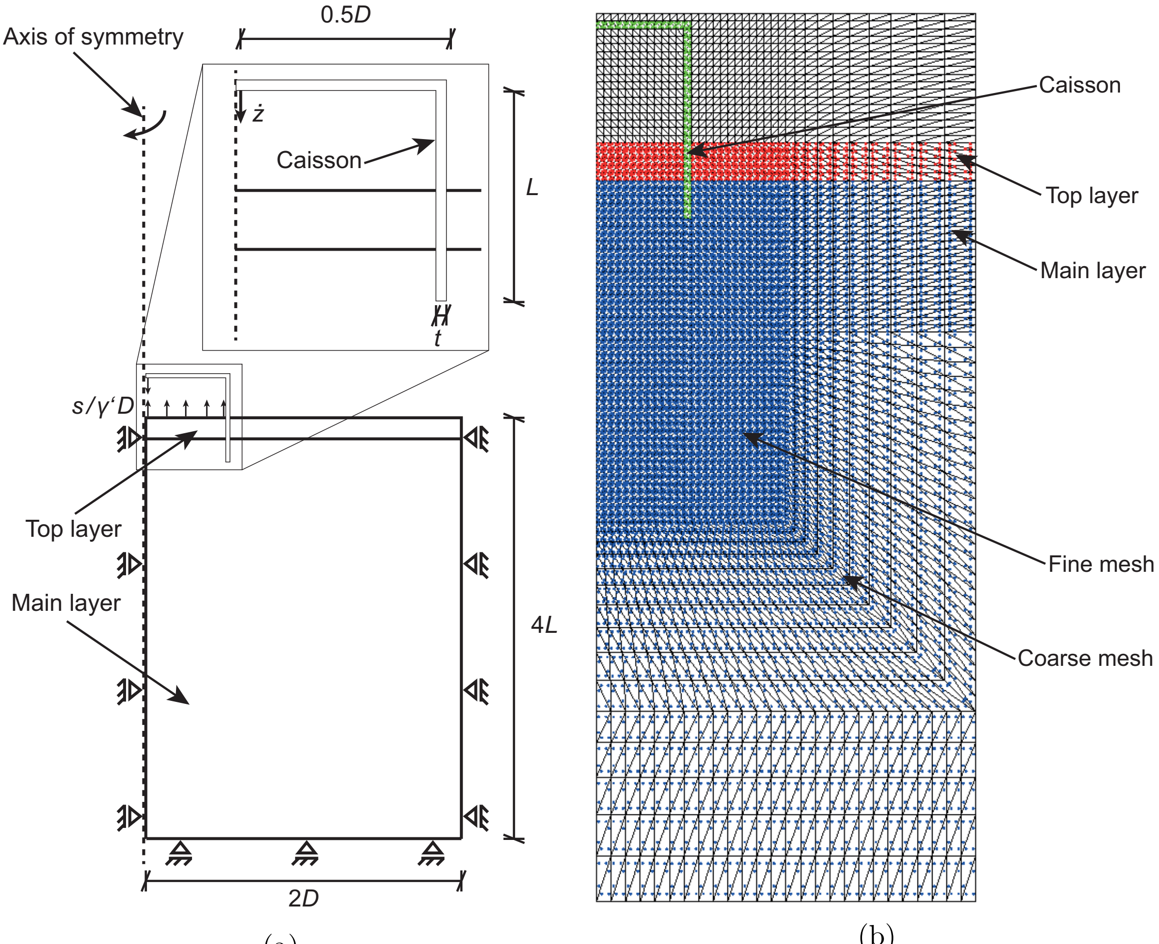

(a) (b)

Figure 7.13: Dimensions (a) and discretization (b) of the numerical model utilised for MPM analyses featuring a layered soil profile.

pressure boundary conditions are applied at the MPs if required. The caisson is modelled as a quasi-rigid body as the horizontal displacement rate is $\dot{z}_h = 0$ and a prescribed vertical displacement rate $\dot{z}_v$ is utilised to control the caisson penetration.

Based on the centrifuge tests, drained conditions are present in sand and undrained behaviour determines the response of the clay during the jacked self-weight penetration. Hence, it is possible to model the soil by means of a one-phase continuum for this kind of simulation.

The simulation of the suction installation requires a separate consideration: A one-phase continuum approach is feasible for simulations featuring SoC profiles, because the soil response is determined by the undrained behaviour of the clay once the skirt tip is embedded in the main clay layer. The internal suction pressure is expected to be transferred through the encapsulated sand plug. Potential changes of the sand plug state are expected to have a minor influence on the overall installation mechanisms. Consequently, the sand top layer can sufficiently be simulated as a one-phase continuum. The only exception here

Table 7.4: Numerical model caisson dimensions for layered soils.

Model No.	D (m)	L (m)	t (cm)
10	5	5	20
11	5	5	5
20	8	4	20

is the start of the suction installation with the skirt tips resting in the sand layer, because seepage flow into the caisson is present at this stage.

Investigations on CoS profiles require the utilisation of a two-phase formulation for the sand underlying a presumingly undrained responding clay layer, which is therefore modelled by means of a one-phase continuum. The uplift of the clay plug transfers the suction pressure into the underlying sand. Consequently, the pore pressure regime changes: Seepage flow towards the inside of the caisson is introduced. This process is relevant for investigations of the underlying mechanisms and has to be captured by the numerical simulation.

The utilisation of the two-phase formulation again implied the utilisation of the mixed integration scheme in order to minimise numerical errors due to grid crossing and artificial peaks of the pore water pressure (Jassim et al., 2013; Fern et al., 2019). Since comparably simple elastic-plastic models are found to satisfy all the requirements targeted in this study, elastic and elastic-plastic constitutive models featuring the Mohr-Coulomb plasticity criterion are employed.

Table 7.5: Model parameters for MPM simulations featuring layered soil profiles.

Parameter	Symbol	Unit	Fine silica sand	Kaolin clay
Friction angle	φ	(°)	38	-
Dilation angle	ψ	(°)	1	-
Effective cohesion	c'	(kPa)	0	-
Undrained shear strength	s_u	(kPa)	-	$10-30$
Young's modulus	E	(MPa)	60	1
Poisson's ratio	ν	(-)	0.25	0.3
Undrained Poisson's ratio	ν_{ud}	(-)	-	0.47
Intrinsic permeability	κ	(m^2)	$1 \cdot 10^{-11}$	-
Dynamic viscosity liquid	η_w	(kPa·s)	$1 \cdot 10^{-6}$	-
Bulk modulus liquid	K_w	(MPa)	20	-
Density water	ρ_w	($\mathrm{t/m}^3$)	1	-
Initial porosity	n	(-)	0.35	0.57
Grain density solid	ρ_s	($\mathrm{t/m}^3$)	2.65	2.6
Interface friction coefficient	μ	(-)	0.15	-
Adhesion factor	a	(-)	-	$0.03-0.1$

The model parameters for fine silica sand summarised in Table 7.5, are determined under consideration of laboratory test results summarised in M. N. Tran (2005), Lehane and Q. B. Liu (2013), and Chow et al. (2018). Additional details are discussed in Section 5.2. The model parameters for kaolin clay, which are also given in Table 7.5, are derived under the consideration of laboratory tests presented in Al-Tabbaa and Wood (1987) and Colreavy et al. (2016). The adhesion factor is adjusted in order to align the simulated and the centrifuge test behaviour during the suction installation.

The simulations are conducted in accordance to the following procedure: First, the effective stresses and, if necessary the hydrostatic pressure, are applied during the K_0 procedure. The caisson is penetrated displacement controlled in a second step. The differential pressure is applied simultaneously if required. The caisson penetration rate and suction pressure vary in each test. Therefore, the actually applied values are given in the following section.

7.2.2 Results and discussion

MPM simulations are performed to address the remaining questions subjecting the suction caisson installation in layered profiles. The calculated results are presented in non-dimensional form, unless stated otherwise. Positive values indicate compression and downward displacements, whereas negative values represent tension and upward displacements.

7.2.2.1 Sand over clay

Suction caisson installation mechanisms

The simulated suction caisson installation in a SoC profile is compared to experimental results in order to ensure that the model features the relevant installation mechanisms. Figure 7.22 compares the calculated results of a jacked caisson installation to the experimental data presented in Ragni et al. (2020).

The numerical analysis results are obtained from a single continuous calculation and are normalised in style of the approach discussed in Ragni et al. (2020). The total shear strains are evaluated here. The results show concentrated shear zones around the skirt. This holds for each normalised penetration depths shown in Figure 7.14. The shear zones below the skirt tip extend in radial direction during the jacked penetration in sand (see Figure 7.14a and 7.14b). The zones of high total shear strains extend into the underlying clay once the skirt tip approaches the layer boundary (see Figure 7.14c and 7.14d). This indicates sand drag down into the clay layer. This is consistently observed in the experiments and numerical simulations. A curved layer boundary was found in the experiments at a relative penetration depth of $z/L = 0.9$. The layer boundary obtained from the numerical simulations remains relatively flat. However, sufficient similarity between experimental and numerical analysis results is found for the investigation on the jacked caisson penetration. Hence, the numerical model is suitable for the simulation of the jacked caisson installation in SoC profiles.

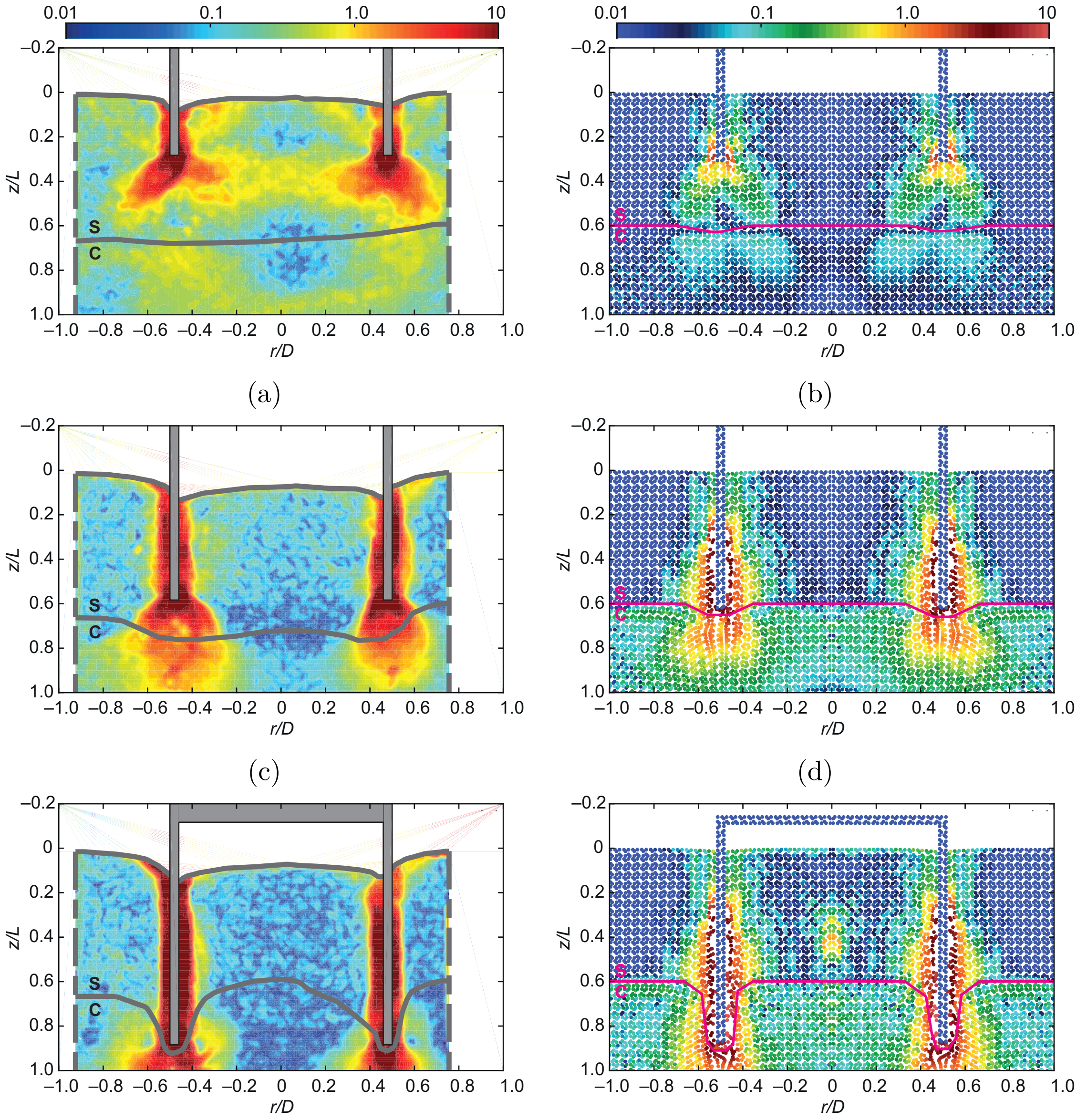

(a) (b)

(c) (d)

(e) (f)

Figure 7.14: Comparison between total shear strains (%) obtained from PIV (Ragni et al., 2020) (LHS) and axisymmetric MPM (RHS) analyses during self-weight penetration in SoC at increasing normalised penetration depths $z/L = 0.3$ (a,b), $z/L = 0.6$ (c,d), and $z/L = 0.9$ (e,f).

The simulation of the suction installation requires additional input: The caisson penetration rate $\dot{z}$ and the internal suction pressure s. A caisson penetration rate starts from $\dot{z} = 0.01\,\mathrm{m/s}$ in the beginning of the penetration in the sand top layer and reach maximum values of $\dot{z} \approx 0.08\,\mathrm{m/s}$ at the punch-through point. The penetration rates are estimated under consideration of experimental results discussed in the previous section and in Ragni et al. (2020). The corresponding internal suction and excess pressures are taken from Ragni et al. (2020). The results are presented in Figure 7.15.

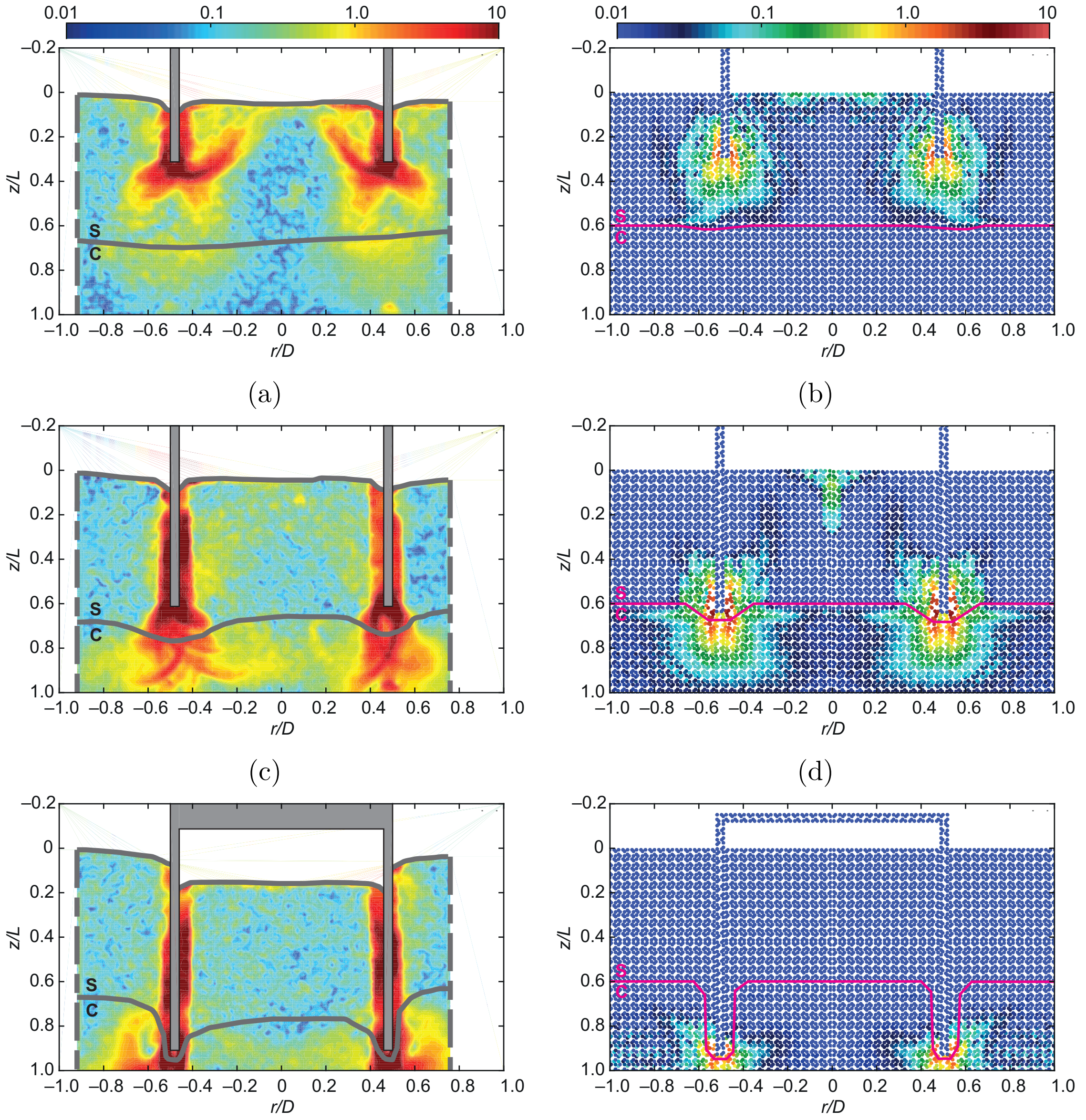

(a) (b)

(c) (d)

(e) (f)

Figure 7.15: Comparison between total shear strains (%) obtained from PIV (Ragni et al., 2020) (LHS) and axisymmetric MPM (RHS) analyses during suction installation in SoC at increasing normalised penetration depths $z/L = 0.3$ (a,b), $z/L = 0.6$ (c,d), and $z/L = 0.9$ (e,f).

The MPM analyses are conducted stepwise as the requirements differ: A fully coupled two-phase simulation is necessary until the skirt tip is embedded in the underlying clay. The numerical models are assembled analogue to the ones utilised for simulations in uniform sand. Once the caisson internal is sealed from ambient, predominately undrained soil behaviour is present during the suction caisson installation. Consequently, a one-phased undrained analysis can be performed in these cases. The results are normalised in style of the approach discussed in Ragni et al. (2020).

The results show again concentrated shear zones around the skirt. This holds for each normalised penetration depth shown in Figure 7.15. The numerically simulated shear zones are limited to a certain area at the lower part of the caisson skirt. However, the experimental results feature shear zones that envelope the entire skirt. A possible influence of the interface friction coefficient on the calculated results is ruled out through a variation of the respective model parameter. Hence, the differing generation of the shown contour plots or the stepwise calculation of the MPM model are possible explanations.

The shear zones concentrate around the skirt during jacked penetration and suction installation. This is similarly shown in the experimental and numerical results. Furthermore, no plug heave is visible in the numerical analyses. Figure 7.15e reveals plug downward movement that occurs in the experiments only. This is plausible, because no suction is required for the caisson penetration once the skirt tip reaches clay layer. The difference between Figure 7.15e and 7.15f is expected: The experiments were conducted continuously, but were evaluated stepwise. This yields a contour plot representing a certain section of the installation process. The overall soil surface shape in contrast is determined by the entire course of the experiment. The stepwise calculation also represents a certain section of the installation process, but includes the change of the soil surface shape. Thus, the calculated soil surface displacements differ from the experimental results. However, adequate similarity between experimental and numerical analysis results is found for the investigation of the suction caisson installation. Hence, the numerical model is considered to be suitable for the simulation of the suction caisson installation in SoC profiles.

Influence of the caisson aspect ratio and sand layer thickness

Section 7.1 has featured a half-model suction caisson installation test in SoC. The utilised model caisson featured an aspect ratio of $z/L = 0.5$ instead of $z/L = 1$ and a sand layer thickness of $h_{sand} = 0.5L$ instead of $h_{sand} = 0.6L$ (Ragni et al., 2020). A recalculation of this experiment and a comparison to the previously discussed results provide insights into the role of the caisson aspect ratio and the sand layer thickness. The MPM simulations are furthermore conducted continuously within a single calculation. An one-phase soil continuum is utilised as predominately undrained behaviour is expected. The caisson penetration rate is set to be $\dot{z} = 0.05\,\mathrm{m/s}$ in order to minimise the computational costs, while quasi-static conditions are maintained. The internal suction and excess pressures are applied in accordance to the experimental results discussed in Section 7.1.

Total shear strains and normalised resultant displacements are presented in Figure 7.16 in order to facilitate comparison to other numerical and experimental results. The results reveal that the calculated total shear strains extend around the entire caisson skirt, if a continuous calculation is performed. This is consistent with the experimental results discussed in Section 7.1. No major plug heave occurs, which matches the expectations as no suction pressure is required for the skirt penetration into the underlying clay.

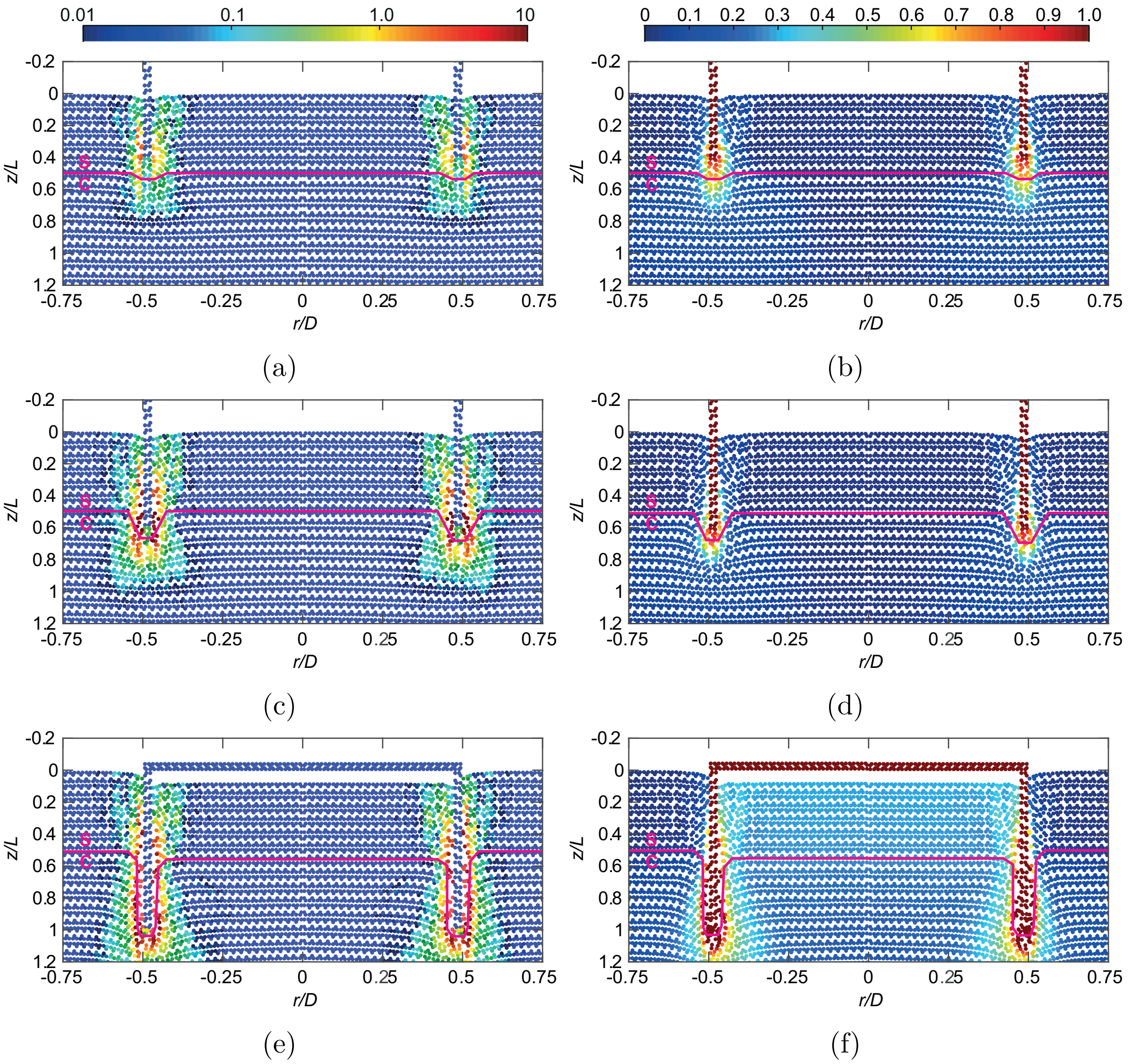

(a) (b)

(c) (d)

(e) (f)

Figure 7.16: Comparison between total shear strains (%) (LHS) and normalised resultant displacements (RHS) obtained from axisymmetric MPM analyses during the suction installation in SoC at increasing normalised penetration depths of $z/L = 0.4$ (a,b), $z/L = 0.6$ (c,d), and $z/L = 1.0$ (e,f).

A comparison between Figure 7.15 and 7.16 shows similar mechanisms underlying the suction caisson installation – independently from the respective SoC profiles and caisson dimensions. However, the suction installation mechanism in the sand top layer differs from the one in clay, because of the increased tip resistance that is mobilised in sand. Hence, the actual thickness of the top layer, the vertical load, and the caisson dimensions determine if suction assisted installation is required to penetrate through the sand layer. Furthermore, the internal suction pressure and the resulting caisson penetration rate, which are present once the skirt tip punches into the underlying clay, effect the ongoing course of the suction caisson installation.

Effect of the lid contact

It is pointed out, that Figure 7.16e and 7.16f show lid touch down and therefore compression of the soil plug. The compression is virtually restricted to the sand plug. This is consistent with the experimental results discussed in Section 7.1. Furthermore, it makes sense that the sand plug is compressed, because the extraction of water through the pumping system enables consolidation despite the assuringly undrained behaviour of the underlying clay layer. Hence, similarity between experimental and numerical results is underpinned.

Influence of the skirt wall thickness

The discussion in Section 5.2 underpinned that numerical simulations of the suction installation of a thin-walled caisson are a reasonable addition to the existing PIV analysis results featuring uniform sand profiles. The centrifuge tests investigating the caisson installation in SoC are also limited to thick-walled half-model caisson, if PIV analyses are targeted. Numerical investigations of thin-walled caissons require a significantly finer mesh compared to the one utilised for the investigations discussed above. A mesh sensitivity study was therefore conducted in advance. This study will evaluate possible mesh dependencies and aims to proof the comparability between the previous and following simulation results.

The geometry of model no. 10 including the SoC profile is meshed with a four times finer mesh compared to the one utilised in the previous simulations. The vertical element height is increased by a factor of two in order to reduce grid-crossings and therefore possible numerical instabilities. Furthermore, the top regions of the sand layer are modelled linear elastic instead of elastic-plastic in order to reduce numerical instabilities. This modified model was utilised to recalculate suction installation presented in Figure 7.16. The results are presented in Figure 7.17.

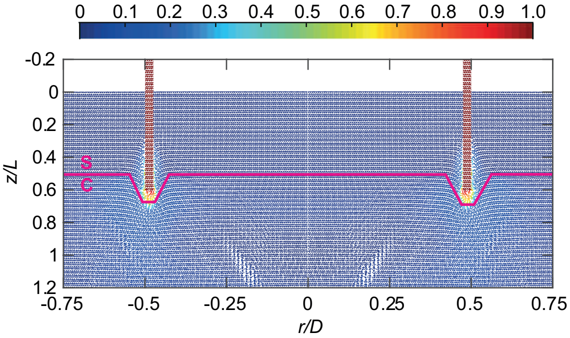

Figure 7.17: Normalised resultant displacements during the suction installation of a thick-walled caisson in SoC at a normalised penetration depths of $z/L = 0.6$ simulated with a fine mesh.

Comparing Figure 7.16d to Figure 7.17 reveals similar displacement contours. The resultant displacements concentrate around the skirt. This area extends further in radial direction, if a coarser mesh is utilised. Figure 7.16d shows settlements close to the skirt tip, whilst these are absent in Figure 7.17. However, both simulations provide displacement contours that are comparable to the experimental results discussed in Section 7.2 – i. e. locally restricted displacements occur around the skirt. Hence, no pivotal influence of the mesh dependency is expected for the following investigations.

The installation of a thin-walled caisson (see Figure 7.18) requires less suction pressure in comparison to a thick-walled caisson in general. Based on predictions conducted in accordance to Houlsby and Byrne (2005b) and Houlsby and Byrne (2005a) no additional

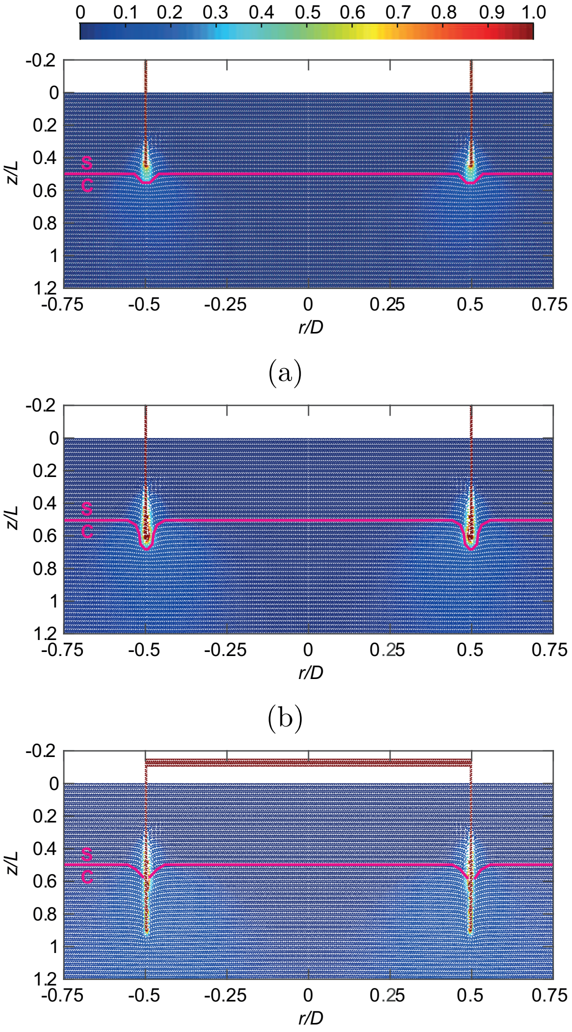

(a)

(b)

(c)

Figure 7.18: Normalised resultant displacements during the suction installation of a thin-walled caisson in SoC at a normalised penetration depths of $z/L = 0.4$ (a), $z/L = 0.6$ (b), and $z/L = 0.9$ (b).

suction would be required once the thin-walled caisson penetrated the sand layer due to its self-weight. Consequently, internal excess pressure is expected. This approach imitates a similar pumping flow rate applied in experiments. Hence, the internal pressure history was overtaken from the simulations featuring the thick-walled caisson. Hereby, the comparison between the results presented in Figure 7.18 to the previous results is facilitated.

The displacement contours resulting from the thin-walled caisson penetration presented in Figure 7.18 are similar to the ones obtained from calculations including the thick-walled caisson. Consequently, the results are also similar to the centrifuge tests. A major influence of the skirt wall thickness on the underlying installation mechanisms is not indicated by these results. However, a further investigation on the migration of sand from the top layer into the underlying clay layer is necessary, because the drag down of relatively high permeable sand could influence the drainage regime along the caisson skirt. The migration of the material points is therefore evaluated. The results are summarised in Figure 7.19 and are obtained from two numerical simulations with a fine mesh – one with a thick- and another one featuring a thin-walled skirt, respectively.

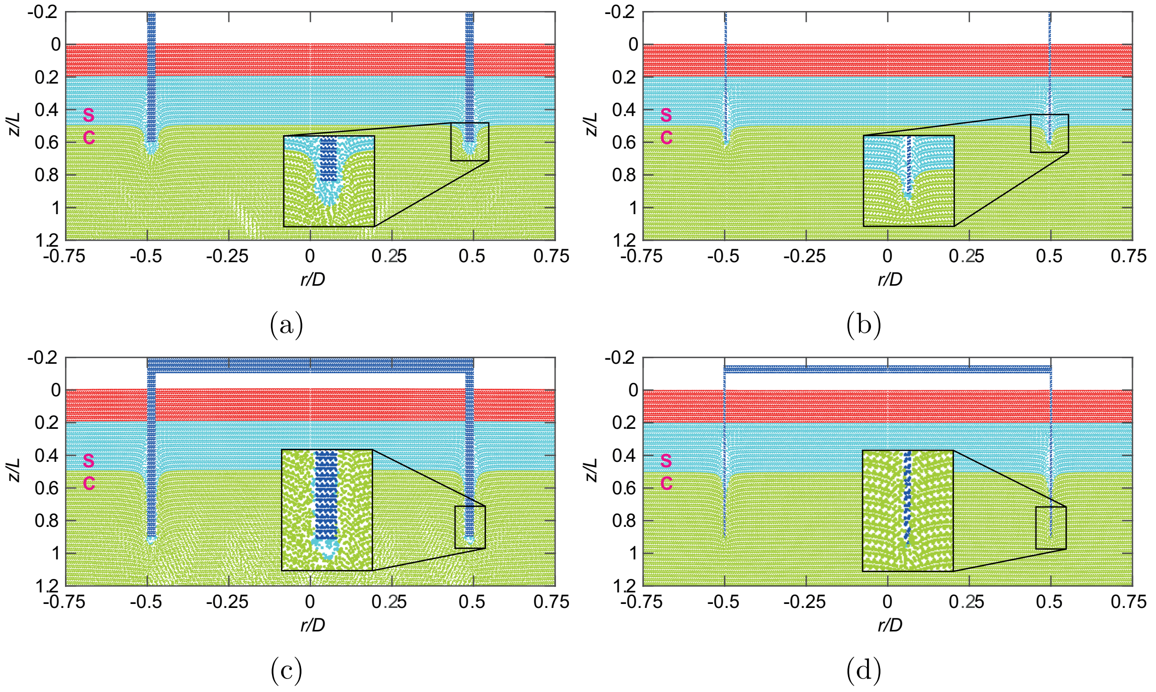

(a) (b)

(c) (d)

Figure 7.19: Soil migration during the suction installation of a thick- (LHS) and a thin-walled (RHS) caisson in SoC at a normalised penetration depths of $z/L = 0.6$ (a,b), and $z/L = 0.9$ (c,d).

The skirt tip just passed the soil layer boundary in Figure 7.19a. Sand is dragged down into the clay layer and a funnel forms around the skirt. This is consistent with observations from experiments discussed in Section 7.1 and (Ragni et al., 2020). Figure 7.19b reveals that the sand drag down also occurs in the simulation featuring a thin-walled caisson. Although, the amount of MPs – i. e. the amount of soil – that is dragged down depends on the skirt wall thickness. Figures 7.19c and 7.19d indicate that the funnel occurring at the layer boundary does not extend significantly with the course of the caisson penetration. The sand volume that is initially captivated below the skirt tip is displaced in radial direction. Almost no sand remains below the thin-walled caisson skirt tip, but a certain amount of sand remains below the thick-walled skirt tip. MPs representing the dragged down soil remain scattered around the skirt in both cases. However, the majority of the skirt that is embedded in the main layer is in contact with the clay. Hence, the presented data does not indicate the formation of a relatively high permeable sand channel around the skirt. This holds for thick- and thin-walled caisson installation analyses and is consistent with the experimental results discussed in Section 7.1.

Effect of the clay shear strength

The following MPM simulations are conducted continuously within a single calculation. A one-phase soil continuum is utilised as predominately undrained behaviour is expected. The caisson penetration rate is set to be $\dot{z} = 0.05\,\mathrm{m/s}$. The simulation of the suction installation starts from a pre-penetration of $z/L = 0.3$, which represents a possible self-weight installation without punch through into the clay layer. The self-weight penetration depths and the corresponding vertical load $V = 5.5\,\mathrm{MN}$ – estimated for the thick-walled $L = 4\,\mathrm{m}$ caisson (Houlsby and Byrne, 2005b) – are taken into account for the calculation of the required suction pressure.

Table 7.6: Input parameters for MPM simulations of the suction caisson installation in SoC profiles featuring varying undrained clay shear strengths.

Model no.	L (m)	s_u (kPa)	$s/(\gamma' D)_{max}$ (-)
20	4	60	0.0
20	4	90	0.99
30	8	60	0.95

Model 20 is employed for investigations on the undrained clay shear strength. The soil profile consists of a sand layer with a thickness of $h_{sand} = 0.5L$ on top of the clay main layer. Two different uniform undrained strength s_u profiles are investigated. An increased undrained shear strength yields larger penetration resistance and therefore alters the required suction pressure. The normalised suction pressure $s/\gamma' D$ that is required for full caisson penetration $z/L = 1$ is listed in Table 7.6 for each analysis. The given values are calculated in accordance to the procedure outlined by Houlsby and Byrne (2005a). The specific weight of the clay is $\gamma' = 7.1\,\mathrm{kN/m^2}$. The adhesion factors of $\alpha_o = \alpha_i = 0.4$ were estimated from the experimental results presented in Section 7.1. The bearing capacity factors of $N_c = 10.5$ and $N_q = 1$ were utilised for undrained conditions.

The results presented in Figure 7.20 add to the previously discussed simulations shown in Figure 7.16. Hence, data for three different shear strengths – $s_u = \{22, 60, 90\}\,\mathrm{kPa}$ – is discussed. It is noted that the contour plots visualised in Figure 7.20 are amplified in order to emphasise differences between the simulations involving $s_u = 60\,\mathrm{kPa}$ and $s_u = 90\,\mathrm{kPa}$, respectively. Similarity of the underlying mechanism is found in all three simulations.

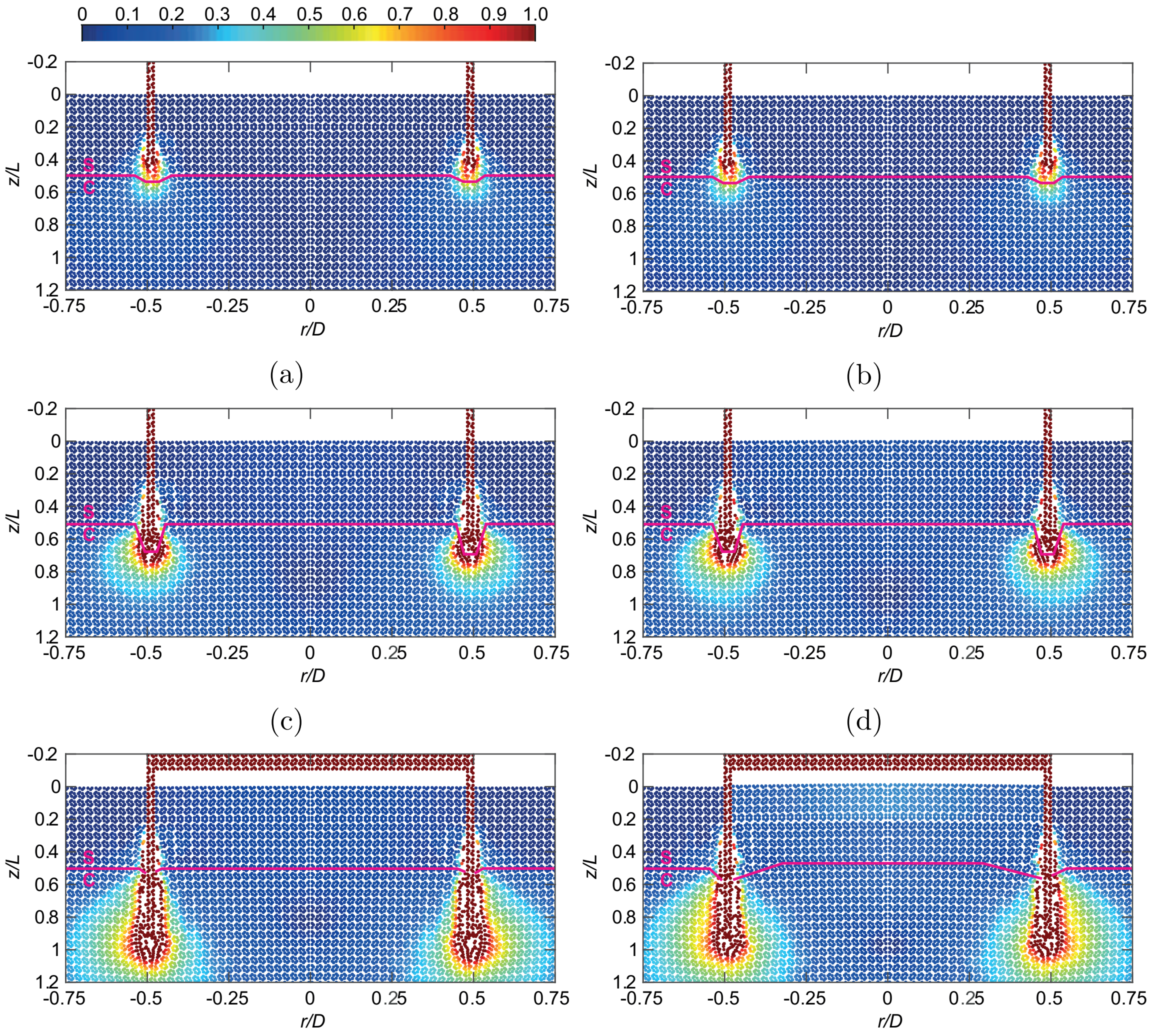

(a) (b)

(c) (d)

(e) (f)

Figure 7.20: Normalised resultant displacements during the suction caisson installation in $s_u = 60\,\text{kPa}$ (LHS) and $s_u = 90\,\text{kPa}$ (RHS) clay overlying sand at a normalised penetration depths of $z/L = 0.4$ (a,b), $z/L = 0.6$ (c,d), and $z/L = 0.9$ (e,f).

The requirement of suction pressure for the installation of the caisson in $s_u = 90\,\text{kPa}$ clay is expectedly influencing the soil plug state. Plug heave is visible in Figure 7.20f, which contrasts the numerical analysis results shown in Figure 7.20e. Hence, the presented MPM analysis results emphasise that the undrained shear strength and therefore the application of suction pressure indeed effects the suction caisson installation in SoC profiles.

This effect is expected to be enhanced, if a caisson with a larger aspect ratio is installed. The suction installation of a caisson with an incidental diameter, but an aspect ratio of $L/D = 1$ is therefore simulated. The results obtained from model 30 are summarised in Figure 7.21. Figure 7.20e and Figure 7.21a show the same absolute penetration depths of the caisson in soil with a similar penetration resistance. However, notable plug heave occurred during the installation of the $L/D = 1$ caisson due to the presence of linearly

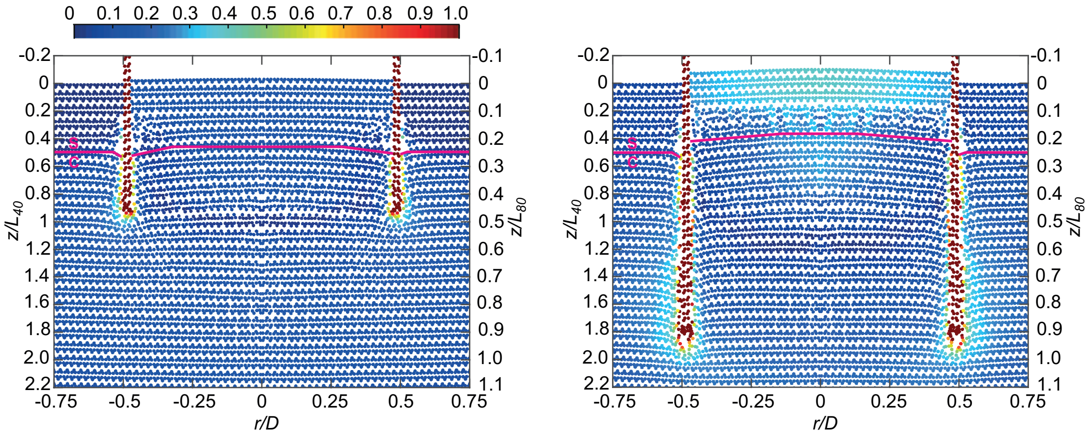

(a) (b)

Figure 7.21: Normalised resultant displacements during the suction installation of a $L = 8\,\mathrm{m}$ caisson in $s_u = 90\,\mathrm{kPa}$ clay overlying sand at a normalised penetration depths of $z/L = 0.45$ (a), and $z/L = 0.9$.

increasing suction pressure. The plug heave continues with the course of the caisson skirt penetration. This is plausible, because the suction pressure is eventually transferred to the clay plug. Clay plug heave results, if the suction pressure at soil layer boundary exceeds the clay plug weight. This is expected to occur once a normalised penetration depth of $z/L_{80} = 0.5$ and a corresponding normalised suction pressure of $s = 0.32$ is reached. Hence, the presented results are plausible. It is concluded that plug heave potentially occurs during the suction installation in SoC profiles featuring shear strength profiles that exceed the existing experimental data base discussed in Section 7.1.

7.2.2.2 Clay over sand

Suction installation mechanism

The simulated suction caisson installation in a CoS profile is compared to experimental results with the purpose to ensure that the model features the relevant installation mechanisms. Figure 7.22 shows the calculated results of a jacked caisson installation and the corresponding experimental data presented in Ragni et al. (2020).

The numerical analysis results are obtained stepwise and are normalised in style of the approach discussed in Ragni et al. (2020). The calculated results show a separated penetration mechanism at shallow penetration depths within the clay layer. This is similar to the experiments, which are also shown in Figure 7.22. An almost combined mechanism is present from a penetration depth of $z/L = 0.3$ in the experimental and the simulated results. The experimental and the simulated results show no significant plug heave during the course of the jacked caisson penetration. It is noted that the area of large displacements at the skirt tip spreads out wider in the numerical simulations compared to the

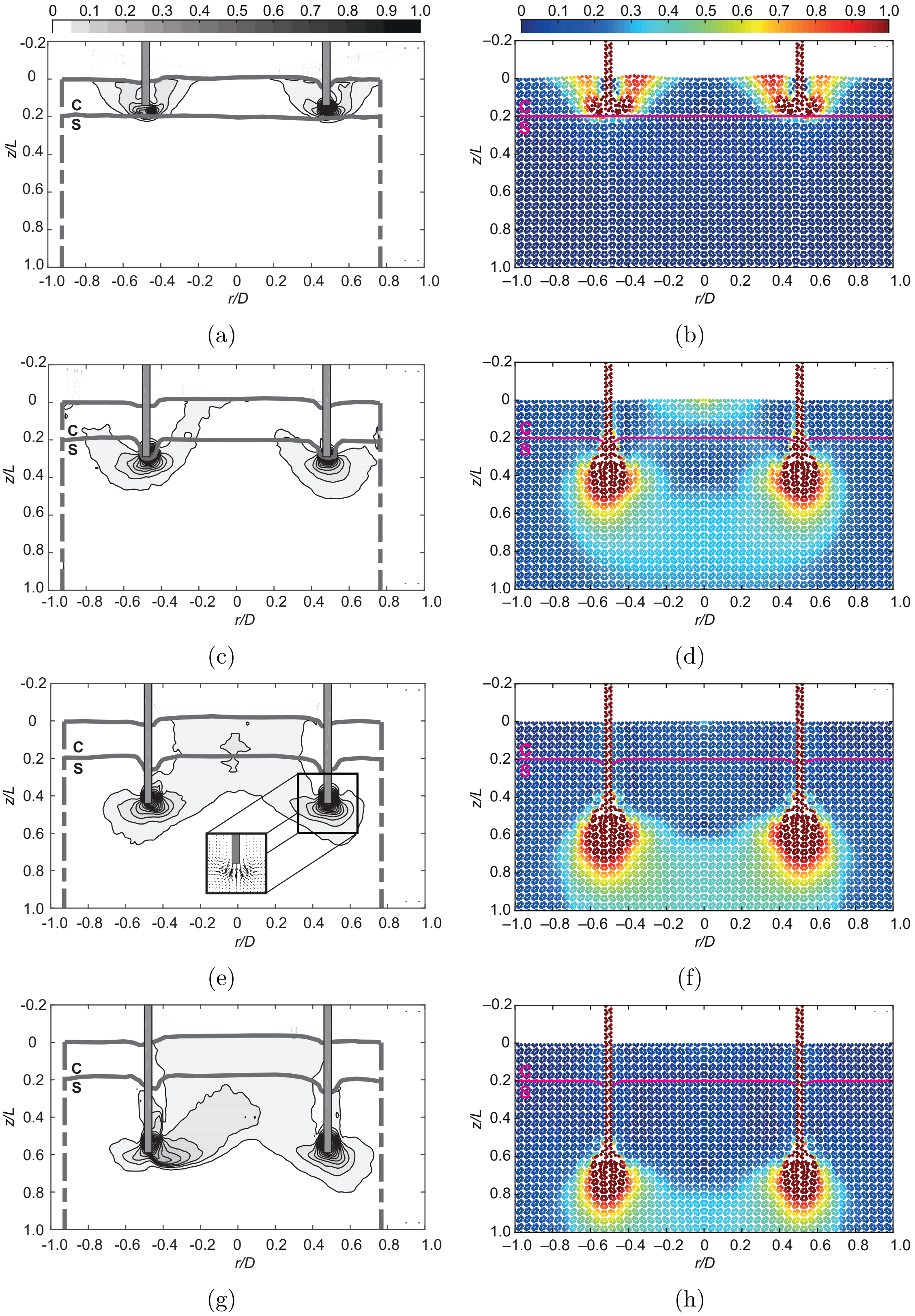

Figure 7.22: Comparison between normalised resultant displacements during self-weight penetration in CoS obtained from PIV (Ragni et al., 2020) (LHS) and axisymmetric MPM (RHS) analyses at increasing normalised penetration depths $z/L = 0.15$ (a,b); $z/L = 0.30$ (c,d); $z/L = 0.45$ (e,f); $z/L = 0.60$ (g,h).

experiments. This is plausible, since the sand that is penetrated by the skirt tip has the same constitutive model parameters like the uniform sand profile discussed in Section 5.2.

It is summarised that the key mechanism underlying the jacked installation in a CoS profile is similar in the experiments and the numerical simulations. Hence, the numerical model is considered to be suitable for the simulation of the jacked caisson installation.

The simulation of the suction installation requires additional input: the caisson penetration rate $\dot{z}$ and the internal suction pressure s. A caisson penetration rate of $\dot{z} = 0.01\,\mathrm{m/s}$ is assumed based on the experiments presented in previous section. The corresponding suction pressures presented in Figure 7.23 are calculated from the history of applied suction discussed in Ragni et al. (2020).

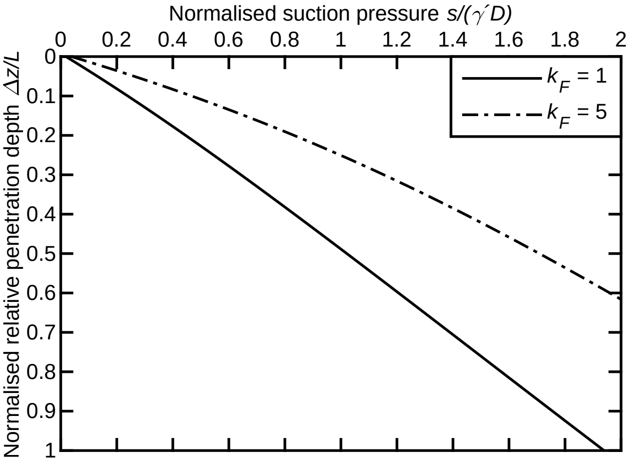

Figure 7.23: Calculated history of the required suction pressure for the installation of a thick-walled $L = D = 5\,\mathrm{m}$ caisson in CoS (Houlsby and Byrne, 2005b; Ragni et al., 2020).

An enveloping lower and upper bound is found through the variation of k_F, while the calculations followed the procedure presented in Houlsby and Byrne (2005b). It is noted that the resulting suction pressure is increased by a factor of $f = 1.9$ in order to account for the indirect application of the suction pressure due to the transferral through the clay plug. The history of required suction pressure presented in Figure 7.23 is normalised by the effective specific density of the sand $\gamma' = 10.5\,\mathrm{kN/m^3}$ and the caisson diameter $D = 5\,\mathrm{m}$.

The calculated results presented in Figure 7.24 show the uplift of the whole clay plug. This yields an inverted V-shaped deformation mechanism in the underlying sand. Similarity is found between the experimentally and numerically obtained resultant displacement contours. However, imperfections and the occurrence of a separation of the clay plug are not considered in the numerical model. The rotation of the soil plug therefore does not occur in the numerical simulation. However, the pivotal mechanisms of the suction caisson installation – i. e. the transferral of suction pressure inducing sand plug heave – are reproduced by the numerical model featuring the CoS profile.

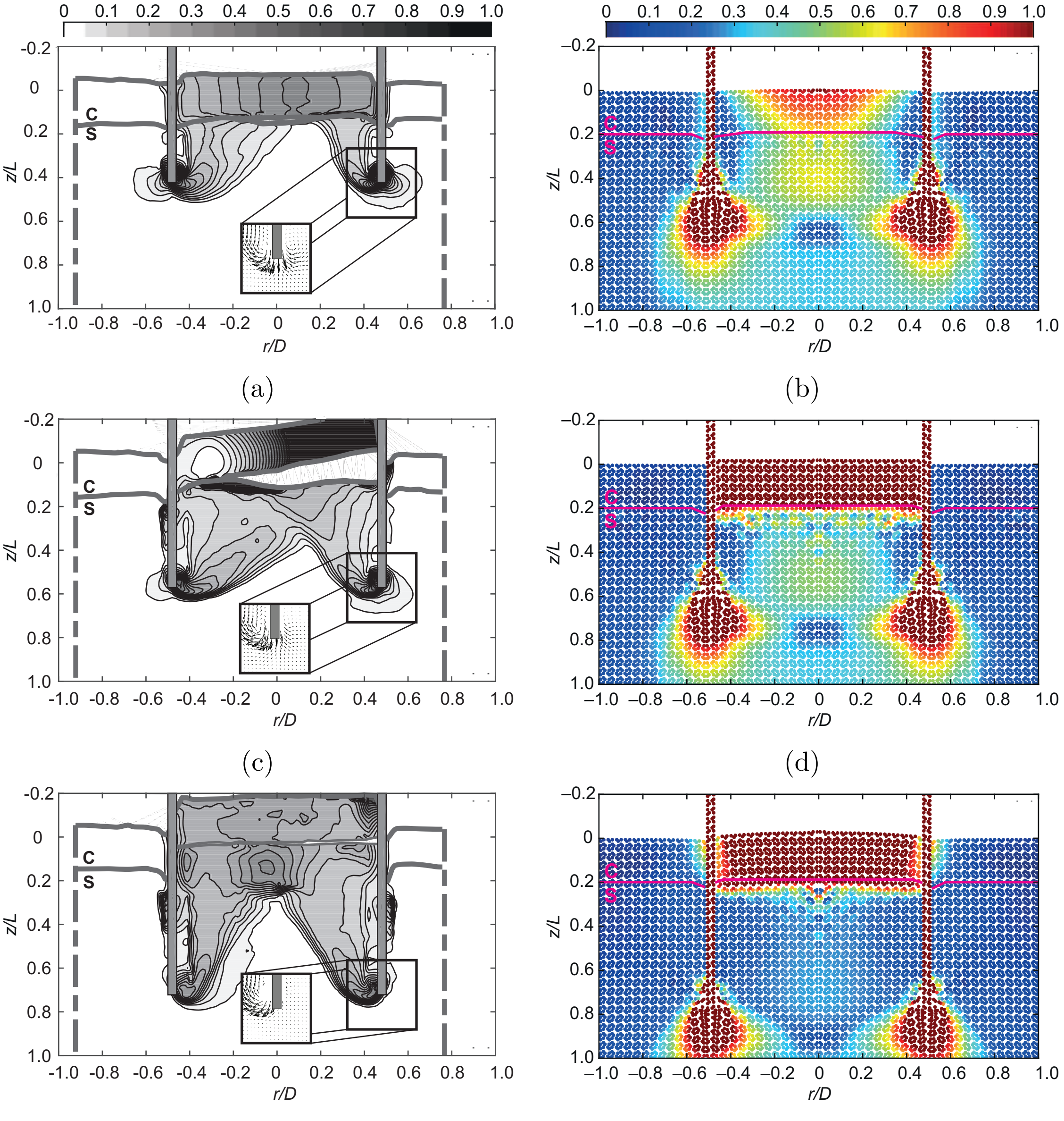

(a) (b)

(c) (d)

(e) (f)

Figure 7.24: Comparison between normalised resultant displacements during suction installation in CoS obtained from PIV (Ragni et al., 2020) (LHS) and axisymmetric MPM (RHS) analyses at increasing normalised penetration depths $z/L = 0.30$ (a,b), $z/L = 0.45$ (c,d), and $z/L = 0.75$ (e,f).

Influence of the skirt wall thickness

The discussion in Section 5.2 underpinned that numerical simulations of the suction installation of a thin-walled caisson are a reasonable addition to the existing centrifuge experiments. A mesh sensitivity study was conducted in order to evaluate an effect on the overall solution: The geometry of model no. 10 including the CoS profile is meshed with a four times finer mesh compared to the one utilised in the previous simulations. The vertical element height is increased by two in order to reduce grid-crossings and therefore possible numerical instabilities. This modified model was utilised to recalculate suction installation. A comparison between Figure 7.24b and Figure 7.25 reveals a similarly shaped mechanism. The clay plug uplift and the extend of deformations at the skirt tip is increased, but the sand plug heave appears to be similar. Thus, a certain mesh dependency is expectedly present as the investigated mechanism involves local shearing failure. However, both simulations overall yield displacement contours that are comparable to the experimental results – i. e. plug heave is occurring to a considerable extend in both calculations. Hence, mesh dependency is assumed to be negligible for the following investigations.

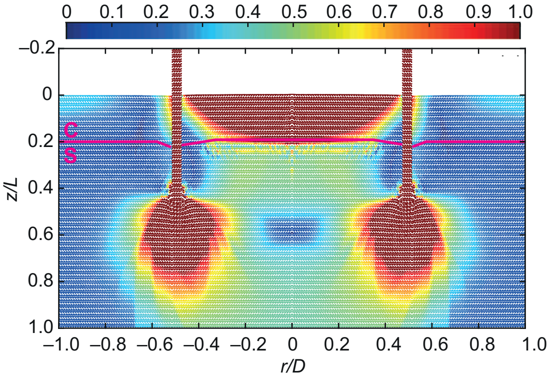

Figure 7.25: Normalised resultant displacements during the suction installation of a thick-walled caisson in CoS at a normalised penetration depths of $z/L = 0.45$ simulated with a fine mesh.

The installation of a thin-walled caisson requires less suction pressure in comparison to the previously investigated thick-walled caisson. Hence, the required suction pressure was re-calculated (Houlsby and Byrne, 2005b). The results are summarised in Figure 7.26 and are employed to apply the differential pressure to the MPM model. The caisson penetration rate from the previous analysis was maintained in order to ensure comparability.

The normalised resultant displacements around the skirt tip, which are visible in Figure 7.27, are similarly shaped to the ones observed in simulations with the thick-walled caisson. However, the displacements of the plug are significantly smaller compared to the ones illustrated in Figure 7.24b and 7.24d. This is plausible, because only approximately 1/8 of the soil volume is displaced during the course of the thin-walled caisson penetration. Additionally, less suction pressure is applied. The mechanisms underlying the suction installation in the CoS profile – i. e. the clay plug uplift inducing suction pressure in the underlying sand – are found to be present in the simulation featuring the thin-walled caisson. Hence, predominately inwards directed soil displacement, sand plug heave as well as a certain influence of the skirt friction are occurring independently from the skirt wall thickness. The only distinction that is found here is the extend of the plug heave due to soil displacement. Thus, the results obtained from the numerical analyses reinforce the validity of the half-model centrifuge test results presented in Ragni et al. (2020).

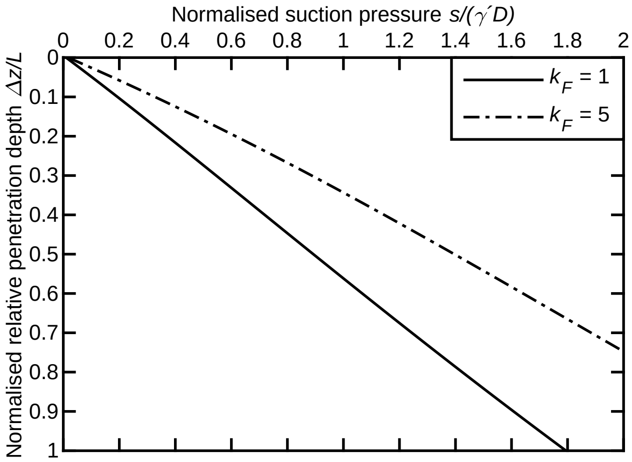

Figure 7.26: Calculated history of suction pressure during the suction installation of a thin-walled caisson in CoS (Houlsby and Byrne, 2005b).

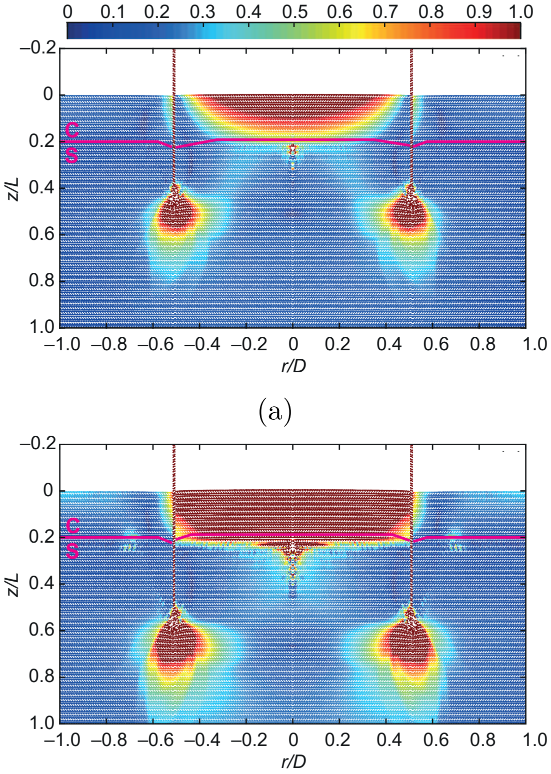

(a)

(b)

Figure 7.27: Normalised resultant displacements during the suction installation of a thin-walled caisson in CoS at a normalised penetration depths of $z/L = 0.45$ (a) and $z/L = 0.6$ (b).

Influence of the caisson aspect ratio and the clay layer thickness

The investigations of the role of the caisson aspect ratio and the clay layer thickness are combined, because of the interdependence between the clay layer thickness h_{clay} and the skirt length L. The numerical model no. 20 featuring two different clay layer thicknesses – $h_{clay} = 0.25L$ and $h_{clay} = 0.5L$ – is utilised. The upper and lower bound of the required suction pressure are back calculated under consideration of measurements from the centrifuge tests discussed in Section 7.1 and in accordance to the procedure described in Houlsby and Byrne (2005b). The results are presented in Figure 7.28.

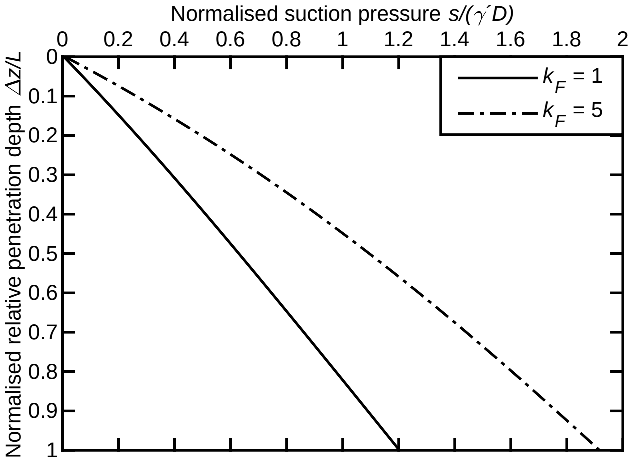

Figure 7.28: Calculated history of suction pressure during the installation of a thick-walled $D = 8\,\mathrm{m}$ and $L = 4\,\mathrm{m}$ caisson in CoS (Houlsby and Byrne, 2005b).

Figure 7.24b and 7.29a and Figure 7.24d and 7.29c feature the same absolute skirt penetration depth of $L = 2.25\,\mathrm{m}$ and $L = 3\,\mathrm{m}$, respectively. The contour plots show similar resultant displacements at both investigated penetration depths. The inverted V-shape is visible in all four plots. The inclination of the displacement contours is furthermore similar. The clay plug uplift concentrates in the middle at first and becomes more uniform with increasing penetration depth, which occurs independently from the caisson diameter. However, increased resultant displacements of the sand plug result from the more confined environment inside the smaller diameter caisson utilised in model no. 10. It is noted that the discussed numerical simulations do not indicate a significant influence of the caisson aspect ratio on the mechanisms underlying the suction caisson installation in a CoS profile.

The results presented in Figure 7.29b and 7.29d are calculated with the same boundary conditions utilised for previous analyses, but the thickness of the clay layer h_{clay} was doubled. The displacement contours show that clay plug uplift occurs at a similar magnitude, but the sand plug heave differs – especially at $z/L = 0.6$. A steeper and predominantly independent displacement mechanism is visible below the clay layer in Figure 7.29d. In contrast, Figure 7.29c reveals a united uplift mechanism inside the caisson. This behaviour is in line with the differing mechanisms at shallow and deeper skirt penetration states in

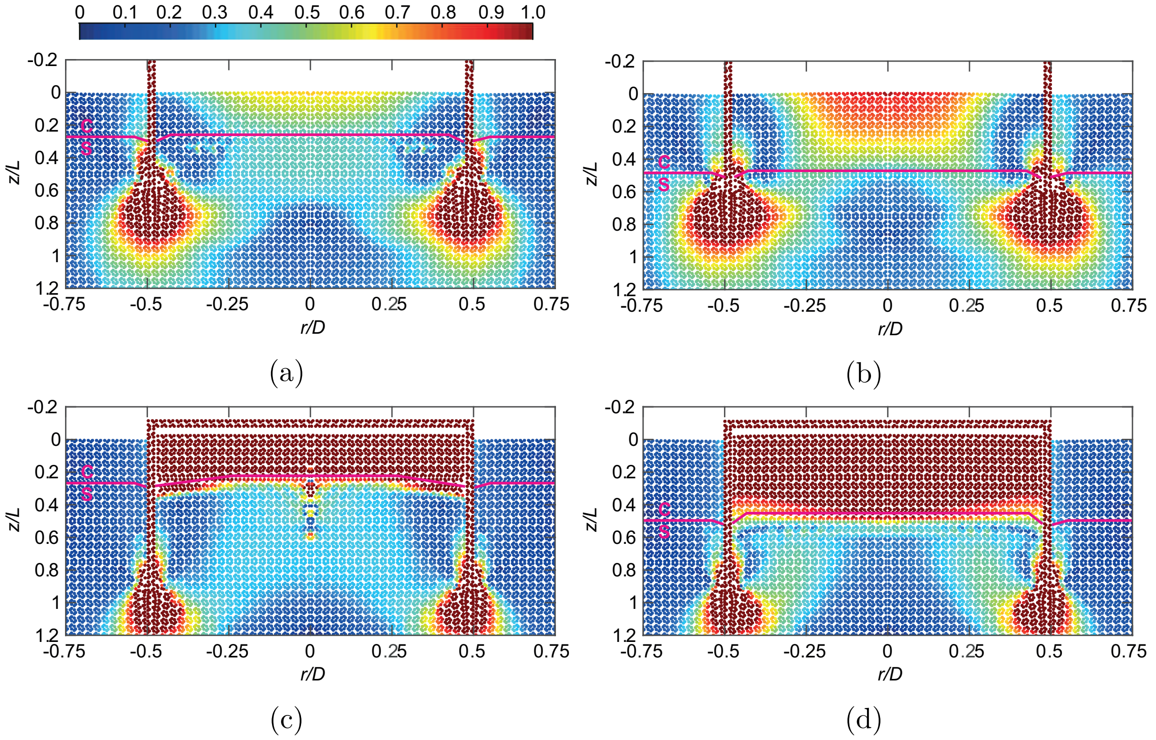

Figure 7.29: Normalised resultant displacements during the suction installation of a thick-walled caisson in CoS at a normalised penetration depths of $z/L = 0.6$ (a,b) and $z/L = 0.9$ (c,d) and clay layer thicknesses of $h_{clay} = 0.25L$ (LHS) and $h_{clay} = 0.5L$(RHS).

uniform sand discussed in Section 5.2. Hence, the shape of the resultant displacement mechanism of the sand in a CoS profile depends on the current penetration depth of the skirt tip in the sand layer. Consequently, the numerical analyses show that the shape and extend of the sand plug heave depend on the ratio of the clay layer thickness and the caisson skirt length h_{clay}/L in CoS profiles.

Effect of the lid contact

The establishment of lid contact and therefore pressure transferral through the caisson lid invert is expected to have an influence on the overall load bearing behaviour. Figure 7.30 shows a comparison between the soil plug state before and after lid touch down. The suction installation stage illustrated in Figure 7.30a shows distinct clay plug uplift and a certain amount of sand plug heave while the caisson skirt penetrates into the sand layer. The clay plug heave is reversed to a certain extend once the lid touches down (see Figure 7.30b).

Based on the presented numerical simulation it is found that the clay plug and sand plug heave is partially reversible in a CoS profile. The plug uplift is reversed as soon as the

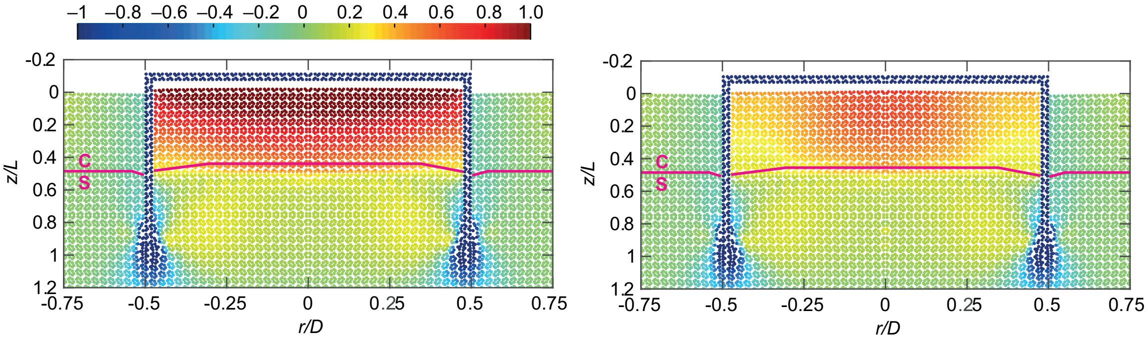

(a) (b)

Figure 7.30: Normalised vertical displacements during the suction installation of a thick-walled caisson in CoS at a normalised penetration depths of $z/L = 0.9$ (a) and $z/L = 0.95$ (b).

top of the clay layer is in contact with the downward moving lid invert. The clay plug transfers compressive stresses into the underlying sand as undrained short term response is expected. Thus, the suction pressure transferral into the underlying sand suddenly terminates. Hence, the reduction of the tip resistance due to seepage flow expires and skirt tip load bearing commences. This is indicated by the ongoing vertical displacements at the skirt tips visible Figure 7.30b. The relatively stiff tip response, which will be further discussed in chapter 8, leaves compressive stresses to be transferred though the caisson lid. Consequently, the numerical simulation results indicate that only partially reversion of the plug heave can be expected for suction caissons installed in CoS profiles.

It is noted that the findings imply that the simulated clay plug remains intact – i. e. no clay plug rotation occurs and no flow channels form. However, even these events are expected to be partially reversible, if the lid touches down and compresses the soil plug within the confinement of the skirt. It is noted that clay plug rotation and the formation of flow channels can yield excessive sand plug heave, which eventually leads to premature refusal.

7.2.3 Remarks on the numerical simulations

The MPM model for the simulation of the self-weight or jacked penetration and the suction installation of a caisson is extended toward layered soil profiles. The model is verified through the comparison to existing results obtained from centrifuge tests. The numerical model visualises the underlying mechanisms and enabled further investigations on the influence of the t/D and L/D ratio and therefore the skirt wall thickness and the diameter. This allowed the re-evaluation of the centrifuge test and underpins the universal validity of the existing experiments. Furthermore, investigations on the clay shear strength in SoC profiles, the influence of varying top layer thickness and the effect of the lid contact add to the existing knowledge.

7.3 Concluding remarks on the suction caisson installation in layered soil

This chapter discussed results of a series of centrifuge tests and numerical simulations of suction caisson installation in layered soil profiles. The suction caisson installation was investigated by the means of PIV post analyses of images acquired in the centrifuge test. The numerical simulations featured the extension of the MPM model towards SoC and CoS profiles. It was employed for additional investigations on the self-weight and suction installation mechanisms.

The experimental and numerical investigations featuring SoC profiles support the following findings:

(1) Suction caisson installation is unproblematic as expected – even in stiff clay. Furthermore, no evidence of a permanent effect on the behaviour found as the soil plug was shown to be compressed through lid contact.

(2) A MPM model that enables the simulation of the jacked and suction assisted caisson installation in SoC is established and validated through the back calculation of centrifuge experiments.

(3) The mechanisms underlying the suction caisson installation in SoC profiles occur independently from the L/D and t/D ratio. The self-weight and the suction pressure that is present when the skirt tip approaches the layer boundary determines the post installation soil plug state.

(4) Significant suction pressures yielding plug heave are required if the L/D ratio and the undrained clay shear strength increase. The plug heave is found to be reversible, if lid touch down is established.

(5) Sand drag down into the underlying clay is observed independently from the t/D ratio. Although, no high permeable sand channel is established – especially not for $t/D \leq 1/160$.

The presented study encourages the utilisation of suction caisson foundations for OWTs located at sites that feature SoC profiles. The presented data points out that the suction caisson installation is feasible – even in high shear strength clay underlying dense sand. Possible effects of the installation are expected to be marginal, because potentially occurring plug heave is found to be reversible.

The experimental and numerical investigations featuring CoS profiles support the following findings:

(1) Suction caisson installation is feasible, with clay plug uplift transferring suction pressure to the underlying sand. The induced seepage reduces the tip resistance and thus enables further penetration. A permanent effect of the installation on the response under vertical cyclic loading was not found. Lid touch down was reliably achieved in the experimental investigations.

(2) The implemented MPM model enables the simulation of the jacked and suction assisted caisson installation in CoS. The numerical model is validated through the back calculation of centrifuge experiments.

(3) A smaller t/D ratio does not change the underlying mechanisms, which are present during the suction caisson installation. Although, the installation of a caisson featuring a reduced t/D ratio requires less suction pressure and therefore the clay plug is lifted at larger penetration depths and the resulting sand plug heave is reduced.

(4) A higher L/D ratio implies more plug confinement and therefore favours plug heave. It is furthermore confirmed that the plug lift depends on the h_{sand}/L ratio.

(5) The plug heave is found to be only partially reversible – even if lid contact is established.

The presented study underpins the feasibility of the suction caisson installation in CoS profiles. The clay plug uplift, which introduces seepage flow in the underlying sand, is identified as the key mechanism. Therefore, skirt tip penetration is found to be feasible even in dense sand overlying by stiff clay.

8 Load bearing behaviour in layered soil

This chapter features investigations of the suction caisson installation in layered soil profiles. The results of two parallel series of centrifuge tests (CoS and SoC) and numerical analyses are discussed. The investigations target the load transfer mechanisms underlying the response to vertical cyclic loading of the suction caissons in layered soil.

8.1 Centrifuge tests

8.1.1 Experimental arrangement and testing procedure

The experiments were performed at 100g in the Acutronic Model 661 centrifuge (Randolph et al., 1991; Randolph and Gaudin, 2017) at UWA. These tests had the following requirements to ensure a realistic stress state during the model scale experiments.

- Caisson installation at stress levels representative for prototype scale was required. Thus, the caisson had to be suspended just above the sand surface until the centrifuge had reached the target acceleration.
- The installation was to be done in a controlled manner to ensure reproducible conditions for each cyclic loading test.
- The cyclic loading was to be performed without stoppage of the centrifuge to retain the soil stress state resulting from the suction installation.
- CPTs and T-bar tests were to be performed before and after the caisson tests to characterise the soil samples itself and to confirm uniformity of each sample.

The caisson models, the test arrangement, the instrumentation, and the soil sample characterisation are described in Section 7.1. Details of the centrifuge set-up are also presented in Appendix B.4. The testing programme is summarised in Table 7.3 presented in the previous chapter.

The cyclic loading histories applied in this series of tests were selected to represent loading on a windward caisson a jacket supporting an 8 MW OWT in approximately 40 m of water. They also facilitate comparison to previous tests performed in uniform sand. LC 10 featured the same cyclic loading history applied in previous tests performed in Baskarp sand (Bienen et al., 2018a; Bienen et al., 2018b) and fine silica sand (see Chapter 5). LC 20 and 30 feature the same average load, but the cyclic loading amplitude was reduced by 25 % and 50 %. The average load was shifted further into compression in LC 11 and 21 compared to the related LC 10 and 20, respectively. LC 11 in this study corresponds to

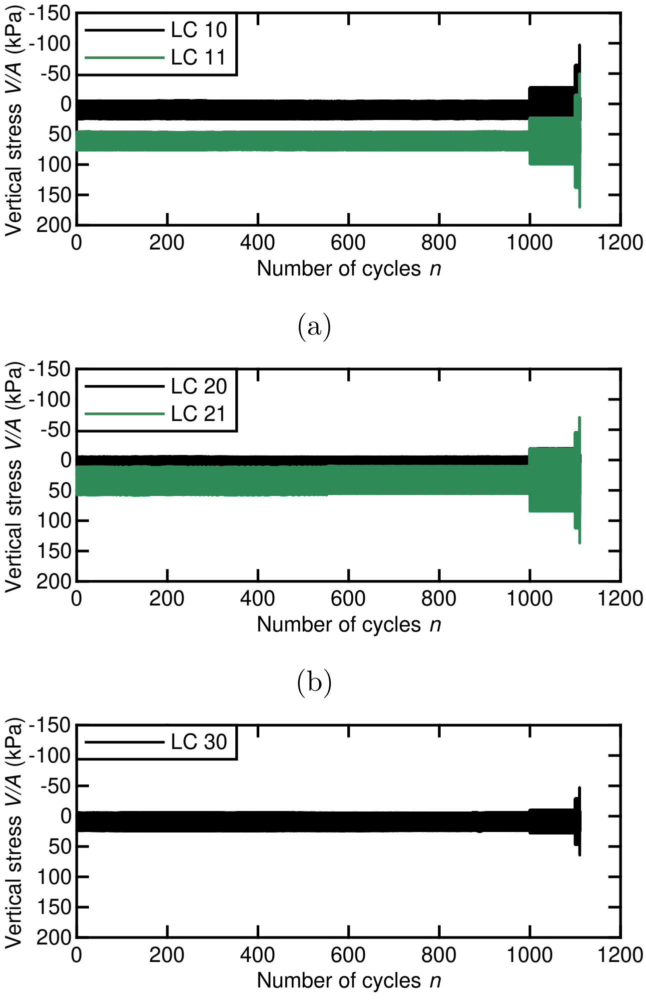

(a)

(b)

(c)

Figure 8.1: History of four vertical cyclic loading sequences in LC 10 & 11 (a), 20 & 21 (b), and 30 (c).

LC 9 in Bienen et al. (2018a) and Bienen et al. (2018b). Without stoppage of the centrifuge in order to retain the soil stress state resulting from the suction installation, loading was applied to the suction caisson as shown in Figure 8.1 and Table 8.1.

(1) A waiting period was maintained to ensure that the suction pressure inside the caisson dissipated before loading commenced.

(2) The self-weight was increased to $V = 585\,\mathrm{N}$ in model scale ($V/A = 116\,\mathrm{kPa}$). This represented the full self-weight of the jacket and the superstructure of the OWT – including tower, nacelle, and rotor – applied to the caisson. This vertical load was maintained until the excess pore pressure at the lid invert dissipated and no further settlements were observed.

(3) The vertical load was reduced to the average vertical load given in Table 8.1. This represents the average vertical load assumed at the windward caisson of a jacket.

(4) The average vertical load was maintained throughout the entire cyclic loading test. The cyclic loads were applied in packages of four sequences, each with a constant cyclic amplitude. The respective load amplitudes and the number of cycles per sequence are shown in Table 8.1. At least six load packages, i.e. a minimum of $n = 6666$ load cycles, were applied in each test (Table 8.1).

(5) Following cyclic loading, the average load was maintained until the pore pressures reached the hydrostatic pressure. Displacement controlled extraction commenced. The three way valve vented to ambient to ensure drained conditions at an uplift rate of $\dot{z}_{ext} = -0.001\,\mathrm{mm/s}$. The caisson was then sealed again for rapid extraction, which was conducted at an uplift rate of $\dot{z}_{ext} = -0.1\,\mathrm{mm/s}$.

Table 8.1: Load cases and specifications of the four respective cyclic loading sequences.

LC	Sequence number	1	2	3	4
	Number of cycles n (-)	1000	100	10	1
10	Load amplitude V (N)	40 ± 80	40 ± 200	40 ± 400	40 ± 600
	Stress amplitude V/A (kPa)	8 ± 16	8 ± 40	8 ± 80	8 ± 120
	Number of cycles n (-)	1000	100	10	1
11	Load amplitude V (N)	300 ± 80	300 ± 200	300 ± 400	300 ± 600
	Stress amplitude V/A (kPa)	60 ± 16	60 ± 40	60 ± 80	60 ± 120
	Number of cycles n (-)	1000	100	10	1
20	Load amplitude V (N)	40 ± 80	40 ± 150	40 ± 300	40 ± 450
	Stress amplitude V/A (kPa)	8 ± 16	8 ± 30	8 ± 60	8 ± 90
	Number of cycles n (-)	1000	100	10	1
21	Load amplitude V (N)	160 ± 120	160 ± 270	160 ± 420	160 ± 570
	Stress amplitude V/A (kPa)	32 ± 24	32 ± 54	32 ± 84	32 ± 114
	Number of cycles n (-)	1000	100	10	1
30	Load amplitude V (N)	40 ± 80	40 ± 100	40 ± 200	40 ± 300
	Stress amplitude V/A (kPa)	8 ± 16	8 ± 20	8 ± 40	8 ± 60

The cyclic loads were applied at a loading frequency of $f = 0.5\,\mathrm{Hz}$ and with regular sinusoidal amplitude. Loading due to wind, waves, and current in a natural environment is expected to be highly irregular. However, the regular loading scheme was conceived to represent realistic drainage conditions in a reproducible manner. In addition, this approach facilitates the evaluation of each load sequence and comparison between tests.

8.1.2 Results and discussion: sand over clay

8.1.2.1 Tensile limiting capacities

The extraction test results presented in Figure 8.2a show drained extraction capacities of $V/A \approx 25\,\mathrm{kPa}$ for an aspect ratio of $L/D = 0.5$ and $V/A \approx 65\,\mathrm{kPa}$ for an aspect ratio of $L/D = 1$. This is consistent with predictions of $(V/A)_{40} = 25\,\mathrm{kPa}$ and $(V/A)_{80} = 65\,\mathrm{kPa}$

calculated in accordance with Houlsby et al. (2005) and the soil parameters given in Table 7.1 and 7.2. In addition, the external and internal friction coefficient $(K\tan(\delta))_o = (K\tan(\delta))_i = 0.15$ and the adhesion factors $\alpha_o = \alpha_i = 0.4$ are taken into account.

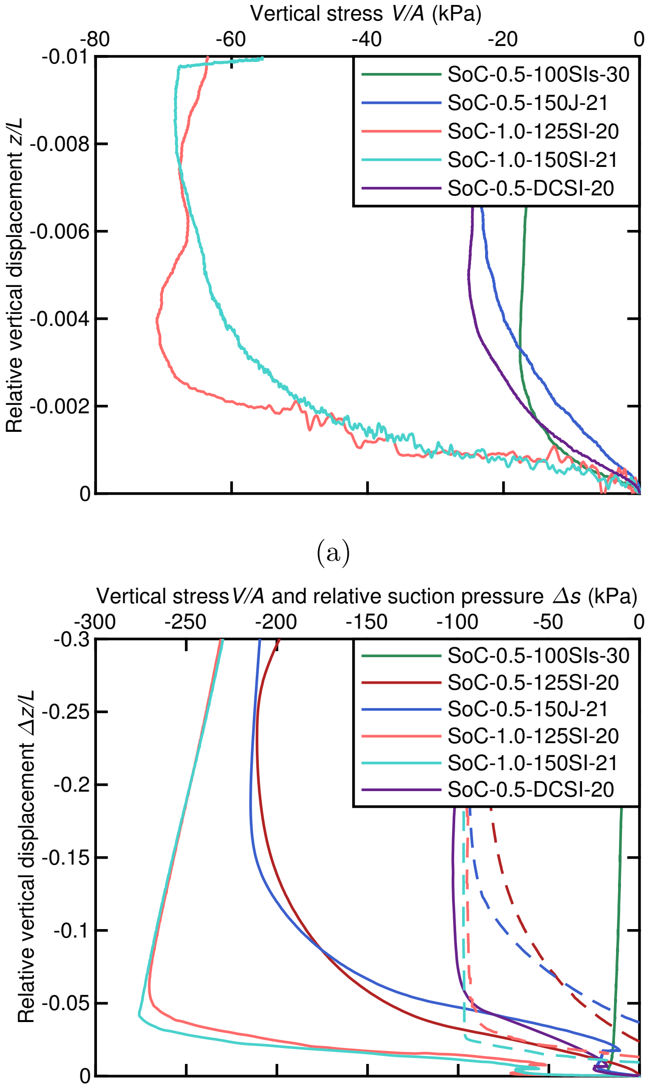

(a)

(b)

Figure 8.2: Drained (a), rapid (b) extraction resistance (solid lines), and relative suction pressure (dashed lines) in SoC profiles.

An uplift displacement of $z/L = 0.006$ was required to completely mobilise the extraction capacity in SoC, which is larger than in uniform sand profiles. The drained extraction tests were conducted after cyclic loading tests with different loading amplitudes and different number of cycles and the drained extraction capacities are approximately two times larger than the values obtained from tests in uniform fine silica sand profiles discussed in Section 6.1 and in Bienen et al. (2018a).

The rapid extraction of test SoC-0.5-125SI-20 and test SoC-0.5-150J-21, performed after drained extraction, show similar results (Figure 8.2b). Hence, the preceding drained extraction is deemed not to affect the capacity mobilised during rapid extraction.

Figure 8.2b shows capacities and mobilisation distances in response to rapid extraction in SoC, which are similar to those in uniform sand as cavitation limits the uplift capacity. The caissons in tests SoC-1.0-125SI-20 and SoC-1.0-150SI-21 have larger capacity due to longer skirts. However, the cavitation limit is similar, because the sum of the atmospheric and the hydrostatic pressure at the soil sample surface was similar. The undrained resistance is maintained further than $\Delta z/L = 0.25$.

Test SoC-0.5-DCSI-20 conducted with the thick-walled model caisson only reached approximately 50 % of the extraction capacity measured in tests performed with the thin-walled model caissons. The internal suction pressure does not exceed the atmospheric pressure and is therefore not visible in Figure 8.2b. The extraction was conducted after the cyclic loading that involved considerable displacements (Section 8.1.2.2). Hence, an influence of the response to vertical cyclic loading cannot be ruled out in this case.

8.1.2.2 Response to vertical cyclic loading

Significance of the suction installation history

LSQ 1 was the same in LC 20 and 30 and results in similar response despite different installation histories as shown in the enlarged section in Figure 8.3 (noting different vertical axis scales). LC 10 yields increased displacement amplitudes resulting from a reduced consolidation period prior to the cyclic loading, which is discussed in the following section. An effect of the installation process is therefore not found. This is consistent with the re-compression of the soil plug due to lid touch-down, which is discussed in Section 7.1.

Load transfer mechanisms in sand over clay

The results of test SoC-0.5-125SI-20 presented in Figure 8.3 show almost elastic behaviour with minor net uplift during LSQ 1 and 2. Figure 8.4a reveals that the response at the lid invert is undrained in each LSQ of every load package as the total stress at the lid invert is fully carried by the excess pore pressure, i. e. $\Delta\sigma = \Delta u$. This behaviour is representative for all tests conducted in SoC profiles. Figure 8.4a further provides an indication of the changing share of skirt and lid contribution in transferring the applied load.

Figure 8.4b shows the applied stress V/A and the proportion transferred through the lid invert Δu. The difference is carried by the skirt-soil interaction. This indicates that the skirt resistance is not fully mobilised, despite the fact that the peak stresses of LSQ 2 exceed the drained extraction capacity in tension $(V/A)_S \approx 25\,\text{kPa}$ and similarly the drained capacity in compression – i.e. the combined skirt and tip resistance of $(V/A)_S + (V/A)_T \approx 25 + 9 \approx 34\,\text{kPa}$. The pore pressures at the lid invert cycle with

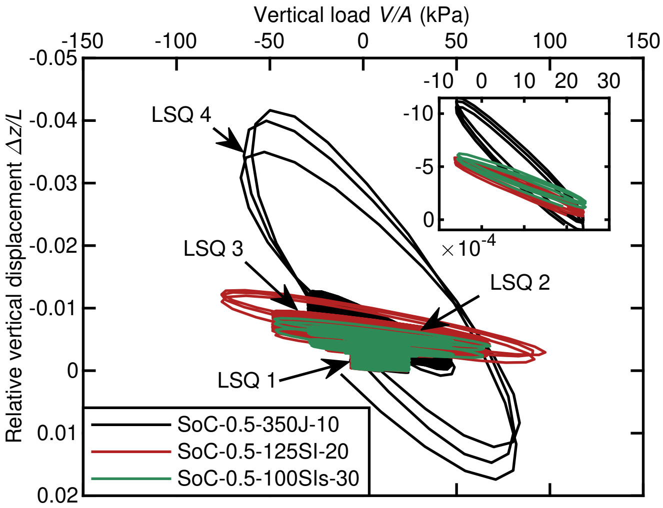

Figure 8.3: History of normalised relative vertical displacements during cyclic loading packages 1, 2 & 3 of load cases 10, 20, and 30.

the applied load so that the degree of mobilisation of the skirt (and tip, in compression) resistance remains constant: below 60% in LSQ 1 and below 80% in LSQ 2.

The skirt resistance is fully mobilised when the suction caisson is subjected to larger cyclic loads in LSQ 3 and 4 in test SoC-0.5-125SI-20. This results in an increasing displacement amplitude shown in Figure 8.3. The stresses transferred through the lid invert gradually increase with each compressive cycle of LSQ 3 and 4 (Figure 8.4b). This indicates that the share of vertical load transferred by the lid increases. Although net accumulation of excess pore pressure exists during these loading sequences, it dissipates during the following LSQ 1. This behaviour repeats with each loading package. This indicates that the soil recovers strength and skirt resistance is regained during low amplitude cyclic loading.

Loading per LC 20 yields maximum displacement amplitudes of approximately $\Delta z/L \approx 0.01$ Minor net uplift emerges, but the results presented in Figure 8.3 show that the vertical space between the hysteresis loops decreases after each load package – i. e. the net vertical displacement plateaus after several thousand load cycles.

The caisson displacement is governed by the soil permeability in homogenous sand profiles, as discussed in Chapter 6. Since the sand plug is hydraulically encapsulated from ambient by the clay layer in SoC, undrained response and therefore smaller displacement amplitudes are likely. The dimensionless displacement rate $v' = (\Delta \dot{z} L)/c_v > 30$ (Finnie and Randolph, 1994), as in LSQ 3 and 4, indicates undrained behaviour. Furthermore, the tip resistance in clay is relatively low. Hence, the suction caisson responds with similar stiffness in compression and tension, which is different to uniform sand profiles where an increased stiffness is present in compression. Test SoC-0.5-125SI-20 shows that the undrained response to vertical loading and the soft tip response in SoC profiles leads to moderate net displacements, which is beneficial considering serviceability criteria in SoC.

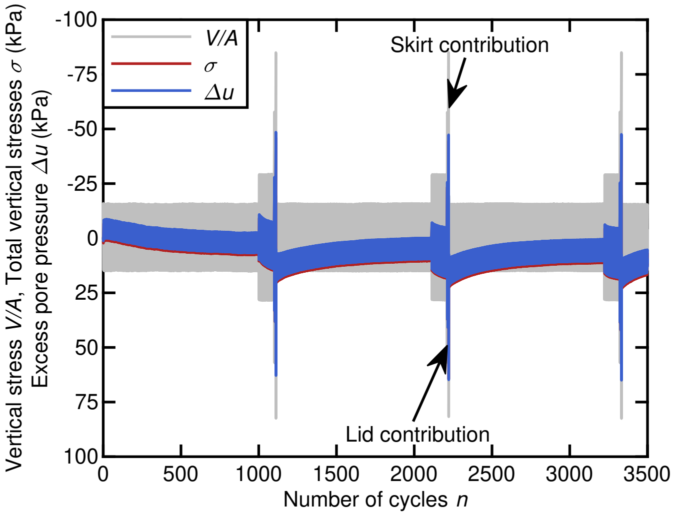

(a)

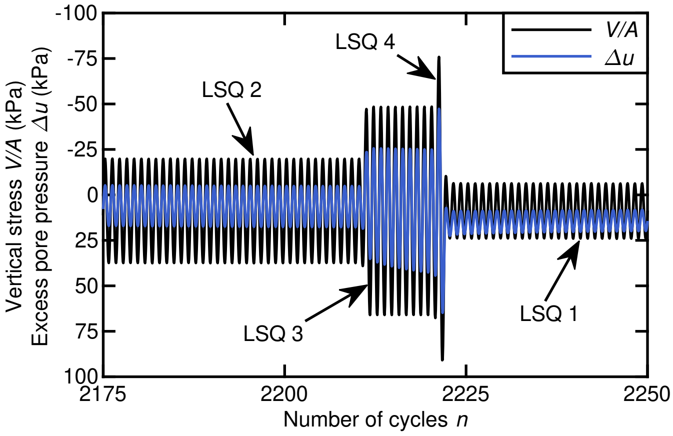

(b)

Figure 8.4: History of the applied stress, total stress and excess pore pressure at the lid invert during LSQ 1, 2, and 3 (a), and vertical stresses and history of the excess pore pressure during LSQ 2 (b) in test SoC-0.5-125SI-20.

The vertical loading amplitudes of LC 10 in LSQ 2, 3, and 4 are 25 % larger compared to LC 20 (Table 8.1) and the consolidation time following installation was substantially shorter in test SoC-0.5-350J-10 compared to test SoC-0.5-125SI-20. This resulted in significantly larger displacement amplitudes and net settlements in the short term (Figure 8.3), with tensile loads being transferred completely through suction pressure at the lid invert. However, the maximum displacement amplitudes and the rate of net settlement gradually decrease (Figure 8.5). The resulting long term displacement amplitudes in LC 10 appear to be proportional to the response during test SoC-0.5-125SI-20 and also plateaus in test SoC-0.5-350J-10 as the soil recovers strength.

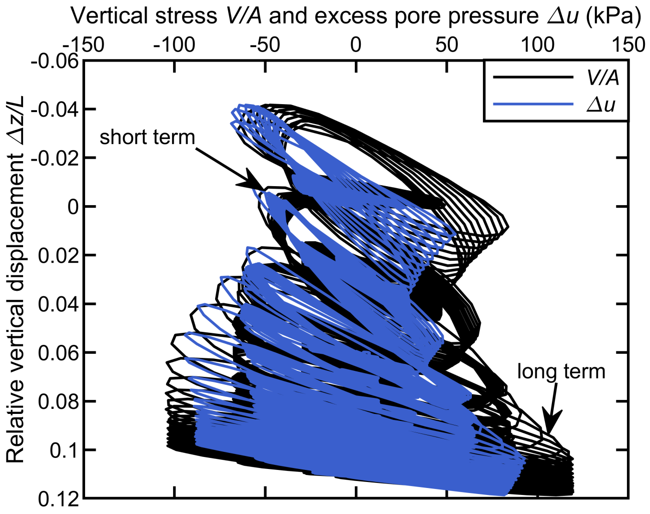

Figure 8.5: Short and long term response and excess pore pressure at the lid invert during cyclic loading in test SoC-0.5-350J-10.

Influence of the skirt wall thickness

The comparison between the response of a thin- and a thick-walled model caisson to cyclic loading per LC 20 is presented in Figure 8.6. The short term response of test SoC-0.5-DCSI-20 shows considerably increased vertical displacement amplitudes and net uplift. However, the long term response is characterised by a gradually increasing stiffness, which eventually leads to considerably reduced relative vertical displacements in each cycle compared to the results of test SoC-0.5-125SI-20 (Figure 8.6). In addition, the settlements measured during the test performed with the thick-walled model caisson contrast the net uplift observed in the thin-walled model caisson test.

The results presented in Figure 8.6b show that the skirt and tip resistance is not fully mobilised during test SoC-0.5-DCSI-20. However, similar long term behaviour observed in test with thin- and thick-walled model caissons. Figure 8.6b further reveals that the skirt did not carry much load short term, but skirt resistance is eventually mobilised after several loading packages, which is in line with the observed long term net settlement response.

Influence of average stress and cyclic loading amplitude

Long-term net settlements instead of net uplift in test SoC-0.5-350J-10 is believed to result from the increased loading amplitude and therefore from the larger maximum compressive loads. The comparison between the displacement response between LC 20 and 30 (Figure 8.3) shows that reduced cyclic loading amplitudes limit the peak displacements while the overall net uplift trend is similar. This observation is plausible, because Figures 8.4b and 8.7b reveal similarity between the underlying load transfer mechanisms that govern the response to vertical cyclic loading in tests SoC-0.5-125SI-20 and SoC-0.5-100SIs-30.

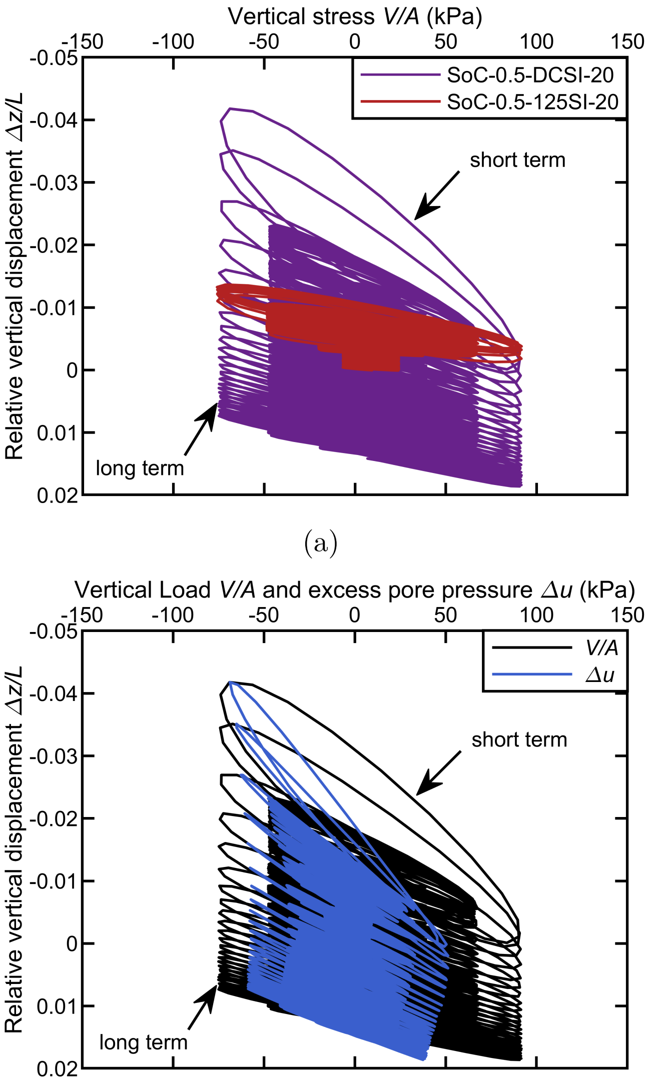

(a)

(b)

Figure 8.6: Comparison between the influence of the skirt wall thickness (a) and development of the excess pore pressure at the lid invert during cyclic loading of test SoC-0.5-DCSI-20 (b).

A shift of the average vertical stress $(V/A)_{ave}$ further into compression changes the response to cyclic loading, even if similar excursion into tension are reached in LSQ 2, 3, and 4. LSQ 1 of LC 21 does not include excursions into tension. The results show that purely compressive cyclic loading in LSQ 1 yields settlements (Figures 8.8 and 8.9), as expected. Figure 8.9 also reveals that LC 21 results in larger relative vertical displacement amplitudes compared to LC 20, which is plausible, because larger cyclic loading amplitudes are required to reach the same tensile peak load starting from an increased compressive average load. Furthermore, test SoC-0.5-150J-21 visualises the occurrence of net settlement in response to LSQs that feature significant excursions into tension.

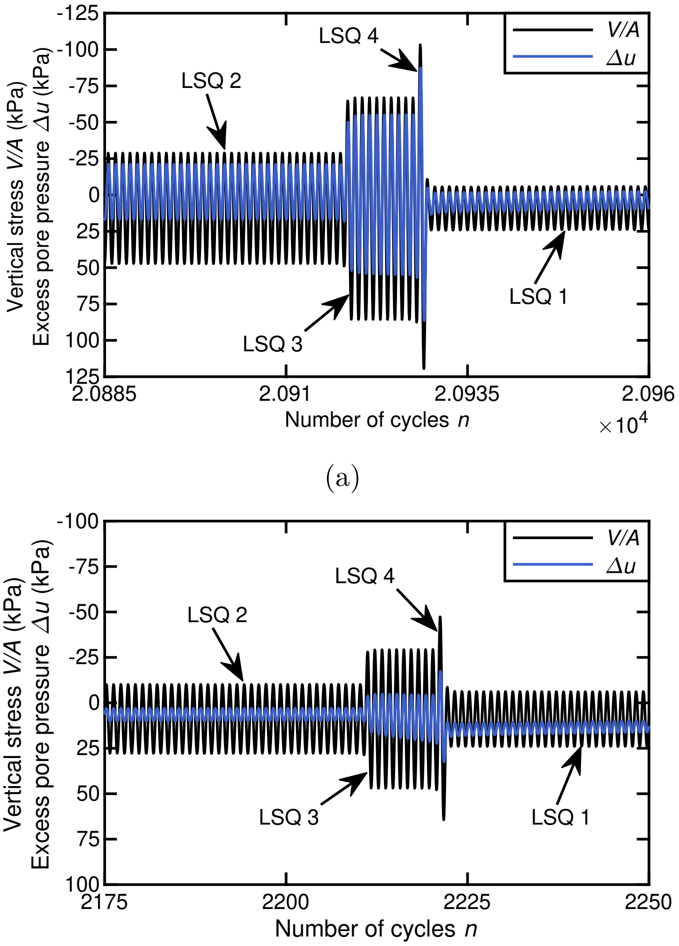

(a)

(b)

Figure 8.7: History of vertical stresses and excess pore pressure at the lid invert during the long term test SoC-0.5-350J-10 (a) and test SoC-0.5-100SI-30 (b).

Figure 8.4 and 8.8 show that compressive loads are transferred by the skirt friction, tip resistance, and the lid similarly in LC 20 and 21. Figure 8.8 shows that the skirt and tip resistance are arguably fully mobilised in LC 21 as significant net settlements result (Figure 8.9) instead of net uplift, which is present in test SoC-0.5-125SI-20.

The transfer mechanisms in tension differs: Tensile loads are completely transferred through suction pressure at the lid invert in LC 21 (Figure 8.8). Tensile loads are in contrast carried by the skirt friction and suction pressure in test SoC-0.5-125SI-20 (Figure 8.4b). Excess pore pressures, which are present in compression, dissipate before tensile loading commences at an increased average vertical stress (LC 21). Internal suction pressure therefore develops immediately and provides sufficient resistance. Excess pore pressures only partially dissipate before tensile loading is reached, if low compressive loads are present (LC 20). Hence, internal suction is mobilised later in this case and a portion of the tensile

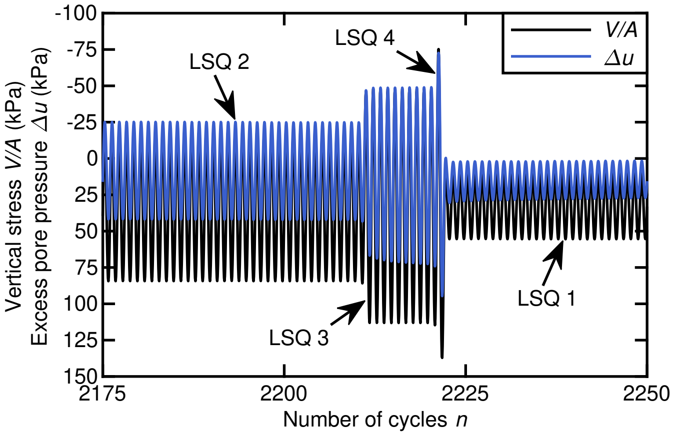

Figure 8.8: History of vertical stresses and excess pore pressure at the lid invert during SoC-0.5-150J-21.

load is transferred by the skirt resistance. Thus, the presented results suggest that the average compressive load determines whether cyclic loading with similar excursions into tension leads to net uplift or net settlement.

Influence of the caisson aspect ratio

The two tests that were performed with a model caisson with an aspect ratio of $L/D = 1$ show a significantly stiffer response to cyclic loading (LC 20 and 21) compared to the tests performed with the $L/D = 0.5$ model caisson (Figure 8.9).

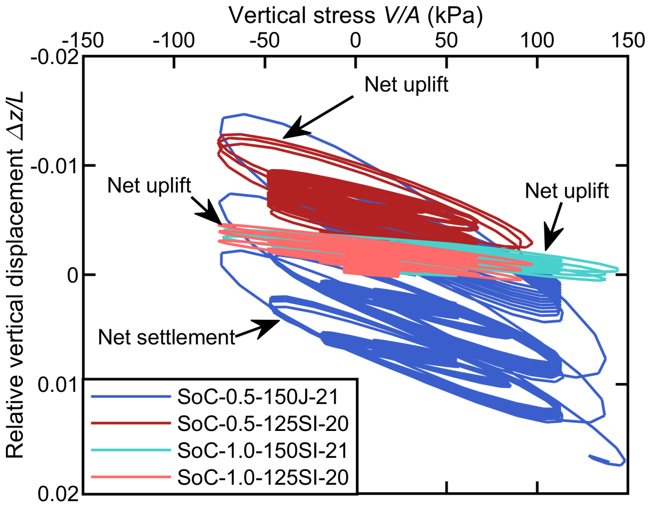

Figure 8.9: History of normalised relative vertical displacements during cyclic loading subjected to model caissons with aspect ratios of $L/D = 0.5$ and $L/D = 1$.

Due to the increased skirt length, the applied loads in LC 20 do not exceed the measured skirt resistance of $(V/A)_S \approx 65\,\text{kPa}$ in tension and the sum of the skirt friction and the calculated tip resistance $(V/A)_{S+T} \approx 74\,\text{kPa}$ (Houlsby et al., 2005) in compression. Figure 8.10a indeed shows that the skirt and the tip carry most of the vertical cyclic load applied to the caisson in test SoC-1.0-150SI-20. Thus, significantly lower excess pore pressures are recorded at the lid invert compared to the test results for a caisson with an aspect ratio of $L/D = 0.5$ (Figure 8.4).

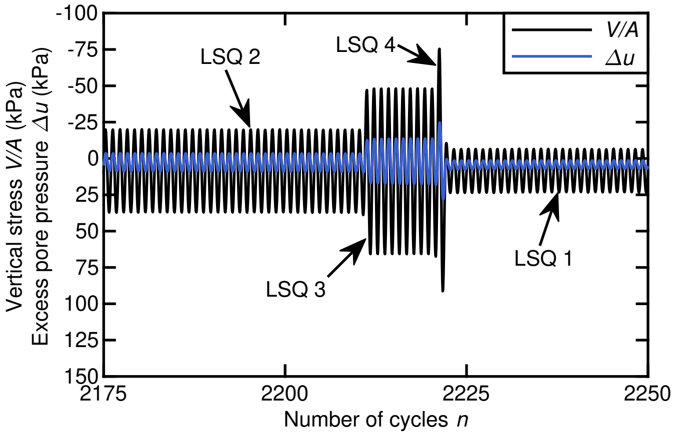

(a)

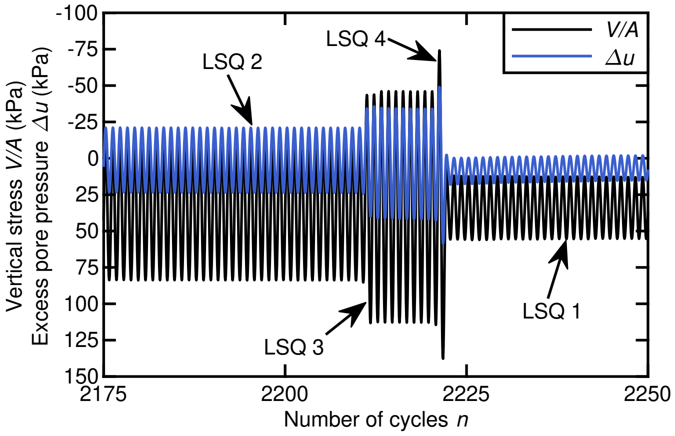

(b)

Figure 8.10: History of vertical stresses and excess pore pressure at the lid invert during test SoC-1.0-150SI-20 (a) and test SoC-1.0-125SI-21 (b).

Similar to the two previously discussed tests conducted with the $L/D = 0.5$ model caisson, the development of suction pressure at the lid invert during unloading from significantly compressive loads applied in LC21, which cycle with the applied load (Figure 8.10b), consistently provides additional resistance against uplift. Therefore, it is expected to limit the resulting displacements. The general trend of increased average compressive stresses shifting the response from net uplift to net settlement occurred in the tests for both aspect ratios. The increased skirt length provides additional resistance and stiffness in compression compared to the $L/D = 0.5$ model caisson, which substantially reduces the vertical displacement amplitudes (Figure 8.9).

8.1.3 Results and discussion: clay over sand

8.1.3.1 Tensile limiting capacities

A maximum resistance of $V/A \approx 10\,\mathrm{kPa}$ was measured during the drained extraction test performed in the CoS profile. Hence, the drained uplift resistance is smaller compared to uniform sand profiles discussed in Chapter 6 and in Bienen et al. (2018a). However, a skirt resistance within the magnitude of the $V/A \approx 25\,\mathrm{kPa}$ measured in SoC profiles is expected for the $L = 40\,\mathrm{mm}$ model caisson, because the skirt is similarly embedded in 20 mm of clay and sand in both cases. These results indicate a possible presence of flow channels, because areas of the skirt that are detached from the clay layer do not provide uplift resistance.

The results presented in Figure 8.11a also reveal a dependency between the uplift resistance and the cyclic loading history: A larger net uplift resulting from cyclic loading expectedly leads to a reduced uplift capacity due to a lower embedded depth z/L in the beginning of the extraction. Tests CoS-0.5-350-SI-10 and CoS-0.5-350-SIf-10 have a similar cyclic loading history. However, the drained uplift capacity differs considerably. The only distinct difference between both tests is an extended waiting period between the cyclic loading and the extraction of test CoS-0.5-350-SI-10.

The capacity during rapid uplift shown in Figure 8.11b is more complex and depends on the behaviour of the clay plug. Two different possible mechanisms are identified to govern the suction caisson extraction in a CoS profile:

(1) It is expected that the clay plug is lifted once the suction pressure at the lid invert exceeds its self-weight. Therefore, suction pressure will be transferred into the underlying sand. The extraction resistance depends on the degree of drainage in the sand layer and is limited by cavitation. This case is believed to be present in test CoS-0.5-350SIf-10. The distinct change in gradient at $\Delta z/L \approx 0.05$ is thought to mark the beginning of the relative movement of the clay plug and therefore the start of the suction pressure transferral. The clay plug in test CoS-0.5-350SIf-10 may have partially obstructed the sensor, resulting in high suction measured at the lid invert but a relatively low extraction resistance. The uplift capacity measured in this test is significantly smaller compared to tests conducted in uniform sand (Bienen et al., 2018a).

(2) If flow channels occur immediately, it is expected that only the drainage conditions of the underlying sand determine the extraction resistance resulting from rapid tensile loading. The results presented in Figure 8.12 reveal the actual presence of this mechanism during test CoS-0.5-DCSI-PIV. Minor clay plug uplift is visible in Figure 8.12a, which corresponds to $\Delta z/L \geq 0.05$, i. e. the state before the two curves relating to this test separate in Figure 8.11b. Significantly reduced clay plug displacements occur (Figure 8.12b). The internal suction pressures developed during

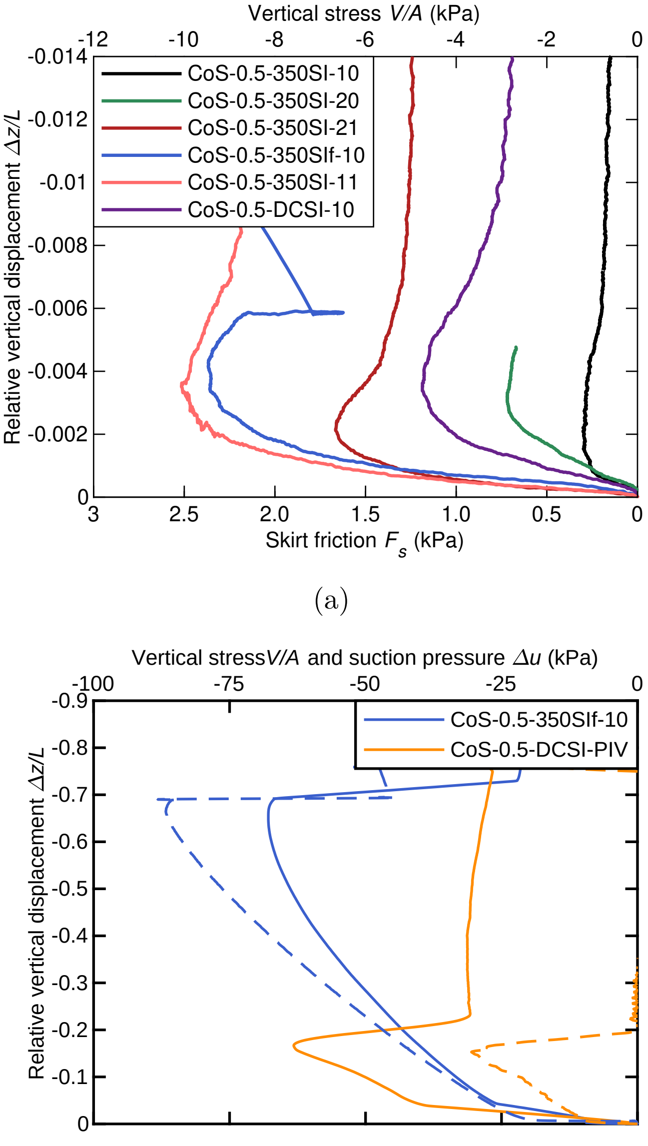

(a)

(b)

Figure 8.11: Drained (a) and rapid (b) extraction resistance (solid lines) and suction pressure (dashed lines) in CoS profiles.

test CoS-0.5-DCSI-PIV (Figure 8.11b) can be explained as the clay plug uplift is present, but slower compared to the caisson upward movement, despite the occurrence of flow channels. It is expected that the suction pressure eventually dissipates completely due to the ongoing development of flow channels, which finally yields the clay plug drop that was observed by Ragni et al. (2020). However this state was not reached in this test, because it terminated before the maximum capacity is reached as the foam seal failed at $\Delta z/L \approx 0.2$.

Both cases demonstrate that the load transfer mechanisms in CoS profiles differ from those present during uplift of suction caisson foundations embedded in uniform sand (Bienen et

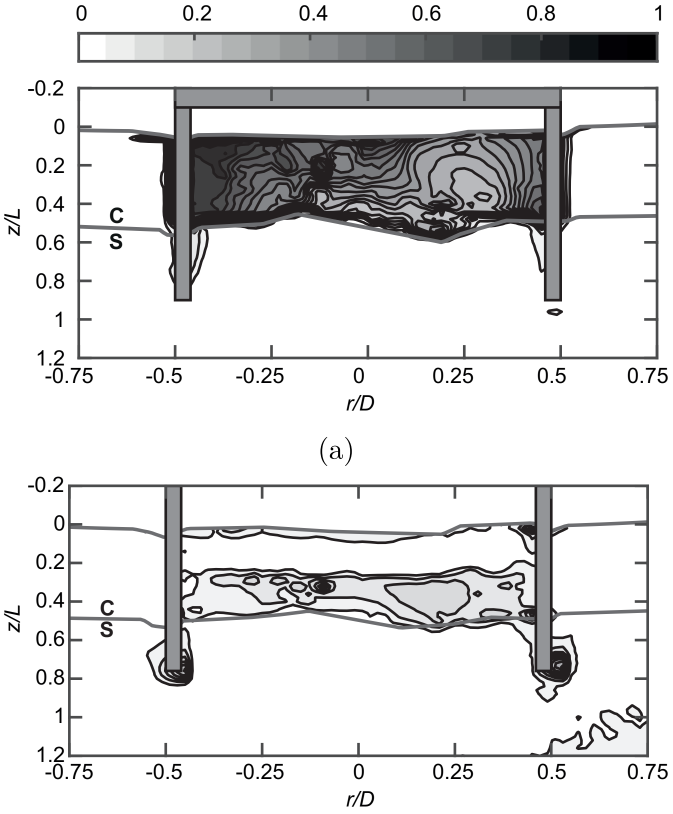

(a)

(b)

Figure 8.12: Normalised resultant clay plug displacement at $\Delta z/L \geq 0.05$ (a) and $\Delta z/L \leq 0.1$ (b) of an undrained extraction test in a CoS profile.

al., 2018a) and are considerably more complex. Clay plug uplift and the resulting drainage conditions in the underlying sand layer critically influence the response.

8.1.3.2 Response to vertical cyclic loading

Significance of the suction installation history

Figure 8.13 presents the response to vertical cyclic loading of two tests with different suction installation histories (Table 8.1) but identical loading cases. The target tensile vertical load in test CoS-0.5.350SIf-10 was underachieved. However, both test show a similar response in compression and comparable net uplift development over five loading packages. No distinct difference was found between these two tests. Consequently, no evidence of a possible influence of the installation history on the vertical cyclic load transfer mechanisms was found in this study. This is consistent with the findings discussed in Section 7.1.

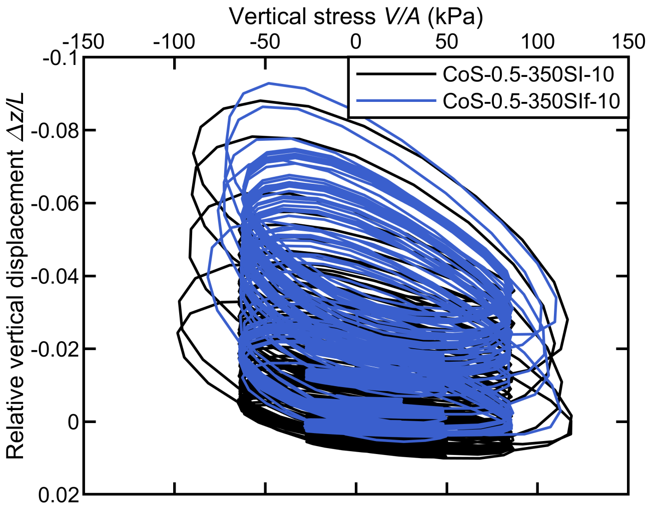

Figure 8.13: History of normalised relative vertical displacements during cyclic loading.

Load transfer mechanisms in clay over sand

The results presented in Figure 8.14 show an almost elastic response to LSQ 1 of LC 10, whereby the maximum targeted tensile load of $V/A \approx 8\,\mathrm{kPa}$ is not expected to exceed the drained skirt resistance. The caisson responds with substantially increased displacement amplitudes in tension once the drained capacity is exceeded – especially in LSQ 3 and 4. The displacement amplitudes are approximately two times larger than in comparable tests conducted in uniform fine silica sand (see also Chapter 6). The pore pressure measured at the lid invert cycles with the vertical load (Figure 8.14a), which is also similar to the behaviour in sand. The history of the effective load further indicates significantly stiffer response in compression (Figure 8.14b). This is also consistent with the caisson response to similar test performed in sand discussed in Chapter 6.

Figure 8.14 represents undrained behaviour at the lid invert in compression and tension as expected due to clay constituting the top of the soil plug. The drainage regime in the sand layer depends on the drainage path length and hence on the uplift of the clay plug and/or any flow channels developing along the skirt interface. The area covered by the hysteresis loops is larger in CoS than in sand, corresponding to a higher degree of drainage overall as already seen in Section 8.1.3.1.

The reasonably stiff response to compressive loads is also influenced by the tip resistance. For instance, Figure 8.14a shows that the tip carries approximately 50 % of the applied compressive load during LSQ 3, which implies net uplift in each load package – especially from the second load package. Based on the presented results, it is concluded that the mobilisation of the tip resistance in compression determines the net uplift response of the suction caisson foundation embedded in a CoS profile when subjected to vertical cyclic loading.

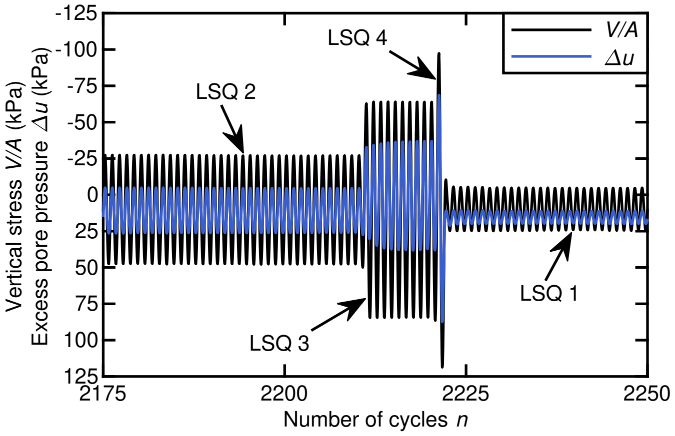

(a)

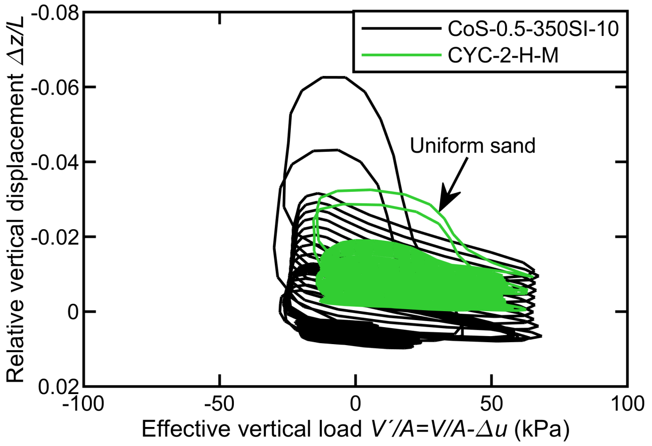

(b)

Figure 8.14: History of vertical stresses and excess pore pressure at the lid invert during test CoS-0.5-350SI-10 (a) and history of the effective vertical load during cyclic loading package 2 & 3 in CoS and uniform sand.

Influence of the skirt wall thickness

The results of the same loading history applied to the thin and thick-walled suction caissons are shown in Figure 8.15. While LC 10 results in net uplift after each loading package in both cases, substantially larger net uplift occurred in the test CoS-0.5-DCSI-10 performed with the thick-walled model caisson. Figure 8.15b reveals the thick skirt tips transfer an increased share of the applied compressive load compared to test CoS-0.5-350SI-10 (Figure 8.14a). However, the response to tensile loading is similar. Consequently, settlements in compression are limited in test CoS-0.5-DCSI-10 (Figure 8.15a) and net uplift emerges – especially after LSQ 4. While the installation response may be similar as the tip resistance is reduced due to the applied suction, the skirt wall thickness affects caisson response under vertical cyclic loading as the $t = 2\,\text{mm}$ skirt wall thickness attracts considerably increased tip resistance compared to the model caisson with $t = 0.5\,\text{mm}$ skirt wall thickness.

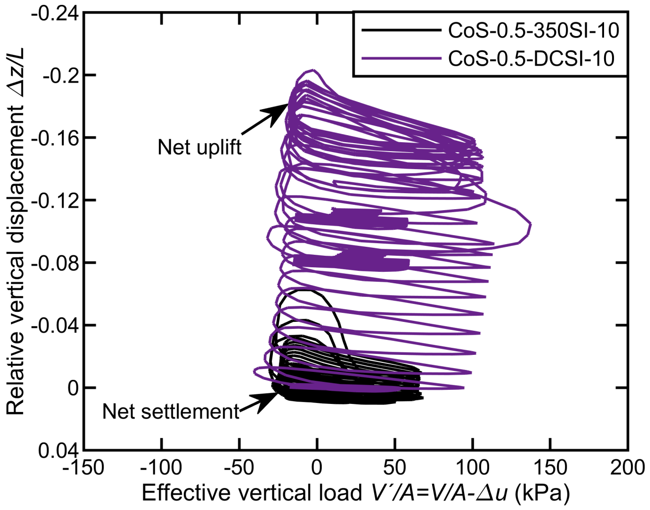

(a)

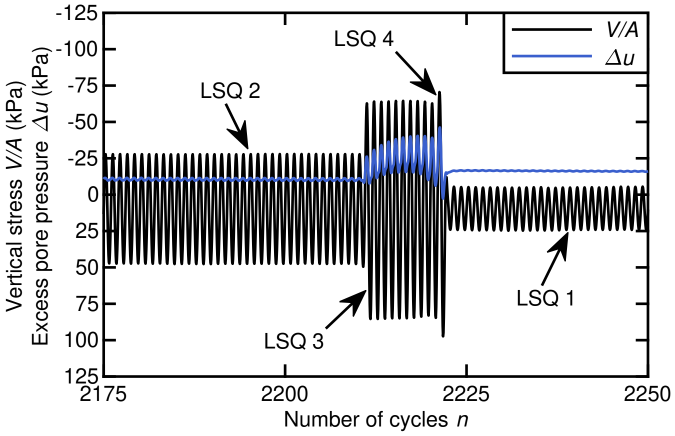

(b)

Figure 8.15: Comparison between the influence the skirt wall thickness (a) and development of the excess pore pressure at the lid invert during cyclic loading of test CoS-0.5-DCSI-10 (b).

Influence of average stress and cyclic loading amplitude

The response to vertical cyclic loading presented in Figure 8.16 is significantly different in each of the four LCs, which differ in terms of average load and cyclic loading amplitude or both (Table 8.1). The results of (1) similar average stress, but different cyclic loading amplitude, (2) different average stress, but similar cyclic amplitude, and (3) different average stress, but similar tensile load are discussed below:

(1) LC 10 and LC 20 have the same average compressive stress, but the amplitude of LSQ 2, 3, and 4 is reduced by 25 % in LC 20. Figure 8.16 shows a significant increase of the net uplift due to the reduction of the loading amplitude – especially during LSQ 3 and 4. The magnitude of uplift in a single cycle during LSQ 3 and 4 is

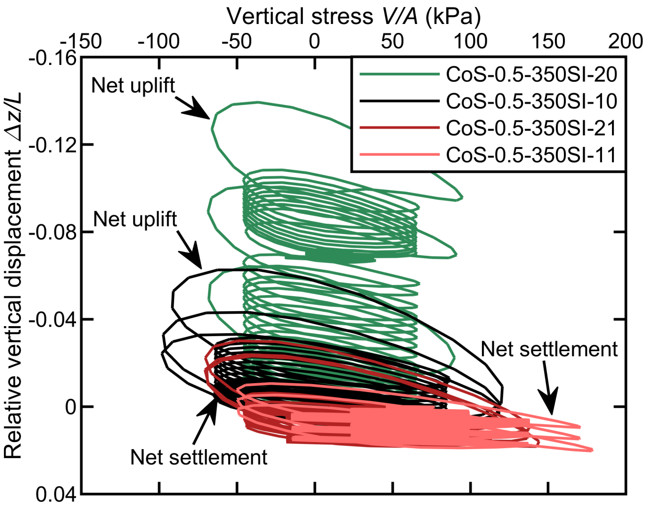

Figure 8.16: History of normalised relative vertical displacements during cyclic loading subjected to model caissons embedded in a CoS profile.

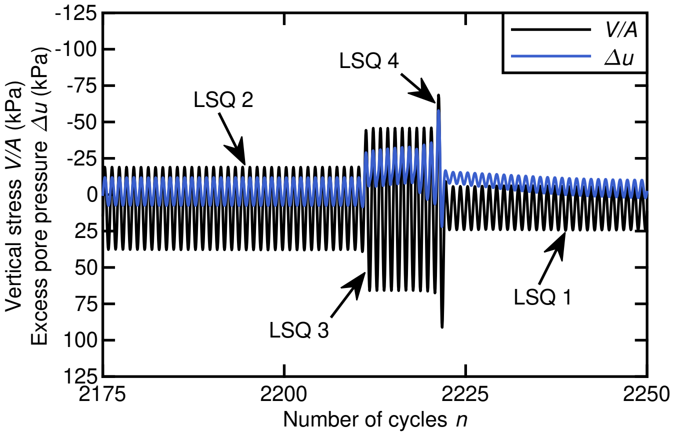

Figure 8.17: History of vertical stresses and excess pore pressure at the lid invert during test CoS-0.5-350SI-20.

comparable. Furthermore, Figures 8.14a and 8.17 show a comparable development of suction pressure at the lid invert during tensile loading. This indicates the presence of a similar tensile load transfer mechanism characterised by a combination of skirt resistance and internal suction pressure, which is believed to be transferred through the clay plug into the underlying sand in both tests.

The suction pressure dissipates once the loading moves into compression and excess pore pressure develops. Figure 8.17 shows that the maximum excess pore pressure is lower in test CoS-0.5-350SI-20 compared to test CoS-0.5-350SI-10. Thus, a reduced share of the vertical load is transferred through the lid. Reduced cyclic amplitudes imply lower maximum compressive stresses and therefore reduce settlements, as expected. Since the overall response in compression is significantly stiffer than in tension, the reduction of the loading amplitude reinforces the imbalance of upward and downward displacement during cyclic loading, which yields increased net uplift. This imbalanced response is also discussed for sand by Bienen et al. (2018b).

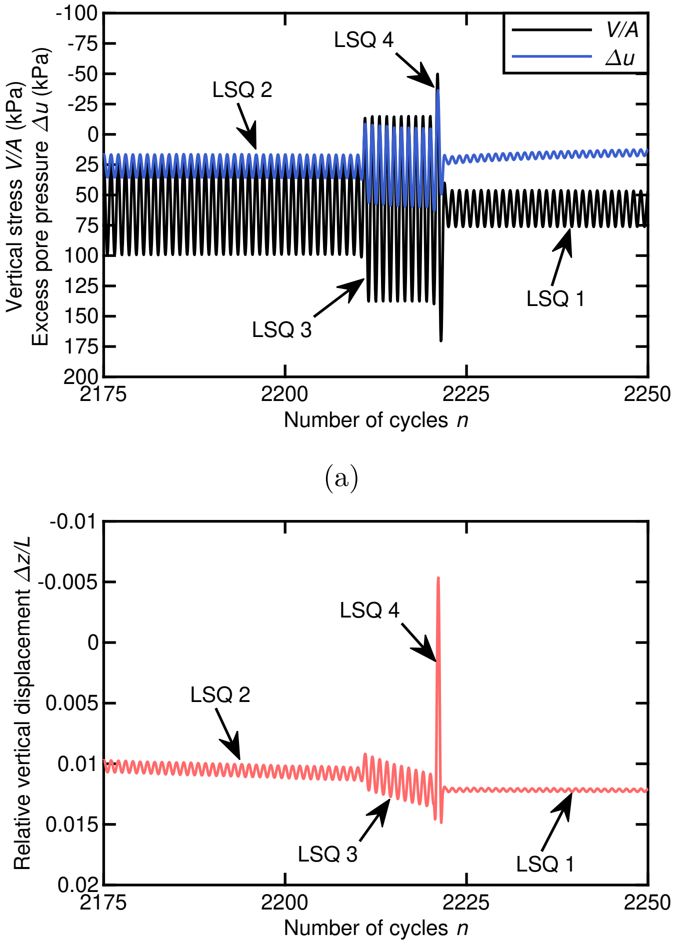

(a)

(b)

Figure 8.18: History of vertical stresses and excess pore pressure at the lid invert (a) and vertical displacements during cyclic loading package 2 (b) of test CoS-0.5-350SI-11.

(2) A shift of the average load into compression while maintaining the cyclic loading amplitude (LC 10, LC 11) results in net settlement instead of net uplift, which is shown in Figure 8.16. Furthermore, the displacement amplitude measured in test CoS-0.5-350SI-11 is significantly smaller compared to test CoS-0.5-350SI-10. Figure 8.18a shows that suction pressure already develops during unloading from compression. This yields additional uplift resistance and is expected to reduce the respective displacement amplitude. Furthermore, Figure 8.18a shows compressive behaviour that is similar to the results of test CoS-0.5-350SI-20 presented in Figure 8.17 – i. e. the majority of the compressive load is carried by the skirt. Similar response was observed in uniform Baskarp sand (Bienen et al., 2018a; Bienen et al., 2018b).

The increased compressive average load also implies that tension is not applied before LSQ 3. This leads to the response illustrated in Figure 8.18b: almost elastic behaviour in LSQ 1, net settlements in LSQ 2 and 3, and zero net displacement in LSQ 4. The occurrence of settlements despite excursions into tension in LSQ 3 and the absence of net uplift in LSQ 4 shown in Figure 8.18b is remarkable here. It indicates that tensile cyclic loading exceeding the drained extraction capacity can be withstood without resulting in net uplift. The comparison between the responses to loading of LC 10 and 11 consequently indicates that the average vertical stress, i. e. the compressive stress following an excursion into tension, determines the direction of net displacements in CoS profiles. This is similar to findings for suction caissons in sand (Bienen et al., 2018b).

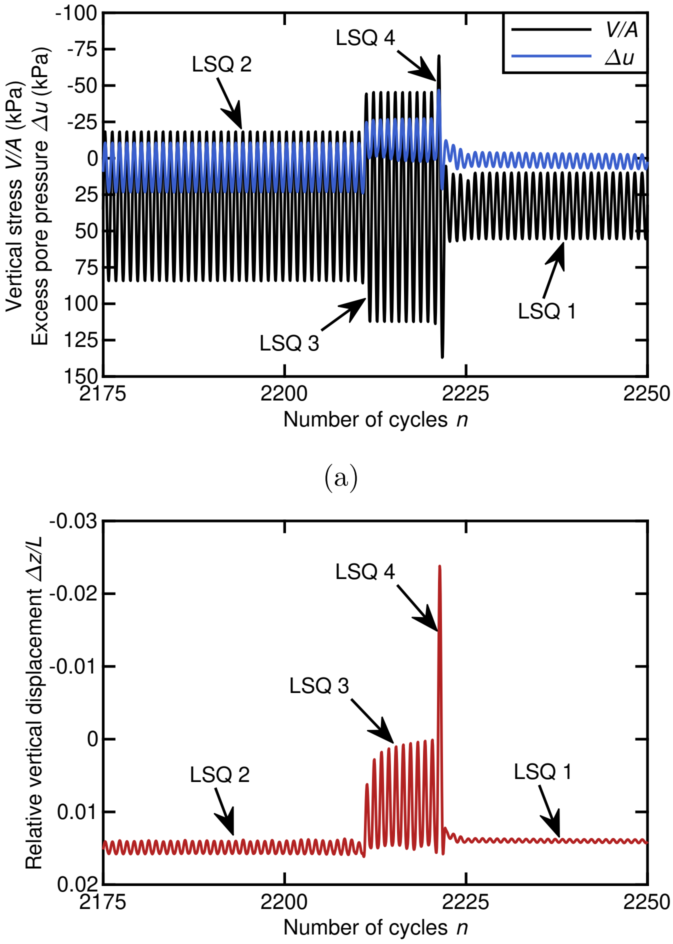

(a)

(b)

Figure 8.19: History of vertical stresses and excess pore pressure at the lid invert (a) and vertical displacements during cyclic loading package 2 (b) of test CoS-0.5-350SI-21.

(3) Results of tests with different average but similar tensile stresses (LC20, 21) provide the following insights: The higher average compressive stress in LC 21 leads to a

> significant change in displacement response compared to LC 20, which is shown in Figure 8.16. Net settlement instead of excessive net uplift was observed during test CoS-0.5-350SI-21, which is consistent with the previous results. The development of pore pressures and the share of load carried by the lid invert presented in Figure 8.19a is similar to the response to LC 11 shown in Figure 8.18a. This confirms that the average vertical load indeed determines the overall response to vertical cyclic loading in CoS profiles.
>
> A more detailed evaluation of LSQ 3 provides the following insights: LC 21 already featured excursions into tension that exceeded the drained extraction capacity from LSQ 2. Figure 8.19b shows that net settlements were measured during LSQ 1 and 2 and net uplift was recorded during LSQ 3 and 4, which result in marginal net vertical displacements overall. This comparison between test CoS-0.5-350-SI-20 and CoS-0.5-350-SI-21 demonstrates a suction caisson foundation in CoS can withstand similar tensile loads without considerable net deformations, if a sufficiently large compressive load follows the tensile load.

Based on the presented group of cyclic loading test, it is concluded that the development of suction pressure inside the caisson has a major effect on the displacement magnitude resulting from tensile loading in CoS profiles. The significantly stiffer response in compression due to the large tip resistance favours net uplift as the tensile and compressive load have a similar magnitude during cyclic loading. A shift towards more compressive average vertical load was found to be beneficial to establish balance between uplift in tension and settlement in compression, which eventually limits the permanent net displacement.

8.1.4 Remarks on the centrifuge tests

The installation history was found not to significantly influence the behaviour under vertical cyclic loading including excursions into tension as SoC and CoS soil profiles have been considered. Undrained conditions are governing the suction caisson response in SoC. The sum of cycling internal excess pore pressures and the skirt and tip resistance yield a relatively balanced response to the investigated LCs. The average vertical load and the loading amplitude certainly influence the in-service caisson performance. The vertical cyclic loading response in CoS is more complex: The interplay between internal excess pore pressures and skirt and tip resistance plays a major role again. The internal clay plug movement and a potential transfer of pore pressures into the underlying sand plug have been identified to play a crucial role in the caisson response to vertical cyclic loading in CoS. Considerably stiff behaviour in compression yields net uplift at relatively low average loads within the range of the investigated LCs.

The presented experiments provide comprehensive insights into the load bearing behaviour of suction caissons in layered soils. The presented data forms a novel database which can be utilised for the development of predictions methods. Methods capturing soil layer and soil-structure interaction need to be implemented. Numerical simulations are considered to be a suitable method to provide further insights and predictions of the in-service behaviour of suction caissons embedded in SoC and CoS.

8.2 Numerical simulations

An extended version of the model presented in Section 6.2 is utilised. This model is capable of the simulation of the loading bearing of a suction caisson foundation embedded in layered soil profiles. The numerical simulations target the underlying load bearing mechanisms and the prediction of the caisson load displacement behaviour. The study consists of two steps: First, the data calculated from the numerical model is compared to the centrifuge test results presented in Section 8.1. In a second step, variations of the numerical model are presented in order to investigate frontiers and opportunities of numerical simulations of suction caisson foundations subjected to vertical cyclic loading.

8.2.1 Numerical modelling and testing procedure

The numerical simulations are performed with Abaqus/Standard 2018 (Dassault Systèmes, 2018). The one-phase formulation is employed, if undrained behaviour is investigated in SoC. The analyses involving sand require the utilisation of the two-phase formulation in order to cover partially drained response. The numerical model utilised for the numerical simulations is shown in Figure 8.20. The dimensions shown in Figure 8.20a slightly differ from the centrifuge tests in order to minimise boundary effects in the numerical simulations. The two-dimensional axisymmetric model geometry is meshed with high order rectangular elements (CAX8) for the one-phase SoC simulations. CAX8P elements featuring a pore pressure degree of freedom are required for calculations involving a CoS soil profile (Dassault Systèmes, 2018).

The caisson is a rigid body meshed with triangular elements (CAX6). A half circular shaped skirt tip reduces artificial stress peaks. The entire mesh is shown exemplary in Figure 8.20b. It illustrates that small elements are located close to the caisson. A more coarse mesh is utilised further away from the area where the largest deformations are expected. The model dimensions actually employed for each numerical model are listed in Table 8.2.

Table 8.2: Numerical model caisson dimensions.

Model No.	D (m)	L (m)	t (cm)
10	8	4	5
20	8	8	5

The horizontal displacements are locked at the axis of symmetry and outside the vertical edge of the model geometry, while vertical displacements are permitted. The bottom features a zero vertical displacement BC. These three edges are also hydraulically impermeable in the two-phase simulations. The displacements at the soil surface are unlocked, while a pore pressure BCs is applied on the free surface in order to allow drainage if required. The vertical load V is applied to the rigid caisson through a concentrated vertical force subjected at the RP that is located at the axis of symmetry.

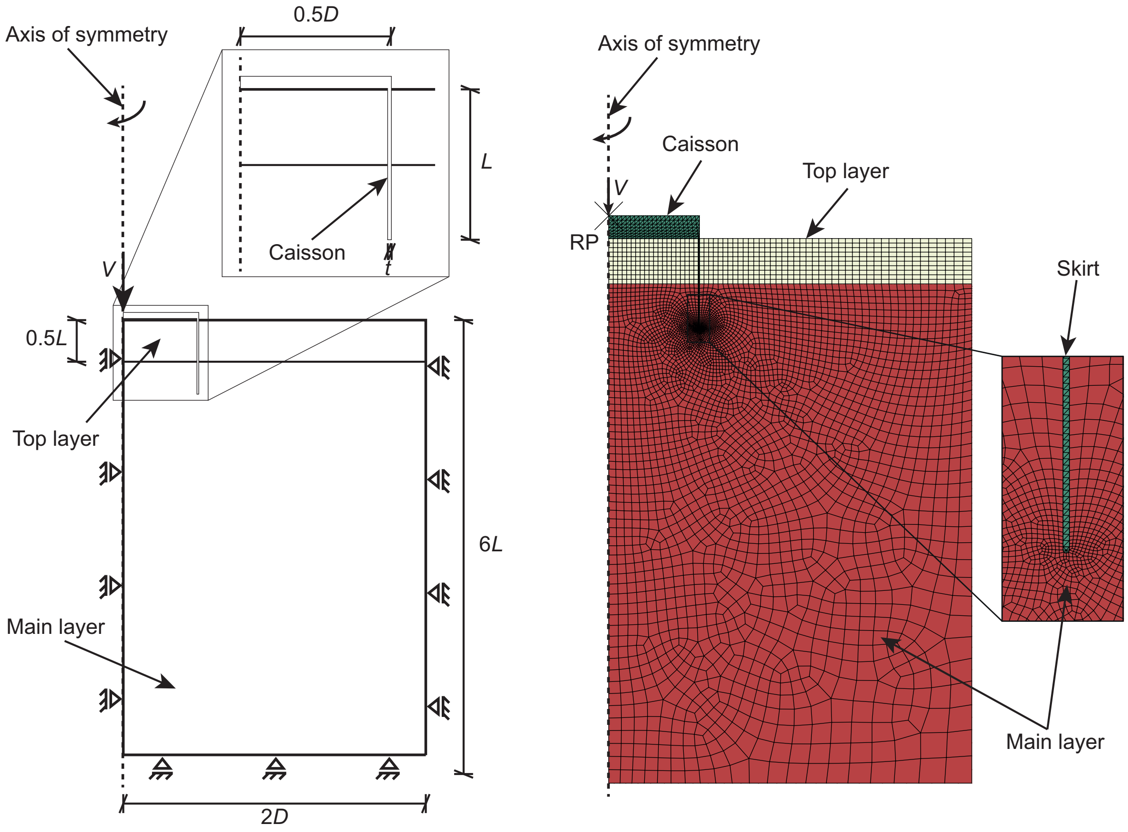

(a) (b)

Figure 8.20: Dimensions (a) and finite element mesh (b) of the numerical model utilised for FEM analyses of the suction caisson response to vertical cyclic loading in a layered soil profile.

The parameters required for the utilised hypoplastic constitutive models (φ_c, h_s, n_B, e_{d0}, e_{c0}, e_{i0}, α, and β) are summarised in Table 8.3, 8.4, and 8.5. The parameters for fine silica sand are determined under consideration of the laboratory test discussed in M. N. Tran (2005), Pucker et al. (2012), and Chow et al. (2018). The laboratory experiment results discussed in Qui (2012) and Mašín (2019) from the basis of the determination of the given parameters for kaolin clay. The parameters required as input for the ISA formulation (m_R, R, β_{h0}, χ_0, χ_{max}, c_a, c_z, and β_{hmax}) are found iteratively through numerical analyses and under consideration of the guidelines referred in Fuentes et al. (2019), Fuentes et al. (2018), and Fuentes et al. (2017a). The initial void ratio e_0 and the interface friction parameters (μ, τ_{max}, and γ_i) listed in Table 8.6 are derived from the results of the centrifuge experiments referred in Section 8.1.

The simulations are conducted in accordance to the following procedure: First, the effective stresses and optionally the hydrostatic pressure, are applied during the K_0 procedure. A minimum load is applied at the caisson in order to minimise an effect on the K_0 conditions. Load controlled caisson static and cyclic loading commences once stable K_0 conditions are reached.

Table 8.3: ISA-hypoplasticity model parameters for FEM simulations featuring fine silica sand and kaolin clay.

Parameter	Symbol	Unit	Fine silica sand	Kaolin clay
Critical friction angle	φ_c	(°)	30	20
Granular hardness	h_s	(MPa)	1354	1354
Barotropy exponent	n_B	(-)	0.34	0.34
Minimal void ratio	e_{d0}	(-)	0.49	0.49
Critical void ratio	e_{c0}	(-)	0.79	0.79
Maximum void ratio	e_{i0}	(-)	0.86	0.86
Dilatancy exponent	α	(-)	0.18	0.18
Pyknotropy exponent	β	(-)	1.27	0.5
Stiffness factor	m_R	(-)	4	5
IS yield surface	R	(-)	$1 \cdot 10^{-4}$	$1 \cdot 10^{-4}$
IS hardening parameter	β_{h0}	(-)	0.2	0.076
Minimum value of IS exponent	χ_0	(-)	4	7
Maximum value of IS exponent	χ_{max}	(-)	25	40
Accumulation rate factor	c_a	(-)	0.04	0.005
Cyclic mobility factor	c_z	(-)	150	150
Maximum IS hardening parameter	β_{hmax}	(-)	3	3
Bulk modulus water	K_w	(MPa)	$2.2 \cdot 10^2$	$2.2 \cdot 10^2$
Effective permeability	k_f	(m/s)	$9.87 \cdot 10^{-5}$	$1.7 \cdot 10^{-9}$
Density water	ρ_w	(t/m^3)	1	1
Grain density solid	ρ_s	(t/m^3)	2.65	2.67

Table 8.4: Visco-hypoplasticity model parameters for FEM simulations featuring kaolin clay.

Parameter	Symbol	Unit	Kaolin clay
Critical friction angle	φ_c	(°)	20
Compression index	λ	(-)	0.205
Swelling index	κ	(-)	0.044
Shape of rendulic surface	β_r	(-)	0.5
Leinenkugel's index of viscosity	I_v	(-)	0.05
Reference creep rate	D_R	$(1/s)$	$1 \cdot 10^{-6}$
Stiffness factor (90 °)	m_T	(-)	2
Stiffness factor (180 °)	m_R	(-)	5
Max. intergranular strain	R	(-)	$1 \cdot 10^{-4}$
IS hardening exponent	β_R	(-)	0.05
Stiffens degradation exponent	χ	(-)	1
Overconsolidation ratio	OCR	(-)	8
Initial void ratio	e_0	(-)	1.09

Table 8.5: Mohr-Coulomb model parameters for FEM simulations featuring kaolin clay.

Parameter	Symbol	Unit	Fine silica sand	Kaolin clay
Undrained shear strength	s_u	(kPa)	-	47.2
Young's modulus	E	(MPa)	60	1.2
Poisson's ratio	ν	(-)	0.475 (0.25)	0.475

Poisson's ratio for drained conditions in brackets

Table 8.6: Model parameters for the soil-structure interaction.

Parameter	Symbol	Unit	Fine silica sand	Kaolin clay
Interface friction coefficient	μ	(-)	0.15	0.15
Shear stress limit	τ_{max}	(kPa)	12	20
Allowable elastic slip	γ_i	(-)	0.005	0.005

The cyclic loading sequences applied in the numerical simulations aim to reproduce the BCs, which are present during the centrifuge experiments. Hence, the loading amplitude and frequency are taken from Table 8.1. However, the number of cycles is reduced to a minimum in order to reduce computational costs. The average load from Table 8.7 is applied to the caisson first. A waiting period of $t = 60\,\text{s}$ that allowed consolidation in the two-phase simulation commenced before the cyclic loading packages are applied. The waiting period is not necessary in the one-phase simulation in order to achieve initial conditions, which are comparable to the centrifuge test. The history of the vertical cyclic loading is shown in Figure 8.21.

8.2.2 Results and discussion: sand over clay

The calculated results are presented in non-dimensional form, unless stated otherwise. Positive values indicate compression and downward displacements, whereas negative values represent tension and upward displacements.

Table 8.7: Load cases and specifications of the four cyclic loading sequences applied in the numerical simulations in layered soil profiles.

LC	Sequence number	1	2	3	4
20N	Number of cycles n (-)	18	5	3	1
	Load amplitude V (N)	40 ± 80	40 ± 150	40 ± 300	40 ± 450
	Stress amplitude V/A (kPa)	8 ± 16	8 ± 30	8 ± 60	8 ± 90
21N	Number of cycles n (-)	18	5	3	1
	Load amplitude V (N)	160 ± 120	160 ± 270	160 ± 420	160 ± 570
	Stress amplitude V/A (kPa)	32 ± 24	32 ± 54	32 ± 84	32 ± 114

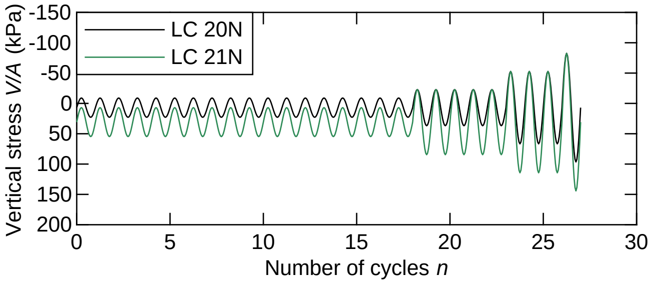

Figure 8.21: History of four vertical cyclic loading sequences in LC 20N and LC 21N.

8.2.2.1 Monotonic load bearing mechanisms

The results obtained from experiments and numerical simulations are compared in order evaluate and validate the numerical model. Consolidation resulting from compressive loading is investigated first. The drained and the rapid caisson extraction are back calculated afterwards. Each calculation is performed with model no. 10 as referred in Table 8.2.

The calculated response to the application of a vertical load of $V = 5850\,\mathrm{kN}$ ($V/A = 116\,\mathrm{kPa}$) and subsequent unloading to $V = 400\,\mathrm{kN}$ ($V/A = 8\,\mathrm{kPa}$) is presented in Figure 8.22. The maximum settlements calculated with the elastic-plastic Tresca and the visco-hypoplastic constitutive model are slightly different, but fall within the magnitude of the measured values. However, the instantly occurring displacements are overestimated and the settlements resulting from consolidation are underestimated. The modification of the effective permeability is therefore not expected to improve the similarity between the measured and calculated results. However, fitting by the means of modifying the input parameters certainly would yield an improved match, but is expected to violate parameters that were obtained from laboratory tests. Hence, fitted results are not presented in order to evaluate the applicability of numerical prediction methods.

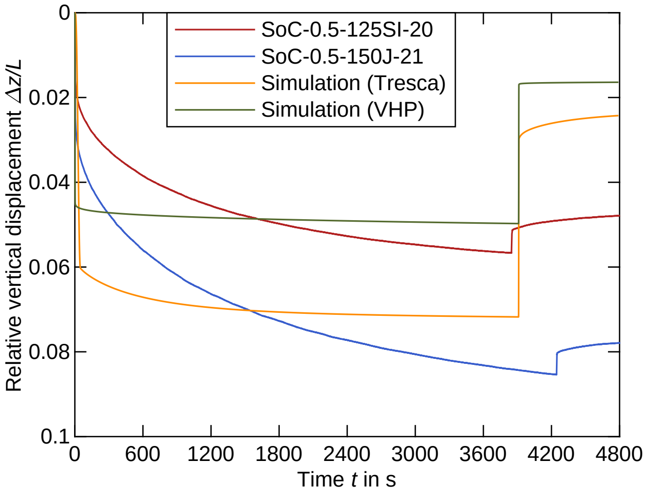

Figure 8.22: History of vertical displacements during static loading in SoC.

The uplift response during unloading from $V/A = 116\,\text{kPa}$ to $V/A = 8\,\text{kPa}$ is overestimated by the numerical simulations with both constitutive models compared in Figure 8.22. This is plausible for the Tresca model, because the same Young's modulus is taken into account for loading and unloading. The utilised visco-hypoplastic constitutive model features the intergranular strain concept, which is expected to increase the unloading stiffness and therefore limit the caisson uplift during unloading. However, the visco-hypoplastic constitutive model also accounts for viscous effects that depend on the loading rate. The instant unloading taken from the centrifuge test yields an unloading rate of $\dot{V}/A \approx 100\,\text{kPa/s}$. Hence, the viscosity-dependence has an influence on the calculated results. Considerable viscosity effects are expected to play a role for normally or slightly overconsolidated clay (Niemunis et al., 2009), but highly overconsolidated clay with an overconsolidation ratio of $OCR = 7.1$ at the skirt tip utilised in the centrifuge experiments is considered in the numerical simulation.

Despite the consideration of the initial overconsolidation ratio $OCR = 8$ in the numerical simulations, it is questionable, if the utilisation of the visco-hypoplastic model is reasonable in this case. However, the numerical model reproduced the expected response in general. Hence, the presented numerical model is considered to be capable of the simulation of the monotonic vertical compressive loading and unloading of a suction caisson foundation.

Figure 8.23 shows the measured and calculated vertical stress required for the drained suction caisson extraction in SoC. The performed one-phase calculation accounts for drained conditions. The contour plot of the normalised vertical displacements presented in Figure 8.24b shows lid separation and no soil plug heave. This confirms that the extraction takes place under virtually drained conditions – i. e. only skirt resistance is mobilised.

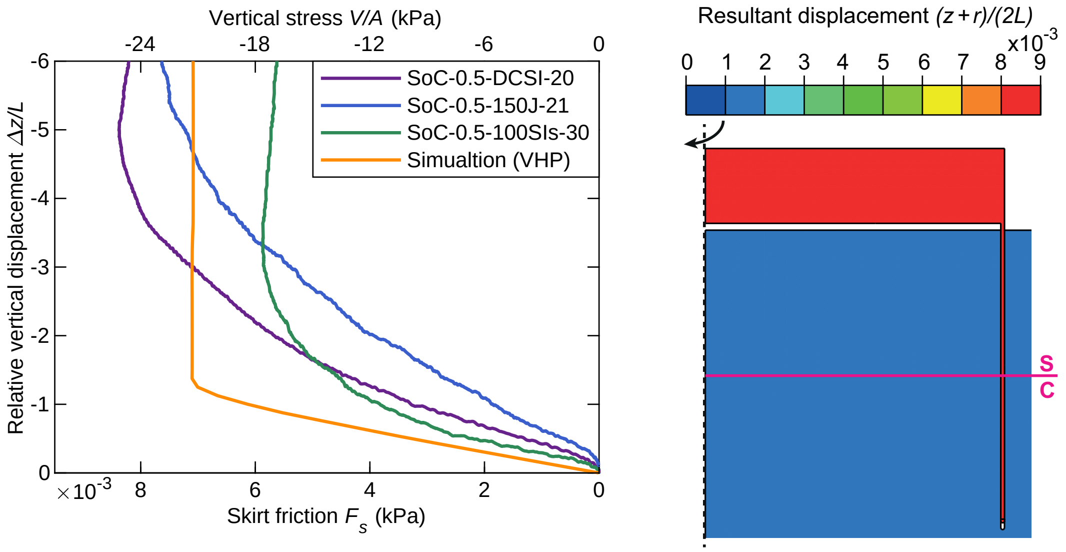

(a) (b)

Figure 8.23: Drained the extraction resistance (a) and normalised resultant displacement contours at a relative caisson displacement of $\Delta z/L = 9 \cdot 10^{-3}$ (b) in SoC.

The calculated drained extraction resistance matches the measured values (Figure 8.23). The required uplift for full mobilisation of the resistance is slightly underestimated. However, the numerical model is considered to be suitable for the simulation of the drained suction caisson extraction from a SoC profile.

Figure 8.24 shows the calculated results of the rapid suction caisson extraction from a SoC soil profile. The undrained response targeted in the centrifuge test is taken into account in the numerical simulation. The extraction resistance obtained from experiments approaches a certain maximum, which is comparable to centrifuge tests conducted with Baskarp sand (Bienen et al., 2018a). However, the calculated results do not reach a maximum, i. e. failure is not reached within the investigated maximum displacement. The measured and calculated vertical stresses increase similarly until the curve obtained from centrifuge test SoC-0.5-150J-21 changes gradient. Cavitation was found to limit the rapid extraction resistance (see Section 8.1). Cavitation is not taken into account in the numerical model, which consistently yields an overestimation of the uplift resistance.

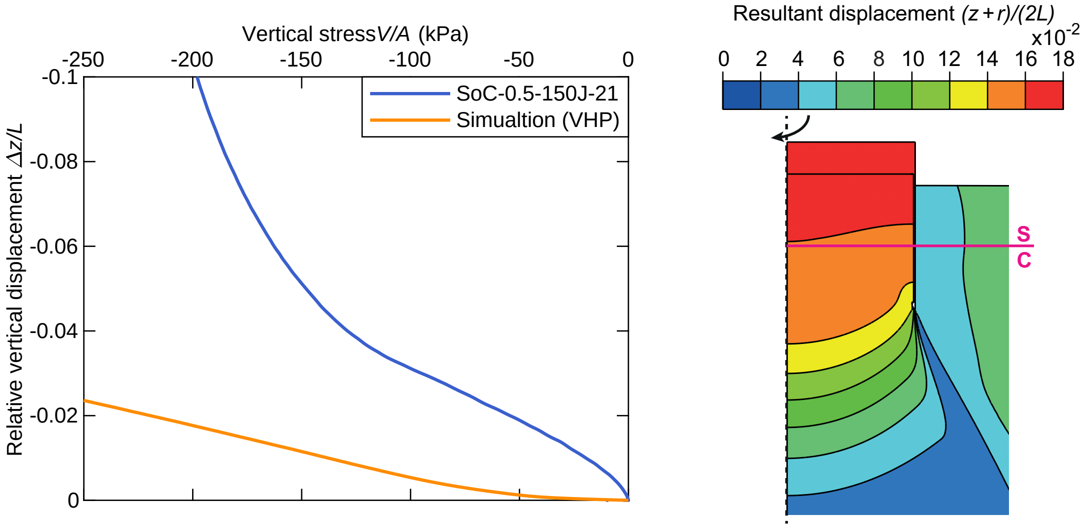

(a) (b)

Figure 8.24: Rapid extraction resistance (a) and normalised resultant displacement contours at a relative caisson displacement of $\Delta z/L = 0.1$ (b) in SoC.

The contour plot presented in Figure 8.24b reveals that the entire soil plug is lifted during rapid extraction. The largest resultant displacements occur inside the caisson as expected. Hence, the numerical model is considered to be suitable for the simulation of rapid extraction of a suction caisson foundation only, if cavitation does not occur. It is noted that cavitation is not expected to be involved in the investigations on vertical cyclic loading, because the maximum applied tensile load is $V/A = 82\,\text{kPa}$ (see Table 8.6). This is sufficiently smaller than the investigated extraction resistance $V/A > 200\,\text{kPa}$.

8.2.2.2 Cyclic load bearing mechanisms

The next group of numerical simulations featuring cyclic loading targets further evaluation of the numerical model. The experimental results discussed in Section 8.1 and a numerical back analysis are compared. It is noted that the number of simulated load cycles is limited to a minimum, which is considered to maintain comparability between experimental and numerical investigations. The caisson response presented in Figure 8.25 features the first two loading packages of the experimental and the numerical data. Three different constitutive models – visco-hypoplasticity (VHP), Tresca (TRE), and ISA-hypoplasticity (ISA) – are utilised due to the uncertainties discussed in the previous section.

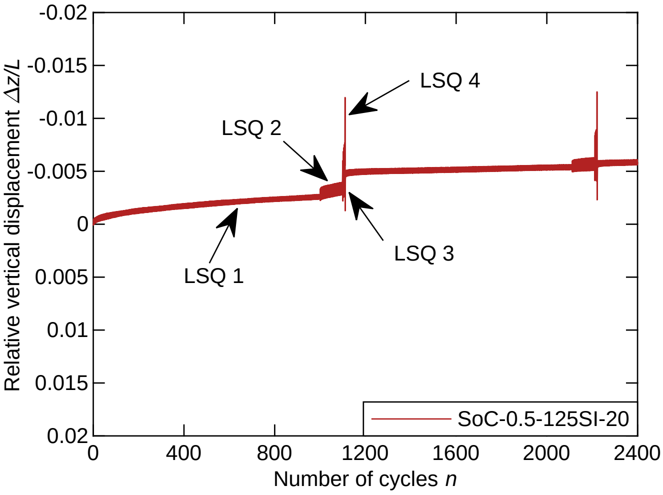

(a)

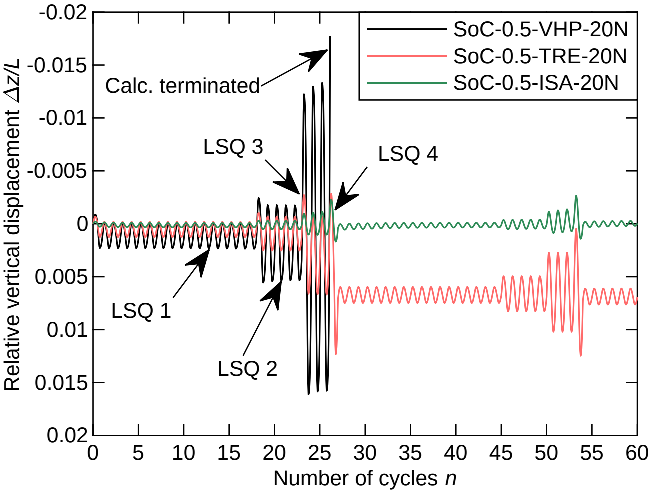

(b)

Figure 8.25: History of vertical displacements during cyclic loading as per LC 20N obtained from experiments (a) and numerical simulations (b) in SoC.

Figure 8.25b shows that each of the three numerical models yields different displacement amplitudes in LSQ 1. An almost elastic long term behaviour during LSQ 1 is observed during the centrifuge test presented in Figure 8.25a. The calculation employing the Tresca constitutive model provides a sufficient match for LSQ 1. This also holds for LSQ 2. The Tresca constitutive model yields elastic-plastic response during the first cycle of each LSQ of the first loading package and elastic response otherwise. The calculated settlement response to LSQ 4 and the elastic behaviour that is simulated in the entire second loading package indicate that the constitutive model is not suitable. However, the calculated displacement amplitudes are within in an comparable magnitude with the measured values (see Figure 8.25).

The utilisation of visco-hypoplastic constitutive model leads to a significant overestimation of the vertical displacement amplitudes. This underpins the discussion regarding monotonic loading. The simulation terminates due to errors during the calculation of LSQ 4. The errors result from the calculation of inadequate stress states eventually causing excessive mesh distortion around the skirt tip. However, it is noted that the overall response to cyclic loading is balanced despite the occurrence of significant displacement amplitudes. This indicates that the soft tip response including potential local failure zones in clay is captured by the numerical model.

The limited tip resistance and undrained behaviour were identified to determine the displacement response based on the centrifuge test results discussed in Section 8.1. The modification of φ_c, β, the ISA input parameters, and the introduction of the bulk modulus of water K_w enable the consideration of both aspects in the hypoplastic constitutive model featuring the ISA formulation. The calculated results presented in Figure 8.25b show similar behaviour, albeit the displacement amplitudes are considerably underestimated. This indicates that the constitutive model, which is originally deemed to simulate the behaviour of sand, does not provide a sufficient solution for overconsolidated clay. Consequently, a constitutive model capturing clay plasticity and cyclic loading effects is required. An ISA implementation in advanced constitutive models for example is presented by Fuentes et al. (2018) and Fuentes et al. (2017a), but remains confidential to date.

8.2.2.3 Influence of the stress and cyclic loading amplitude

Significantly larger displacement amplitudes resulting in net uplift instead of settlements are evident from the physical experiments (see Figure 8.26a). The net displacements emerge in particular during LSQ 3 and 4. The numerical analyses results presented in Figure 8.26b have the same shortcomings that were discussed in the previous section. The increased average vertical load and the higher loading amplitudes do not have a significant influence on the analysis results. The constitutive models utilised to simulate the undrained behaviour of significantly overconsolidated kaolin clay do not yield sufficient results. This holds for simple and advanced constitutive models.

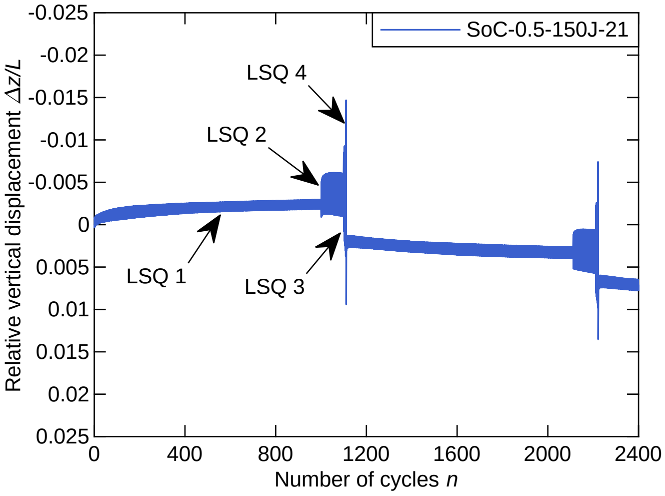

(a)

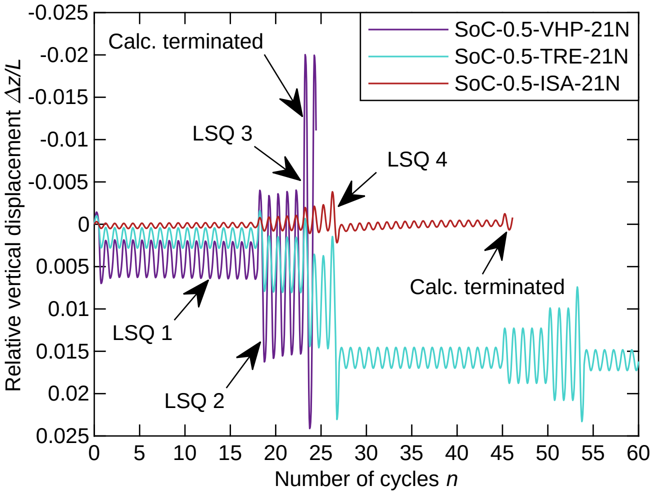

(b)

Figure 8.26: History of vertical displacements during cyclic loading as per LC 21N obtained from experiments (a) and numerical simulations (b) in SoC.

8.2.2.4 Influence of the caisson aspect ratio

The response to vertical cyclic loading of a caisson with an increased skirt length yielding an aspect ratio of $L/D = 1$ is investigated by the means of the model no. 20 listed in Table 8.2. LC 20 is applied for comparison to the results discussed in the previous sections.

The analysis results presented in Figure 8.27 show that the skirt length has a significant influence on the displacement response, as expected. Reduced displacement amplitudes and predominately elastic behaviour are observed in all four LSQs. The increased skirt length provides additional resistance in tension and in compression. Thus, it carries a significant share of the applied vertical load. This changes the load bearing behaviour and

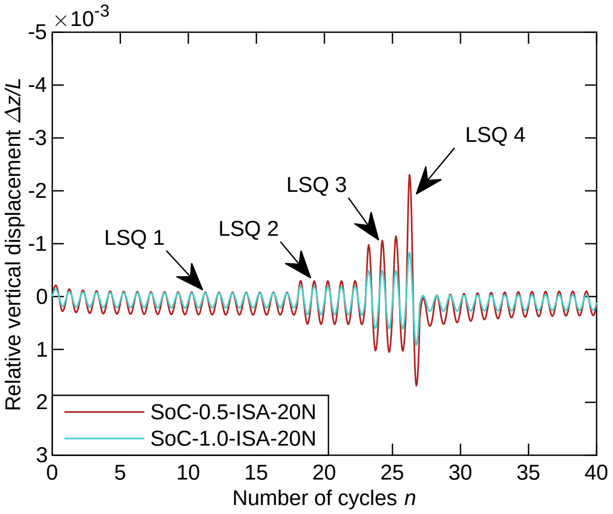

Figure 8.27: History of normalised vertical displacements during cyclic loading during subjected to caissons with aspect ratios of $L/D = 0.5$ and $L/D = 1$.

is consistent with the experimental results discussed in Section 8.1. Hence, the presented analysis results illustrate that an increased aspect ratio benefits the in-service performance of a suction caisson in SoC subjected to vertical cyclic loading. This is consistent with the experimental results discussed in Section 8.1.

8.2.3 Results and discussion: clay over sand

The calculated results are presented in non-dimensional form, unless stated otherwise. Positive values indicate compression and downward displacements, whereas negative values represent tension and upward displacements.

8.2.3.1 Monotonic load bearing mechanisms

Results obtained from experiments and numerical simulations are compared in order to evaluate and validate the numerical model. A first step includes compressive loading featuring consolidation. The drained and the rapid caisson extraction is also investigated. Each calculation is performed with model no. 10 as referred in Table 8.2.

The calculated response to the application of a vertical load of $V = 5850\,\text{kN}$ ($V/A = 116\,\text{kPa}$) and subsequent unloading to $V = 400\,\text{kN}$ ($V/A = 8\,\text{kPa}$) is presented in Figure 8.28. The calculated vertical displacements resulting from compressive loading are enveloped by the experimental results. The displacements resulting unloading to $V/A = 8\,\text{kPa}$ is measured in test Cos-0.5-350SIf-10 and the back calculation have a similar magnitude. Hence, the numerical model is suitable for the simulation of the monotonic vertical compressive loading and unloading of a suction caisson foundation.

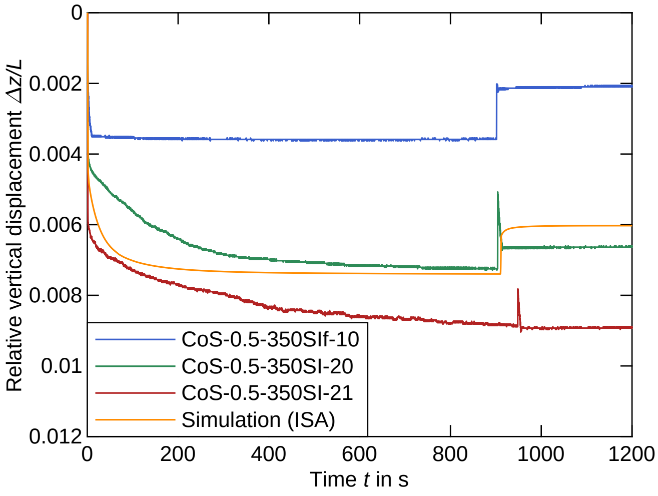

Figure 8.28: History of vertical displacements during static loading in CoS.

Figure 8.29a shows the measured and calculated vertical stress required for the drained suction caisson extraction in CoS. A sufficiently low dimensionless loading rate $v' = (\Delta\dot{z}L)/c_v$ (Finnie and Randolph, 1994) is applied to ensure drained conditions. The contour plot of the normalised vertical displacements presented in Figure 8.29b shows lid separation and no soil plug heave. This confirms that drained conditions are present.

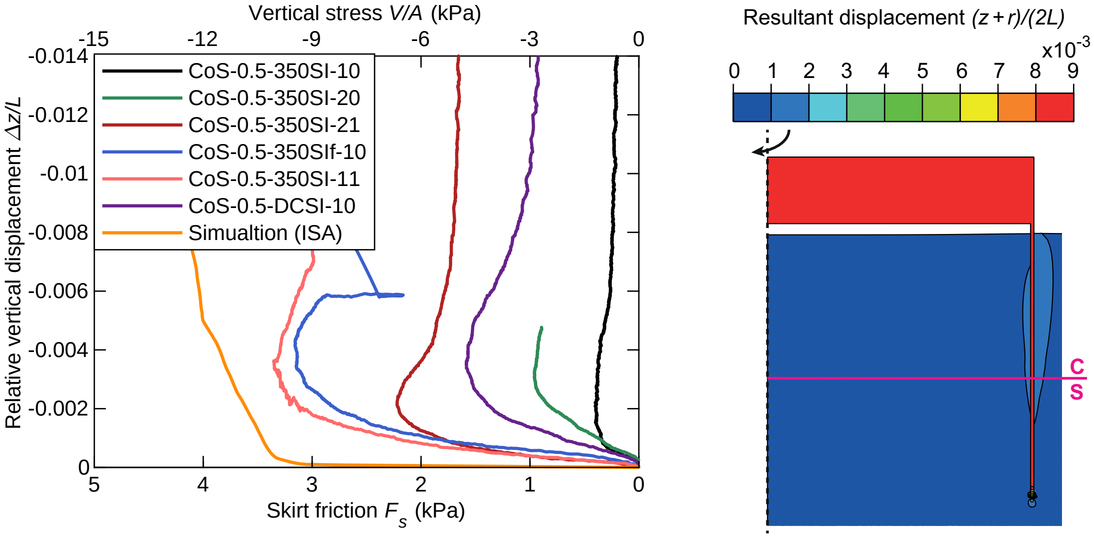

(a) (b)

Figure 8.29: Drained the extraction resistance (a) and normalised resultant displacement contours at a relative caisson displacement of $\Delta z/L = 9 \cdot 10^{-3}$ (b) in CoS.

The calculated drained extraction resistance is slightly higher than the measured values. The uplift distance required for full mobilisation of the resistance is underestimated. A considerable influence of the loading history and the skirt penetration depth is likely to effect the experimental results. This point is discussed in Subsection 8.1.3. A generalised simulation neglecting the loading history is therefore not expected to match each experimental result presented in Figure 8.29a. Hence, the numerical model is considered to be suitable for the simulation of the drained extraction of suction caissons embedded in CoS.

The results from the simulation of the rapid suction caisson extraction are presented in Figure 8.30. The calculated history of the vertical stresses and excess pore pressures shown in Figure 8.30a reveals that predominantly undrained response is present as a normalised displacement rate $v' > 30$ is applied in the numerical simulation. The contour plot presented in Figure 6.13b reveals that the entire soil plug is lifted during rapid extraction. Thus, undrained response is indeed achieved.

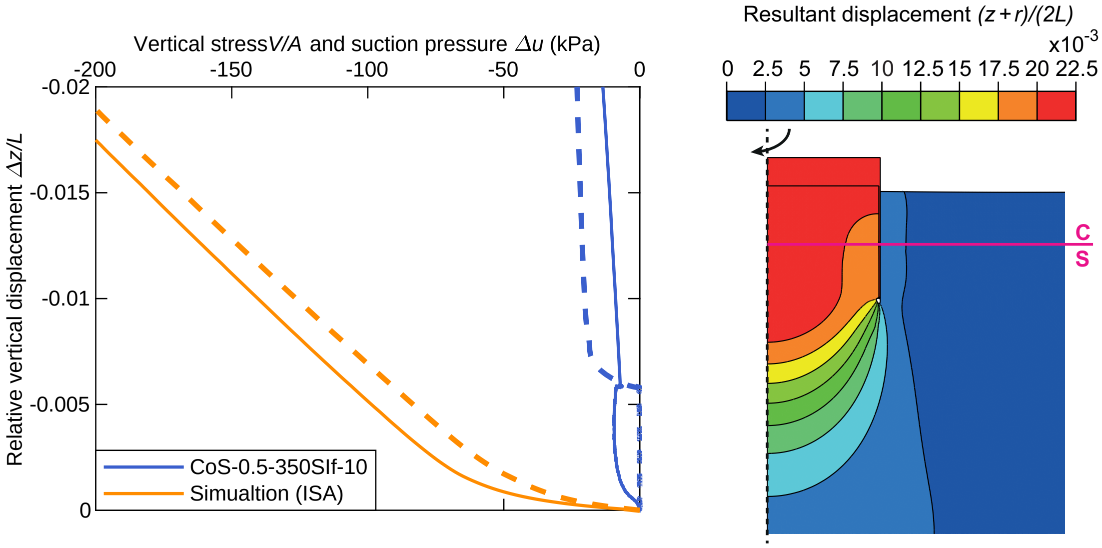

(a)

(b)

Figure 8.30: Rapid extraction resistance (solid lines) and relative suction pressure (dashed lines) (a) and normalised resultant displacement contours at a relative caisson displacement of $\Delta z/L = 22.5 \cdot 10^{-3}$ (b) in CoS.

Figure 8.30a shows that the extraction resistance approaches a certain maximum in the experiment, but increases rapidly without approaching any maximum in the numerical analysis. Cavitation and liquefaction, which are not taken into account in the calculations, are expected to play a minor role due to the soil stratification, albeit the stratification itself does. Clay plug uplift is required to mobilise resistance beyond the skirt resistance. The potential occurrence of local flow channels has been identified as a limiting factor based on the discussion in Subsection 8.1.3. Figure 8.31 shows two photographs taken during the rapid half-model caisson extraction before and after flow channels formed. Figure 8.31b also shows that clay plug uplift is present during the experiment. The local occurrence of flow channels cannot be considered in an axisymmetric numerical model employing a mesh-based method. Hence, the presented numerical model is not suitable for investigations on the rapid caisson extraction from CoS.

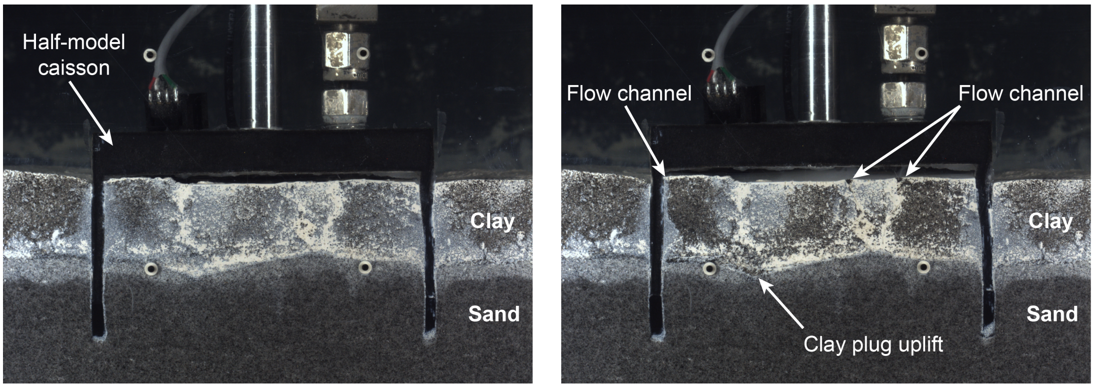

(a) (b)

Figure 8.31: Photographs of the rapid half-model caisson extraction before (a) and after (b) the formation of flow channels in CoS.

It is noted that further numerical investigations on this specific problem require large deformation methods that capture water flow through porous sand and around nearly impermeable clay. Furthermore, soil layer and soil-structure interaction must be captured as well as the localisation of failure zones in order to model arbitrarily occurring local flow channels. A double point MPM formulation (Fern et al., 2019) is a reasonable approach for instance. However, based on the current state of the art substantial development is required. The undrained caisson extraction from a CoS profile is a highly specific problem, which furthermore plays only a minor role considering the in-service performance of a suction caisson (see Subsection 8.1). Hence, the implementation is assessed not worthwhile, because of the limited overall benefit.

8.2.3.2 Cyclic load bearing mechanisms

This numerical investigation on cyclic loading targets further evaluation of the numerical model. The experimental results discussed in Section 8.1 and a numerical back analysis are compared. It is noted that the number simulated load of cycles is limited to a minimum which is considered to maintain comparability between experimental and numerical investigations.

The caisson response presented in Figure 8.32 features the first loading package of the experimental and the numerical data. The caisson response in LSQ 1 is similar: The vertical displacement response shows almost elastic behaviour in LC 20 and marginal settlements in LC 21. LSQ 2 yields marginal net settlements in LC 20 and approximately $\Delta z/L = 0.01$ total caisson downward displacement in LC 21. The numerical simulation results feature a similar trend in both LCs. The calculated response during LSQ 3 and 4 is comparable to the experimental results in LC 21. This holds for the displacement amplitude and for the net displacements. The experimental and the calculated results differ considerably in LSQ 3 and 4 of LC 20. Net settlement response is calculated from the numerical analysis. Net uplift and significantly larger displacement amplitudes are observed during LSQ 3 and 4 during the centrifuge experiment (see Figure 8.32a).

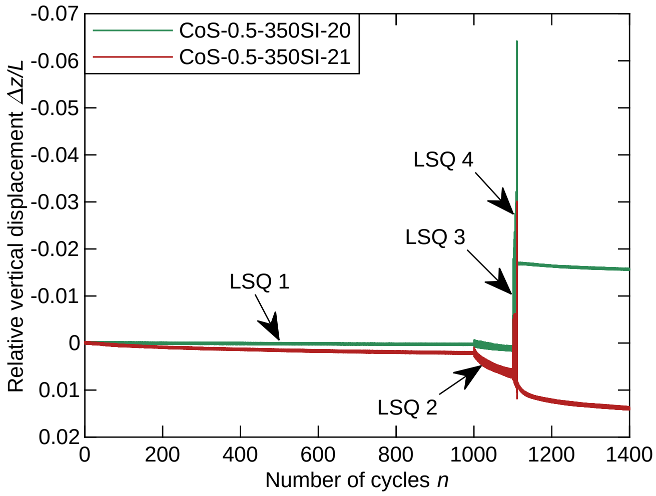

(a)

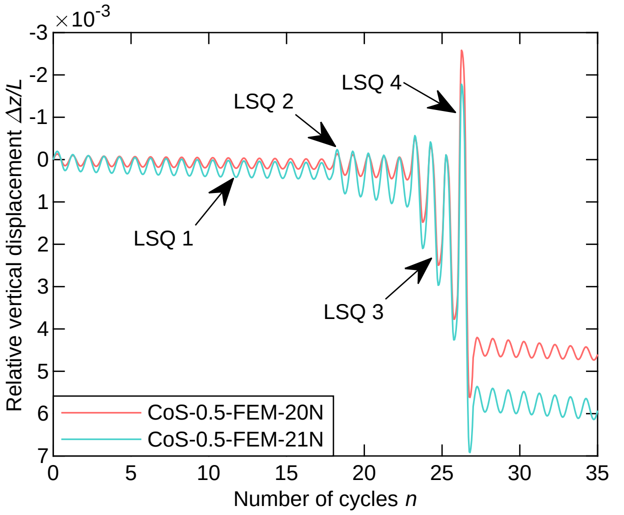

(b)

Figure 8.32: History of vertical displacements during cyclic loading during obtained from experiments (a) and numerical simulations (b) in CoS.

Figure 8.33 shows the calculated pore pressure development at the lid invert and below the clay plug. The numerical analyses indicate distinct excess pore pressure development in compression, but the centrifuge tests, discussed in Section 8.1, only show minimal excess pore pressures during LSQ 1 and 2. The pore pressures at the lid invert remain negative during LSQ 3 and 4 in the centrifuge experiments featuring LC 20 (see Figure 8.17) and LC 21 (see Figure 8.19a). However, the load transfer mechanisms in tension are similar. This indicates that the mobilisation of the skirt resistance is modelled sufficiently. This leaves the tip resistance to be the source for inaccuracy: The skirt tip region consists of small elements in the numerical analyses. In addition, separation of the contact surfaces at the skirt tip is required in order to achieve appropriate response in tension. This results

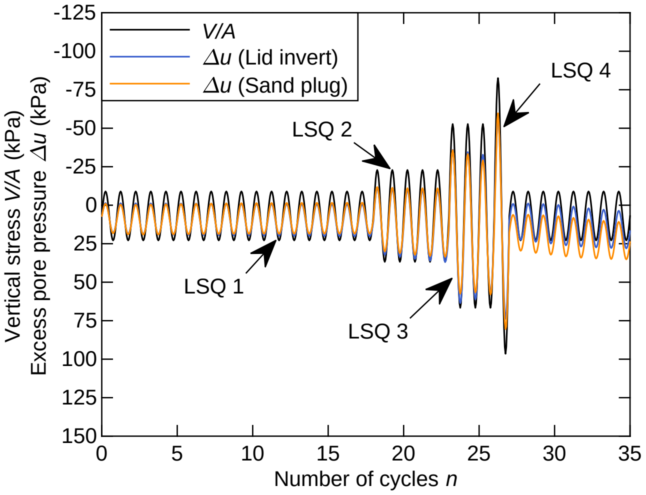

(a)

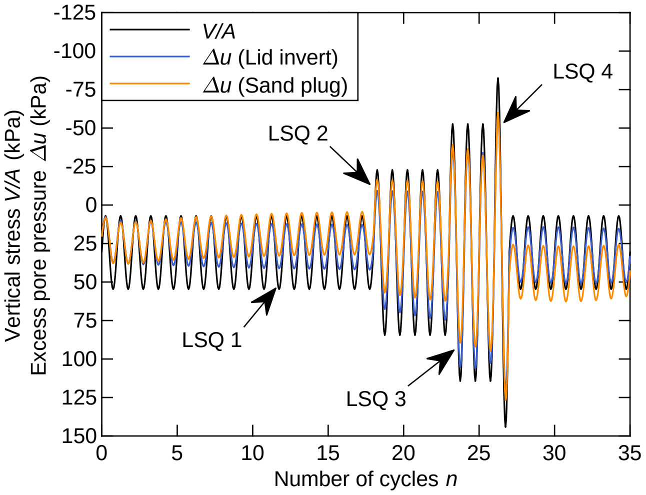

(b)

Figure 8.33: History of the applied stress and excess pore pressure at the lid invert during LSQ 1, 2, and 3 in simulation CoS-0.5-FEM-20 (a) and CoS-0.5-FEM-21 (b).

in an underestimation of the tip resistance in compression. Hence, the conceptual limitations of the Lagrangian FEM restrict the applicability of numerical predictionism methods when it comes to vertical cyclic loading including compressions and tension. Hence, the tip resistance is underestimated by the numerical analyses due to modelling limitations.

8.2.3.3 Influence of the stress and cyclic loading amplitude

Significantly larger displacement amplitudes resulting in net uplift (Figure 8.32a) instead of settlements are evident from the physical experiments at a low magnitude compressive average load (LC 20). The net uplift emerges in particular during LSQ 3 and 4, when clay plug uplift is expected to occur due to the magnitude of the applied tensile load exceeding the plug self-weight and internal skirt friction. Seepage flow into the sand plug results. This mechanism is considered in the two-phase numerical analysis. The calculated suction pressure development in the sand part of the soil plug is shown in Figure 8.33. However, accompanying material displacement around the skirt tip is not captured in the numerical model due to insufficient element deformation. Consequently, the mobilisation of the tip resistance and therefore the stiffness response in the compressive cycle following tensile loading becomes inaccurate in the numerical simulation with cyclic increased loading amplitudes. Numerical analyses featuring low magnitude compressive average loads (LC 20) and excursions into tension that considerably exceeding the drained frictional capacity are particularly inaccurate. However, predictions are more accurate for increased average compressive average load – e. g. for LC 21.

8.2.3.4 Influence of the caisson aspect ratio

The response to vertical cyclic loading of a caisson with an increased skirt length yielding an aspect ratio of $L/D = 1$ is investigated by the means of model 20 listed in Table 8.2. LC 20 is applied for comparison to the results discussed in the previous sections.

The analysis results presented in Figure 8.34 show that the skirt length has a major influence on the displacement response. Significantly reduced displacement amplitudes and predominately elastic behaviour is observed in all four LSQs, if the aspect ratio is increased from $L/D = 0.5$ to $L/D = 1$. The comparison between Figure 8.33a and Figure 8.34b emphasises that the increased skirt length provides additional resistance in tension and compression and therefore carries a significant share of the applied vertical load. This is accompanied by a reduction of the internal pore pressure amplitudes. The numerical results indicate that the pore pressures at the lid invert are still transferred into the underlying sand part of the soil plug. Hence, the presented results illustrate that an increased aspect ratio indeed benefits the in-service performance of a suction caisson subjected to vertical cyclic loading.

8.2.4 Remarks on the numerical simulations

The performed numerical analyses show that monotonic loading is captured sufficiently by the utilised numerical models, if liquefaction and cavitation are not considered. A back calculation of the experimental results, i. e. the consolidation time, settlements, and the drained extraction resistance is feasible in SoC and SoC. Cavitation and liquefaction typically limit the rapid extraction resistance, which should be taken into account, if further insights into this specific topic are required. The presented numerical simulations featuring repetitive loading provide sufficient results, if only moderate loading amplitudes are considered. Limitations of the currently available constitutive models restrain numerical analyses involving SoC.

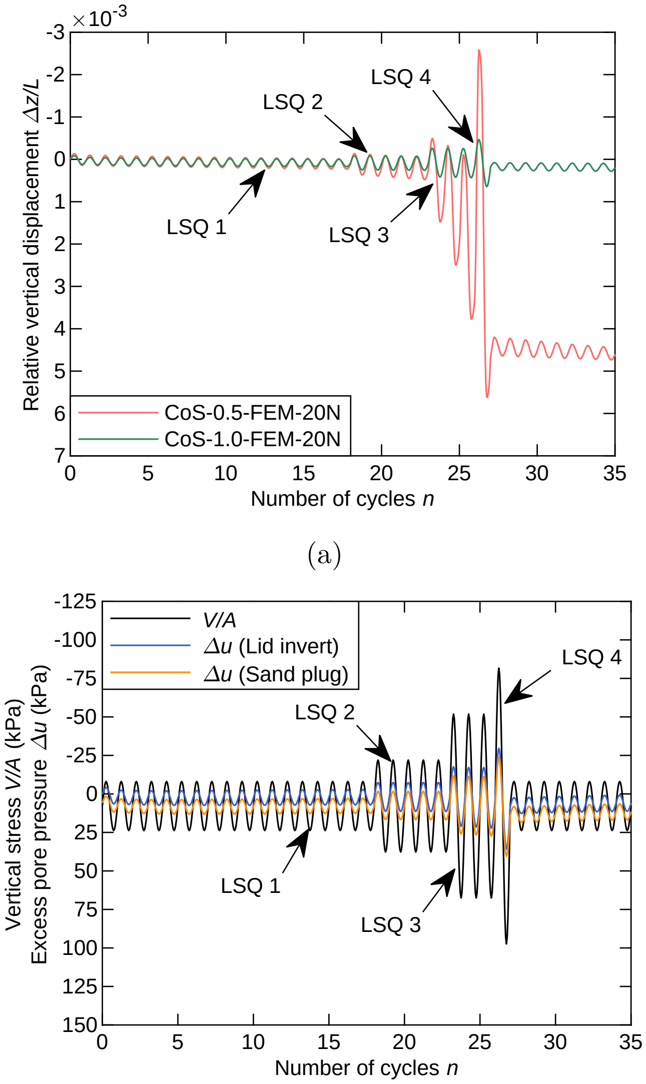

(a)

(b)

Figure 8.34: History of normalised vertical displacements during cyclic loading subjected to caissons with aspect ratios of $L/D = 0.5$ and $L/D = 1$ (a) and history of applied stress and excess pore pressure at the lid invert in simulation CoS-1.0-FEM-20N (b).

8.3 Concluding remarks on the response to vertical cyclic loading in layered soil

Investigations of the suction caisson performance under vertical cyclic loading test into tension in layered soils have been discussed in this chapter. The experimental and numerical investigations featuring SoC profiles support the following findings:

(1) No evidence of a permanent effect on the behaviour under vertical cyclic loading was found as the soil plug was shown to be compressed through lid contact.

(2) The skirt embedment into underlying low permeability clay encapsulates the internal sand plug and leads to predominately undrained behaviour in compression and tension. The relatively low tip resistance in clay balances the displacement response to cyclic loading around a compressive average load – including significant excursions into tension.

(3) The displacement amplitudes relate to the cyclic loading amplitude and the net displacement direction is governed by the average vertical stress. The model caissons in SoC withstood maximum tensile loads that significantly exceeded the drained capacity in numerous loading cycles without excessive net displacements.

(4) An increased aspect ratio – i. e. skirt length – leads to an overall stiffer response during cyclic vertical loading, as expected.

(5) Predictions on the response to monotonic and cyclic vertical loading are feasible by the means of numerical simulations within certain frontiers in SoC.

The experimental and numerical investigations featuring CoS profiles support the following findings:

(1) A permanent effect of the installation on the response under vertical cyclic loading was not found.

(2) The response to tensile loading is complex. Clay plug uplift and the resulting suction pressure transferral into the underlying sand were identified to affect the extraction resistance and response under cyclic vertical loading. As in homogeneous sand, the resulting drainage regime crucially affects the response. Furthermore, the relatively large tip resistance in the underlying sand limits settlements. This favours net uplift in response to vertical cyclic loading. Consequently, sufficiently compressive average vertical stresses or limited excursions into tension appear to be required to limit net uplift.

(3) An increased skirt wall thickness is accompanied by additional tip resistance. This yields reduced settlements, while the response to tensile loading remains unaffected. Consequently, an increased skirt wall thickness intensifies the net uplift response to vertical cyclic loading featuring excursions into tension in clay over profiles.

(4) Predictions on the response to monotonic and cyclic vertical loading are feasible by the means of numerical simulations within certain limitations in CoS.

The presented series of centrifuge tests and numerical analyses demonstrates the applicability of suction caisson foundations in SoC and CoS. The results also set physical and analytical frontiers for the utilisation of suction caisson foundations for OWTs in layered soil. However, the results are considered to encourage the utilisation of suction caisson foundations for OWTs.

9 Conclusion

9.1 Sand

A total of 15 centrifuge tests and complementary numerical simulations featuring the material point method and the finite element method were performed. The investigations covering uniform sand profiles aim to improve the currently recommended design practice. A potential influence of the suction installation on the in-service performance and significant excursions into tension during cyclic loading are complex processes, which are only roughly predictable and therefore a source of uncertainty.

The presented results confirm the feasibility of the suction caisson installation in sand featuring different effective permeabilities of the soil and pumping flow rates. The pumping flow rate applied during suction caisson installation is not found to influence the soil plug, as shown by cone tip resistance profiles obtained inside the caisson following installation. The underlying mechanisms visualised through validated numerical simulations utilising the material point method are found to be virtually independent from the caisson wall thickness and the diameter. Only the actual extend of the *in situ* deformations is determined by the caisson dimensions. The suction installation is naturally accompanied by plug heave and potential loosening to a certain extend. No evidence for a permanent influence of the suction caisson installation on the in-service performance is found. The achieved skirt penetration depth and the establishment of lid contact are identified to have an influence on the in-service performance.

The response to vertical cyclic loading is determined by the drainage regime: The excess pore pressures at the lid invert cycle with the applied stresses. There is no indication of accumulative effects within the scope of the presented investigations. Undrained behaviour at the lid invert is concluded as the total stresses transferred to the lid are entirely carried by excess pore pressures. The magnitude of the respective vertical displacement is found to be highly depended on the *in situ* effective soil permeability and therefore on the drainage regime.

The caisson foundation mobilised resistance beyond the drained frictional capacity without permanent displacement when subjected to tensile loads during cyclic loading. Predominately elastic response is observed, if the drained frictional capacity is exceeded up to a maximum of 2.5 times. Based on the presented results, substantial permanent net heave, which is expected to be critical for the serviceability of an OWT, occurs beyond this threshold. It is noted that cavitation and liquefaction within the soil plug are found to be involved at these extreme loading scenarios.

The presented findings underpin that suction caissons are suitable to support offshore wind turbines. Potential consequences for the in-service performance only arise from incomplete skirt penetration. Plug heave and loosening have no significant effect on the in-service performance – especially if lid contact is established. A potentially existing gap between the soil plug and the lid invert can be grouted in prototype applications. Hence, the requirement of lid contact can be satisfied. A skirt penetration of more than $0.9L$ is expected to be feasible for a $L/D = 0.5$ caisson based on the presented results. Consequently, lid contact and an embedded skirt length of $0.9L$ are recommended to be taken into account for predictions on the in-service performance. The response to vertical cyclic loading can be predicted with analytical and numerical methods. The presented methods cover excursions into tension during cyclic loading of at least 2.5 times the drained frictional capacity. Based on the presented results, it is concluded that tensile loads exceeding the drained frictional capacity can be considered for the suction caisson design in uniform sand.

9.2 Layered soil

9.2.1 Sand over clay

A total of eight centrifuge tests and complementary numerical simulations featuring the material point method and the finite element method were performed. The investigations covering sand over clay soil profiles aim to develop improved recommendations for the suction caisson design. The influence of the sand top layer on the suction installation and the in-service performance of the caisson when subjected to cyclic loading featuring compression and tension are sources of uncertainty.

The presented investigations confirm that the suction installation in sand over clay is unproblematic. It is feasible to apply different pumping flow rates, while in most cases only moderate suction pressure is required – even in stiff, overconsolidated clay. No evidence of a permanent effect of the suction installation on the in-service performance is found. Complete skirt penetration is sufficiently reached and lid contact including plug re-compression is confirmed through the presented results. Sand drag down into the underlying clay is observed, albeit no high permeable flow channels form – especially not if thin-walled caisson skirts ($t/L \leq 160$) are considered. Consequently, no evidence of a permanent effect on the displacement behaviour under vertical cyclic loading is expected in sand over clay.

Undrained response is found to determine the caisson in-service performance when subjected to vertical cyclic loading. The relatively low tip resistance in clay balances the displacement response around a compressive average load – including significant excursions into tension. The model caissons utilised in the centrifuge tests in sand over clay withstood maximum tensile loads that significantly exceeded the drained capacity in numerous loading cycles without excessive net displacements.

Based on the discussed findings, it is concluded that the suction caisson installation is feasible and predictable in sand over clay. No evidence for potential consequences for the in-service performance is found. Therefore, the installation process is found to be negligible for predictions on the in-service performance – especially if lid contact is established. Predictions on the in-service performance of suction caissons embedded in sand over clay require numerical methods. However, these are limited when cyclic loading and substantially overconsolidated clays are involved. The numerical investigations demonstrate that accessible constitutive models for clay usually do not cover repetitive loading sufficiently and others focus on normally consolidated clay. It is concluded that further research on suitable constitutive models is required in order to improve design methods for cyclic vertical loading. This demand is motivated by the presented experimental investigations. The results show a reasonable potential for suction caissons servicing as foundations for offshore wind turbines, because of the balanced displacement response to vertical cyclic loading. Furthermore, an increased caisson aspect ratio – i. e. skirt length – leads to an overall stiffer response without significantly compromising the balanced foundation stiffness, which is certainly beneficial for the design process.

9.2.2 Clay over sand

A total of eight centrifuge tests and complementary numerical simulations featuring the material point method and the finite element method were performed. The presented investigations aim to prove the feasibility of the installation of suction caisson foundations in clay over sand profiles. The clay top layer was expected to play a major role in the suction installation mechanisms. Furthermore, the influence on the in-service performance of the caisson when subjected to significant tensile loading is a major source of uncertainty.

The experimental and numerical results demonstrate that the suction caisson installation in clay over sand is indeed feasible. The clay plug uplift transfers suction pressure into the underlying sand. The induced seepage flow reduces the tip resistance and thus enables further penetration. A permanent effect of the installation on the response under vertical cyclic loading is not found as lid touch down is reliably established. A permanent effect on the in-service performance is therefore not expected.

The response to vertical loading, particularly in tension, is complex: Clay plug uplift and the resulting suction pressure transferral into the underlying sand is identified to have a major effect on the uplift resistance to monotonic and cyclic vertical loading. As it is the case in homogeneous sand profiles, the resulting drainage regime crucially affects the response. Furthermore, the relatively large tip resistance in the underlying sand limits settlements. This favours net uplift in response to vertical cyclic loading. Consequently, sufficiently compressive average vertical stresses or limited excursions into tension appear to be required to limit net uplift response.

Based on the discussed findings it is concluded that the suction caisson installation is feasible in clay over sand. No evidence for potential consequences for the in-service performance is found. Hence, the suction installation is found to be negligible for predictions on the in-service performance – especially if lid contact is established. Predictions on the in-service performance of suction caisson embedded in clay over sand require numerical models. The available methods capture essential mechanisms, like undrained response of the clay top layer and pore pressure transferral into the underlying sand. Hence, predictions of the suction caisson response when subjected with vertical loading are possible within the limitations pointed out through the experiments: A sufficient average vertical load is required to allow moderate excursions into tension. Under consideration of the presented experimental and numerical results it is concluded that tensile loads exceeding the drained frictional capacity can be taken into account for the suction caisson foundation design in clay over sand profiles.

9.3 Concluding remarks

The suction caisson installation is feasible in every investigated soil condition: sand, sand over clay, and clay over sand. The risk of premature refusal or severe plug heave and loosening is considered to be marginal based on numerous $L/D = 0.5$ model caisson installations in centrifuge tests. However, the substantial tip resistance in dense sand compromises the installation of caissons with aspect ratios $L/D > 0.5$. Advanced installation techniques, involving cyclic pumping for instance, are expected to be improved through future research activities in order to enable the installation of a higher aspect ratio caisson in dense sand and clay over dense sand.

Cyclic loading into tension is possible to an extend that exceeds the drained frictional capacity of a caisson embedded in uniform sand. Physical evidence is gathered and advanced numerical methods can provide sufficient predictions for vertical cyclic loading: The internal suction pressure developing in response to tensile loading reliably provides uplift resistance. The serviceability is expected not to be compromised, if the generated suction pressures fall sufficiently below the cavitation and liquefaction limit. Based on the presented data, it is recommended to consider the development of internal suction pressure in the suction caisson design.

The presented centrifuge test results show that cyclic loading featuring significant tensile loads can be withstood by a caisson embedded in sand over clay without severe damage. The underlying load transfer mechanisms are similar to caissons embedded in uniform clay as undrained response is presented. Estimating the limiting load bearing capacities is therefore unproblematic. However, predictions on the in-service performance featuring cyclic loading effects are complicated: Numerical methods utilising advanced constitutive models are required. Constitutive models covering cyclic loading effects in normally and overconsolidated clay are rare, currently under development, or confidential and therefore hardly accessible. However, if improved constitutive models become available in the future, they are expected to improve the currently recommended design practice.

A caisson embedded in a clay over sand soil profile can be subjected to cyclic loading into tension to an extend that exceeds the drained frictional capacity. Physical evidence is gathered and advanced numerical methods can provide sufficient predictions for vertical cyclic loading: The internal suction pressure is indeed transferred into the underlying sand and therefore provides uplift resistance. The serviceability is expected not to be compromised, if the generated suction pressures fall sufficiently below the cavitation and liquefaction limit and flow channels do not occur. Based on the presented data, it is recommended to consider the development of internal suction pressure in the suction caisson design.

It is summarised that this thesis provides a novel experimental database and guidelines for improvements on the design of suction caisson foundations subjected to vertical cyclic loading featuring excursions into tension. It is desired that the presented results will help to improve the existing recommended practice and develop future guidelines for the suction caisson design for offshore wind turbines.

10 Summary

The growing number of offshore wind farm developments implies an increased demand for offshore foundation systems. Suction caissons, which support some of the largest offshore platforms ever build for the oil and gas industry (Hansteen et al., 2003), are also suitable foundation systems for most bottom fixed offshore wind turbines located at North Sea developments (Tjelta, 2015). The technology transfer from caissons supporting heavy oil and gas platforms towards caisson based offshore wind turbines, which are substantially lighter, began almost two decades ago (Byrne et al., 2002; Ibsen et al., 2005) and is not completed yet.

Uncertainties regarding the suction installation and the response to vertical cyclic loading featuring small average loads still exist. A possible effect of the suction caisson installation on the in-service performance cannot be ruled out to date. The consideration of developing internal suction pressure during rapid vertical loading in the foundation design is questionable to date. Furthermore, suitable prediction methods for the response of suction caissons subjected to vertical cyclic loading including excursions into tension are limited.

Considering layered soil profiles – sand over clay and clay over sand – and therefore the influence of low permeable layers on the suction installation and caisson in-service performance adds further complexity. Publications featuring caissons embedded in layered soils are limited compared to investigations on uniform clay or sand profiles. An experimental basis featuring tests on the suction caisson response to vertical cyclic loading has not been published to the author's knowledge. Suitable predictions of the in-service performance of a caisson subjected to vertical cyclic loading including excursions into tension are hardly feasible today. However, significant excursions into tension are arguably targeted for future geotechnical design.

Two series of centrifuge tests featuring sand and layered soil profiles were conducted. The first series focusing on uniform sand includes installation tests, cone penetration tests inside a previously installed caisson, and vertical cyclic loading tests. Next, the experimental studies were extended towards sand over clay and clay over sand profiles. Full-model installation and cyclic loading tests were complemented by half-model tests employing particle image velocimetry post analyses. The suction caisson installation was further investigated through numerical calculations. In order to do so, an axisymmetric, coupled two-phase material point method model has been implemented and utilised for investigations on the suction caisson installation. Potential prediction methods for the vertical cyclic load bearing behaviour including analytical and numerical analyses were developed and enhanced, respectively. The novel prediction methods were benchmarked and validated under consideration of the experimental data.

The suction caisson installation is found to be feasible in uniform sand, in sand over clay, and in clay over sand soil profiles. No evidence for a systematic influence of the suction installation on the in-service performance is noticed as vertical cyclic loading was investigated. The caisson internal excess pore pressures provide additional resistance in tension. Consequently, tensile loads exceeding the frictional capacity can be sustained to a certain extend without permanent settlement or uplift, i. e. without potentially violating serviceability criteria. Significant excursions into tension – more than three times the frictional capacity – yield net uplift during cyclic loading, if the skirt tip is embedded in sand. A low permeable (clay) top layer increases the resulting displacement amplitudes. Softer tip response, i. e. a skirt tip that is embedded in clay, appears to be beneficial as settlements and uplift are more balanced. A shift of the average vertical load into compression also balances the vertical displacements. An increased caisson aspect ratio, which provides more skirt friction, decreases the vertical displacement amplitude in general.

Numerical simulations involving suction caissons are arguably appealing as experimental investigations require a state of the art centrifuge lab. However, they are highly complex: Advanced soil-structure iteration, large deformations, pore pressure development, liquefaction, cavitation, void ratio, and permeability change cyclic loading effects, as well as uniform and layered soil profiles can play a role. The developed analytical and numerical models and the presented analyses results provide basic guidelines for computational based suction caisson design. The presented work's goal is to reinforce confidence in the suction caisson technology for offshore wind turbines. Hence, this work aims to unlock the full potential of carbon neutral and more sustainable energy supply from offshore wind farms. Therefore, this thesis is dedicated to contributing to the fight against the climate change.

Literature

Achmus, M., C. T. Akdag, and K. Thieken (2013). “Load-Bearing Behavior of Suction Bucket Foundations in Sand”. In: *Applied Ocean Research* 43, pp. 157–165. DOI: `10.1016/j.apor.2013.09.001`.

Achmus, M. and K. Thieken (2014). “Numerical Simulation of the Tensile Resistance of Suction Buckets in Sand”. In: *The 24th International Ocean and Polar Engineering Conference*. Ed. by Jin S. Chung. Vol. 4. Cupertino, California: ISOPE, pp. 231–239.

Adrian, R. J. (1991). “Particle-Imaging Techniques for Experimental Fluid Mechanics”. In: *Annual Review of Fluid Mechanics* 23.1, pp. 261–304. DOI: `10.1146/annurev.fl.23.010191.001401`.

Allersma, H. G. B. (2003). “Centrifuge Research on Suction Piles: Installation and Bearing Capacity”. In: *Proceedings BGA Int. Conf. On Foundations*, pp. 91–98.

Allersma, H. G. B., J. R. Hogervorst, and M. Pimoulle (2001). “Centrifuge Modelling of Suction Pile Installation Using a Percussion Technique”. In: *Proceedings 11th International on Offshore and Polar Engineering Conference*. Vol. 2, pp. 620–625.

Allersma, H. G. B., A. A. Kierstein, and D. Maes (2000). “Centrifuge Modelling on Suction Piles under Cyclic and Long Term Vertical Loading”. In: *Proceedings of the 10th International Offshore an Polar Engineering Conference (ISOPE-2000)*. Vol. 2, pp. 334–341.

Allersma, H. G. B., F. J. A. Plenevaux, and J.-F. P. C. M. E. Wintgens (1997). “Simulation of Suction Pile Installation in Sand in a Centrifuge”. In: *Proceedings 7th International Offshore and Polar Engineering Conference*, pp. 761–766.

Andersen, K. H., H. P. Jostad, and R. Dyvik (2008). “Penetration Resistance of Offshore Skirted Foundations and Anchors in Dense Sand”. In: *Journal of Geotechnical and Geoenvironmental Engineering* 134.1, pp. 106–116. DOI: `10.1061/(ASCE)1090-0241(2008)134:1(106)`.

Bardenhagen, S. G., J. U. Brackbill, and D. Sulsky (2000). “The material-point method for granular materials”. In: *Computer Methods in Applied Mechanics and Engineering* 187.3-4, pp. 529–541. DOI: `10.1016/S0045-7825(99)00338-2`.

Bardenhagen, S. G., J. E. Guilkey, K. M. Roessig, J. U. Brackbill, W. M. Witzel, and J. C. Foster (2001). “An Improved Contact Algorithm for the Material Point Method and Application to Stress Propagation in Granular Material”. In: *Computer Modeling in Engineering & Sciences* 2.4, pp. 509–522. DOI: `10.3970/cmes.2001.002.509`.

Bienen, B. and M. J. Cassidy (2006). “Advances in the three-dimensional fluid–structure–soil interaction analysis of offshore jack-up structures”. In: *Marine Structures* 19.2-3, pp. 110–140. DOI: `10.1016/j.marstruc.2006.09.002`.

Bienen, B., R. T. Klinkvort, C. D. O’Loughlin, F. Zhu, and B. W. Byrne (2018a). “Suction caissons in dense sand, part I: Installation, limiting capacity and drainage”. In: *Géotechnique* 68.11, pp. 937–952. DOI: `10.1680/jgeot.16.P.281`.

– (2018b). “Suction caissons in dense sand, part II: Vertical cyclic loading into tension”. In: *Géotechnique* 68.11, pp. 953–967. DOI: `10.1680/jgeot.16.P.282`.

Boussinesq, M. J. (1885). *Application des potentiels et d’analysea l’étude de l’équilibre et du mouvement des solides élastiques, avec des notes étendues sur divers points de physique mathématique.* Paris: Gauthier-Villard Imprimeur Libraire.

Broughton, P., R. L. Davies, and J. Jenkins (2013). “The Removal of the Maureen Steel Gravity Platform”. In: *Offshore Technology Conference 2013.* Vol. OTC 11027. Offshore Technology Conference, pp. 1–14. DOI: `10.4043/11027-MS`.

Bye, A., C. T. Erbrich, and B. Rognlien (1995). “Geotechnical Design of Bucket Foundations”. In: *Offshore Technology Conference 1995.* Vol. OTC7793 (OTC1193). Offshore Technology Conference, pp. 869–883. DOI: `10.4043/7793-MS`.

Byrne, B. W. and G. T. Houlsby (2002). “Experimental Investigations of Response of Suction Caissons to Transient Vertical Loading”. In: *Journal of Geotechnical and Geoenvironmental Engineering* 128.11, pp. 926–939. DOI: `10.1061/(ASCE)1090-0241(2002)128:11(926)`.

– (2004). “Experimental Investigations of the Response of Suction Caissons to Transistent Combined Loading”. In: *Journal of Geotechnical an Geoenvironmental Engineering* 130.3, pp. 240–253. DOI: `10.1061/(ASCE)1090-0241(2004)130:3(240)`.

Byrne, B. W., G. T. Houlsby, C. Martin, and P. Fish (2002). “Suction Caisson Foundations for Offshore Wind Turbines”. In: *Wind Engineering* 26.3, pp. 145–155. DOI: `10.1260/030952402762056063`.

Cerfontaine, B., F. Collin, and R. Charlier (2016). “Numerical modelling of transient cyclic vertical loading of suction caissons in sand”. In: *Géotechnique* 66.2, pp. 121–136. DOI: `10.1680/jgeot.15.P.061`.

Chow, S. H., C. D. O’Loughlin, C. Gaudin, and J. T. Lieng (2018). “Drained monotonic and cyclic capacity of a dynamically installed plate anchor in sand”. In: *Ocean Engineering* 148, pp. 588–601. DOI: `10.1016/j.oceaneng.2017.11.051`.

Colliat, J-L. (2002). “Anchors for Deepwater to Ultradeepwater Moorings”. In: *Offshore Technology Conference 2002.* Vol. OTC 14306. Offshore Technology Conference. DOI: `10.4043/14306-MS`.

Colreavy, C., C. D. O’Loughlin, and M. F. Randolph (2016). “Experience with a dual pore pressure element piezoball”. In: *International Journal of Physical Modelling in Geotechnics* 16.3, pp. 101–118. DOI: `10.1680/jphmg.15.00011`.

Cotter, O. (2010). “Installation of suction caisson foundations for offshore renewable energy structures”. PhD thesis. Oxford: University of Oxford.

Dassault Systèmes (2018). *Abaqus User’s Manual.* France.

DOW (2002). *Methocel cellulose ethers: Technical handbook.* United States of America.

Fern, E. J., A. Rohe, K. Soga, and E. Alonso (2019). *Material Point Method for Geotechnical Engineering: A Practical Guide.* [S.l.]: CRC Press.

Finnie, I.M.S. and M. F. Randolph (1994). “Punch-through and liquefaction induced failure of shallow foundations on calcareous sediments”. In: *Seventh International Conference on the Behaviour of Offshore Structures.* Vol. 1. United Kingdom: Pergamon, pp. 217–230.

Fiumana, N., C. Gaudin, Y. Tian, and C. D. O'Loughlin (2018). "Physical modelling of active suction for offshore renewables". In: *Physical Modelling In Geotechnics, Volume 1*. [S.l.]: CRC Press, pp. 603–608.

Foglia, A., L. B. Ibsen, L. V. Andersen, and H. R. Roesen (2012). "Physical Modelling of Bucket Foundation Under Long-Term Cyclic Lateral Loading. International Society of Offshore and Polar Engineers". In: *ISOPE-2012 Rhodes*. Ed. by J. S. Chung. Cupertino, California: International Society of Offshore and Polar Engineers (ISOPE).

Fuentes, W., M. Hadzibeti, and T. Triantafyllidis (2017a). "Constitutive Model for Clays Under the ISA Framework". In: *Holistic simulation of geotechnical installation processes*. Ed. by T. Triantafyllidis. Vol. 80. Lecture notes in applied and computational mechanics. Cham: Springer, pp. 115–129. DOI: `10.1007/978-3-319-23159-4_6`.

Fuentes, W., M. Tafili, and T. Triantafyllidis (2018). "An ISA-plasticity-based model for viscous and non-viscous clays". In: *Acta Geotechnica* 13.2, pp. 367–386. DOI: `10.1007/s11440-017-0548-y`.

Fuentes, W. and T. Triantafyllidis (2015a). "ISA model: A constitutive model for soils with yield surface in the intergranular strain space". In: *International Journal for Numerical and Analytical Methods in Geomechanics* 39.11, pp. 1235–1254. DOI: `10.1002/nag.2370`.

– (2015b). "ISA: A constitutive model for deposited sand". In: *Aktuelle Forschung in der Bodenmechanik 2015*. Ed. by T. Schanz and A. Hettler. Vol. 112. Berlin: Springer Vieweg, pp. 169–187. DOI: `10.1007/978-3-662-45991-1_10`.

Fuentes, W., T. Triantafyllidis, and C. Lascarro (2017b). "Evaluating the Performance of an ISA-Hypoplasticity Constitutive Model on Problems with Repetitive Loading". In: *Holistic simulation of geotechnical installation processes*. Ed. by T. Triantafyllidis. Vol. 82. Lecture notes in applied and computational mechanics. Cham: Springer, pp. 341–362. DOI: `10.1007/978-3-319-52590-7_16`.

Fuentes, W., T. Wichtmann, M. Gil, and C. Lascarro (2019). "ISA-Hypoplasticity accounting for cyclic mobility effects for liquefaction analysis". In: *Acta Geotechnica* 30.10, p. 895. DOI: `10.1007/s11440-019-00846-2`.

Goodman, L. J. (1961). "The Feasibility of Vacuum Anchorage in Soil". In: *Géotechnique* 11.4, pp. 356–359. DOI: `10.1680/geot.1961.11.4.356`.

Hansen, B., F. Nowiacki, E. Skomedal, and J. Hermstad (1992). "Foundation Design Troll platfrom". In: *Proceedings of the sixth international conference 1992 (BOSS '92)*. Ed. by BPP Technical Services Ldt. London, pp. 921–936.

Hansteen, O., H. Jostad, and T. Tjelta (2003). "Observed platform response to a "monster" wave". In: *Field measurements in geomechanics*. Ed. by F. Myrvoll. Lisse: Balkema, pp. 73–86. DOI: `10.1201/9781439833483.ch11`.

Houlsby, G. T. and B. W. Byrne (2005a). "Design procedures for installation of suction caissons in clay and other materials". In: *Proceedings of the Institution of Civil Engineers - Geotechnical Engineering* 158.2, pp. 75–82. DOI: `10.1680/geng.2005.158.2.75`.

– (2005b). "Design procedures for installation of suction caissons in sand". In: *Geotechnical Engineering* 158.3, pp. 135–144. DOI: `10.1680/geng.158.3.135.66297`.

Houlsby, G. T., R. Kelly, and B. W. Byrne (2005). "The tensile capacity of suction caissons in sand under rapid loading". In: *Frontiers in offshore geotechnics*. Ed. by S. Gourvenec and M. J. Cassidy. Balkema. London: Taylor & Francis. DOI: `10.1201/NOE0415390637.ch40`.

Houlsby, G. T., R. B. Kelly, J. Huxtable, and B. W. Byrne (2006). “Field trials of suction caissons in sand for offshore wind turbine foundations”. In: *Géotechnique* 56.1, pp. 3–10. DOI: `10.1680/geot.2006.56.1.3`.

House, A. R. (2002). “Suction Caisson Foundations for Buoyant Offshore Facilities”. Dissertation. Perth: The University of Western Australia.

Ibsen, L. B. (2008). “Implementation of a New Foundations Concept for Offshore Wind Farms”. In: *Proceedings Nordisk Geoteknikermøte nr. 15*, pp. 19–33.

Ibsen, L. B., M. Liingaard, and S. A. Nielsen (2005). “Bucket Foundation, a status”. In: pp. 1–15.

Ibsen, L. B. and C. Thilsted (2010). “Numerical study of piping limits for suction installation of offshore skirted foundations and anchors in layered sand”. In: *Numerical methods in geotechnical engineering.* Ed. by T. Benz and S. Nordal. Boca Raton, FL.: CRC Press, pp. 421–426. DOI: `10.1201/b10132-50`.

Jassim, I., D. Stolle, and P. Vermeer (2013). “Two-phase dynamic analysis by material point method”. In: *International Journal for Numerical and Analytical Methods in Geomechanics* 37.15, pp. 2502–2522. DOI: `10.1002/nag.2146`.

Jeong, Y. H., H. J. Park, D. S. Kim, and J. H. Kim (2018). “Cyclic behaviour of unit bucket for tripod foundation system under various loading characteristics via centrifuge”. In: *Physical Modelling In Geotechnics, Volume 1.* [S.l.]: CRC Press, pp. 609–614.

Jostad, H. and K. H. Andersen (2015). “Calculation of undrained holding capacity of suction anchors in clays”. In: *Frontiers in offshore geotechnics III.* Ed. by V. Meyer. Leiden, Netherlands: CRC Press/Balkema, pp. 263–268. DOI: `10.1201/b18442-21`.

Kelly, R. B., G. T. Houlsby, and B. W. Byrne (2006a). “A comparison of field and laboratory tests of caisson foundations in sand and clay”. In: *Géotechnique* 56.9, pp. 617–626.

– (2006b). “Transient Vertical Loading of Model Suction Caissons in a Pressure Chamber”. In: *Géotechnique* 10, pp. 665–675. DOI: `10.1680/geot.2006.56.10.665`.

Kim, D. J., J. U. Youn, S. H. Jee, J. Shoi, Y. W. Choo, S. Kim, J. H. Kim, D. S. Kim, and J. S. Lee (2013). “Centrifuge test and numerical modeling for a suction bucket monopod foundation”. In: *Proceedings of the 18th International Conference on Soil Mechanics and Geotechnical Engineering, Paris 2013.* Ed. by P. Delage, J. Desrues, R. Frank, A. Puech, and F. Schlosser. Paris: Presses des Ponts, pp. 2355–2358.

Kita, K, T. Utsunomiya, and K. Sekita (2018). “Centrifuge model tests on holding capacity of suction anchors in sandy deposits”. In: *Physical Modelling In Geotechnics, Volume 1.* [S.l.]: CRC Press, pp. 713–717.

Ladd, C. C., R. Foot, K. Ishihara, F. Schlosser, and H. G. Poulos (1977). “Stress-Deformation and Strength Characteristics”. In: *Proceedings of the 9th International Conference on Soil Mechanics and Foundation Engineering.* Ed. by Japanese Society of Soil Mechanics and Foundation Engineering, pp. 421–494.

Larsen, K. A. (2008). “Static Behaviour of Bucket Foundations”. Dissertation. Aalborg: Aalborg University.

Lehane, B. M. and Q. B. Liu (2013). “Measurement of Shearing Characteristics of Granular Materials at Low Stress Levels in a Shear Box”. In: *Geotechnical and Geological Engineering* 31.1, pp. 329–336. DOI: `10.1007/s10706-012-9571-9`.

Lehane, B. M., C. D. O'Loughlin, C. Gaudin, and M. F. Randolph (2009). "Rate effects on penetrometer resistance in kaolin". In: *Géotechnique* 59.1, pp. 41–52. DOI: `10.1680/geot.2007.00072`.

Liu, M., J. Lian, and M. Yang (2017). "Experimental and numerical studies on lateral bearing capacity of bucket foundation in saturated sand". In: *Ocean Engineering* 144, pp. 14–20. DOI: `10.1016/j.oceaneng.2016.04.001`.

Low, H. E., T. Lunne, K. H. Andersen, M. A. Sjursen, X. LI, M. F. Randolph, and K. H. Andersen (2010). "Estimation of intact and remoulded undrained shear strengths from penetration tests in soft clays". In: *Géotechnique* 60.11, pp. 843–859. DOI: `10.1680/geot.9.P.017`.

Madsen, S., L. V. Andersen, and L. B. Ibsen (2013). "Numerical buckling analysis of large suction caissons for wind turbines on deep water". In: *Engineering Structures* 57, pp. 443–452. DOI: `10.1016/j.engstruct.2013.09.041`.

Mana, D. S. K., S. M. Gourvenec, M. F. Randolph, and M. S. Hossain (2012). "Failure mechanisms of skirted foundations in uplift and compression". In: *International Journal of Physical Modelling in Geotechnics* 12.2, pp. 47–62. DOI: `10.1680/ijpmg.11.00007`.

Mašín, D. (2019). *Modelling of Soil Behaviour with Hypoplasticity: Another Approach to Soil Constitutive Modelling.* Springer Series in Geomechanics and Geoengineering. Cham: Springer International Publishing. DOI: `10.1007/978-3-030-03976-9`.

Masui, N., H. Yoneda, Y. Zenda, M. Ito, Y. Iida, and J. Hermstad (2001). "Installation of Offshore Concrete Structure with Skirt Foundation". In: *Proceedings 11th International on Offshore and Polar Engineering Conference*, pp. 626–630.

Nielsen, S., L. B. Ibsen, and B. Nielsen (2015). "Dynamic behaviour of mono bucket foundations subjected to combined transient loading". In: *Frontiers in offshore geotechnics III*. Ed. by V. Meyer. Leiden, Netherlands: CRC Press/Balkema, pp. 313–318. DOI: `10.1201/b18442-29`.

Niemunis, A. (1996). "A visco-plastic model for clay and its FE-implementation". In: *Resultats recents en mechanique des sols et des roches XI Colloque Franco-Polonais.* Gdańsk.

– (2003). "Extended hypoplastic models for soils". Habilitation. Gdanska: Politechnika Gdanska. URL: `http://www.pg.gda.pl/~aniem/an-liter.html`.

Niemunis, A., C. E. Grandas-Tavera, and L. F. Prada-Sarmiento (2009). "Anisotropic visco-hypoplasticity". In: *Acta Geotechnica* 4.4, pp. 293–314. DOI: `10.1007/s11440-009-0106-3`.

Niemunis, A. and I. Herle (1997). "Hypoplastic model for cohesionless soils with elastic strain range". In: *Mechanics of Cohesive-frictional Materials* 2.4, pp. 279–299. DOI: `10.1002/(SICI)1099-1484(199710)2:4279::AID-CFM293.0.CO;2-8`.

Niemunis, A. and S. Krieg (1996). "Viscous behaviour of soil under oedometric conditions". In: *Canadian Geotechnical Journal* 33.1, pp. 159–168. DOI: `10.1139/t96-031`.

Poblete, M., W. Fuentes, and T. Triantafyllidis (2016). "On the simulation of multidimensional cyclic loading with intergranular strain". In: *Acta Geotechnica* 11.6, pp. 1263–1285. DOI: `10.1007/s11440-016-0492-2`.

Pucker, T., B. Bienen, and S. Henke (2012). "Numerical Simulation of Spudcan Penetration Into Silica Sand and Prediction of Bearing Behaviour". In: *Proceedings of the ASME*

31st International Conference on Ocean, Offshore and Arctic Engineering - 2012. New York, NY: ASME, pp. 47–56. DOI: `10.1115/OMAE2012-83042`.

Qui, G. (2012). “Coupled Eulerian Lagrangian Simulations of Selected Soil-Structure Interaction Problems”. PhD thesis. Hamburg: Hamburg University of Technology.

Ragni, R., B. Bienen, C. D. O’Loughlin, S. A. Stanier, M. J. Cassidy, and N. Morgan (2020). “Observations of the Effects of a Clay Layer on Suction Bucket Installation in Sand”. In: *Journal of Geotechnical and Geoenvironmental Engineering* 146.5.

Ragni, R., B. Bienen, S. A. Stanier, M. J. Cassidy, and C. D. O’Loughlin (2018). “Visualisation of mechanisms governing suction bucket installation in dense sand”. In: *Physical Modelling In Geotechnics, Volume 1.* [S.l.]: CRC Press, pp. 651–565.

Ragni, R., B. Bienen, S. A. Stanier, C. D. O’Loughlin, and M. J. Cassidy (2019). “Observations during suction bucket installation in sand”. In: *International Journal of Physical Modelling in Geotechnics*, pp. 1–49. DOI: `10.1680/jphmg.18.00071`.

Raines, R. D., O. Ugaz, and J. Garnier (2005). “Centrifuge modeling of suction piles in clay”. In: *Frontiers in offshore geotechnics.* Ed. by S. Gourvenec and M. J. Cassidy. Balkema. London: Taylor & Francis, pp. 303–308.

Randolph, M. F. and C. Gaudin (2017). “Genesis of the national geotechnical centrifuge facility - a 30 year perspective.” In: *Australian Geomechanics Journal* 52.2, pp. 1–14.

Randolph, M. F., R. J. Jewell, K. J. L. Stone, and T. A. Brown (1991). “Establishing a new Centrifuge Facility”. In: *Proceedings International Conference Centrifuge 1991.* Ed. by H.-J. Ko and F. G. McLean. Rotterdamm: Belkema, pp. 3–9.

Randolph, M. F., M. P. O’Neill, D. P. Stewart, and C. Erbrich (1998). “Performance of Suction Anchors in Fine-Grained Calcareous Soils”. In: *Offshore Technology Conference 1998.* Vol. OTC 8831. Offshore Technology Conference, pp. 521–529. DOI: `10.4043/8831-MS`.

Schofield, A. N. and Peter Wroth (1968). *Critical state soil mechanics.* European civil engineering series. London and New York: McGraw-Hill.

Senders, M. (2008). “Suction Caissons in Sand as Tripod Foundations for Offshore Wind Turbines”. PhD thesis. Perth: The University of Western Australia.

Senders, M. and M. F. Randolph (2007). “Theory for the Installation of Suction Caissons in Sand Overlaid by Clay”. In: *Offshore site investigation and geotechnics.* London: Soc. for Underwater Techn, pp. 429–438.

– (2009). “CPT-Based Method for the Installation of Suction Caissons in Sand”. In: *Journal of Geotechnical and Geoenvironmental Engineering* 135.1, pp. 14–25. DOI: `10.1061/(ASCE)1090-0241(2009)135:1(14)`.

Senpere, D. and G. A. Auvergne (1982). “Suction Anchor Piles - A Proven Alternative to Driving or Drilling”. In: *Offshore Technology Conference 1982.* Vol. OTC 4206. Offshore Technology Conference, pp. 483–493. DOI: `10.4043/4206-MS`.

Shen, K., Y. Zhang, R. T. Klinkvort, H. Sturm, H. P. Jostad, N. Sivasithamparam, and Z. Guo (2017). “Numerical Simulation of Suction Bucket Under Vertical Tension Loading”. In: *Offshore site investigation and geotechnics.* Ed. by Society for Underwater Technology. London, UK: Society for Underwater Technology, pp. 488–497. DOI: `10.3723/OSIG17.488`.

Skau, K. S., H. P. Jostad, G. Eiksund, and H. Sturm (2019). "Modelling of soil-structure-interaction for flexible caissons for offshore wind turbines". In: *Ocean Engineering* 171, pp. 273–285. DOI: `10.1016/j.oceaneng.2018.10.035`.

Stanier, S. A., J. Blaber, W. A. Take, and D. J. White (2016a). "Improved image-based deformation measurement for geotechnical applications". In: *Canadian Geotechnical Journal* 53.5, pp. 727–739.

Stanier, S. A., J. Breen, and D. J. White (2014). "A Compact High-Speed Image Capture System for a Drum Centrifuge". In: *Physical modelling in geotechnics*. Ed. by C. Gaudin and D. J. White. Boca Raton et al.: CRC Press a Balkema book, pp. 241–246. DOI: `10.1201/b16200-27`.

Stanier, S. A., J. Dijkstra, D. Leśniewska, J. Hambleton, D. J. White, and D. Muir Wood (2016b). "Vermiculate artefacts in image analysis of granular materials". In: *Computers and Geotechnics* 72, pp. 100–113.

Stanier, S. A. and D. J. White (2013). "Improved Image-Based Deformation Measurement in the Centrifuge Environment". In: *Geotechnical Testing Journal* 36.6, pp. 915–928. DOI: `10.1520/GTJ20130044`.

Stapelfeldt, M., D. Alkateeb, J. Grabe, and B. Bienen (2020). "Numerical simulation of cone penetration tests inside suction caisson foundations in sand". In: *Proceedings of the 39th International Conference on Ocean, Offshore and Arctic Engineering*. Virtual, Online.

Stapelfeldt, M., B. Bienen, and J. Grabe (2018). "Centrifuge tests investigating the effect of suction caisson installation in dense sand on the state of the soil plug". In: *Physical Modelling In Geotechnics, Volume 1*. [S.l.]: CRC Press, pp. 669–674.

Stapelfeldt, M., J. Bubel, and J. Grabe (2015). "Numerical Investigation of the Installation Process and the Bearing Capacity of Suction Bucket Foundations". In: *Proceedings of the 34th International Conference on Ocean, Offshore and Arctic Engineering*. St. John's, Newfoundland.

Sturm, H. (2017). "Design Aspects of Suction Caissons for Offshore Wind Turbine Foundations". In: *Proceedings of TC 209 workshop*. Ed. by ISSMGE Technical Committee TC 209, pp. 45–63.

Stutz, H., D. Mašín, A. S. Sattari, and F. Wuttke (2017). "A general approach to model interfaces using existing soil constitutive models application to hypoplasticity". In: *Computers and Geotechnics* 87, pp. 115–127. DOI: `10.1016/j.compgeo.2017.02.010`.

Stutz, H., D. Mašín, and F. Wuttke (2016). "Enhancement of a hypoplastic model for granular soil–structure interface behaviour". In: *Acta Geotechnica* 11.6, pp. 1249–1261. DOI: `10.1007/s11440-016-0440-1`.

Sulsky, D., Z. Chen, and H. L. Schreyer (1994). "A particle method for history-dependent materials". In: *Computer Methods in Applied Mechanics and Engineering* 118.1-2, pp. 179–196.

Sulsky, D. and H. L. Schreyer (1996). "Axisymmetric form of the material point method with applications to upsetting and Taylor impact problems". In: *Computer Methods in Applied Mechanics and Engineering* 139.1-4, pp. 409–429.

Sulsky, D., S.-J. Zhou, and H. L. Schreyer (1995). "Application of a particle-in-cell method to solid mechanics". In: *Computer Physics Communications* 87.1-2, pp. 236–252.

Sutton, M. A., W. J. Wolters, W. H. Peters, W. F. Ranson, and McNeill (1983). "Determination of displacements using an improved digital correlation method". In: *Image and Vision Computing* 1.3, pp. 133–139. DOI: `10.1016/0262-8856(83)90064-1`.

Al-Tabbaa, A. and D. M. Wood (1987). "Some measurements of the permeability of kaolin". In: *Géotechnique* 37.4, pp. 499–514. DOI: `10.1680/geot.1987.37.4.499`.

Tafili, M. and T. Triantafyllidis (2018). "On constitutive modelling of anisotropic viscous and non-viscous soft soils". In: *Numerical Methods in Geotechnical Engineering IX, Volume 1*. Ed. by M. de Matos Fernandes. Milton: Chapman and Hall/CRC, pp. 481–486.

Tan, T.-S. and R. F. Scott (1985). "Centrifuge scaling considerations for fluid-particle systems: Centrifuge scaling considerations for fluid-particle systems". In: *Géotechnique* 35.4, pp. 461–470. DOI: `10.1680/geot.1985.35.4.461`.

– (1987). "Discussion: Centrifuge scaling considerations for fluid-particle systems". In: *Géotechnique* 37.1, pp. 131–133. DOI: `10.1680/geot.1987.37.1.131`.

Taylor, R. N. (2011). *Geotechnical centrifuge technology*. London: Taylor & Francis.

Teng, Y., S. A. Stanier, and S. M. Gourvenec (2017). "Synchronised multi-scale image analysis of soil deformations". In: *International Journal of Physical Modelling in Geotechnics* 17.1, pp. 53–71. DOI: `10.1680/jphmg.15.00058`.

Terzaghi, K. and O. K. Fröhlich (1936). *Theorie der Setzung von Tonschichten: eine Einführung in die analytische Tonmechanik*. Leipzig and Wien: Deuticke.

Tjelta, T. I. (1994). "Geotechnical Aspects Of Bucket Foundations Replacing Piles For The Europipe 16/11-E Jacket". In: *Offshore Technology Conference 1994*. Vol. OTC 7379. Offshore Technology Conference, pp. 73–82. DOI: `10.4043/7379-MS`.

– (1995). "Geotechnical Experience from the Installation of the Europipe Jacket with Bucket Foundations". In: *Offshore Technology Conference 1995*. Vol. OTC 7795. Offshore Technology Conference, pp. 897–908. DOI: `10.4043/7795-MS`.

– (2015). "The suction foundation technology". In: *Frontiers in offshore geotechnics III*. Ed. by V. Meyer. Leiden, Netherlands: CRC Press/Balkema, pp. 85–93. DOI: `10.1201/b18442-6`.

Tjelta, T. I., P. M. Aas, J. Hermstad, and E. Andenaes (1990). "The Skirt Piled Gullfaks C Platform Installation". In: *Offshore Technology Conference 1990*. Vol. OTC 7379. Offshore Technology Conference, pp. 453–462. DOI: `10.4043/6473-MS`.

Tjelta, T. I., T. R. Guttormsen, and J. Hermstad (1986). "Large-Scale Penetration Test at a Deepwater Site". In: *Offshore Technology Conference 1986*. Vol. OTC 5103. Offshore Technology Conference, pp. 201–2012. DOI: `10.4043/5103-MS`.

Tran, M. N. (2005). "Installation of Suction Caissons in Dense Sand and the Influence of Silt and Cemented Layers". PhD thesis. Sydney: The University of Sydney.

Tran, M. N. and M. F. Randolph (2008). "Variation of Suction Pressure During Caisson Installation in Sand". In: *Géotechnique* 58.1, pp. 1–11. DOI: `10.1680/geot.2008.58.1.1`.

Tran, M. N., M. F. Randolph, and D. W. Airey (2004). "Experimental Study of Suction Installation of Caissons in Dense Sand". In: *Proceedings of the 23rd International Conference on Offshore Mechanics and Arctic Engineering - 2004*. New York, NY: ASME, pp. 105–112. DOI: `10.1115/OMAE2004-51076`.

– (2007). “Installation of Suction Caissons in Sand with Silt Layers”. In: *Journal of Geotechnical and Geoenvironmental Engineering* 133.10, pp. 1183–1191. DOI: `10.1061/(ASCE)1090-0241(2007)133:10(1183)`.

Tran, N. X., L. Chi Hung, and S.-R. Kim (2017). “Evaluation of horizontal and moment bearing capacities of tripod bucket foundations in sand”. In: *Ocean Engineering* 140, pp. 209–221. DOI: `10.1016/j.oceaneng.2017.05.012`.

van Esch, J. M., D. Stolle, and I. Jassim (2011). “Finite Element Method for Coupled Dynamic Flow-Deformation Simulation”. In: *Proceedings of the 2nd International Symposium on Computational Geomechanics (COMGEO II).* Cavtat-Dubrovnik, Croatia, pp. 415–424.

Verruijt, A. (2010). *An introduction to soil dynamics.* Vol. 24. Theory and Applications of Transport in Porous Media. Dordrecht: Springer Netherland.

von Wolffersdorff, P.-A. (1996). “A hypoplastic relation for granular materials with a predefined limit state surface”. In: *Mechanics of Cohesive-frictional Materials* 1.3, pp. 251–271. DOI: `10.1002/(SICI)1099-1484(199607)1:3251::AID-CFM133.0.CO;2-3`.

Watson, P. G., C. Gaudin, M. Senders, and M. F. Randolph (2006). “Installation of Suction Caissons in Layered Soil”. In: *6th International Conference on Physical Modelling in Geotechnics (ICPMG) // Physical Modelling in Geotechnics, Two Volume Set.* Ed. by C.W.W. Ng, Y. H. Wang, and L. M. Zhang. Hoboken: CRC Press, pp. 685–692.

Wegener, D. and I. Herle (2013). “Akkumulation bleibender Verformungen infolge dynamischer Belastung mittels numerischer Verfahren”. In: *Vorträge zum 9. Hans-Lorenz-Symposium.* Ed. by Bettina Albers. Veröffentlichungen des Grundbauinstitutes der Technischen Universität Berlin. Aachen: Shaker, pp. 153–172.

White, D. J., W. A. Take, and M. D. Bolton (2003). “Soil deformation measurement using particle image velocimetry (PIV) and photogrammetry”. In: *Géotechnique* 53.7, pp. 619–631. DOI: `10.1680/geot.53.7.619.37383`.

White, D. J., W. A. Take, M. D. Bolton, and S. E. Munachen (2001). “A deformation measurement system for geotechnical testing based on digital imaging, close-range photogrammetry, and PIV image analysis”. In: *Proceedings of the Fifteenth International Conference on Soil Mechanics and Geotechnical Engineering.* Lisse: Balkema, pp. 539–542.

Whyte, S., C. M. Martin, H. J. Burd, B. Bienen, M. F. Randolph, M. Rattley, and M. Stapelfeldt (2020). “Suitability of bounding surface model for numerical simulations of centrifuge suction bucket pull-out tests in dense sand”. In: *Computers and Geotechnics* 0. under review, pp. 1–20.

Zeinoddini, M., S. A. Mousavi, and M. R. Abdi (2011). “Simulation of Suction Caisson Penetration in Seabed Using an Adaptive Mesh Technique”. In: *Procedia Engineering* 14, pp. 1721–1728. DOI: `10.1016/j.proeng.2011.07.216`.

Zhang, X., Z. Chen, and Y. Liu (2017). *The Material Point Method: A Continuum-Based Particle Method.* First edition. Elsevier and Tsinghua University Press computational mechanics series. Amsterdam and Oxford, UK: Elsevier and Academic Press.

Zhu, F., B Bienen, C. D. O’Loughlin, N. Morgan, and M. J. Cassidy (2018a). “The response of suction caissons to multidirectional lateral cyclic loading in sand over clay”. In: *Ocean Engineering* 170, pp. 43–54.

Zhu, F., C. D. O’Loughlin, B. Bienen, M. J. Cassidy, and N. Morgan (2018b). “The response of suction caissons to long-term lateral cyclic loading in single-layer and layered seabeds”. In: *Géotechnique* 68.8, pp. 729–741.

Zhu, F., C. D. O’Loughlin, B. Bienen, and C. D. O’Loughlin (2017). “Physical modelling of suction bucket installation and response under long-term cyclic loading”. In: *Offshore site investigation and geotechnics*. Ed. by Society for Underwater Technology. London, UK: Society for Underwater Technology, pp. 524–531.

Zienkiewicz, O. C., C. T. Chang, and P. Bettess (1980). “Drained, undrained, consolidating and dynamic behaviour assumptions in soils”. In: *Géotechnique* 30.4, pp. 385–395.

Zienkiewicz, O. C. and T. Shiomi (1984). “Dynamic behaviour of saturated porous media; The generalized Biot formulation and its numerical solution”. In: *International Journal for Numerical and Analytical Methods in Geomechanics* 8.1, pp. 71–96.

Zografou, D., S. Gourvenec, and C. D. O’Loughlin (2019). “Vertical cyclic loading response of shallow skirted foundation in soft normally consolidated clay”. In: *Canadian Geotechnical Journal* 56.4, pp. 473–483. DOI: `10.1139/cgj-2018-0179`.

Appendix A Notation

The following list includes symbols that will be used in this document.

Abbreviations

BC	Boundary condition
CoS	Clay over sand
CPT	Cone penetration test
CYC	Cyclic loading test
DC	Displacement controlled
DIC	Digital image correlation
F, f	Fast pumping flow rate
FEM	Finite element method
H	High effective permeability
INST	Installation test
ISA	Intergranular strain anisotropy
J	Jacked installation
L	Low effective permeability
LC	Load case
LDT	Linear displacement transducer
LHS	Left hand side
LSQ	Load sequence
M	Moderate pumping flow rate
MCM	Mohr-Coulomb constitutive model
MP	Material point
MPM	Material point method

MS	Medium slow pumping flow rate
OWT	Offshore wind turbine
PFLR	Pumping flow rate
PIV	Particle image velocimetry
PPT	Pore pressure transducer
RHS	Right hand side
S, s	Slow pumping flow rate
SF	Super fast pumping flow rate
SI	Suction installation
SL	Static loading
SoC	Sand over clay
SWP	Self-weight penetration
TPT	Total pressure transducer
TRE	Tresca constitutive model
TUHH	Hamburg University of Technology
UL	Static un-loading
UWA	The University of Western Australia
VHP	Visco-hypoplastic constitutive model

Greek symbols

α	Adhesion factor
α	Dilatancy exponent
β	Pyknotropy exponent
β_{h0}	Intergranular strain hardening exponent
β_{hmax}	Maximum intergranular strain hardening parameter
β_R	Intergranular strain hardening parameter
β_r	Shape of rendulic surface
χ_0	Minimum value of intergranular strain exponent

χ_{max}	Maximum value of intergranular strain exponent
Δ	Differential of a related variable
δ	Interface friction angle
η	Dynamic viscosity
γ	Shear strain
γ_w	Specific weight of water
γ_i	Allowable elastic slip
κ	Intrinsic permeability
κ	Swelling index
λ	Compression index
μ	Interface frictional coefficient
μ_c	Degree of consolidation
ν	Poisson’s ratio
ω	Integration weight
ψ	Dilation angle
ρ	Density
ρ_s	Grain density, solid density
ρ_s	Density solid
ρ_w	Density Water
σ	Stresses
τ	Dimensionless time factor
τ_{max}	Shear stress limit
ε	Strains
φ	Friction angle
φ'	Peak friction angle
φ_c	Critical friction angle
ξ	Location within an element

chi	Stiffens degradation exponent

Roman symbols

$\dot{z}$	Penetration rate
$\mathbf{B}$	Matrix of shape functions
A	Area
a	Amplitude
a_p	Pressure factor
C	Courant number
c	Dimensionless coefficient
c'	Effective cohesion
c_a	Accumulation rate factor
c_v	Coefficient of consolidation
c_z	Cyclic mobility factor
D	Diameter
d	Soil layer thickness
D_r	Relative density
D_R	Reference creep rate
E	Young's modulus
e_0	Initial void ratio
e_{max}	Maximum void ratio
e_{min}	Minimum void ratio
E_s	Stiffness modulus
F	Force
f	Frequency
f^{int}	Internal forces
f^{trac}	Traction forces
F_{flow}	Dimensionless flow factor

F_{in}, F_{out}	Internal and external frictional resistance
g	Gravity acceleration
h	Height
i	Hydraulic gradient
I_v	Leinenkugel's index of viscosity
K_0	Lateral pressure coefficient
k_F	Ratio of internal and external permeability
k_f	Effective permeability
k_i, k_o	Internal and external effective permeability
K_w	Bulk modulus water
L	Length, Skirt Length
m_R	Stiffness factor (180 °)
m_T	Stiffness factor (90 °)
N	Scaling factor
n	Porosity
n_B	Barotropy exponent
N_c	Bearing capacity cohesion factor
$N_i, N_{mp}, \mathbf{N}$	Shape functions
N_q	Bearing capacity depth factor
OCR	Over consolidation ratio
q	Pumping flow rate
q_c	Cone tip resistance
R	Intergranular strain yield surface
R	Resistance
r	Radius
s	Suction pressure
s_u	Undrained shear strength

T	Time
t	Wall thickness
u	Displacement
V	Vertical load
v	Velocity
z	Vertical displacement with reference the soil surface

Subsets

40	$L = 40\,\mathrm{mm}$ model caisson
80	$L = 80\,\mathrm{mm}$ model caisson
ν_{ud}	Undrained Poisson's ratio
cav	Cavitation
cpt	Cone penetrometer
el	Element
h	Horizontal component
i, j	Universal counters
in	Inside, internal
m	Model
max	Maximum
min	Minimum
mp	Material point
n	Element node
out	Outside, external
p	Prototype
$pump$	syringe pump
$r, y,$	Cylindrical coordinate system axis
s	Skirt
t	Skirt tip

ud	Undrained
ul	Unloading
v	Vertical component
w	Water
x, y, z	Cartesian coordinate system axis

Appendix B Experimental arrangement

B.1 Centrifuge tests featuring CPTs inside the caisson in sand

Figure B.1: The Acutronic Model 661 centrifuge at the National Geotechnical Centrifuge Facility (NGCF) in Perth, Western Australia.

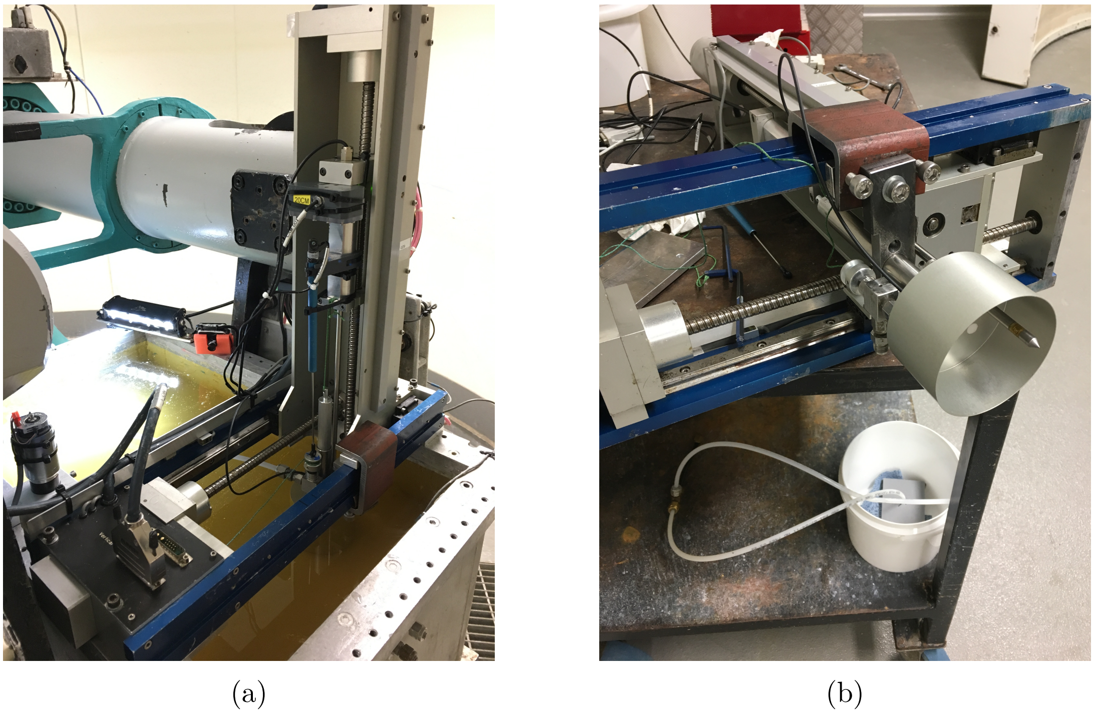

(a) (b)

Figure B.2: Centrifuge test set-up for CPTs through the lid mounted on the the strong box (a) and dismounted after a centrifuge test (b).

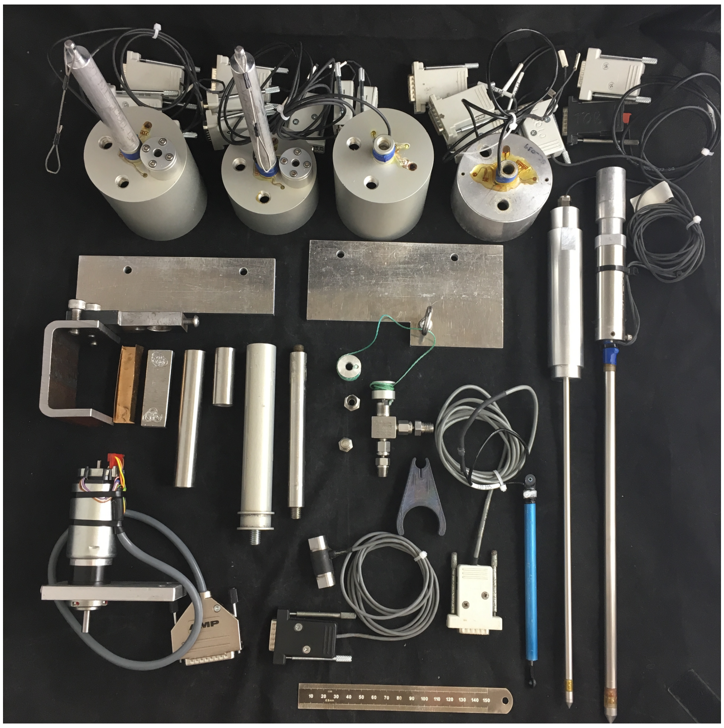

Figure B.3: Overview of the utilised equipment for the centrifuge tests.

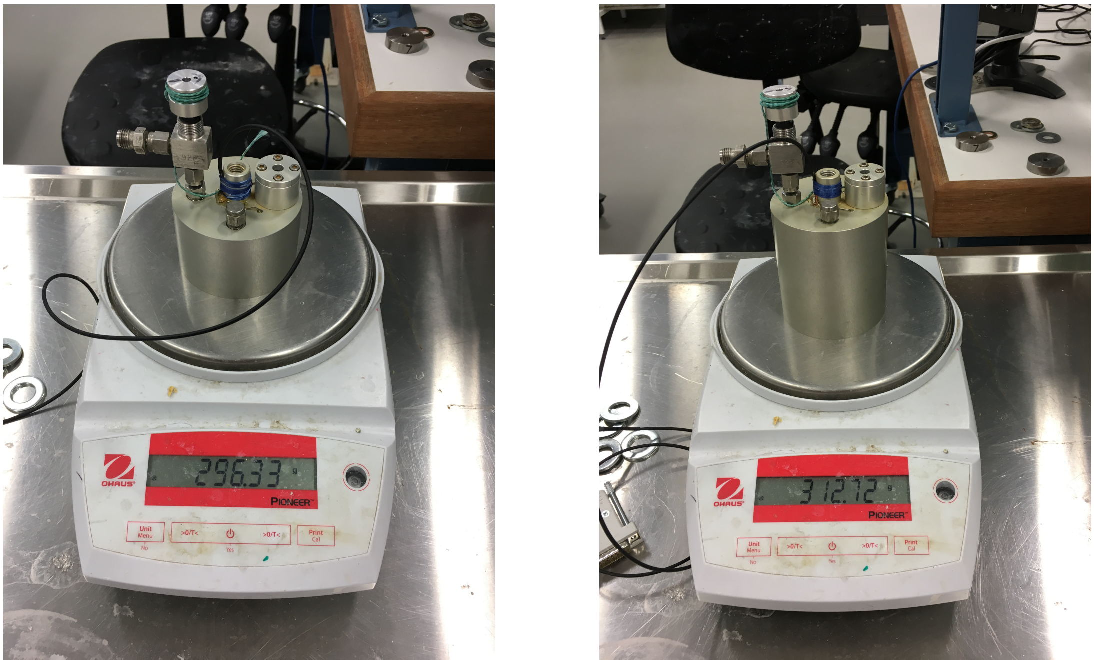

(a) (b)

Figure B.4: Model caissons for CPT through the lid with a diameter of $D = 80\,\mathrm{mm}$ and a skirt length of $L = 40\,\mathrm{mm}$ (a) and $L = 80\,\mathrm{mm}$ (b).

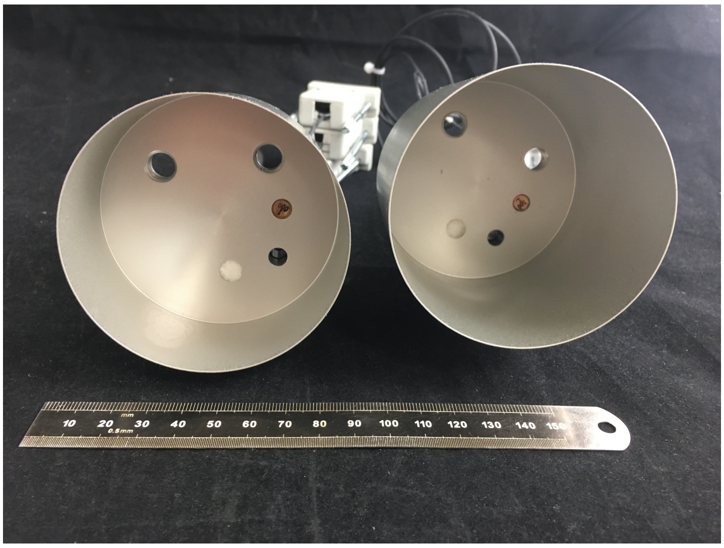

Figure B.5: Bottom view of the $L = 40\,\mathrm{mm}$ (left hand side) and $L = 80\,\mathrm{mm}$ (right hand side) model caisson for CPTs through the lid.

(a) (b)

Figure B.6: Three way valve (a) and bold plug (b).

(a) (b)

Figure B.7: Guide rod for the $L = 40\,\mathrm{mm}$ (a) and the $L = 80\,\mathrm{mm}$ (b) model caisson.

Figure B.8: Syringe pump mounted at the backside of the strong box.

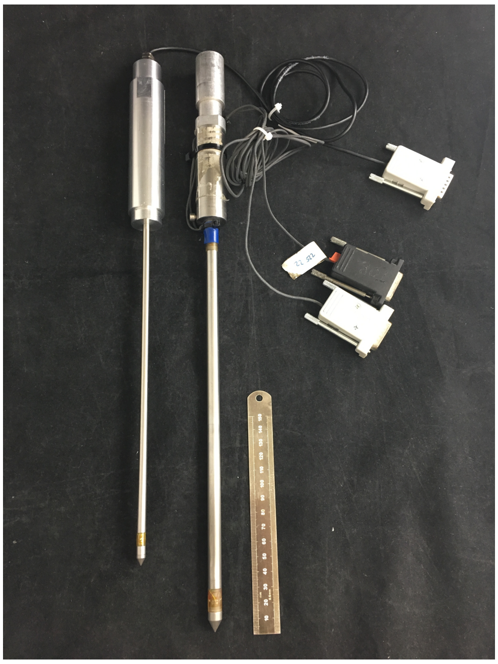

Figure B.9: Miniature cone penetrometer with diameters of $D_{cpt} = 6.3\,\mathrm{mm}$ (left hand side) and $D_{cpt} = 10\,\mathrm{mm}$ (right hand side).

B.2 Centrifuge tests featuring cyclic loading test in sand

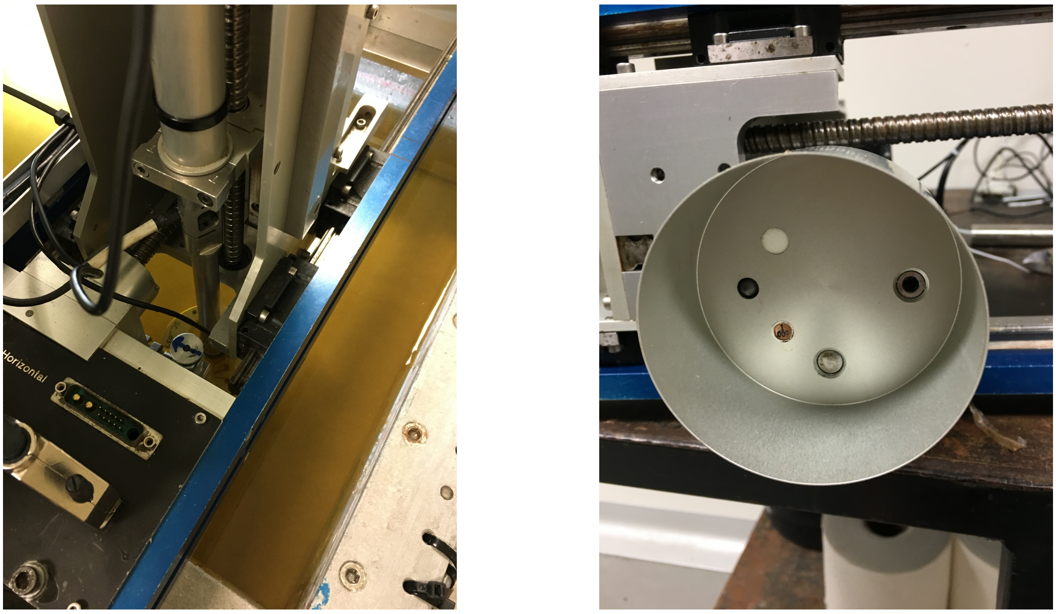

(a) (b)

Figure B.10: Centrifuge test set-up for cyclic loading tests mounted on the the strong box (a) and dismounted after a centrifuge test (b).

(a) (b)

Figure B.11: Model caissons for cyclic loading test with a diameter of $D = 80\,\mathrm{mm}$ and a skirt length of $L = 40\,\mathrm{mm}$ (a) and $L = 80\,\mathrm{mm}$ (b).

B.3 Centrifuge tests featuring PIV post-analyses in layered soil

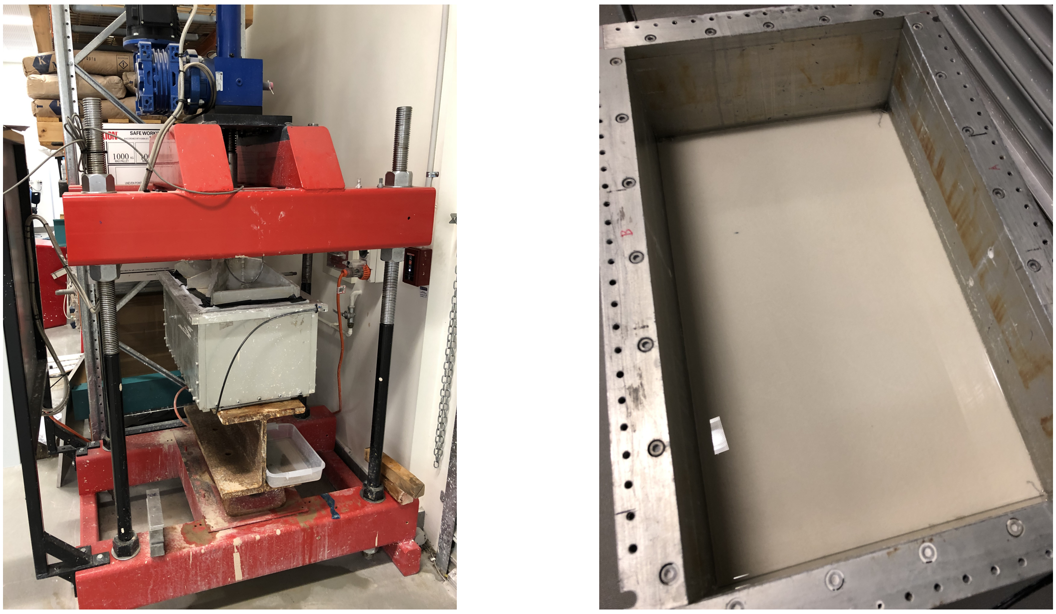

(a) (b)

Figure B.12: Clay consolidation press (a) and consolidated kaolin clay sample (b).

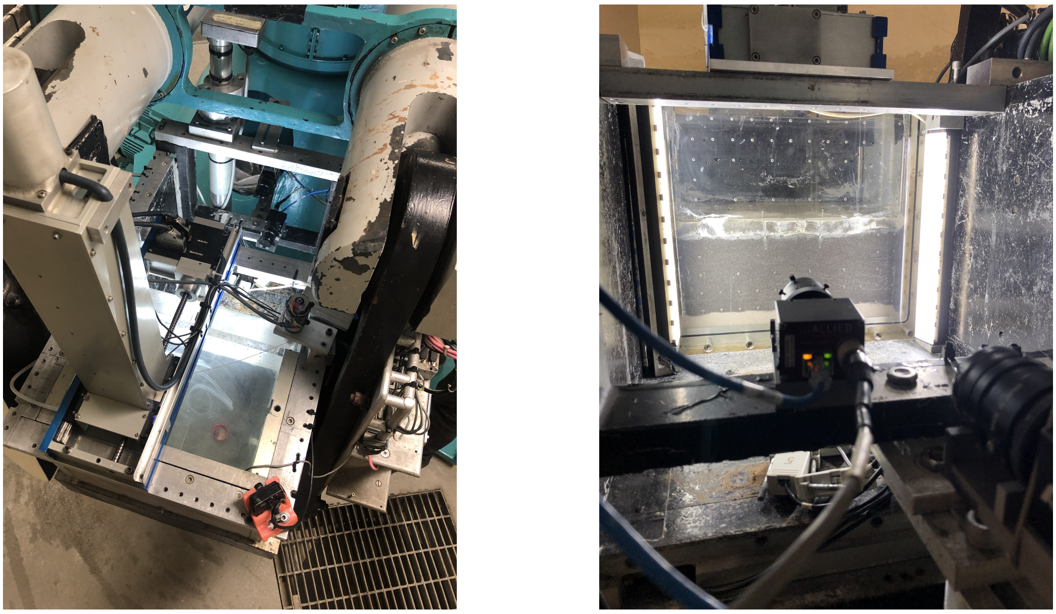

(a) (b)

Figure B.13: Centrifuge test set-up for PIV post analyses mounted on the the strong box (a) and camera perspective after testing (b).

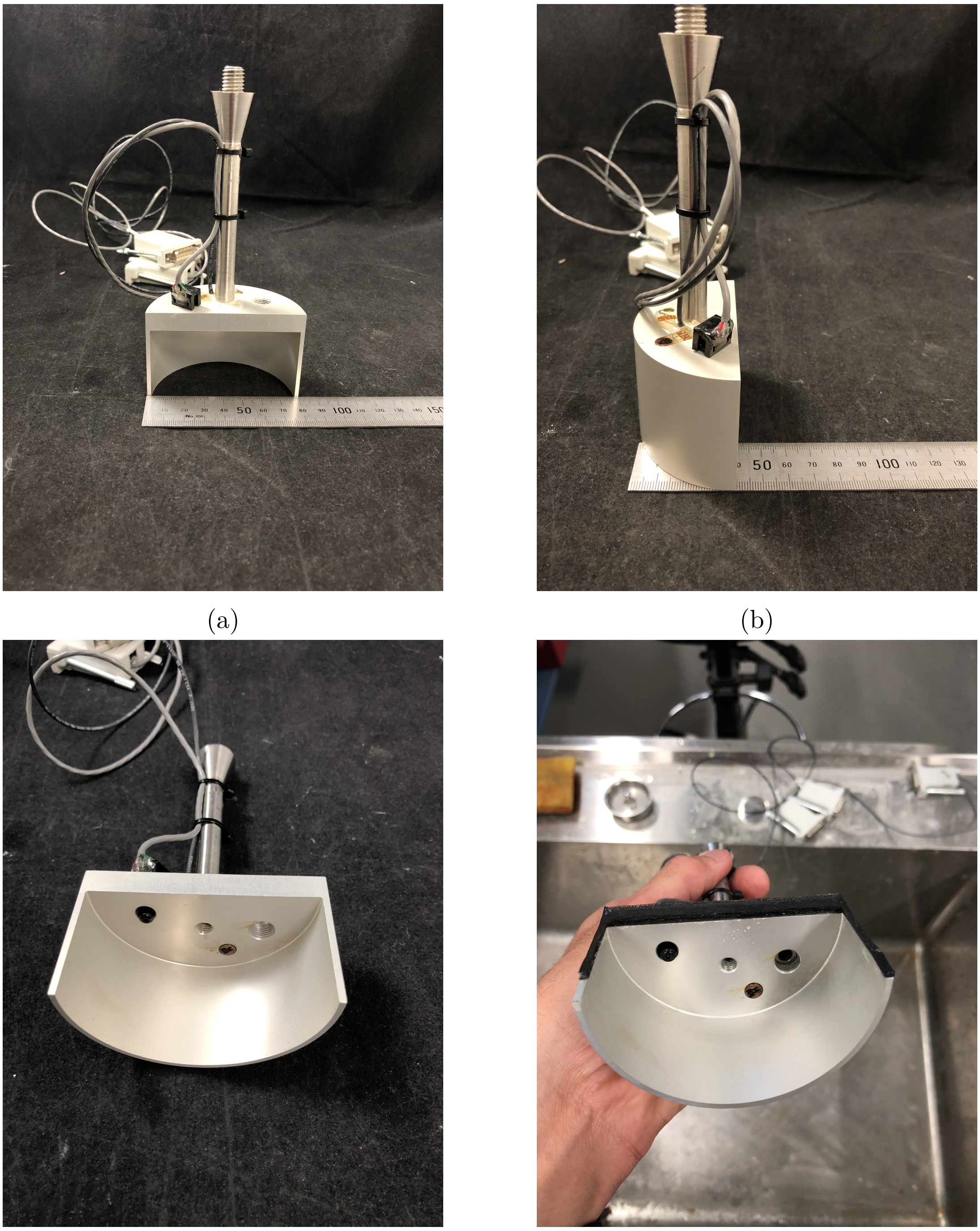
(a) (b)

(c) (d)

Figure B.14: Front (a), side (b), and bottom view (c) of the $D = 80\,\mathrm{mm}$ and $D = 40\,\mathrm{mm}$ half-model suction caisson equipped with a combined foam and rubber seal (d) that was damaged during the centrifuge test.

B.4 Centrifuge tests featuring cyclic loading test in layered soil

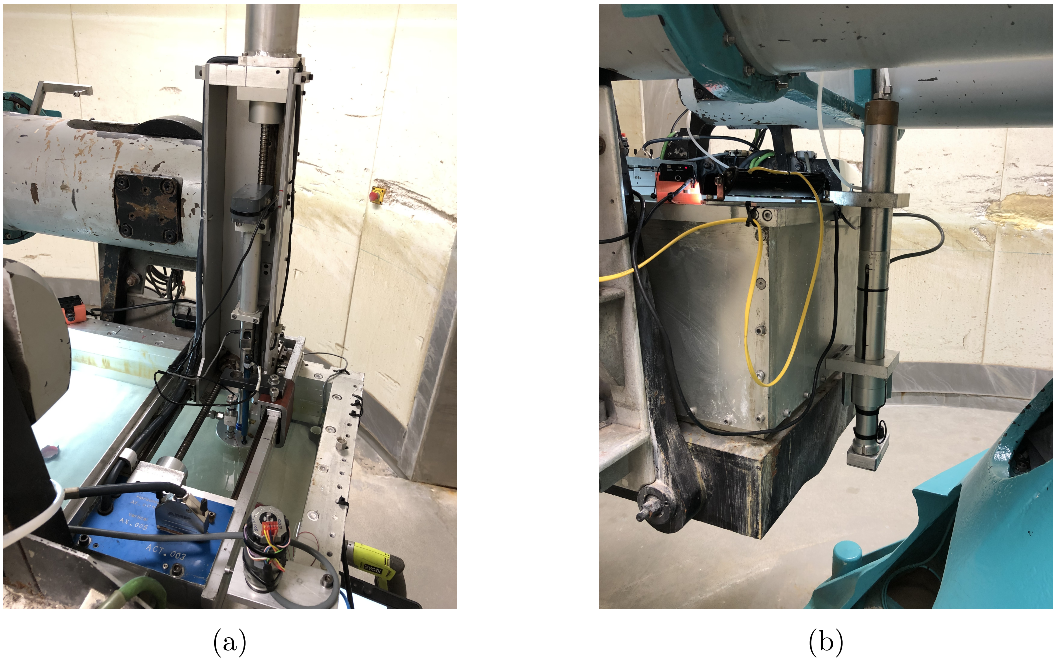
(a) (b)

Figure B.15: Centrifuge test set-up for cyclic loading (a) and syringe pump turned upside down and mounted on the the strong box (b) between tow tests.

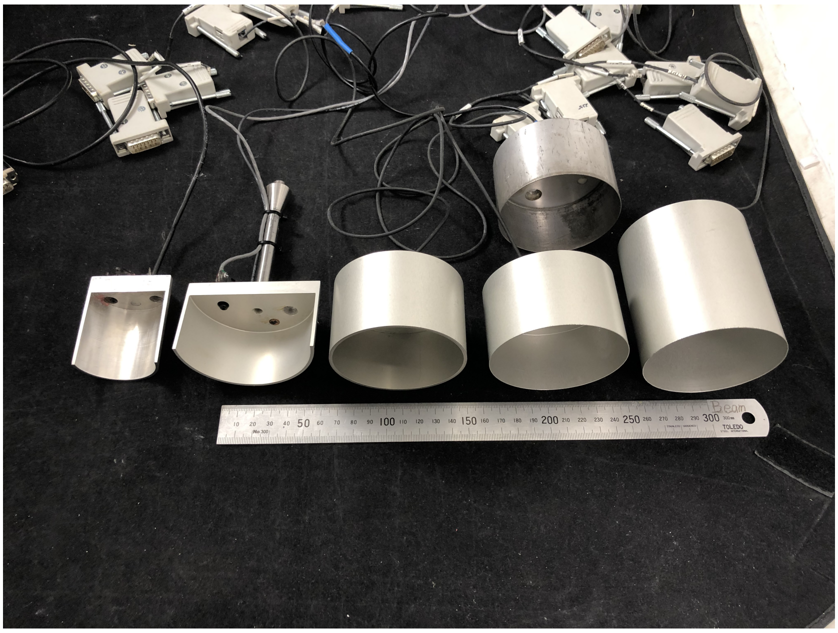

Figure B.16: Half-model caissons (left hand side), $L = 40\,\mathrm{mm}$ full-model caissons (middle), and $L = 80\,\mathrm{mm}$ full-model caisson (right hand side).

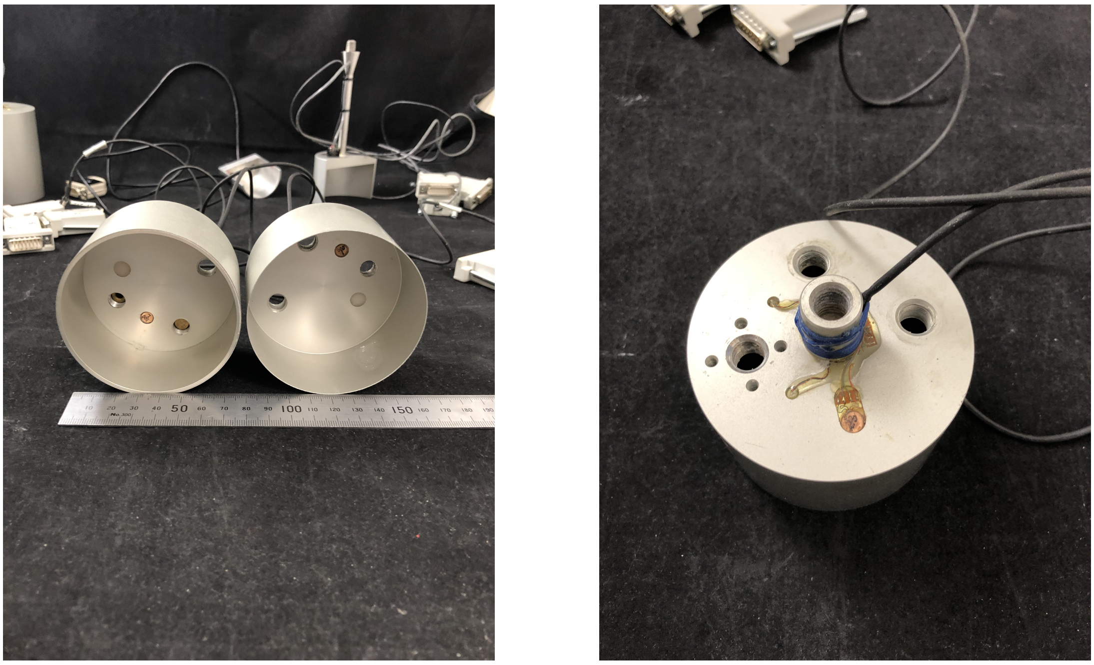

(a) (b)

Figure B.17: Bottom view of model caissons with $t = 2\,\text{mm}$ (left hand side) and $t = 0.5\,\text{mm}$ (right hand side) (a) and top view of the modified $L = 40\,\text{mm}$ caisson (b).

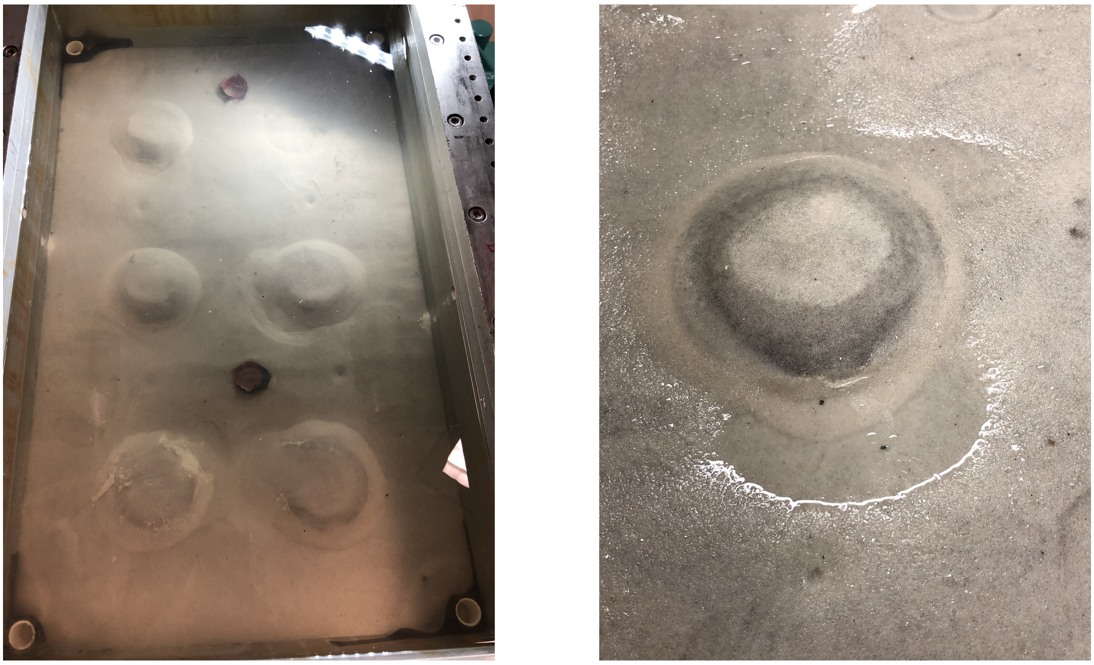

(a) (b)

Figure B.18: Soil surface of the sand over clay sample after centrifuge testing (a) and soil surface after a rapid extraction test (a).

(a) (b)

Figure B.19: Cross-section of a drained (a) and a rapid (b) extraction site in the sand over clay sample.

Figure B.20: Cross-section of two rapid extraction sites in the sand over clay sample.

(a) (b)

Figure B.21: Soil surface of a drained (a) and a rapid (b) extraction site in the clay over sand sample.

(a) (b)

Figure B.22: Left (a) and right (a) hand site of the soil layer boundary of the clay over sand sample after centrifuge testing.